FREQUENCY SELECTIVE GRATING FILTERS FOR INTEGRATED OPTICS

A THESIS

submitted to the Faculty of Engineering

of the University of Glasgow

for the degree of

Doctor of Philosophy

by

Alfredo Yi Yan

JUNE 1978

VOLUME CONTAINS CLEAR OVERLAYS

OVERLAYS SCANNED SEPERATELY AND OVER THE RELEVANT PAGE.

ACKNOWLEDGEMENTS.

I wish to express my sincere gratitude to Professor J. Lamb for his interest and encouragement during the course of this work as well as for providing the research facilities in the Department of Electronics and Electrical Engineering.

I would also like to thank Dr. C.D.W. Wilkinson and Dr. P.J.R. Laybourn for their constant help and advice in the supervision of this work and in the preparation of this thesis.

Mention must also be made of Dr. I. Anderson and Dr. R. Dunsmuir for many helpful discussions and Dr. J.A.H. Wilkinson for the elaboration of the computer programs.

I would like to address my special thanks to Mr. R.H. Hutchins for his constant encouragement and for looking after my personal well-being.

I appreciated the interest that Mr. R.J. Esdaile and Mr. J.G. Gallagher showed at the various stages of this investigation. The technical assistance of Mr. G. Boyle, Mr. J. Clark, Mr. H. Anderson, Mr. S. Orr, Mr. S. Brownlie, Mr. K. Piechowiak and Mrs. L. Hobson is greatfully acknowledged.

Finally, I wish to extend my appreciation to Mrs. A. Cunningham and Miss A. Munro who typed the thesis and to Mlle L. Allain and Mlle C. Baret who helped to proof read the manuscript.

This work was supported by a grant from the Faculty of Engineering, University of Glasgow.

ABSTRACT

The object of this thesis is the study of the filtering properties of periodically corrugated waveguides. Furthermore, the interest has been focussed, throughout this investigation, on single mode propagation.

Homogeneous and inhomogeneous waveguides have been used in the construction of the filters. Homogeneous waveguides have been fabricated by sputtering Corning 7059 glass on standard microscope slides. Inhomogeneous waveguides have been fabricated by the silver-sodium ion exchange process. The periodic corrugation was introduced by forming a thin photoresist phase grating on the surface of the guide or by etching the pattern directly on it. In this investigation, filters with photoresist gratings are referred to as four-layer filters whereas etched grating devices are denominated three-layer filters.

A review of planar slab waveguide theory for homogeneous guides is presented and the expressions for the fields are given. Inhomogeneous waveguides are analysed using approximate WKB and multilayer division techniques and the results obtained using both techniques are compared. The properties of the various filters considered are investigated using the coupled mode formalism. Modifications of the filter response due to tapered and chirped grating are also analysed.

Techniques for the production of short period gratings are studied in some detail and the results discussed. Gratings have been made in Shipley AZ1350J and AZ1370 photoresists, the physical

and optical properties of which have also been investigated.

The responses of experimental filters have been measured using a dye laser. With the exception of the effective guide index, all waveguide parameters were measured using standard techniques. The grating periodicities were measured by the determination of the autocollimation angle for the first order diffracted wave; the grating heights were determined from diffraction efficiency measurements and the results calculated from an exact theory on the scattering of a plane wave incident at an angle to the grating plane. In the three-layer filters the effective guide index of the uncorrugated part of the waveguide was measured with a prism coupler. In the four-layer filters the effective guide index of the corrugated waveguide was measured by an indirect method from a determination of the centre wavelength of the filter and the periodicity of the grating.

The experimental results for all three-layer type filters are in excellent agreement with the theoretical predictions. The fabrication of three-layer inhomogeneous waveguide filters has very low yield and only one device is reported in this work. Good agreement with theoretical predictions has been obtained in the four-layer type homogeneous filters when account is taken of the accuracy with which the effective guide index and the refractive index of the resist film are determined. In general, the waveguide mode field pattern in the four layer filters are distorted by the overlaying film of resist which has a higher refractive index than the waveguide film. The field distortion was considerably stronger in the case of four-layer inhomogeneous waveguides; this results

in a increased perturbation of the field in the corrugated guide which makes it difficult to correlate the experimental filter responses with the theoretical predictions.

An experimental demultiplexer which uses a two-dimensional crossed grating for the reflection of the incident wave is demonstrated and its properties discussed. The device is of a four-layer homogeneous type.

Finally, the results from this investigation suggest that the three-layer type waveguides are the most viable structures for the fabrication of corrugated waveguide filters. These structures provide more latitude in the design of filters and are mechanically rugged.

This is the first detailed experimental investigation of periodically corrugated inhomogeneous waveguide filters.

INDEX

		PAGE
ACKNOWLEDGEMENTS		i
ABSTRACT		ii
CHAPTER I	INTRODUCTION	
CHAPTER II	THEORETICAL ANALYSIS OF PLANAR DIELECTRIC OPTICAL WAVEGUIDES	7
2.1	Wave Propagation in a Three-Layer Step Index Homogeneous Asymetic Slab Waveguide	7
2.1.1	The Ray Optics Approach	7
2.1.2	The Electromagnetic Field Theory Approach	11
2.1.3	Normalization of the Field Coefficient A	15
2.1.4	Phase and Group Velocities for Guided Modes	18
2.2	Wave Propagation in a Four-Layer Step Index Homogeneous Slab Waveguide	20
2.2.1	Expressions for the Fields	23
2.2.2	Normalization of the Field Coefficient A	26
2.2.3	Phase and Group Velocities for Guided Modes	29

2.3 Wave Propagation in an Inhomogeneous Slab Waveguide 29

2.3.1 Solution by the Multilayer Technique 30

2.3.2 Solution by the WKB Technique 33

2.3.3 Solution by the Linear Profile Approximation 34

2.4 Silver-Sodium Ion Exchanged Waveguides 35

2.4.1 Four-Layer Inhomogeneous Waveguides 36

2.5 Beam Coupling to Thin Film Waveguides 43

2.5.1 The Grating Coupler 43

2.5.2 The Prism Coupler 43

APPENDIX 2A 46

APPENDIX 2B 48

APPENDIX 2C 50

CHAPTER III ANALYSIS OF BRAGG WAVEGUIDE FILTERS 54

3.1 Wave Propagation in a Periodic Slab Waveguide 56

3.1.1 Wave Equation for Propagation in Periodic Media : Floquet Theorem and the Dispersion Diagram 60

3.1.2 The Coupled Mode Formalism 64

3.2 Thin Film Bragg Filters 68

3.2.1 The Coupling Coefficient 69

3.2.2 The Band-Gap Width 71

3.2.3 Fractional Bandwidth and Reflectivities 72

3.2.4 High Frequency Cut-Off Properties 76

3.2.5 Effects of Taper Functions 77

3.2.6 Filter Response and Fourier Transform 79

3.3 Waveguide Structures and Design Considerations 80

3.3.1 Normalized Reflectivity Curves 80

3.3.2 Normalized Coupling Coefficient Curves 84

3.3.3 Design Considerations 92

APPENDIX 3A 94

APPENDIX 3B 97

CHAPTER IV PRODUCTION OF GRATING FILTERS AND OPTICAL PROPERTIES OF MATERIALS 100

4.1 Production of Thin Film Waveguides by Sputtering 100

4.1.1 Sputtering Equipment 101

4.1.2 Experimental Waveguides 103

4.2 Production of Thin Film Waveguides by Diffusion 107

4.2.1 Silver Ion Exchanged Waveguides 108

4.2.2 Experimental Waveguides 109

4.3 Photoresist Materials 109

4.3.1 Shipley AZ1300 Photoresists 112

4.3.2 Properties of Shipley AZ1350J and AZ1370 Resists 115

4.3.3 Effects of Temperature on AZ Resists 119

4.4 Holographic Diffraction Gratings 122

4.4.1 Interferometric Equipment 124

4.4.2 Experimental Limitations on the Grating Period 132

4.4.3 Simultaneous Exposure and Development Technique 134

4.4.4 Holographic Short Period Gratings 138

(i) HeCd UV Laser 138

(ii) High Index Liquid Media 139

(iii) Front Prism Techniques 140

4.4.5 Experimental Gratings for Bragg Waveguide Filters 143

4.5 Ion Beam Etching 144

4.5.1 Experimental Equipment 146

4.5.2 Modifications on the Equipment 149

4.5.3 Etched Gratings on Ion Exchanged Waveguides 152

4.6 Grating Modelling 153

4.6.1 Singly-Tapered Gratings 153

4.6.2 Doubly-Tapered Gratings 154

4.6.3 Abrupt Phase Change in Periodicity 157

4.7 Measurements of Device Parameters 158

4.7.1 Refractive Index Measurements 158

4.7.2 Grating Constants 161

4.7.3 Geometrical Measurements 162

4.7.4 Waveguide Loss Measurements 162

APPENDIX 4A 165

CHAPTER V EXPERIMENTAL RESULTS 167

5.1 Experimental Equipment for Filter Evaluation 167

5.2 Measurement Procedure 172

5.3 Results for Three-Layer Experimental Filters 179

5.4 Results for Four-Layer Experimental Filters 187

5.5 An Experimental Unit Cell Demultiplexer 195

CHAPTER VI CONCLUSIONS 198

6.1 General 198

6.2 Future Work 203

REFERENCES 207

CHAPTER I

INTRODUCTION

Integrated optics[1-5] is a field of research in which a wide variety of devices and phenomena, that involve light guidance in thin dielectric films, are being investigated for possible applications in the general field of optical signal processing, which includes optical communications. This field of research was introduced in 1969 by Miller[1], who stated the difficulties of a free space optical communications link, using conventional optical components. The basic philosophy behind integrated optics is the achievement of miniaturised assemblages of several optical components on a common substrate, so that light generation, modulation, coupling, detection, etc., can be combined to provide large bandwidth optical communications links.

The use of dielectric waveguides to guide electromagnetic waves was discussed as far back as 1910 by Hondros et al.[6]. In 1960, Collin[7] presented an analysis of the symmetric guide and specified the field distributions. Prior to Miller's proposals, several workers had studied dielectric waveguides[8,9], in which light was coupled into the structures by focussing onto a polished end of the film. Such structures were invariably multimode and it was not until Tien et al[10] developed the prism-coupler*, which enabled efficient excitation of discrete modes in thin film waveguides, that integrated optics began to expand rapidly. Since then, many thin film waveguide devices have been demonstrated. In addition to the

---

* The prism-coupler was first reported by Iogansen, L.V., Sov.Tech.Phys., 7, p.295, (1962).

many passive devices, such as directional couplers[11], lenses[12], beam splitters[13] and prisms[14], laser action[15], frequency conversion[16], deflection[17], switching[18] and modulation[19], have all been reported.

The main goal of integrated optics has been towards the production of high bandwidth optical communications systems. One may envision that such systems will eventually be comparable to present microwave systems. In fact, there is a great deal of similarity between microwave and integrated optical components. However, because of the shorter optical wavelength, many microwave techniques, utilizing the matching of the transverse field variations for the fabrication of devices, are not applicable. Instead, techniques using periodic structures play a dominant role in integrated optical device fabrication. There are two special properties that make these structures important: a) their eigenmodes consist of an infinite number of space harmonics with phase velocities varying from zero to infinity; and b) they can support propagating waves only in well-specified propagation bands. The usefulness of the first property lies in the fact that it allows the coupling of different types of waves, or similar waves in different modes, without requiring them to have inherently identical wave vectors (in the absence of the periodicity). The second property is commonly known as the distributed feedback Bragg reflection, which is a result of the cumulative phase synchronized reflection from each element of the structure. As we shall see later, in certain frequency bands, the propagation wave vector can only be complex. This implies that a wave propagating in the structure, with a frequency in the stop band, will encounter successive reflection and can not extend far away from its source. This is the reason for the presence of forbidden bands

in the dispersion diagrams of these structures. Applications of periodic structures in integrated optics have already led to the achievement of a number of devices, such as the input-output coupler[20-22], filters[23-25], distributed feedback lasers[26], distributed Bragg lasers[27], modulators[28] and directional couplers[29].

It has been apparent, since work began on integrated optics, that frequency multiplexing would be an essential feature of any optical communications system[2,30,31]. At the commencement of this research, the low-pass[23] and band-stop[24] filter properties of corrugated periodic homogeneous waveguides had been reported. Devices had high rejection and 3 dB bandwidth as narrow as 0.01 nm was achieved in the band-stop filter[25]. Concurrent with these investigations, the properties of semiconductor DFB lasers were being analysed. These devices radiate in a single longitudinal mode, whose frequency is determined by the period of the structure. Because they do not employ cleaved mirrors for optical feedback, DFB lasers can be integrated with other optical devices on a single substrate such as GaAs, in which it is envisaged that all the functions required for an integrated optical circuit can be performed[32]. During the course of this research, theoretical analysis were reported with a view to synthesizing filter responses, by altering the geometry of the corrugation in the Bragg waveguide filters[33-37]. Recently, a major advance towards the achievement of integrated frequency multiplexed light sources has been reported by Aiki et al[38]. Six DFB lasers, with different corrugation period, were monolithically integrated. The individual laser output beams are guided and collected into a single launching waveguide; each laser has a spectral width of 0.05 nm and the wavelength separation is typically 2.0 nm. The

response of Bragg waveguide filters depends strongly on the parameters of the corrugation (grating). The response of the device can, therefore, be tailored by changing the corrugation height and altering the periodicity of the grating. Experiments on surface acoustic waves (SAW) devices have given clear evidences of the major effects caused by these alterations[39,40]. However, because of the shorter optical wavelength, the actual size of the gratings required do not allow the alterations to be introduced easily during the fabrication process. Recently a technique has been reported, whereby a quadratic chirp in the period can be introduced during the formation of the gratings[41]. Corrugated waveguides formed in this way have been experimentally tested as output couplers[42] and demultiplexers[43].

Periodic structures are obtained by recording the interference pattern of two collimated beams from a single laser onto a photo-sensitive material such as photoresist. A relief pattern is then obtained after development of the resist. Corrugated waveguides result from the transfer of the resist pattern onto the surface of the waveguide film by chemical means or by ion beam etching. A second type of periodic waveguide consists of a photosensitive thin film, which has the property of changing its dielectric constant on exposure to light. These materials, however, are not particularly rugged and in general, are chemically and thermally unstable. The realisation of periodic waveguides is normally achieved by introduction of a periodic corrugation on the surface of the guide. A great deal of research has been devoted to the understanding of the behaviour of photoresist[44-54] in order to obtain a faithful recording of the patterns through exposure to light. In addition to the normal expose and develop (ED) technique, a novel method for the production of gratings has been reported. The technique is known as simultaneous

exposure and development (SED)[55] and it claims to have better control on the processing and to give improved shape of the grating grooves. The shortest grating period achievable in practice is a function of the wavelength of the source and the quality of the wavefront of the interfering beams. Bragg waveguide filters require gratings with periods which are generally below the limits set by practical conditions. However, a technique has been developed to fabricate these gratings by spatially reducing the wavelength in a high index medium[56,57].

The aims of this research were essentially threefold.

(1) To fabricate short period gratings and establish the experimental conditions that are necessary for the repeatable and reliable formation of Bragg waveguide filters.

(2) To study, both theoretically and experimentally, Bragg waveguide filters formed on homogeneous and inhomogeneous waveguides. Each type of guiding structure comprises two main types of filters: a) with a photoresist grating on the surface of the guide and b) with the corrugation etched directly onto the guiding layer. The particular type of inhomogeneous waveguides used in this work are formed by the silver-sodium ion exchanged process[58]. Homogeneous waveguides are fabricated by sputtering Corning 7059 glass[59].

(3) To investigate the possibilities of introducing alterations in the grating depth and periodicity and to evaluate the corresponding filter responses.

This thesis is organised into six chapters. Following this introductory chapter, Chapter II deals with the theoretical analysis of the properties of guided modes in the waveguiding structures used in this investigation. Chapter III is concerned with the theoretical analysis of the Bragg waveguide filters. The experimental procedures and techniques developed to produce grating filters are given in Chapter IV. The results of the experimental investigations are compared with the theoretical predictions in Chapter V. An experimental demultiplexer is also presented in this chapter. The last chapter, Chapter VI, contains the conclusions of this investigation and suggestions for future work.

CHAPTER II

THEORETICAL ANALYSIS OF PLANAR DIELECTRIC OPTICAL WAVEGUIDES

The analysis of Bragg filters requires the knowledge of the field distribution and properties of guided modes in a thin film dielectric slab waveguide. It is the purpose of this chapter to present the waveguide theory for the different guiding structures used in this investigation. The three- and four-layer homogeneous waveguides are studied using Maxwell's equations. The corresponding cases for inhomogeneous waveguides are solved using approximate WKB and multilayer division techniques. A comparison of the results of both approximate techniques is given. The chapter concludes with a brief description of grating and prism couplers.

2.1 Wave Propagation in a Three-Layer Step Index Homogeneous Asymmetric Slab Waveguide

The guiding structure is shown schematically in Fig.2.1(a). The variation of the refractive index as a function of depth is shown in Fig.2.1(b). The waveguide is considered infinitely wide in the y-direction.

2.1.1 The Ray Optics Approach

The ray optics approach considers the light waves to be a series of plane waves, which propagate along the guide following a zig-zag path (Fig.2.2); the rays being in the same direction as the plane wave normals. In order to comply with the criteria of guided modes, two important conditions must be satisfied; firstly, total confinement of the rays inside the guiding layer, and, secondly, the 'transverse resonant' or constructive interference condition. The total confinement of the rays requires the existence of total internal reflection at the substrate-film and film-superstrate boundaries.

This can be achieved if the refractive indices of the media follow the relation

$$n_0 < n_1 > n_2$$

The case when $n_0 = n_2$ corresponds to the special case of a symmetrical waveguide.

When the wave is totally reflected, it undergoes a phase change, which can be described geometrically as a lateral shift of the ray in the z-direction. This shift is referred to by Tien[60] as the Goos-Haenchen shift and is given by[61]

$$\phi_{10} = \tan^{-1}\left[U_{10} \frac{(n_1^2 \sin^2\theta_1 - n_0^2)^{\frac{1}{2}}}{n_1 \cos\theta_1} \right] \qquad (2.1(a))$$

$$\phi_{12} = \tan^{-1}\left[U_{12} \frac{(n_1^2 \sin^2\theta_1 - n_2^2)^{\frac{1}{2}}}{n_1 \cos\theta_1} \right] \qquad (2.1(b))$$

where $U_{10} = U_{12} = 1$ for TE modes and $U_{10} = n_1^2/n_0^2$ and $U_{12} = n_1^2/n_2^2$ for TM modes. θ_1 is the angle between the ray and the x-axis of the guide.

The vertical components k_x of the rays forming one complete zig-zag path, have opposite signs and their magnitude is given by

$$k_x = k_0 n_1 \cos\theta_1 \qquad (2.2)$$

where

$$k_0 = 2\pi/\lambda \qquad (2.3)$$

λ being the free space wavelength.

The 'transverse resonant' condition requires the k_x components to interfere constructively. In other words, the total phase change undergone by the wave in one complete round trip must be some multiple of 2π. This condition can be expressed as

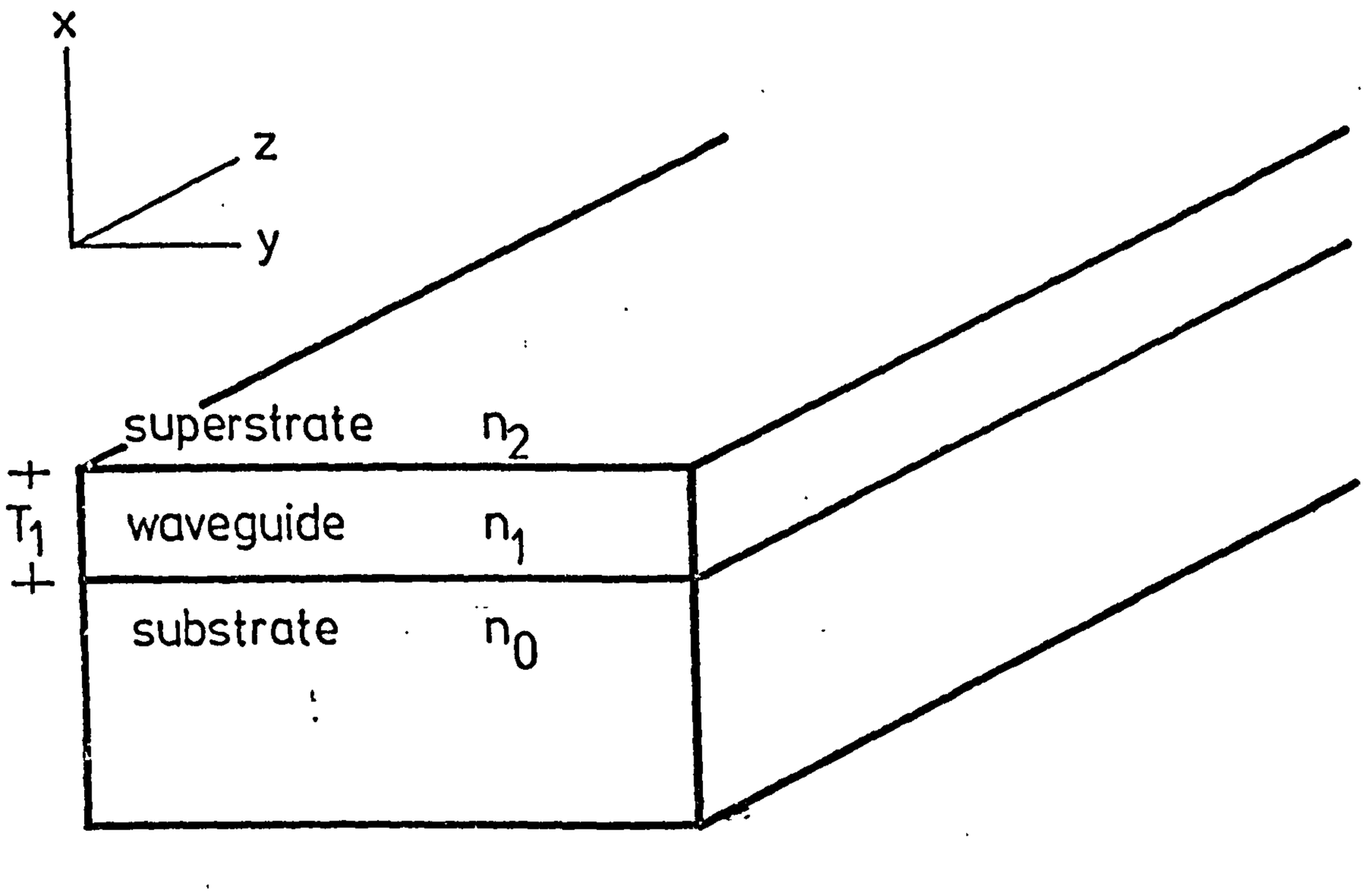

FIG. 2.1 Three-Layer Homogeneous Waveguide

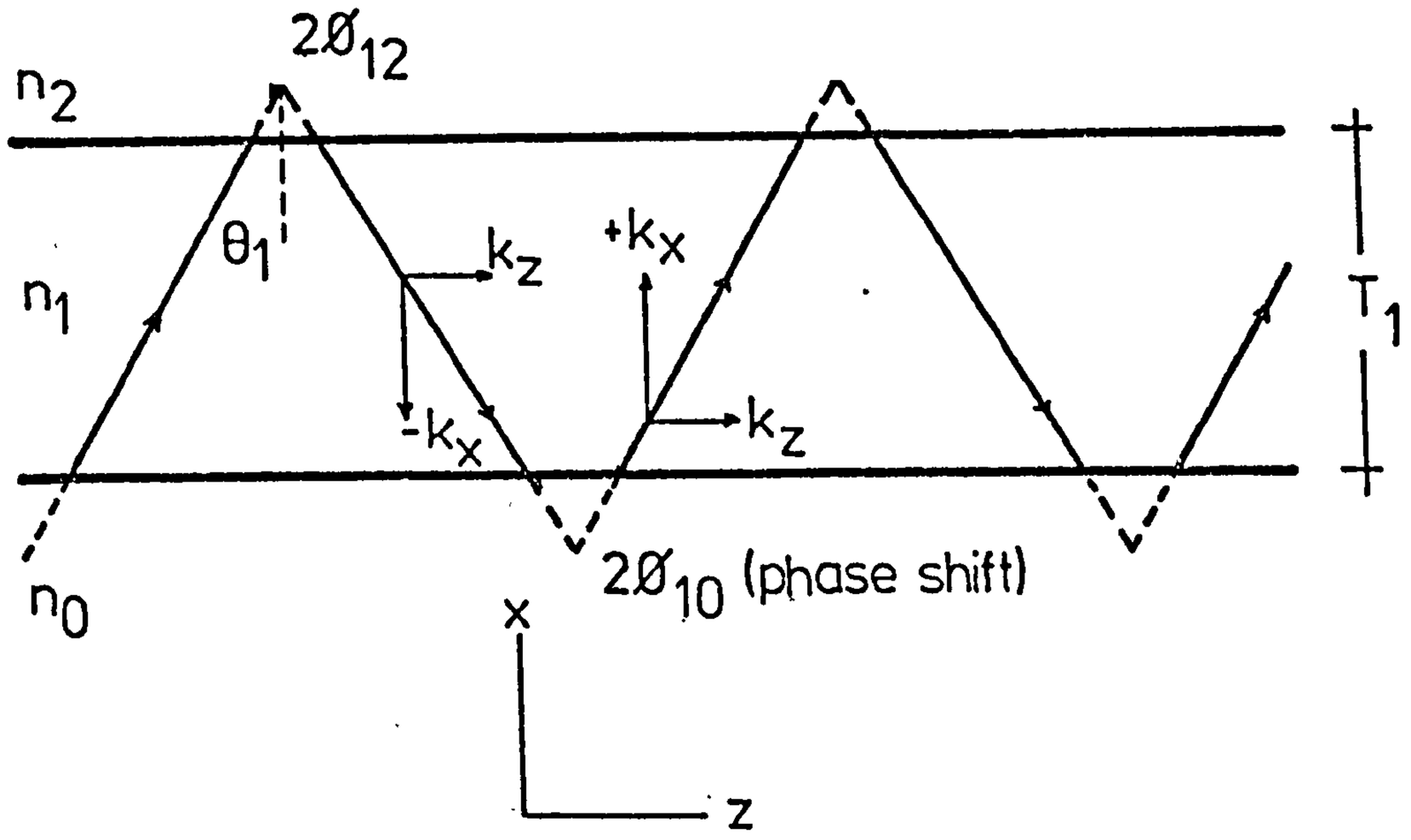

FIG 2.2 Ray Optics Representation of a Guided Wave

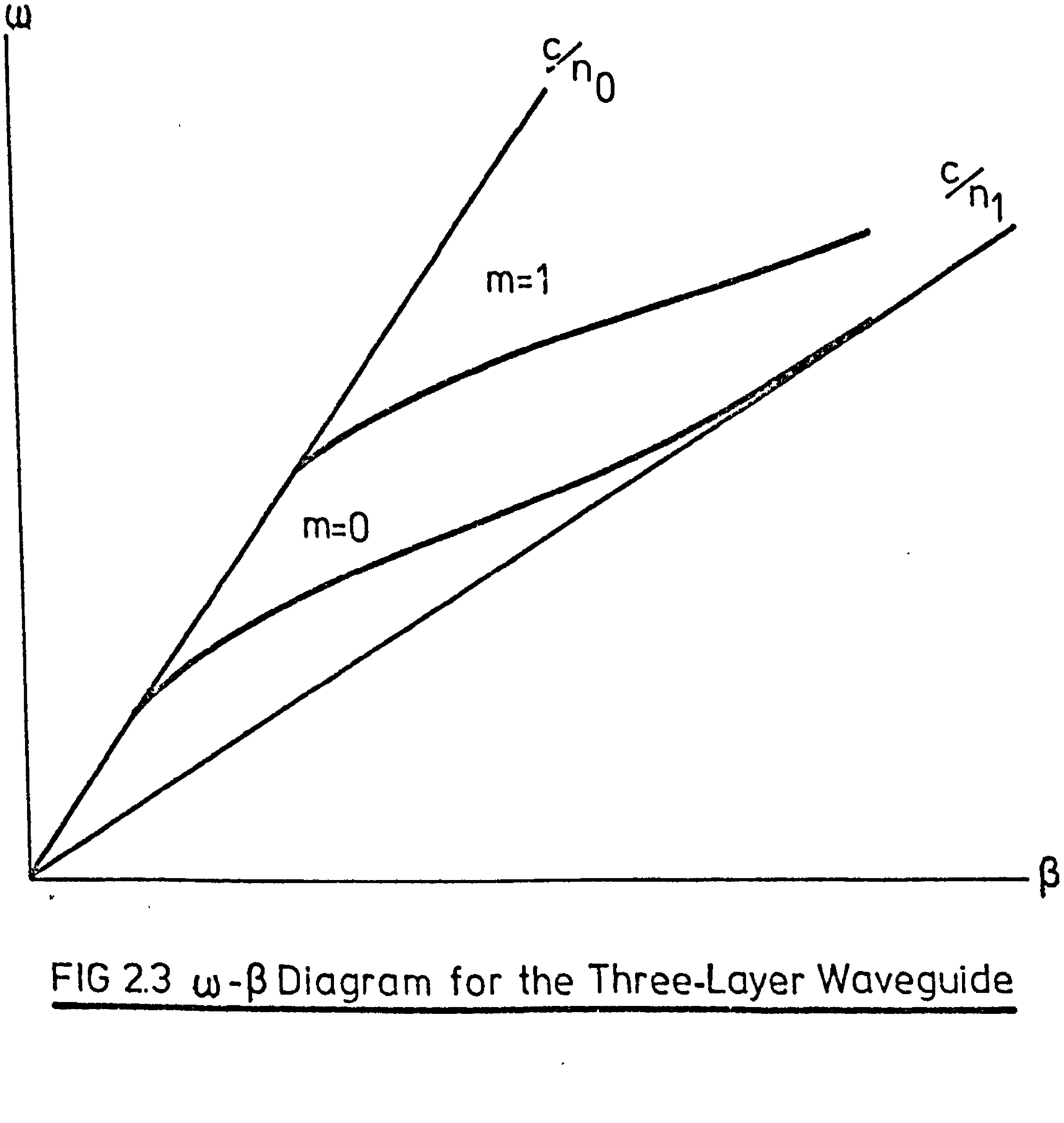

FIG 2.3 ω-β Diagram for the Three-Layer Waveguide

$$2k_0 n_1 T_1 \cos\theta_1 = 2\phi_{10} + 2\phi_{12} + 2m\pi \qquad m = 0,1,2... \tag{2.4}$$

where the parameter m denotes the mode number and it is related to the number of nodes in the standing wave pattern across the thickness of the guiding layer. The horizontal compcnents k_z, on the other hand, have the same signs and they represent a consistent feature for wave propagation along the z-direction. Their magnitude is given by

$$k_z = \beta = k_0 n_1 \sin\theta_1 \tag{2.5}$$

Using equations (2.1), (2.2) and (2.5) equation (2.4) can be written as

$$(k_0^2 n_1^2 - \beta^2)^{\frac{1}{2}} T_1 = \tan^{-1}\left[U_{10}^2 \frac{\beta^2 - n_0^2 k_0^2}{n_1^2 k_0^2 - \beta^2}\right]^{\frac{1}{2}} + \tan^{-1}\left[U_{12}^2 \frac{\beta^2 - k_0^2 n_2^2}{n_1^2 k_0^2 - \beta^2}\right]^{\frac{1}{2}} + m\pi \tag{2.6}$$

For guided modes the arguments of the inverse circular functions are real. This condition requires

$$n_0 \leq \beta/k_0 \leq n_1 \tag{2.7}$$

Equation (2.6) is known as the transcendental mode equation and it is used to predict waveguide propagation in any three-layer, homogeneous, lossless slab waveguide.

2.1.2 The Electromagnetic Field Theory Approach

This method uses the rigorous Maxwell's equations. The eigensolutions for the fields are obtained by applying the boundary conditions at the dielectric interfaces. For a time harmonic field in non-magnetic, isotropic, source free media,Maxwell's equations can be written as

$$\nabla \times \bar{E} = -\mu_0 (\partial\bar{H}/\partial t) \tag{2.8}$$

$$\nabla \times \bar{H} = \varepsilon_0 \varepsilon_r (\partial\bar{E}/\partial t) \tag{2.9}$$

$$\nabla.\overline{E} = 0 \qquad (2.10)$$

$$\nabla.\overline{H} = 0 \qquad (2.11)$$

and yield the wave equation

$$\nabla^2 \overline{E} = \mu_0\varepsilon_0\varepsilon_r \ (\partial^2 \overline{E}/\partial t^2) \qquad (2.12)$$

Throughout this work wave propagation in the waveguide is assumed to be along the z-axis and a time dependence of the form $\exp(j\omega t)$ is used. These assumptions can be represented by the factor

$$\exp\ (j(\omega t - \beta z)) \qquad (2.13)$$

and represents a plane wave travelling in the positive z-direction, with a phase velocity given by

$$V_p = \omega/\beta \qquad (2.14)$$

For the slab waveguide there is no variation of the fields in the y-direction, that is

$$\partial\overline{F}/\partial y = 0 \qquad (2.15)$$

where $\overline{F}$ represents any arbitrary field.

Similar to microwave guided waves,there exists two types of polarization of the waves in a dielectric slab optical guide. For TE modes,the field components are E_y,H_x and H_z and for TM modes,the field components are H_y,E_x and E_z. Detailed solution for the TE modes is given here and the procedure can be generalised for the case of TM modes. Making use of equations (2.8), (2.9), (2.15) and the E_y component of the field,the following expressions are obtained

$$-j\beta H_x - (\partial H_z/\partial x) = j\omega\varepsilon_0\varepsilon_r E_y \qquad (2.16)$$

$$j\beta E_y = -j\omega\mu_0 H_x \qquad (2.17)$$

$$\partial E_y/\partial x = -j\omega\mu_0 H_z \qquad (2.18)$$

and yield the wave equation in its one-dimensional reduced form

$$(\partial^2 E_y/\partial x^2) + (n_i^2 k_0^2 - \beta^2)E_y = 0 \qquad i = 0,1,2... \tag{2.19}$$

where

$$\varepsilon_r = n^2 \tag{2.20}$$

and

$$k_0^2 = \omega^2 \varepsilon_0 \mu_0 = \omega^2/c^2 = (2\pi/\lambda)^2 \tag{2.21}$$

c being the speed of light in free space.

Solutions for the wave equation (2.19) which ensure that the field vanishes at $x = \pm \infty$ are

$$E_{y2} = A_1 \exp(-p_2 x) \qquad 0 < x < \infty \tag{2.22(a)}$$

$$E_{y1} = A_2 \cos b_1 x + A_3 \sin b_1 x \qquad 0 > x > -T_1 \tag{2.22(b)}$$

$$E_{y0} = A_4 \exp(p_0(x+T_1)) \qquad -T_1 > x > -\infty \tag{2.22(c)}$$

where the real parameters p_0, b_1 and p_2 are given by

$$p_0 = (\beta^2 - k_0^2 n_0^2)^{\frac{1}{2}} \tag{2.23(a)}$$

$$b_1 = (k_0^2 n_1^2 - \beta^2)^{\frac{1}{2}} \tag{2.23(b)}$$

$$p_2 = (\beta^2 - k_0^2 n_2^2)^{\frac{1}{2}} \tag{2.23(c)}$$

The boundary conditions require the continuity of the fields and its derivatives at the dielectric interfaces $x = 0$ and $x = -T_1$. This results in a system of four simultaneous equations whose solution is given in Appendix 2A. The nontriviality condition for the system gives

$$b_1 T_1 = \tan^{-1}(p_2/b_1) + \tan^{-1}(p_0/b_1) + m\pi \tag{2.24}$$

Expressing the coefficients A_i (i=1,3,4) in terms of A_2=A yields the final form of the field equations. From Appendix 2A we have

$$E_{y2} = A \exp(-p_2 x) \qquad \infty > x > 0 \qquad (2.25(a))$$

$$E_{y1} = A(\cos b_1 x - (p_2/b_1)\sin b_1 x) \qquad 0 > x > -T_1 \qquad (2.25(b))$$

$$E_{y0} = A(\cos b_1 T_1 + (p_2/b_1)\sin b_1 T_1)\exp(p_0(x+T_1)) \qquad -T_1 > x > -\infty \qquad (2.25(c))$$

The field, therefore, has an oscillatory behaviour inside the guiding layer and it is decaying in the surrounding media. The expressions for the magnetic field components can be easily derived from equations (2.17) and (2.18). Equation (2.24) is the same as (2.6), which was derived from the geometrical optics approach. The expression can not be solved explicitly for β, the propagation constant. However, by choosing values of β, the guide thickness can be calculated from a knowledge of the refractive indices, wavelength of operation and mode number.

The effective guide index N is defined by

$$N = \beta/k_0 \qquad (2.26)$$

and for guided modes $n_0 < N < n_1$. We show in Fig.2.3 a typical dispersion diagram, calculated from equation (2.24). Fig.2.4 shows the variation in N as a function of the guide thickness T_1*. The cut-off point for

---

* Figures used for the calculations of theoretical curves given in Chapters II and III are related to the dye laser wavelength of 610 nm. This particular choice is dictated by the stability and power output of the laser. Values of the refractive indices correspond to available material used in this investigation; they are as follows

Material	Refractive Index
Sputtered Corning 7059 glass	1.568
Fisher microscope slide substrate	1.515
AZ1350J Resist	1.633
AZ1370 Resist	1.803
Schott BaK5 glass (substrate)	1.555
Schott BaK2 glass (substrate)	1.538

a mode corresponds to $N = n_0$. As the guide thickness increases the number of possible modes also increases and the value of N for each mode tends to the guide refractive index. Similar procedure for TM modes leads to the dispersion equation (2.6) and the magnetic field component H_y is given by

$$H_{y2} = A \exp(-p_2 x) \qquad \infty > x > 0$$

$$H_{y1} = A(\cos b_1 x - (n_1^2/n_2^2)(p_2/b_1)\sin b_1 x) \qquad 0 > x > -T_1$$

$$H_{y0} = A(\cos b_1 T_1 + (n_1^2/n_2^2)(p_2/b_1)\sin b_1 T_1)\exp(p_0(x+T_1)) \qquad -T_1 > x > -\infty$$

where the parameters p_0, b_1 and p_2 have the same meaning as in equation (2.23). The electric field components are obtained from

$$E_{xi} = (\beta/n_i^2 \omega \varepsilon_0) H_{yi}$$

$$E_{zi} = (-j/n_i^2 \omega \varepsilon_0)(\partial H_{yi}/\partial x)$$

$$i = 0,1,2$$

2.1.3 Normalization of the Field Coefficient A.

The amplitude coefficient of the field can be related to the power carried by the mode. The power is obtained by integrating the z-component of the Poynting vector

$$\overline{S} = \frac{1}{2} \mathrm{Re} \ (\overline{E} \times \overline{H}^*) \qquad (2.27)$$

over the infinite transverse cross section of the guide. The asterisk (*) denotes complex conjugate. Using equations (2.25) for TE modes the power is given by

$$P = \frac{\beta}{2\omega\varepsilon_0} \int_{-\infty}^{\infty} |E_y|^2 \, dx \qquad (2.28)$$

i.e.

$$P = \frac{A^2\beta}{4\omega\mu_0} \left[\left[\frac{(b_1^2+p_2^2)(1+p_2T_1)}{b_1^2 p_2} \right] + \left[\frac{b_1^2(p_2+p_0)+p_2(b_1^2-p_0p_2)}{b_1^3 p_0} \cdot \tan b_1T_1 + \frac{b_1^2-p_0p_2}{b_1^2p_0} + \frac{(p_0+p_2)p_2}{p_0 b_1^2} \tan^2 b_1T_1 \right] \cos b_1T_1 \right] \qquad (2.29)$$

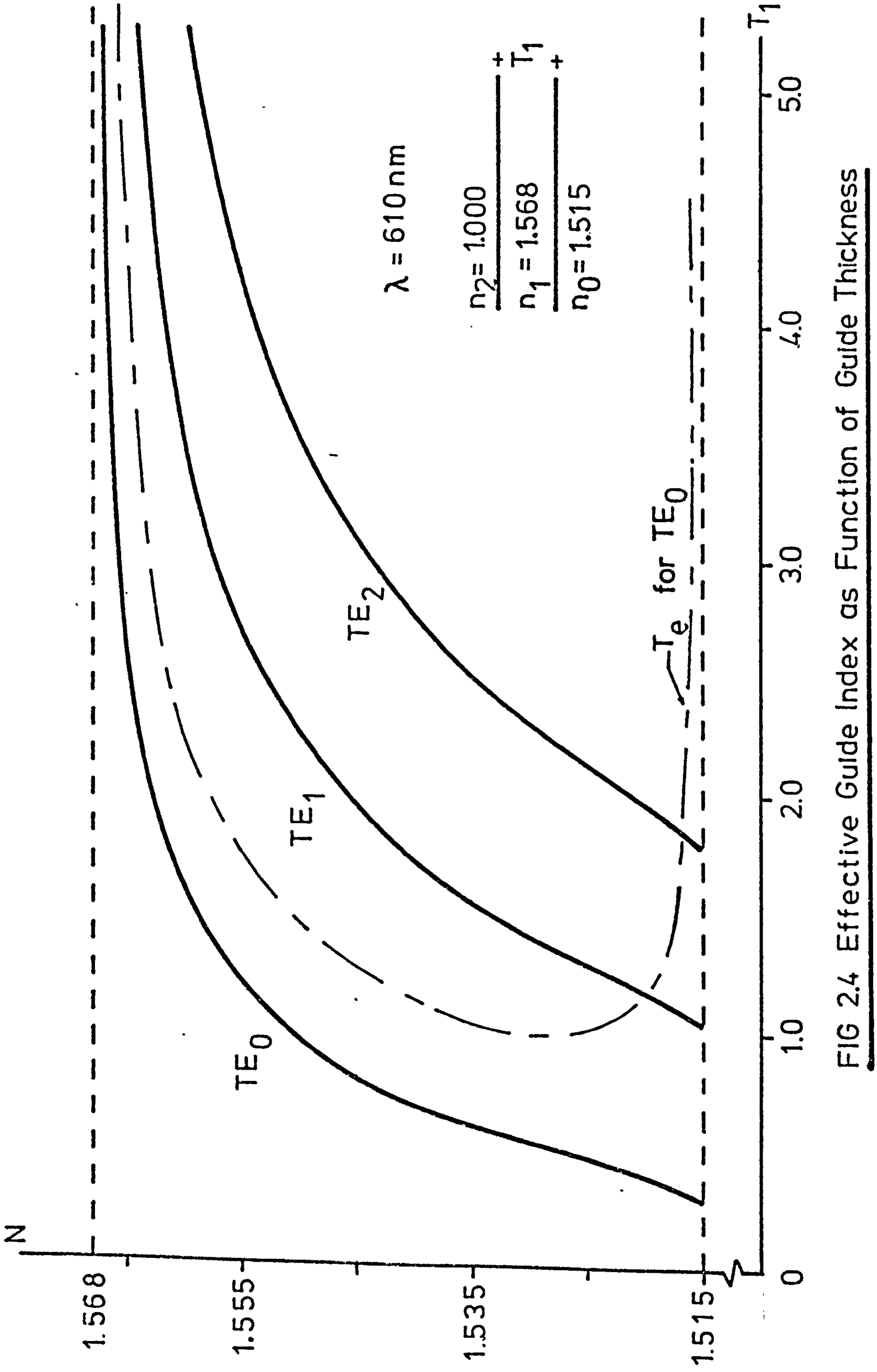

FIG 2.4 Effective Guide Index as Function of Guide Thickness

From Appendix 2A the values of the circular functions cos and tan are given by

$$\cos b_1 T_1 = (b_1^2 - p_0 p_2)/\left[(b_1^2+p_2^2)(b_1^2+p_0^2)\right]^{\frac{1}{2}}$$

$$\tan b_1 T_1 = b_1(p_0+p_2)/(b_1^2 - p_0 p_2)$$

With the above expressions and after some algebra equation (2.29) becomes

$$P = \frac{A^2\beta}{4\omega\varepsilon_0} \frac{(b_1^2+p_2^2)}{b_1^2} \left[T_1 + \frac{1}{p_0} + \frac{1}{p_2}\right] \qquad (2.30)$$

The term in square brackets is known as the effective guide thickness T_e and has the following general expression

$$T_e = T_1 + 1/(V_{10}p_0) + 1/(V_{12}p_2) \qquad (2.31)$$

where

$$V_{10} = V_{12} = 1 \quad \text{for TE modes}$$

$$V_{10} = (N^2(n_0^2 + n_1^2) - n_0^2 n_1^2)/(n_1^2 n_0^2)$$

$$V_{12} = (N^2(n_2^2 + n_1^2) - n_2^2 n_1^2)/(n_1^2 n_2^2)$$

for TM modes. Fig.2.4 shows, in thin dashed line, the variation of T_e as function of N for the TE_0 mode. The field amplitude A can, therefore, be expressed as

$$A^2 = \frac{4 P b_1^2 \omega\mu_0}{(b_1^2 + p_2^2)\, T_e \beta}$$

Similarly for TM modes, equation (2.27) becomes

$$P = \frac{\beta}{2\omega\varepsilon_0} \int_{-\infty}^{\infty} n^2(x)^{-1} |H_y|^2 \, dx$$

and the field coefficient is given by

$$A^2 = \frac{4\omega\varepsilon_0 P}{\beta} n_1^2 n_2^2 b_1^2 \left[\frac{1}{(n_2^4 b_1^2 + n_1^4 p_2^2) T_e}\right]$$

where T_e, in the above expression, refers to the effective thickness

for TM modes, as defined by equation (2.31).

2.1.4 Phase and Group Velocities for Guided Modes

The phase velocity V_p was defined previously by equation (2.14). Using equation (2.21) V_p can be expressed in terms of the effective guide index and has the form

$$V_p = c/N \tag{2.33}$$

and for guided modes

$$c/n_0 < V_p < c/n_1$$

The energy carried by the mode is given by equation (2.28) and it travels with a group velocity given by

$$V_g = d\omega/d\beta \tag{2.34}$$

Substitution of equation (2.21) into the mode equation (2.6) and taking the derivative with respect to β we obtain

$$V_g = \frac{\beta c^2}{\omega} \frac{T_1+\omega^2 c(B_{10}+B_{12})}{T_1 n_1^2+\beta^2 c^3(B_{10}+B_{12})} \tag{2.35}$$

where

$$B_{10} = \frac{U_{10}(n_1^2-n_0^2)}{(\beta^2 c^2-n_0^2\omega^2)^{1/2}\,\omega^2(n_1^2-n_0^2U_{10}^2)+\beta^2c^2(U_{10}^2-1)}$$

$$B_{12} = \frac{U_{12}(n_1^2-n_2^2)}{(\beta^2 c^2-n_2^2\omega^2)^{1/2}\,\omega^2(n_1^2-n_2^2U_{12}^2)+\beta^2c^2(U_{12}^2-1)}$$

and the terms U_{10} and U_{12} have the same meaning as in equation (2.1). The expression for V_g can be simplified by using the definition for the effective guide thickness in equation (2.31). Working with terms in (2.35) which contain B_{10} and B_{12} we obtain

$$\omega^2 c(B_{10}+B_{12}) = T_e - T_1$$

$$\beta^2 c^3(B_{10}+B_{12}) = N^2(T_e - T_1)$$

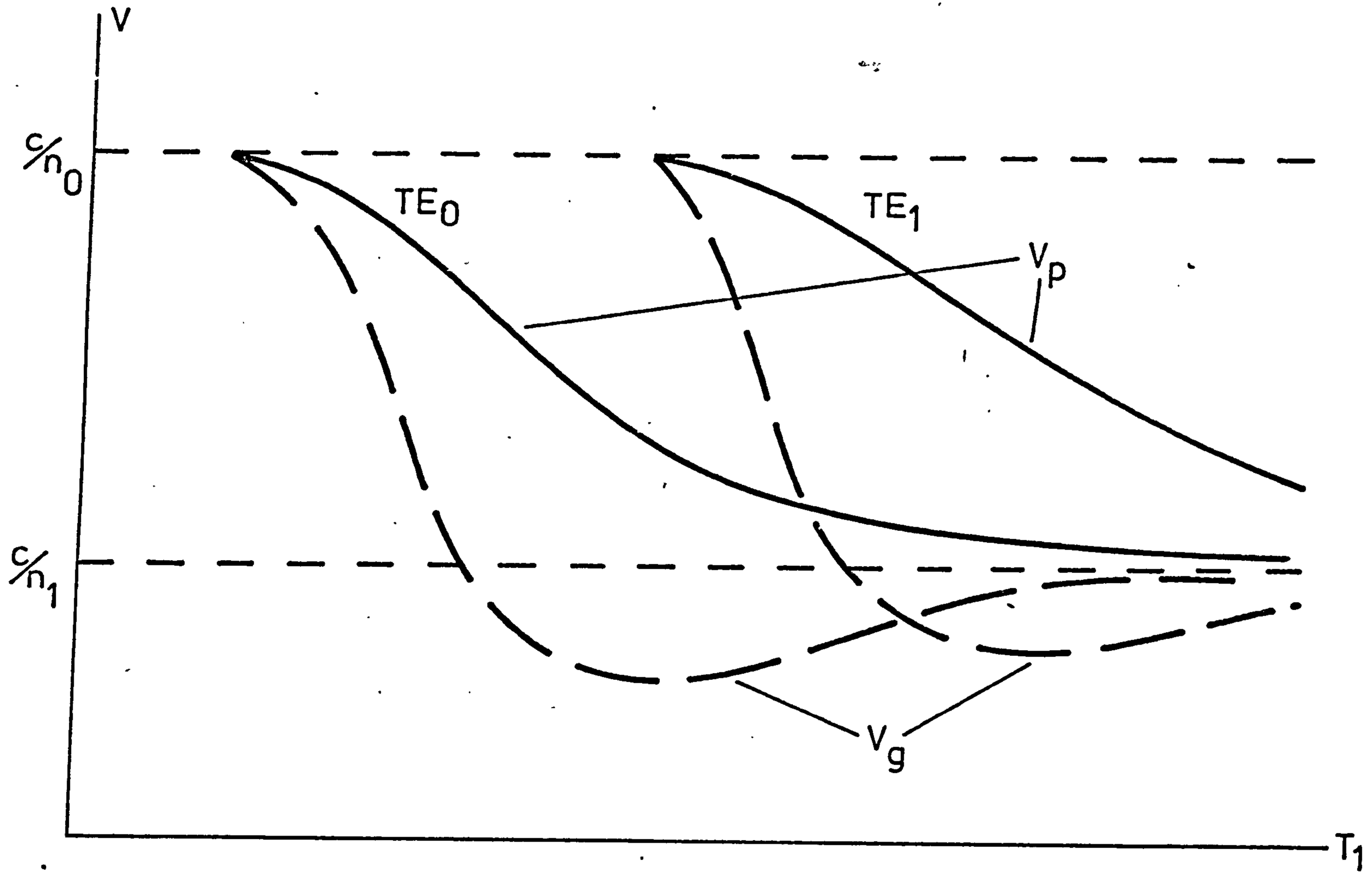

FIG 2.5 Phase and Group Velocities for the Three-Layer Waveguide

where T_e is the effective thickness for either TE or TM modes. Substituting the above results into equation (2.35)we obtain a general expression for the group velocity which has the form

$$V_g = \frac{cNT_e}{T_1(n_1^2-N^2)+N^2T_e} \qquad (2.36)$$

The group index n_g of the mode is defined by

$$n_g = c/V_g \qquad (2.37)$$

and it is the counterpart of the effective guide index N as applied to the phase velocity in equation (2.32). Figure 2.5 shows the variation of V_p and V_g as function of the guide thickness T_1.

2.2 Wave Propagation in a Four-Layer Step Index Homogeneous Slab Waveguide

The particular guiding structure considered in this work is shown schematically in Fig.2.6. The additional layer has a thickness of T_2 and a refractive index $n_2>n_1$. To ensure propagation of the modes within the two highest index media,the effective guide index must be within the range $n_0<N<n_1$. This condition ensures the absence of total internal reflection at the $x = -T_2$ dielectric interface. The ray optics model for the structure is shown in Fig.2.7(a) and the 'transverse resonant' condition can be written as

$$2b_1T_1 = 2\phi_{10} + 2\phi_{123} + 2m\pi \qquad (2.38)$$

where ϕ_{123} is the phase change due to reflection at the $x = -T_2$ boundary. This value for the phase can be calculated by means of a transmission line analogue as shown in Fig.2.7(b). The transmission line consists of two sections with characteristic admittances Y_1 and Y_2 and load admittances Y_0 and Y_3 respectively. The loads must be reactive in order for the transmission line to resonate. For TE modes the admittances are given by

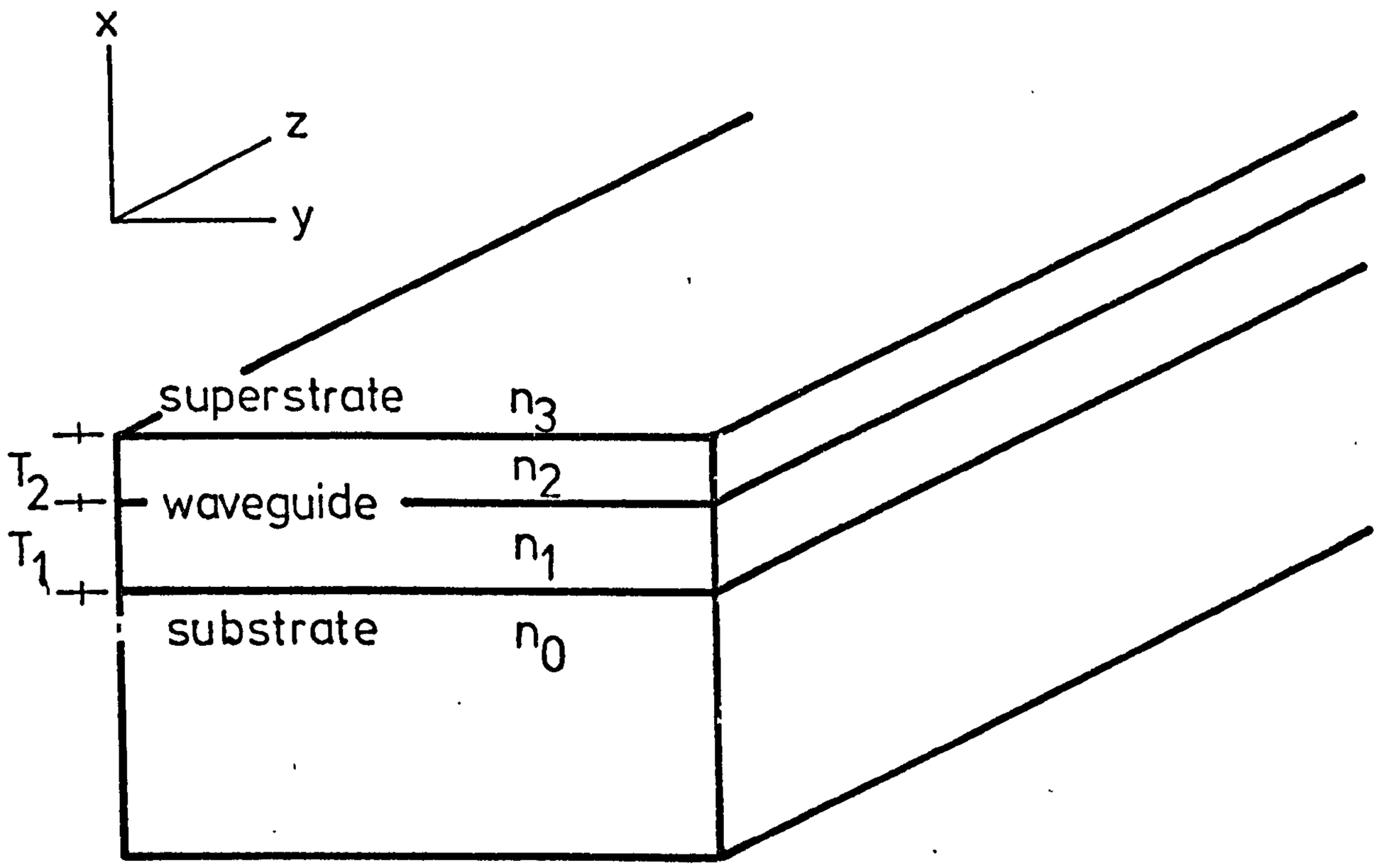

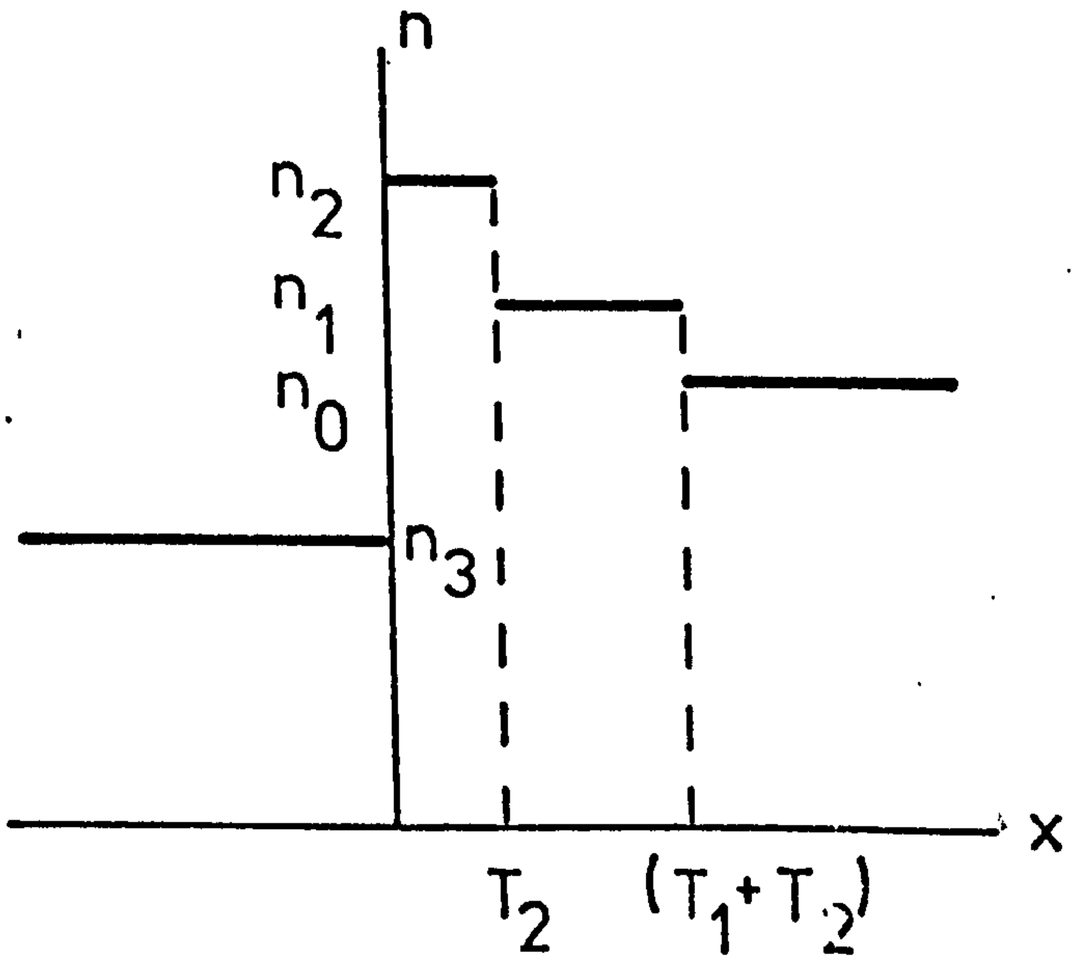

FIG 2.6 Four-Layer Homogeneous Waveguide

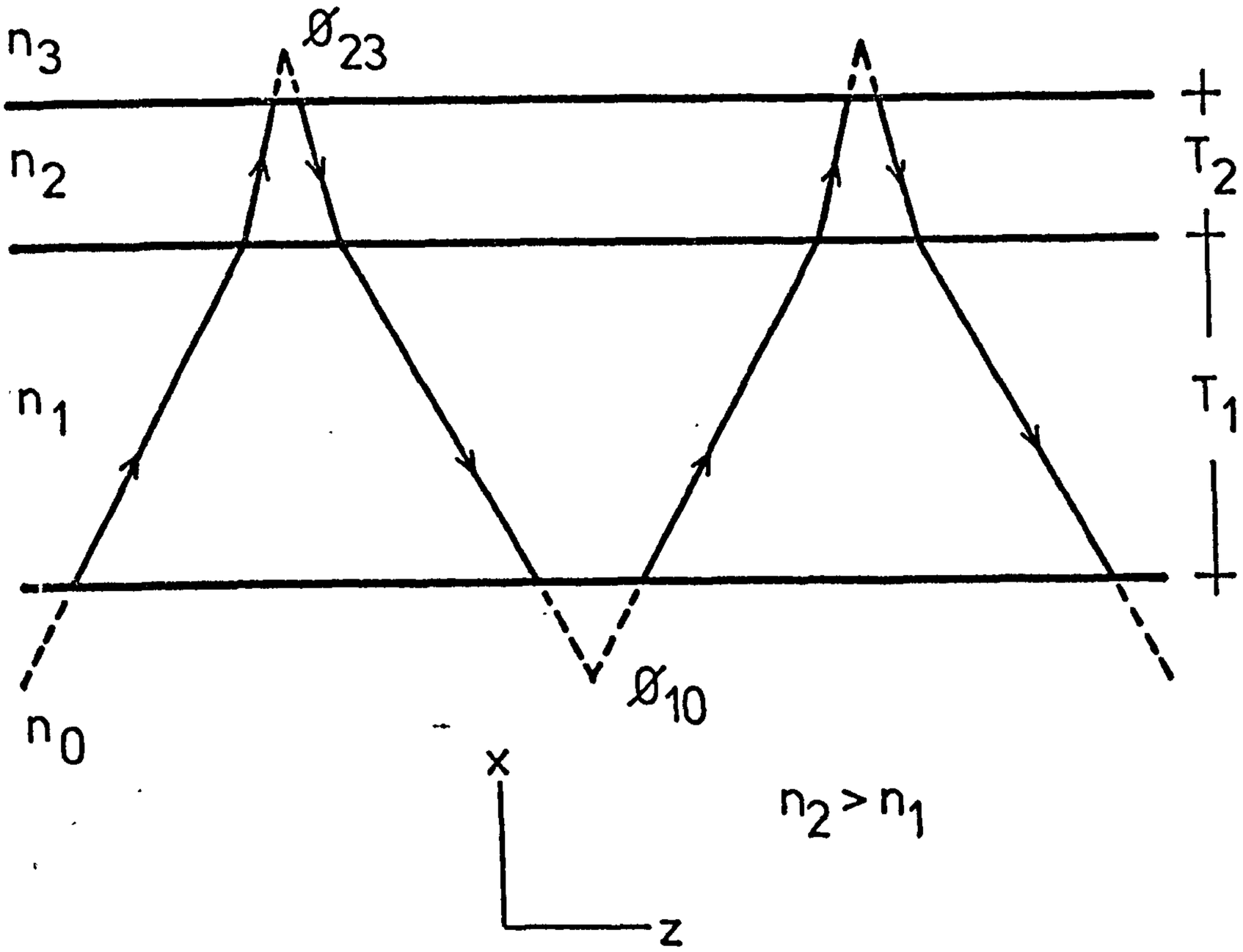

FIG 2.7a Ray Optics Representation of a Guided Wave in a Four-Layer Homogeneous Waveguide

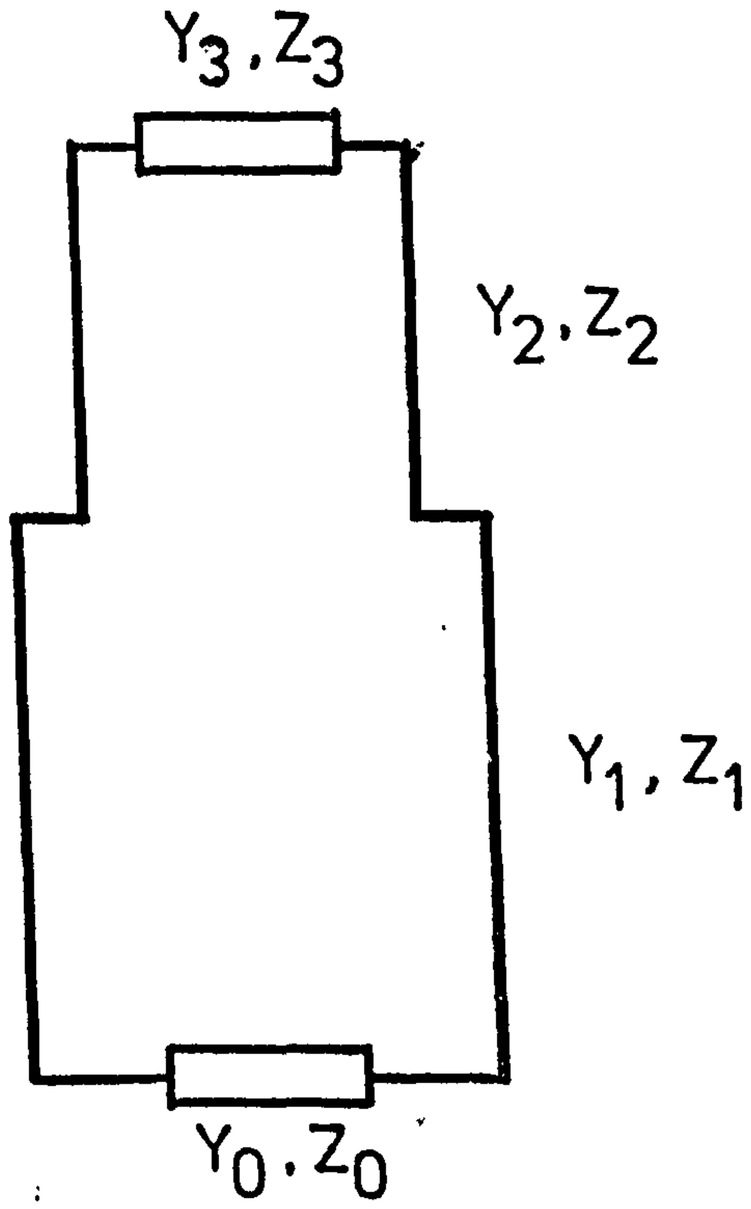

FIG 2.7b Transmission Line Analogue for the Four-Layer Waveguide

$$Y_i = (N^2 - n_i^2)^{\frac{1}{2}}/(j\omega\mu_0)$$

Making use of the following transmission line relationships[62]

$$Y_{iq} = Y_i \frac{Y_q + jY_i \tan b_i T_i}{Y_i + jY_q \tan b_i T_i}$$

and

$$r = \frac{Y_0 - Y_L}{Y_0 + Y_L} = |r| \exp(2\phi_{123})$$

the phase ϕ_{123} can be determined and the transcendental mode equation (3.38) can be written as

$$b_1 T_1 = \tan^{-1}(p_0/b_1) + \tan^{-1}\left[\left[\frac{-b_2}{b_1}\right] \frac{b_2 \tan b_2 T_2 - p_3}{b_2 + p_3 \tan b_2 T_2}\right] + m\pi \qquad (2.39)$$

where

$$p_0 = (\beta^2 - k_0^2 n_0^2)^{\frac{1}{2}} \qquad (2.40(a))$$

$$b_1 = (k_0^2 n_1^2 - \beta^2)^{\frac{1}{2}} \qquad (2.40(b))$$

$$b_2 = (k_0^2 n_2^2 - \beta^2)^{\frac{1}{2}} \qquad (2.40(c))$$

$$p_3 = (\beta^2 - k_0^2 n_3^2)^{\frac{1}{2}} \qquad (2.40(d))$$

Equation (2.39) is similar in character to equation (2.6), however, it is not single-valued. For a given mode, the same propagation constant β exists for a combination of values for the layer thicknesses T_1 and T_2. Knowledge of at least one of the layer thicknesses is, therefore, required in order to characterize a particular waveguide.

The expression for TM modes can be similarly obtained by using the relevant relationships in terms of the transmission line impedances.

2.2.1 Expressions for the Fields

Due to the complexity of the resulting field expressions, we restrict the present analysis for the case of TE modes only. Solving

the wave equation (2.19) and applying the boundary conditions at the $x=0, x=-T_2$ and $x=-(T_1+T_2)$ interfaces result in a system of six simultaneous equations. Detailed solution of the system is given in Appendix 2B. The nontriviality condition gives the dispersion relation which has the form given by

$$\frac{b_2}{b_1}\tan(b_2T_2-\tan^{-1}(p_3/b_2)+m_2\pi) = -\tan(b_1T_1-\tan^{-1}(p_0/b_1)+m_1\pi) \qquad (2.41)$$

$$m_i(i=1,2) = 0,1,2,3..$$

where the parameters m_i are given by the largest integer of

$$m_1 : \quad (b_1T_1 - \tan^{-1}(p_0/b_1))/\pi \qquad (2.42(a))$$

$$m_2 : \quad (b_2T_2 - \tan^{-1}(p_3/b_2))/\pi \qquad (2.42(b))$$

Solution for equation (2.41) is possible if the arguments of the circular functions have opposite signs. The overall mode index is given by

$$m = m_1 + m_2 \qquad (2.43)$$

Solution also exists for the case when

$$(b_2T_2-\tan^{-1}(p_3/b_2)-m_2\pi) > \pi/2 \qquad (2.44(a))$$

$$0 < (b_1T_1-\tan^{-1}(p_0/b_1)-m_1\pi) < \pi/2 \qquad (2.44(b))$$

A simple analysis of the field pattern will indicate that, in the latter case, the mode index is given by

$$m = m_1 + m_2 + 1 \qquad (2.45)$$

Equation (2.41) is equivalent to (2.39). Computationally, it is more difficult to use, however, by having separate mode numbers, it provides additional information on the number of nodes which exists in each separate layer. Fig.2.8 shows the variation in N as a function

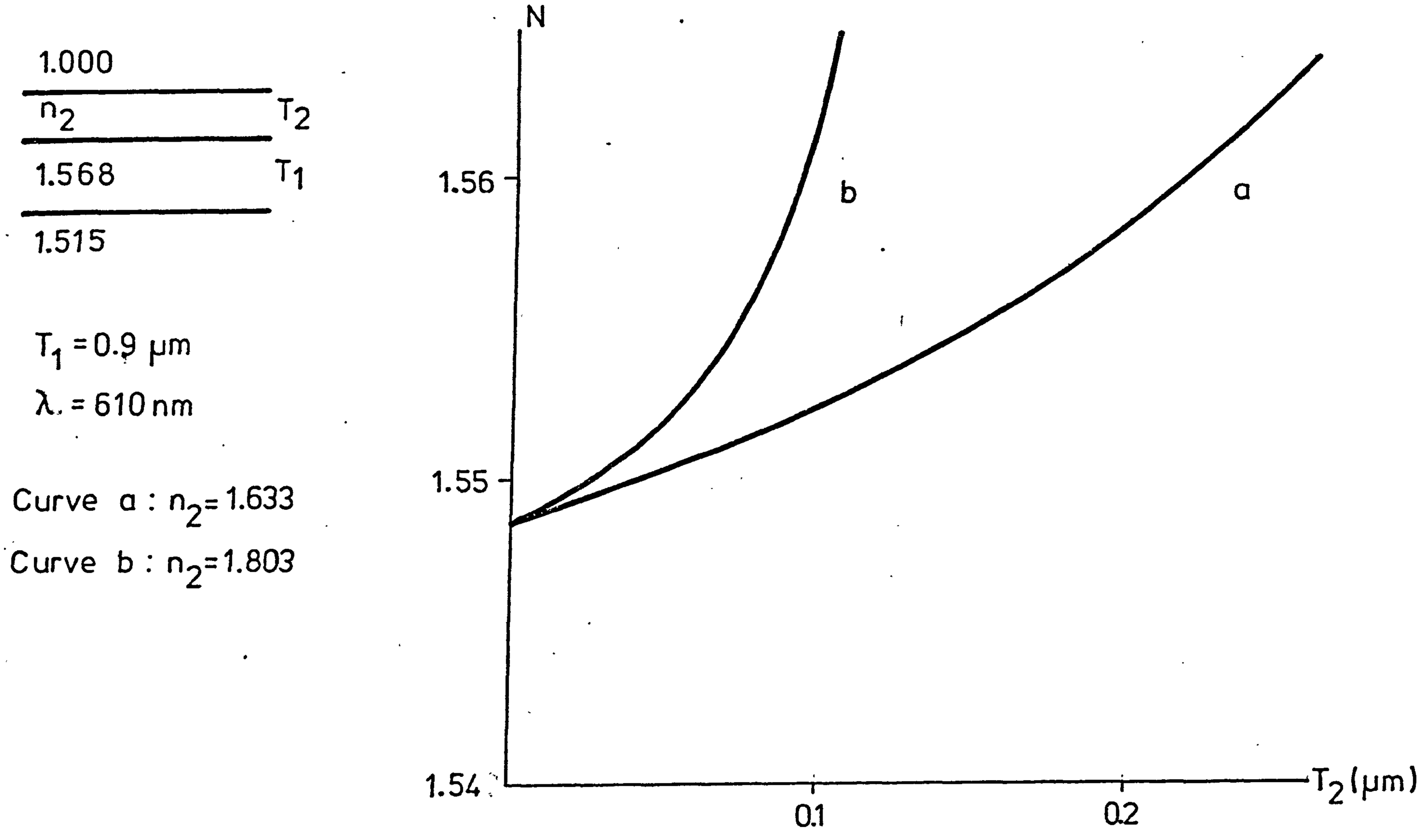

FIG 2.8 Effective Guide Index as Function of T_2

of the thickness T_2 for a typical waveguide with T_1 = 0.9μm.

For the work in filters we use single mode waveguides and Fig.2.9 shows the maximum value of T_2, for a range of values of T_1 which ensures propagation of the TE_0 mode only.

From Appendix 2B, the field expressions are given by

$$E_{y3} = A\exp(-p_3x) \qquad \infty>x>0 \qquad (2.46(a))$$

$$E_{y2} = A(\cos b_2x-(p_3/b_2)\sin b_2x) \qquad 0>x>-T_2 \qquad (2.46(b))$$

$$E_{y1} = A(X\cos b_1(x+T_2)+Y\sin b_1(x+T_2)) \qquad -T_2>x>-(T_1+T_2) \qquad (2.46(c))$$

$$E_{y0} = A(Z\exp(p_0(x+T_1+T_2))) \qquad -(T_1+T_2)>x>-\infty \qquad (2.46(d))$$

where

$$X = \cos b_2T_2 + (p_3/b_2)\sin b_2T_2 \qquad (2.47(a))$$

$$Y = (b_2/b_1)\sin b_2T_2 - (p_3/b_1)\cos b_2T_2 \qquad (2.47(b))$$

$$Z = X\cos b_1T_1 - Y\sin b_1T_1 \qquad (2.47(c))$$

and p_0, b_1, b_2 and p_3 are as defined in equations (2.40). The corresponding expressions, for the magnetic field components, can be obtained using equations (2.17) and (2.18). Fig.2.10 shows the electric field distribution for typical four-layer waveguides used in this work. Also shown in the graph, is the field distribution for the basic three-layer waveguide, onto which the fourth layer has been added. The degree of asymmetry of the field is observed to increase with increasing values of T_2 and/or n_2.

2.2.2 Normalization of the Field Coefficient A

Using the same procedure as in the three layer case, the power carried by the mode can be calculated from equations (2.28) and (2.46). The field amplitude is found to be given by

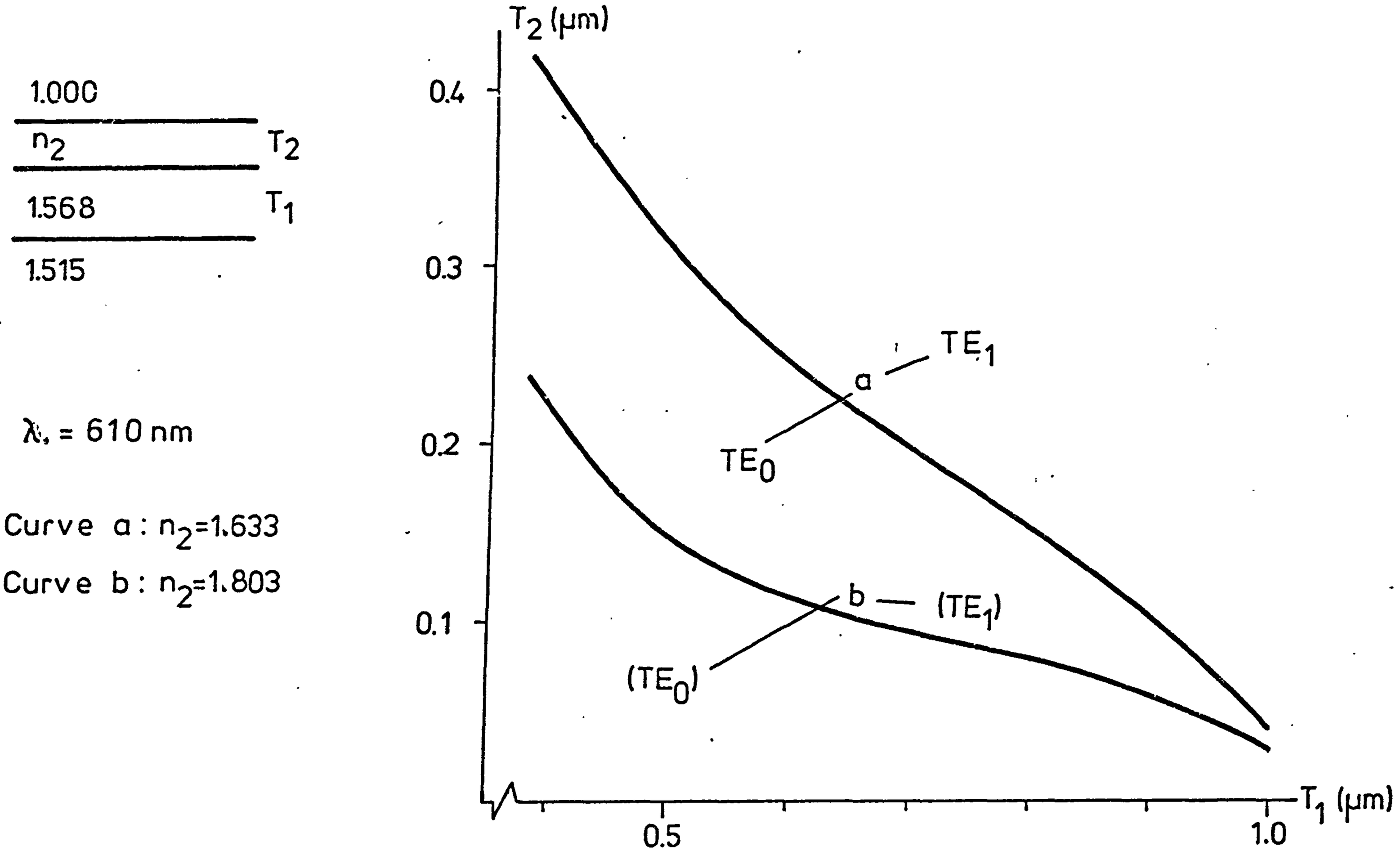

FIG 2.9 T_1 and T_2 Values for Single TE_0 Mode Operation

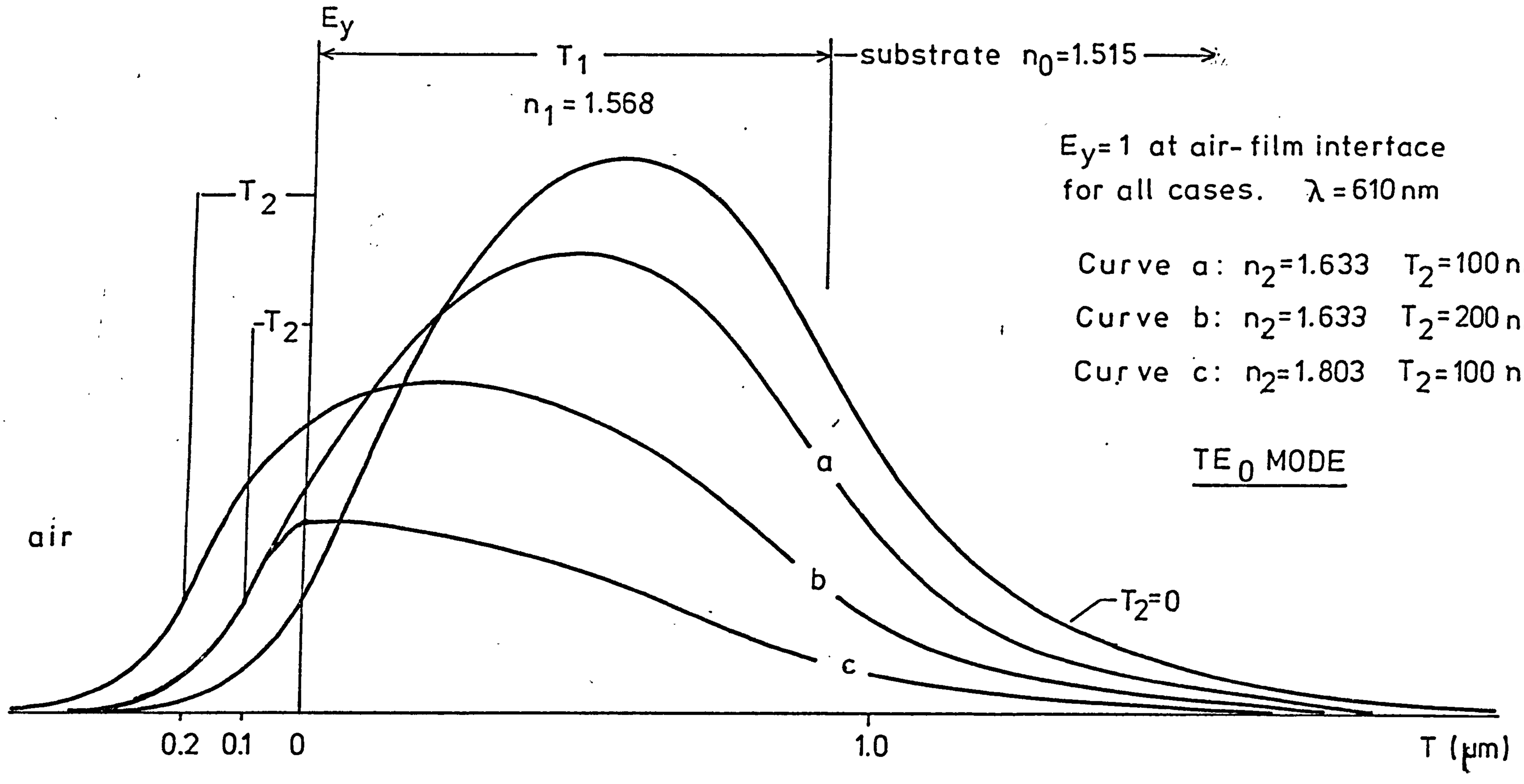

FIG 2.10 Field Distribution in Four-Layer Homogeneous Waveguides.

$$A^2 = \frac{4\omega\mu_o P}{\beta}\left[\frac{1}{p_3} + \frac{Z^2}{p_0} + \frac{p_3}{b_2^2}(1-\cos 2b_2T_2) + \left[1 + \frac{p_3^2}{b_2^2}\right]T_2\right.$$

$$+\left[1 - \frac{p_3^2}{b_2^2}\right]\frac{\sin 2b_2T_2}{2b_2} + (X^2 + Y^2)T_1 + \frac{(X^2-Y^2)\sin 2b_2T_2}{2b_1}$$

$$\left. + \frac{XY(\cos 2b_1T_1 - 1)}{b_1}\right]^{-1} \qquad (2.48)$$

2.2.3. Phase and Group Velocities for Guided Modes

Using the definitions in the previous section, the phase velocity is given by

$$V_p = c/N$$

and the group velocity results in

$$V_g = \frac{\beta\left[\left[\frac{\tan\alpha_2}{b_2} + \frac{\tan\alpha_1}{b_1}\right] + \left[T_1 + \frac{1}{p_0}\right]\sec^2\alpha_1 + \left[T_2 + \frac{1}{p_3}\right]\sec^2\alpha_2\right]}{\frac{\omega}{c^2}\left[\frac{n_2^2\tan\alpha_2}{b_2} + \frac{n_1^2\tan\alpha_1}{b_1}\right] + \left[\frac{\omega n_2^2 T_2}{c^2} + \frac{\beta^2}{\omega p_3}\right]\sec^2\alpha_2 + \left[\frac{\omega n_1^2 T_1}{c^2} + \frac{\beta^2}{\omega p_0}\right]\sec^2\alpha_1} \qquad (2.49)$$

where

$$\alpha_1 = b_1T_1 - \tan^{-1}(p_0/b_1) + m_1\pi$$

$$\alpha_2 = b_2T_2 - \tan^{-1}(p_3/b_2) + m_2\pi$$

2.3 Wave Propagation in an Inhomogeneous Slab Waveguide

Several fabrication processes, in particular diffusion[58,63-66] and ion implantation[67], lead to dielectric waveguide layers with graded index profiles, where the refractive index n(x) varies gradually over the depth of the guide. The ray optics representation of a guided wave, in such structures, is shown in Fig.2.11. It will be seen that, in contrast with the case of homogeneous waveguides, the rays are no longer

straight but follow a curved trajectory. The vertical component of the wave vector is a function of depth, i.e. $k_x(x)$, and the point where the gradient of the ray path is zero is known as the turning point $-x_t$.

Maxwell's equations (2.8)-(2.11) yield the following wave equations, for the TE and TM modes respectively

$$\frac{d^2E_y}{dx^2} + (k_0^2n^2(x) - \beta^2)E_y = 0 \qquad (2.50(a))$$

$$\frac{d^2H_y}{dx^2} + (k_0^2n^2(x) - \beta^2 - n^{-2}(x)\frac{d\epsilon_r}{dx}\frac{d}{dx})H_y = 0 \qquad (2.50(b))$$

The similarity of equation (2.50(a)) to the Schroedinger equation allows the implementation of solutions and methods of analysis from quantum mechanics. Exact solutions for TE modes exist for certain functions of the index profile n(x). Furthermore, if the gradient of n(x) is small, such solutions can be adapted to serve as approximations for the TM modes[68]. In practice, however, the functional forms n(x) of fabricated waveguides are such that the wave equation can not be solved exactly and approximate methods are used to determine the waveguide properties.

In what follows in this section, we describe three alternative methods of solution which can be used in the analysis of inhomogeneous waveguides.

2.3.1 Solution by the Multilayer Technique

The inhomogeneous waveguide can be considered to be formed by a stack of infinitely thin homogeneous sublayers. The constant refractive index of each sublayer is determined by the index profile n(x) and according to its relative position with respect to the depth of the original waveguide. The problem, then, reduces to applying the

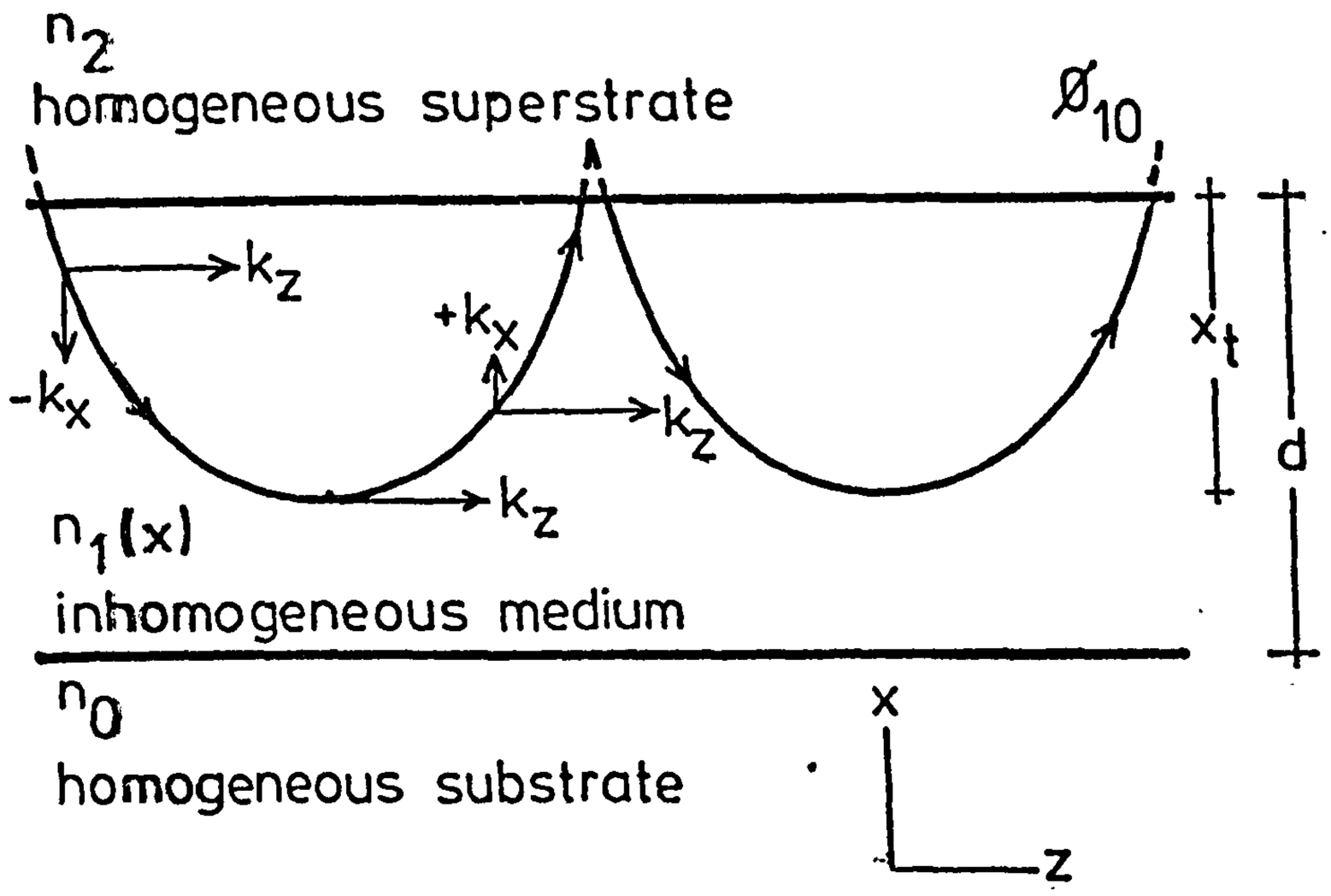

FIG 2.11 Ray Optics Representation of a Guided Wave in an Inhomogeneous Waveguide.

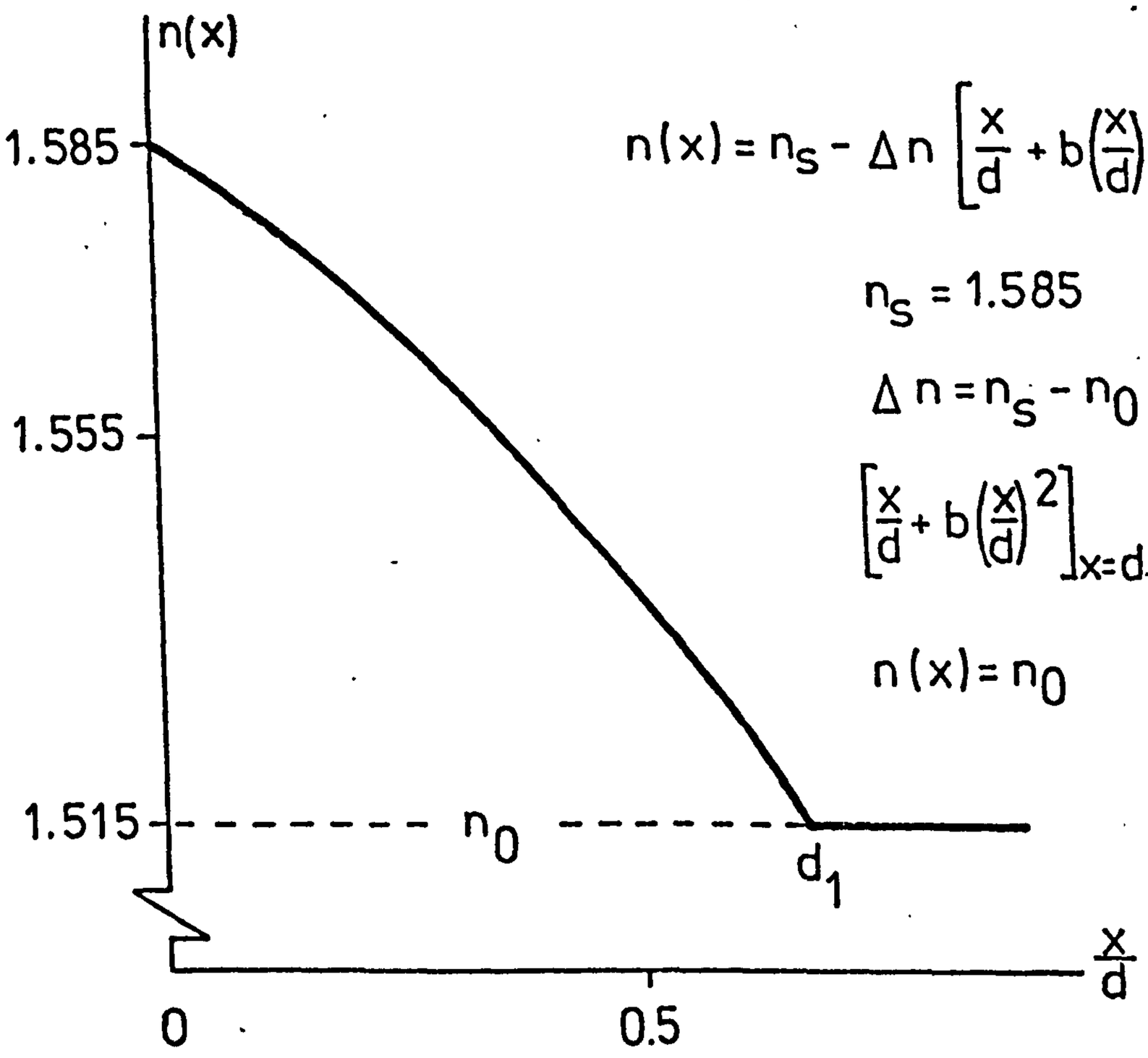

$$n(x) = n_s - \Delta n \left[\frac{x}{d} + b\left(\frac{x}{d}\right)^2\right] \qquad x<d_1$$

$n_s = 1.585 \qquad b=0.64$

$\Delta n = n_s - n_0$

$$\left[\frac{x}{d} + b\left(\frac{x}{d}\right)^2\right]_{x=d_1} = 1$$

$n(x) = n_0 \qquad x>d_1$

FIG 2.12 Second Order Polynomial Refractive Index Distribution for Ag-Na Ion Exchanged Waveguides.

boundary conditions at the interfaces and solving the resulting system of simultaneous equations. The technique is, in essence, the same as that used to solve the four-layer waveguide (see Appendix 2B) and a general formulation for the multilayer case has been given by Harris et al[69].

An extended technique, which includes anisotropic waveguides, has been developed by Vassell[70]. The method of solution consists of matching four vectors, corresponding to the tangential electric and magnetic fields at the boundary of each layer. The field amplitudes of the waves propagating along the z-direction in the two regions outside the waveguide layer are then related by an overall 4 x 4 transfer matrix T i.e.

$$\left[F(x=-d)\right] = \left[T\right]\left[F(x=0)\right] \tag{2.51}$$

where

$$\left[F(x)\right] = \begin{bmatrix} E_x \\ H_y \\ E_y \\ H_x \end{bmatrix} \tag{2.52}$$

and

$$\left[T\right] = \prod \left[U_i\right] \tag{2.53}$$

$|U_i|$ being the transfer matrix of layer i. The guiding condition is given by the nontrivial solution of the determinant of equation (2.51). Once the propagation constants are determined, the values for the field can be calculated from relation (2.51).

The accuracy of the multilayer technique depends on the number of sublayers in which the original guide is divided. Both of the above approaches require the use of a computer.

2.3.2 Solution by the WKB Technique[71]

This technique was developed for quantum mechanics by Wentzel, Kramers and Brillouin[72]. The method of solution is basically that of the geometrical optics approach[73,74]. The inhomogeneous waveguide layer is subdivided as before and the WKB technique applies only for cases where the reflection of the rays at the interfaces of two consecutive sublayers is vanishingly small. The transverse resonant condition in these cases is given by

$$2k_0 \int_{-x_t}^{0} (n^2(x)-N^2)^{\frac{1}{2}} dx = 2\tan^{-1}\phi_{10} + \frac{\pi}{2} + 2m\pi \qquad (2.54)$$

where ϕ_{10} is as defined in equation (2.1(a)) with n_1 replaced by n_s the value of refractive index at the guide-superstrate inteface. The turning point x_t is determined from

$$n(-x_t) = N \qquad k_x(-x_t) = 0 \qquad (2.55)$$

The integral in equation (2.54) represents the total phase change over the round trip path length and the $\pi/2$ contribution accounts for the phase reflection at the WKB turning point.

For TE modes the electric field expressions are given by[75]

$$E_y = \left[\frac{b_1(0)}{b_1(x)}\right]^{\frac{1}{2}} CA \cos\left[\frac{\pi}{4} - \int_{-x_t}^{0} b_1(x)dx\right]_{0>x>-x_t} \qquad (2.56(a))$$

$$E_y = \left[\frac{b_1(0)}{b_1(x)}\right]^{\frac{1}{2}} \frac{CA}{2j} \exp\left[-\int_{-x_t}^{0} |b_1(x)|\, dx\right]_{-x_t>x>-\infty} \qquad (2.56(b))$$

where

$$C = \left[1 + \left[\frac{p_2}{b_1(0)} + \frac{a}{4b_1^3(0)}\right]^2\right]^{\frac{1}{2}} \qquad (2.57(a))$$

$$a = \frac{n_0^2 - n_s^2}{d} k_0 \qquad (2.57(b))$$

$$b_1(x) = k_0(n^2(x) - N^2)^{\frac{1}{2}} \qquad (2.57(c))$$

$$b_1(0) = k_0(n_s^2 - N^2)^{\frac{1}{2}} \qquad (2.57(d))$$

$$p_2 = k_0(N^2 - n_2^2)^{\frac{1}{2}} \qquad (2.57(e))$$

d is the depth of the guiding layer.

Equation (2.57(c)) is zero valued at the turning point and represents a pole in equations (2.56). If the refractive index profile is approximated by a linear distribution in the vicinity of $-x_t$, the WKB expressions hold everywhere and at the turning point the field is given by[75]

$$E_y = (b_1(0))^{\frac{1}{2}} CA \frac{\Gamma(1/3)\sin(\pi/6)}{(3\pi)^{\frac{1}{2}}(g)^{1/3}} \qquad (2.58)$$

where

$$g = \left[\left[2n(x) \left| \frac{dn}{dx} \right| \right]_{x=-x_t} \right]^{\frac{1}{2}}$$

and Γ is the Gamma function.

The above equations hold valid for any index profile n(x), the variation of which is slow, over a distance of the order of a wavelength. The WKB equation (2.54) has been extensively used in the determination of n(x) for various inhomogeneous waveguides[58,76-79] and the accuracy of the method improves as the number of modes increases[80].

2.3.3 Solution by the Linear Profile Approximation

The wave equation for TE modes can be solved exactly if the index profile n(x) is linear. The fields of the modes are given in terms of Bessel functions of order $\pm 1/3$. An alternative form of solution can,

therefore, be obtained by fitting straight line segments to the actual index distribution and subsequently, solving for the resulting multilayer case, by the first technique described in this section. This form of solution, however, suffers from computational problems and for further details we refer to the work by Marcuse[75].

2.4 Silver-Sodium Ion Exchanged Waveguides

Several index distributions have been reported in connection with this particular guiding structure. In this thesis, we use the results reported by Stewart et al[78]. The index profile has a maximum n_s at the surface and changes with depth, according to a second order polynomial function of the form (see Fig.2.12)

$$n(x) = n_s - (n_s - n_0)\left[\frac{x}{d} + b\left[\frac{x}{d}\right]^2\right] \qquad (2.59)$$

where b = 0.64 and d, the diffusion depth, is given by

$$d = 1.16\times10^{4}\ t^{\frac{1}{2}}\ \exp(-1.02\times10^{4}/(2T))\ \ \text{um} \qquad (2.60)$$

t being the diffusion time in minutes and T the diffusion temperature in degrees Kelvin. In this work, we take $n_s = 1.585$ and use $T = 215^{\circ}C$. With these parameters and using the WKB equation (2.54), we have calculated the relationship between the effective guide index N and the diffusion time t. Results are shown graphically in Fig.2.13.

The error in N, due to variations in diffusion time and temperature during the fabrication process, has been recently reported by Millar et al[81]. Working on Stewart's linear approximation to the refractive index profile (2.59), the total error in N is given by

$$\delta N_{tot}^2 = \delta N_T^2 + \delta N_t^2 + 3.46\times10^{-8} \qquad (2.61)$$

where

$$\delta N_t = (\alpha/t)\ \delta t$$

$$\delta N_t = (1.02\times10^{4}\alpha)(\delta T/T^2)$$

$$\alpha = (b_1^4(0)d)/(6k_0^4 n_s(N/p_2+3/b_1(0)))$$

The last term on the right hand side of equation (2.61) accounts for the standard deviation about the mean substrate refractive index ($\pm\ 1.1\times10^{-4}$) and an error of $\pm\ 1.5\times10^{-4}$ in the determination of N, using the prism coupler.

In this work we have analysed the properties of these guides, using the WKB and Vassell's multilayer techniques. Both methods of solutions predict the value of N well with a maximum discrepancy of 0.07% (0.4% in d). A comparison of the field distribution in the guide, however, showed considerable differences at depths near the WKB turning point (see Fig.2.14). As the WKB expressions for the field (2.56) break down at $-x_t$, the value of E_y in the vicinity of the $-x_t$ point was determined graphically. This is shown with dashed lines in Fig.2.14. Remembering that the value of E_y at the turning point is obtained from a linear approximation of the index profile, this comparison reveals that the solution from Vassell's technique gives a better approximation. We have used the latter in this work and a listing of the relevant computer program* is given in Appendix 2C.

2.4.1 Four-Layer Inhomogeneous Waveguides

Although the transcendental WKB mode equation (2.54) predicts the value of N with good accuracy, it cannot, however, be applied in the case when a homogeneous thin layer is present on the surface of the inhomogeneous guide. In the spirit of the technique it should not be applicable in the analysis of inhomogeneous waveguides at all. The

---

* Developed by Dr. J.A.H. Wilkinson

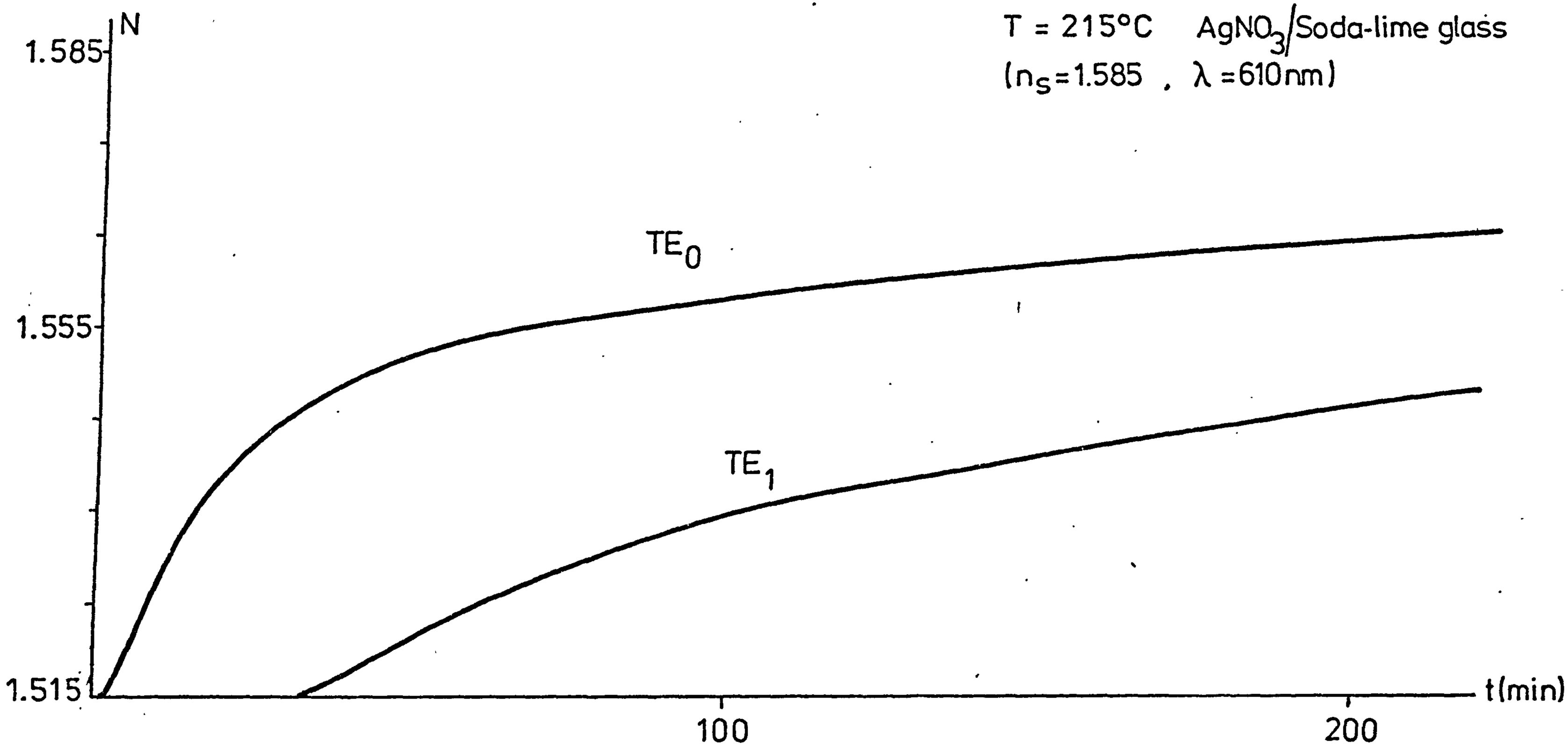

FIG 2.13 Effective Guide Index as Function of Diffusion Time

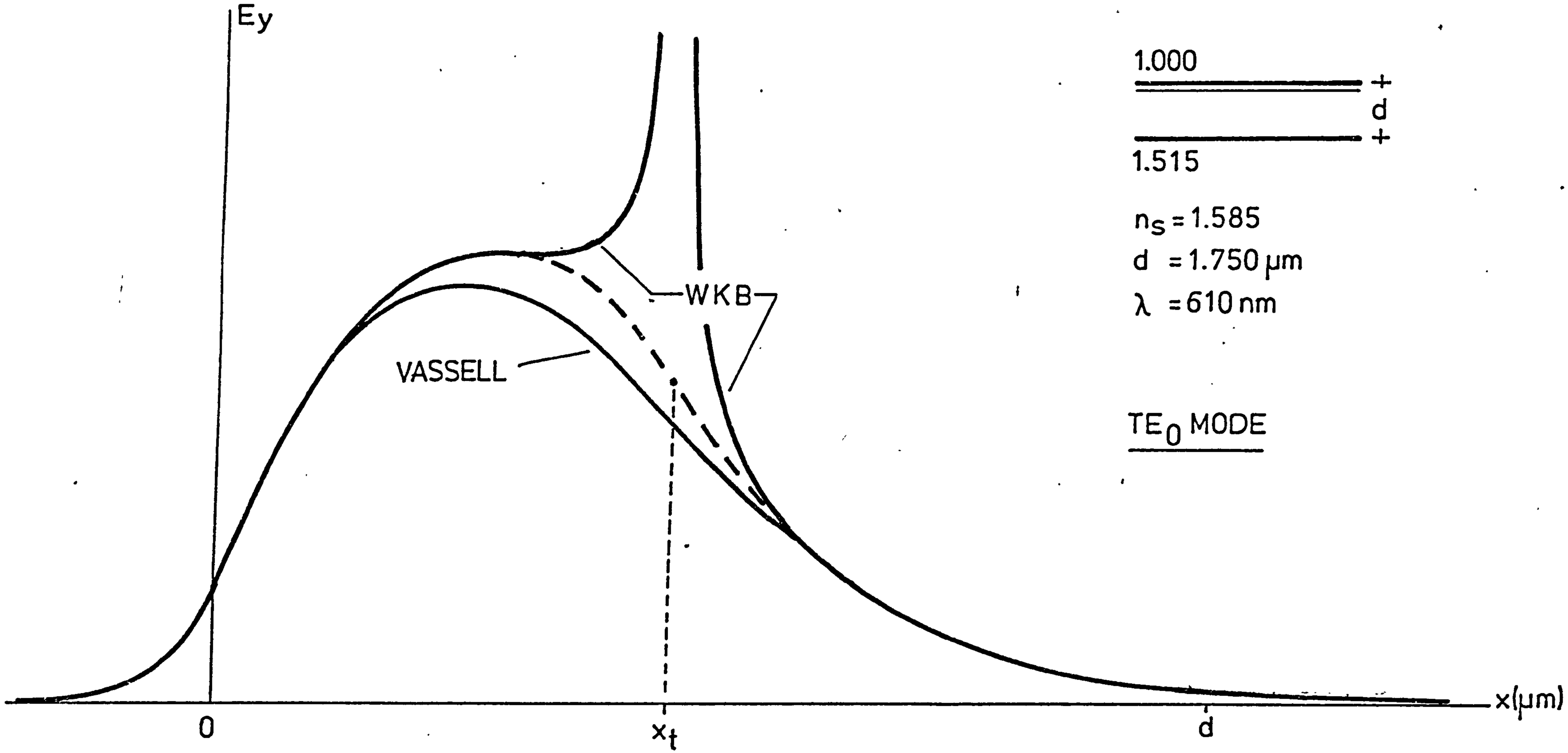

FIG 2.14 Comparison of Field Distributions Calculated from Two Different Formulations

strong mismatch, at the air-waveguide interface, precludes its use. However, results have shown[80,82] that this does not have serious drawbacks in the prediction of the field near the surface or in the value of N. When a high index homogeneous layer is present, the situation changes under the concept that the additional layer becomes part of the waveguide. This is the case encountered in the realisation of Bragg filters, using a photoresist grating. To a first approximation, the reflection coefficient at the resist-guide interface can be estimated by assuming the uppermost sublayer of the guide to have an index of 1.585. Making use of equation (2.5) and the Fresnel formula for TE modes[61]

$$r = \frac{n_1\cos\theta_1 - n_2\cos\theta_2}{n_1\cos\theta_1 + n_2\cos\theta_2}$$

r works out to be of the order of 0.2 for n_2=1.633 and 0.45 for n_2=1.803, in the case of a waveguide with N=1.54. In order to obtain a feeling for the magnitude of the expected discrepancies between the WKB and Vassell's techniques, we programmed the computer to calculate the value of T_2 for a given value of a four-layer effective guide index. For a inhomogeneous guide (three-layer) with r=1.5435 and n_2=1.803, the values of T_2, calculated from the WKB technique, were found to be 35% smaller than expected. Correspondingly, large discrepancies were found in the shape of the field distribution, when compared to that obtained from Vassell's formulation, (see Fig.2.15).

Similar to the case of the four-layer homogeneous waveguides, we have calculated (Vassell's technique) the change in N due to variation of the thickness of the resist layer. The results are shown in Fig.2.16. The maximum values for combinations of T_2 and d which ensure propagation of the TE_0 mode only are given in Fig.2.17.

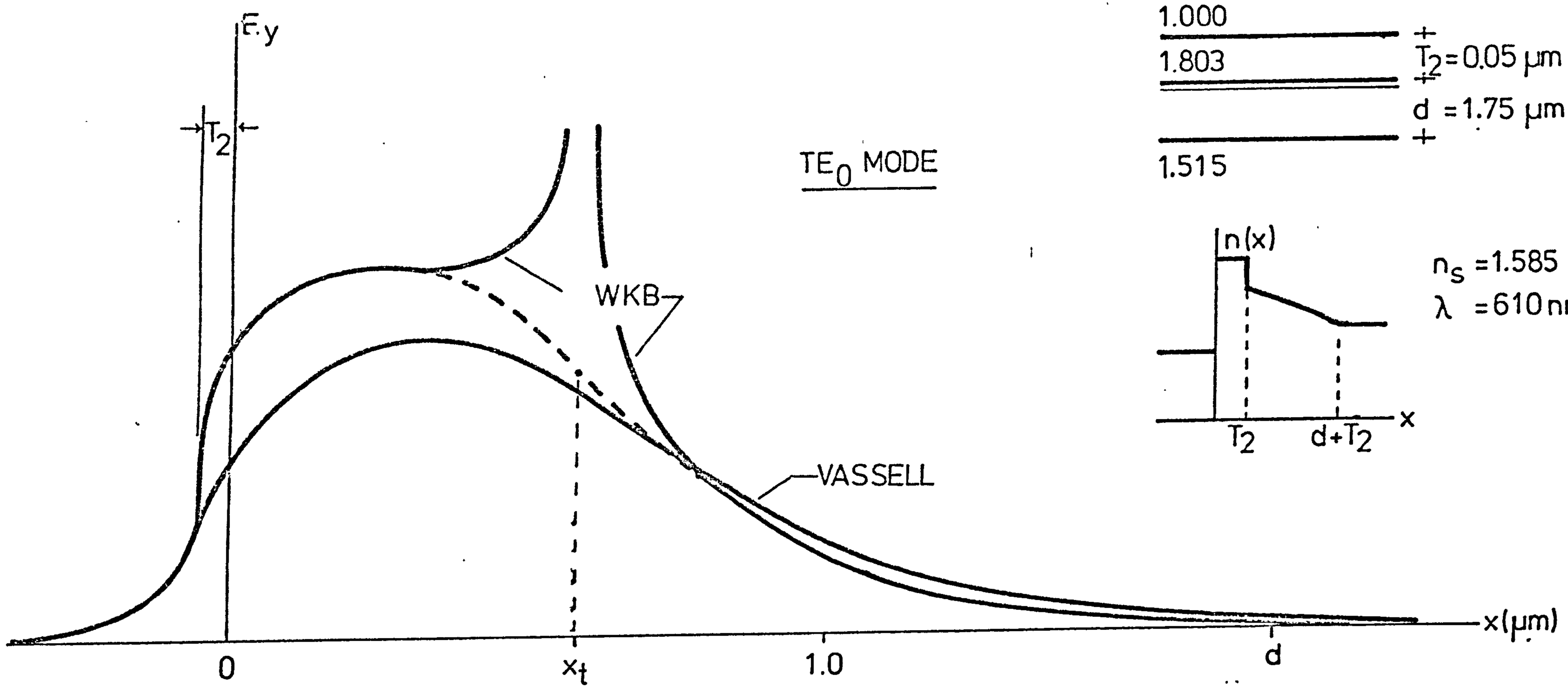

FIG 2.15 Field Distribution in a Four Layer Inhomogeneous Waveguide.

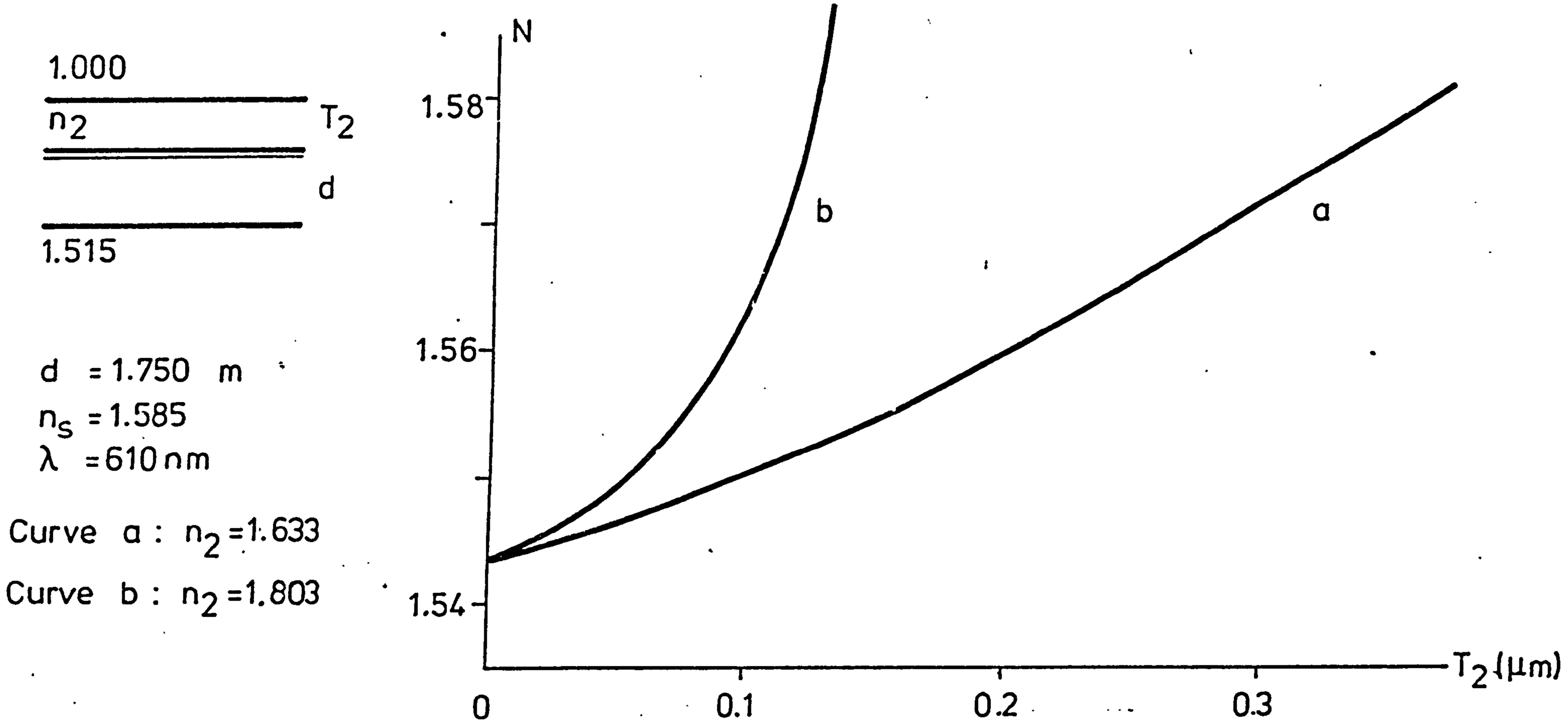

FIG 2.16 Effective Guide Index as Fuction of T_2

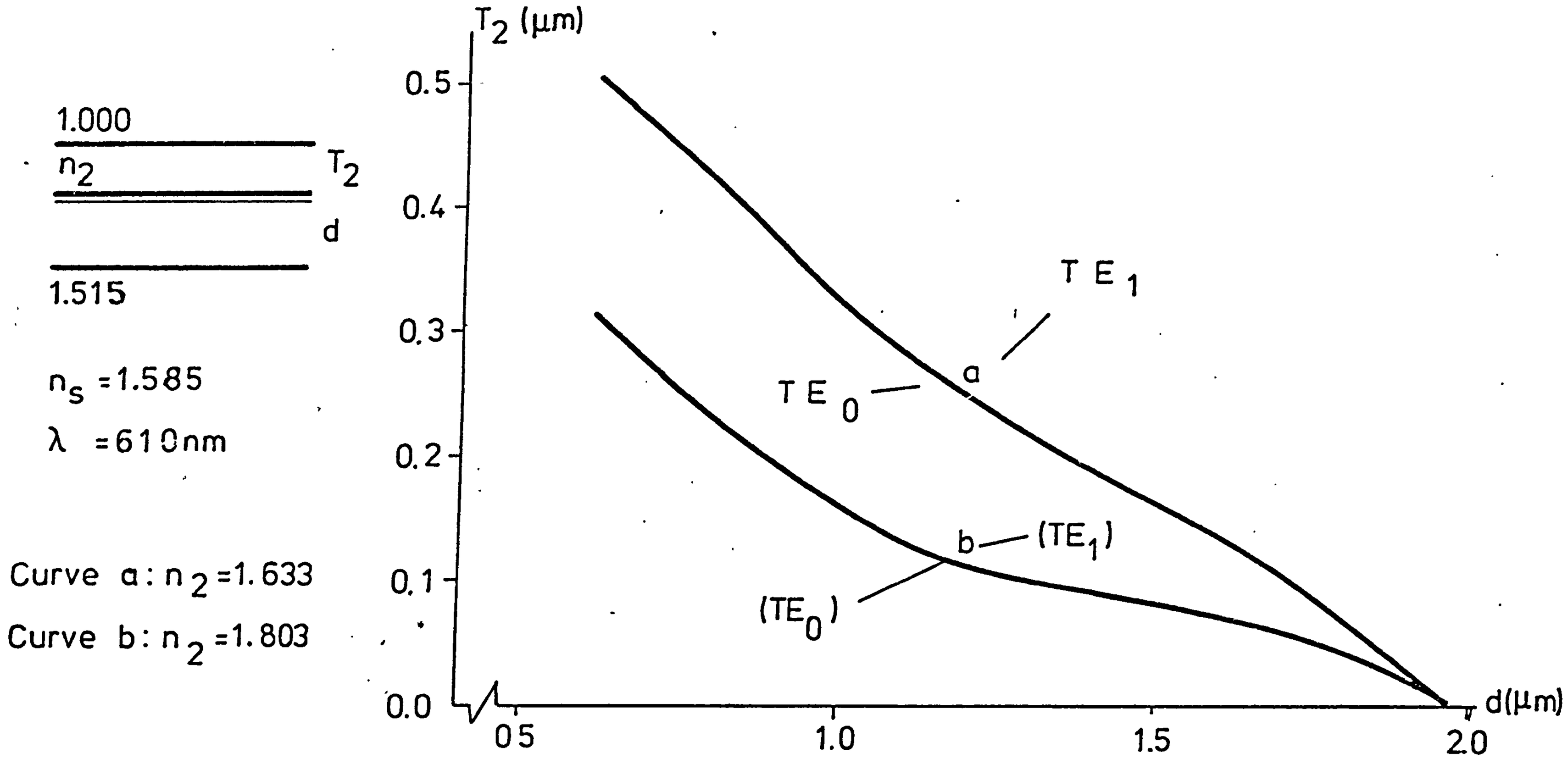

FIG 2.17 d and T_2 Values for Single TE_0 Mode Operation

2.5 Beam Coupling to Thin Film Waveguides

There are many methods of efficiently coupling free space propagating light into a mode of a thin film waveguide. These include edge focussing[83], tapered film coupler[84], holographic coupler[21], grating coupler[20,22] and prism coupler[10]. In this section, we give a brief description of the latter two, since they form an integral part of the experiments described in later chapters.

2.5.1 The Grating Coupler

This type of coupler is produced by forming a thin phase grating (usually in photoresist) on the surface of the guide or by etching the pattern directly into the waveguide or substrate (see Fig.2.18). One of the diffraction orders of the grating is used to couple light into the waveguide mode, by adjusting the angle of the incoming beam, such that the diffracted beam has the same phase velocity along the film direction as the guided mode. The equation governing the grating coupler is given by

$$N = n_2 \sin\theta_i + q\lambda/\Lambda \qquad (2.62)$$

where θ_i is the incident angle in free space, q is the diffracted order and Λ is the grating period. These couplers have typical input efficiencies of 40%, although an efficiency of 70% has been reported[22].

2.5.2 The Prism Coupler

Prism couplers enable accurate calculation of mode propagation constants N, the launching of light at any chosen point on the film and have a theoretical maximum efficiency[85] of 88%. In this type of coupler, coupling takes place through the surface of the film. The evanescent field, associated with the total internal reflection of light at the prism base-air gap interface, allows the light to 'tunnel' into the waveguide (see Fig.2.19). Coupling to a guided mode occurs when

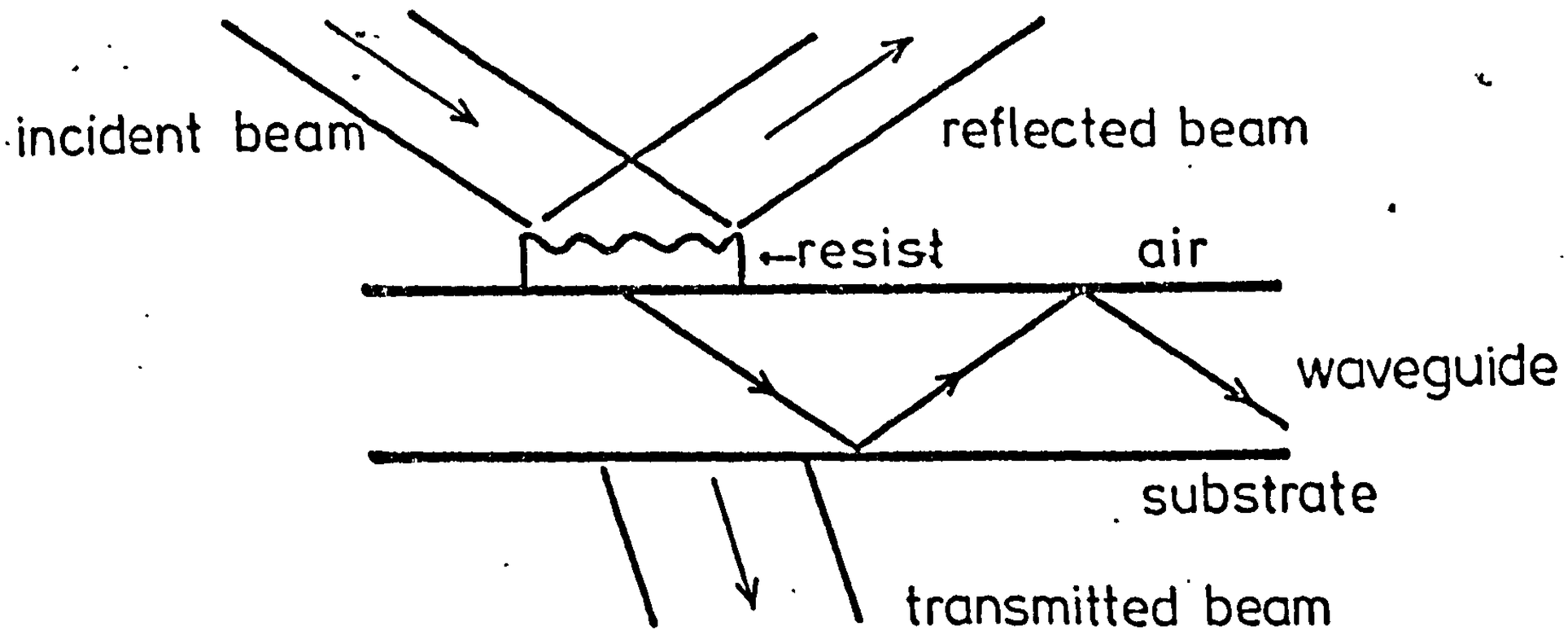

Photoresist Grating

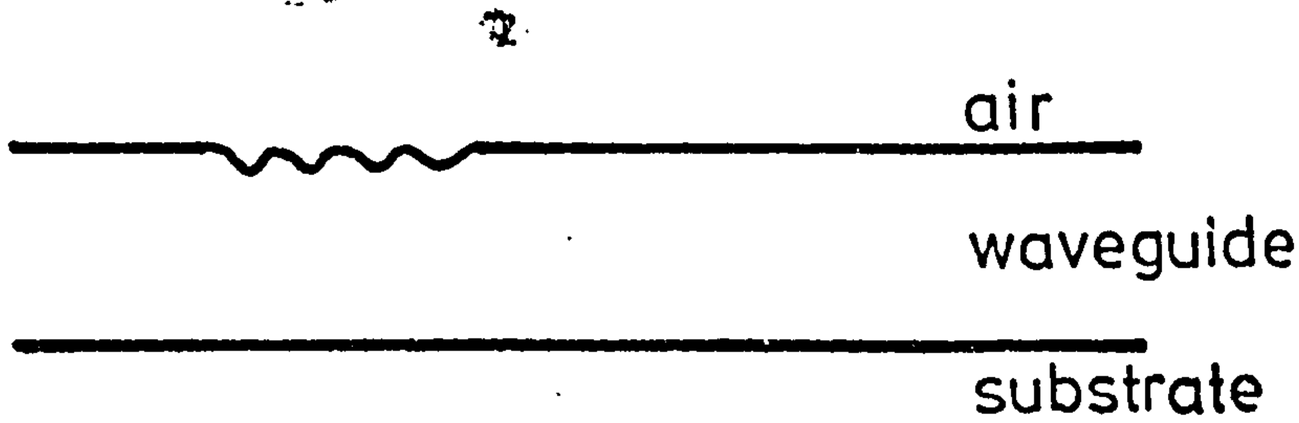

Etched Grating

FIG 2.18 Grating Couplers

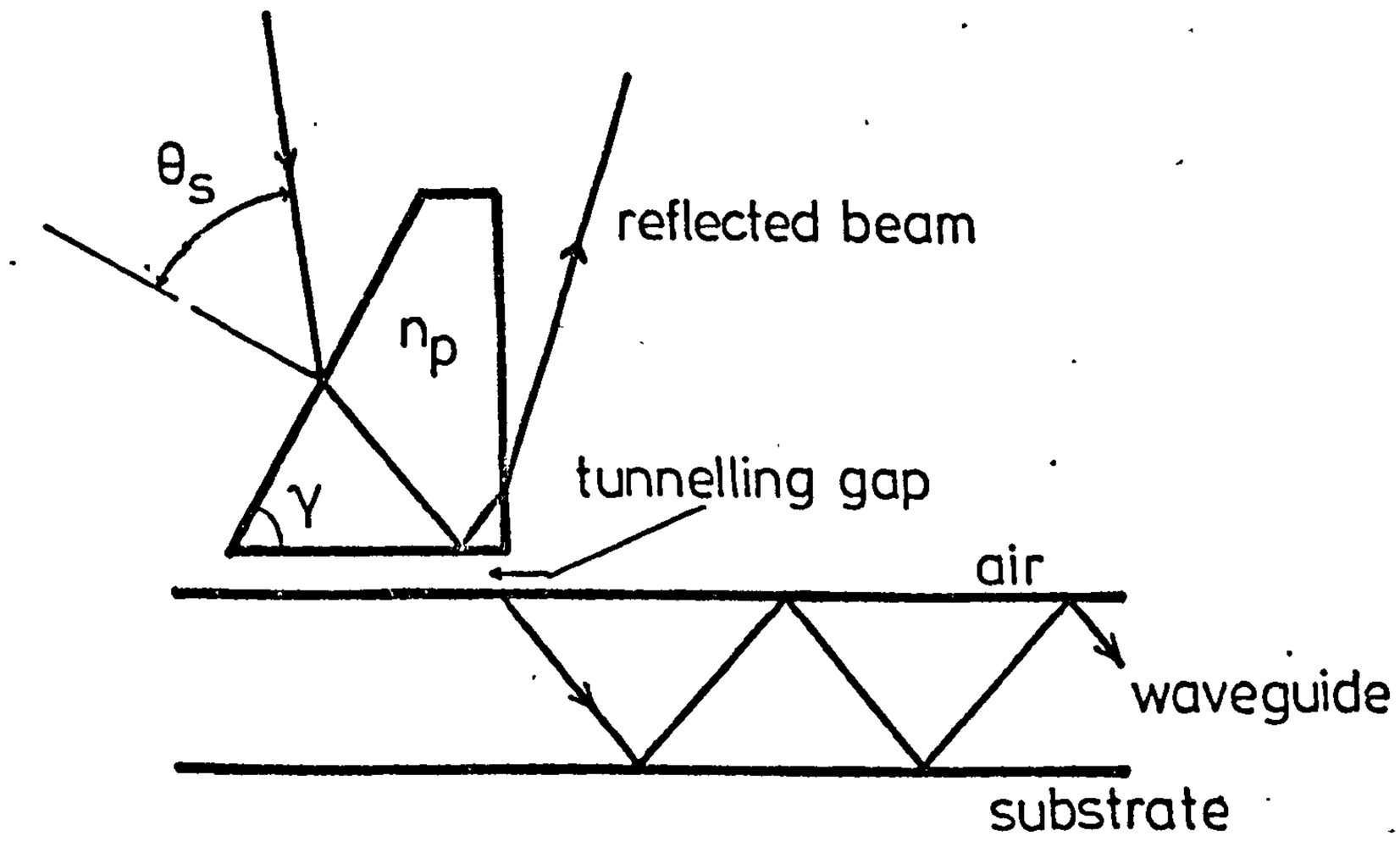

FIG 2.19 Prism-Film Coupler

the angle of incidence on the lower prism face is such, that the evanescent field in the gap region travels with the same phase velocity along the film direction as the guided mode. To prevent the light leaking back out of the guide, the prism is truncated after the maximum light energy has been transferred to the film.

The propagation constants of the modes can be obtained by measuring the synchronous coupling angles for the modes. These are related by

$$N = n_p \sin\left[\sin^{-1}\left[\frac{\sin\theta_s}{n_p}\right] + \gamma\right] \qquad (2.63)$$

where θ_s is the synchronous incident angle and γ is the internal angle of the prism.

The measurement of two or more mode angles θ_s permits the film refractive index and thickness to be calculated from the mode equation, provided the surrounding indices and wavelength of operation are known[86].

Appendix 2A.

Using equations (2.22) the boundary conditions yield

$$A_1 = A_2 \qquad (2A.1(a))$$

$$A_2\cos b_1T_1 - A_3\sin b_1T_1 = A_4 \qquad (2A.1(b))$$

$$-p_2A_1 = A_3b_1 \qquad (2A.1(c))$$

$$A_2b_1\sin b_1T_1 + A_3b_1\cos b_1T_1 = p_3A_4 \qquad (2A.1(d))$$

The determinant, for the above system of simultaneous equations, can be represented by

$$|C_{ij}|$$

whose elements are

$$C_{11} = -C_{12} = -C_{24} = 1 \qquad C_{33} = -b_1$$

$$C_{31} = -p_2 \qquad C_{44} = -p_3 \qquad C_{22} = \cos b_1T_1$$

$$C_{23} = -\sin b_1T_1 \quad C_{43} = -C_{33}C_{22} \quad C_{42} = C_{33}C_{23}$$

Nontrivial solution exists if $|C_{ij}| = 0$, i.e.

$$C_{11}(C_{22}C_{33}C_{44}-C_{42}C_{33}C_{24})-C_{12}(C_{31}C_{43}C_{24}+C_{31}C_{23}C_{44}) = 0$$

i.e.

$$\tan b_1T_1 = \frac{-(p_2/b_1 + p_3/b_1)}{(1 - p_2p_3/b_1b_1)}$$

or in a more general form

$$b_1T_1 = \tan^{-1}(-p_2/b_1) + \tan^{-1}(-p_3/b_1) + m$$

Letting $A_2 = A$ equations (2A.1) yield

$$A_1 = (-C_{12}/C_{11})A$$

$$A_3 = (C_{31}C_{12}/C_{33}C_{11})A$$

$$A_4 = (-C_{22}/C_{24})A + (C_{23}C_{31}/C_{24}C_{33})A$$

Equations (2A.1(b)) and (2A.1(d)) now give

$$\cos b_1 T_1 = (b_1^2 - p_0 p_2)/((b_1^2+p_2^2)(b_1^2+p_0^2))^{\frac{1}{2}}$$

$$\sin b_1 T_1 = b_1(p_0+p_2)/((b_1^2+p_2^2)(b_1^2+p_0^2))^{\frac{1}{2}}$$

Appendix 2B

Solutions to the wave equation (2.19) are

$$E_y = A_1 \exp(-p_3 x) \qquad \infty > x > 0$$

$$E_y = A_2 \cos b_2 x + A_3 \sin b_2 x \qquad 0 > x > -T_2$$

$$E_y = A_4 \cos b_1 (x+T_2) + A_5 \sin b_1 (x+T_2) \qquad -T_2 > x > -(T_1+T_2)$$

$$E_y = A_6 \exp(p_0 (x+(T_1+T_2))) \qquad -(T_1+T_2) > x > -\infty$$

The corresponding determinant for this case has the following elements

$$C_{11} = -C_{12} = -C_{34} = -C_{56} = 1 \qquad C_{21} = -p_3$$

$$C_{23} = -b_2 \qquad C_{45} = -b_1 \qquad C_{66} = -p_0$$

$$C_{32} = \cos b_2 T_2 \qquad C_{33} = -\sin b_2 T_2 \qquad C_{54} = \cos b_1 T_1$$

$$C_{55} = -\sin b_1 T_1 \qquad C_{42} = C_{23} C_{33} \qquad C_{65} = -C_{45} C_{54}$$

$$C_{43} = -C_{23} C_{32} \qquad C_{64} = C_{45} C_{55}$$

$|C_{ij}| = 0$ gives, after some algebra,

$$b_2 (b_2 C_{33} + p_3 C_{32})(p_0 C_{55} - b_1 C_{54}) =$$

$$-b_1 (b_1 C_{55} + p_0 C_{54})(p_3 C_{33} - b_2 C_{32})$$

i.e.

$$\frac{b_2 (b_2 \sin b_2 T_2 - p_3 \cos b_2 T_2)}{(p_3 \sin b_2 T_2 + b_2 \cos b_2 T_2)} = -\frac{b_1 (b_1 \sin b_1 T_1 - p_0 \cos b_1 T_1)}{(p_0 \sin b_1 T_1 + b_1 \cos b_1 T_1)}$$

or in terms of tangents and in a more general form

$$b_2 \tan(b_2 T_2 - \tan^{-1}(p_3/b_2) + m_2 \pi) =$$

$$-b_1 \tan(b_1 T_1 - \tan^{-1}(p_0/b_1) + m_1 \pi)$$

The coefficients A_i are related by the following

$$A_1 = A_2 = A$$

$$A_3 = -(p_3/b_2)A$$

$$A_4 = (C_{32}-C_{33}(p_3/b_2))A$$

$$A_5 = -(b_2C_{33}+C_{32}p_3)A/b_1$$

$$A_6 = (C_{54}(C_{32}-C_{33}p_3/b_2)-C_{55}(C_{33}b_2/b_1+C_{32}p_3/b_1))A$$

Appendix 2C

Program 'VASEL' computes the waveguide parameters of inhomogeneous optical waveguides by the multilayer sub-division technique.

Four different programs are available. The unknown parameter and the input data of each program are listed in the following table:

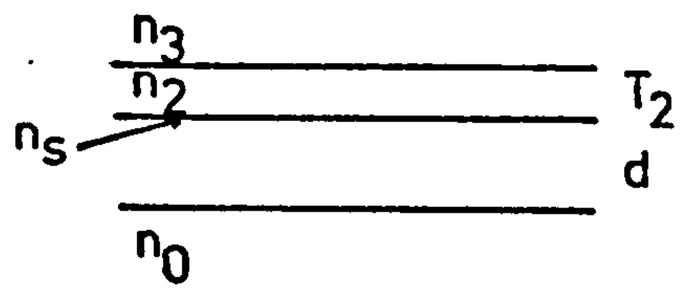

Program	λ	n_0	n_s	n_2	N	d	T_2	b	nl
VASEL 1	*	*	*	-	?	*	-	*	*
VASEL 2	*	*	*	*	?	*	*	*	*
VASEL 3	*	*	*	-	*	?	-	*	*
VASEL 4	*	*	*	*	*	*	?	*	*

where nl is the number of sublayers and b has the same meaning as in equation (2.59).

Program VASEL 4 includes a numerical integration of $\int E_y^2 dx$ inside regions 1 and 2 and prints out the value of E_y^2 at the guide-substrate interface. The printout of this program is given in the following pages and the notation for the input data is as follows:

LAMDA = λ NE = N

N(2) = n_0 NP = nl

N5 = n_2 D = d

```
      REAL N(4),N9,N3,N5,K1,K,K9,M,LAMDA,K8
      REAL NE
      DIMENSION T(16),P9(16),U(8),A1(4),E1(4),B1(4),EY(1000)
      DIMENSION EY1(1000),XUS(1000),XUT(1000)
      WRITE (5,105)
105    FORMAT(' LAMDA,N(2),N5,RIP,NE,NP,D,BBB')
      READ(5,*) LAMDA,N(2),N5,RIP,NE,NP,D,BBB
      PI=3.1415926536
      W=2.*PI/LAMDA
      WRITE(5,106)LAMDA,N5
106   FORMAT(' WAVELENGTH -',F10.5,'R.I. 1ST LAYER=',F10.5)
      WRITE(5,112) RIP,D,BBB
112   FORMAT(' PEAK R.I.=',F10.5,'DIFFUSION DEPTH',F10.5,'BBB',F10.5)
      WRITE(5,113) H1
113   FORMAT(' THICKNESS OF 1ST LAYER=',F10.5)
      WRITE(5,107) N(2)
107   FORMAT(' R.I. OF SUBSTRATE =',F10.5)
100   WRITE(5,108)
108   FORMAT(' ENTER EST. RESIST THICKNESS')
      READ(5,*) H1
      A=NE
      NIQ=NP+1
      N3=N(2)
      N(1)=1.
      H=D*(SQRT(1.+4.*BBB)-1.)*.5/BBB
      DO 1 J=1,8
      T(J)=0.
      P9(J)=0.
1     CONTINUE
      DO 2 J=1,4
      T(J)=1.
2     CONTINUE
      DO 5 J=1,2
      E1(J)=N(J)*N(J)
      B1(J)=SQRT(A*A-E1(J))
5     CONTINUE
      NP1=NP-1
      H9=H/NP1
      DO 20 I=1,NP
      IF(I.EQ.1) GOTO 50
      H9=H/NP1
      K=I-1.5
      K9=K*H9/D
      E=RIP-(RIP-N3)*(K9+BBB*K9*K9)
      E=E*E

35    Y=E-A*A
      IF(Y.LT.0.) GO TO 60
      B=SQRT(Y)
      M=W*H9*B
      SI=SIN(M)
      U(1)=COS(M)
      U(4)=-SI/B
      U(5)=-B*SI
      U(2)=-U(5)/E
      U(3)=-E*U(4)
      GO TO 80

50    E=N5*N5
      H9=H1
      GOTO 35
```

```
60      Y=-Y
        B=SQRT(Y)
        M=W*H9*B
        U(1)=COSH(M)
        U(4)=-SINH(M)/B
        U(5)=B*SINH(M)
        U(2)=-U(5)/E
        U(3)=-E*U(4)
80      T(9)=T(1)*U(1)-P9(6)*U(2)
        P9(13)=T(2)*U(2)+P9(5)*U(1)
        P9(14)=P9(6)*U(1)+T(1)*U(3)
        T(10)=T(2)*U(1)-P9(5)*U(3)
        T(11)=T(3)*U(1)-P9(8)*U(4)
        P9(15)=T(4)*U(4)+P9(7)*U(1)
        P9(16)=P9(8)*U(1)+T(3)*U(5)
        T(12)=T(4)*U(1)-P9(7)*U(5)
        DO 85 J=1,8
        L=J+8
        T(J)=T(L)
        P9(J)=P9(L)
85      CONTINUE
20      CONTINUE
        A1(2)=P9(6)+E1(1)*T(2)/B1(1)+E1(2)*T(1)/B1(2)
        A1(2)=A1(2)-E1(1)*E1(2)*P9(5)/(B1(1)*B1(2))
        A1(4)=P9(8)+B1(1)*T(4)+B1(2)*T(3)-B1(1)*B1(2)*P9(7)
        WRITE(5,110) A1(2),A1(4)
110      FORMAT(' A(1)(TM)=',E15.6,'A(2)(TE)=',E15.6)
        WRITE(5,211)
211     FORMAT(' IF NE OK AND EY REQUIRED TYPE 1 OTHERWISE 0')
        READ(5,*) NFI
        IF(NFI.EQ.1) GOTO 300
        GO TO 100
300     N3=N(2)
        EY(1)=1.
        EY1(1)=1.
        N(1)=1.
        H=D*(SQRT(1.+4.*BBB)-1.)*.5/BBB
        DO 11 J=1,8
        T(J)=0.
        P9(J)=0.
11      CONTINUE
        DO 21 J=1,4
        T(J)=1.
21      CONTINUE
        DO 51 J=1,2
        E1(J)=N(J)*N(J)
        B1(J)=SQRT(A*A-E1(J))
51      CONTINUE
        NP1=NP-1
        H9=H/NP1
        DO 201 I=1,NP
        IF(I.EQ.1) GOTO 501
        H9=H/NP1
        K=I-1.5
        K9=K*H9/D
        E=RIP-(RIP-N3)*(K9+BBB*K9*K9)
        E=E*E

351     Y=E-A*A
        IF(Y.LT.0.) GO TO 601
        B=SQRT(Y)
        M=W*H9*B
        SI=SIN(M)
        U(1)=COS(M)
        U(4)=-SI/B
```

```
      U(5)=-B*SI
      U(2)=-U(5)/E
      U(3)=-E*U(4)
      GO TO 801

501   E=N5*N5
      H9=H1
      GOTO 351

601   Y=-Y
      B=SQRT(Y)
      M=W*H9*B
      U(1)=COSH(M)
      U(4)=-SINH(M)/B
      U(5)=B*SINH(M)
      U(2)=-U(5)/E
      U(3)=-E*U(4)
801   T(9)=T(1)*U(1)-P9(6)*U(2)
      P9(13)=T(2)*U(2)+P9(5)*U(1)
      P9(14)=P9(6)*U(1)+T(1)*U(3)
      T(10)=T(2)*U(1)-P9(5)*U(3)
      T(11)=T(3)*U(1)-P9(8)*U(4)
      P9(15)=T(4)*U(4)+P9(7)*U(1)
      P9(16)=P9(8)*U(1)+T(3)*U(5)
      T(12)=T(4)*U(1)-P9(7)*U(5)
      DO 851 J=1,8
      L=J+8
      T(J)=T(L)
      P9(J)=P9(L)
851   CONTINUE
      EY(I+1)=(T(3)-B1(1)*P9(7))*EY(1)
      X=H1+H9*(I-1)
      EYOUT=EY(I+1)
      EY(I+1)=EY(I+1)*EY(I+1)
      XUT(I+1)=X

      IF(I.EQ.1)EY2=EYOUT
201   CONTINUE
      A1(2)=P9(6)+E1(1)*T(2)/B1(1)+E1(2)*T(1)/B1(2)
      A1(2)=A1(2)-E1(1)*E1(2)*P9(5)/(B1(1)*B1(2))
      A1(4)=P9(8)+B1(2)*T(3)+B1(1)*T(4)-B1(1)*B1(2)*P9(7)
      WRITE(5,110) A1(2),A1(4)
      XN1=W*SQRT(N5*N5-NE*NE)*H1
      BYY=(EY2-COS(XN1))/SIN(XN1)
      DO 503 J=1,11
      XN1N=XN1*(J-1)*.1
      XU=H1*(J-1)*.1
      EY3=COS(XN1N)+BYY*SIN(XN1N)
      WRITE(5,1000) XU,EY3
1000  FORMAT(2F20.5)
      XUS(J)=XU
      EY1(J)=EY3*EY3
503   CONTINUE
      IFAIL=0
      CALL D01GAF(XUS,EY1,11,ANS,ER,IFAIL)
      WRITE(5,1001) ANS
1001  FORMAT('  INTEGRAL OF EY**2 OVER RESIST  ',F10.5)
      NPP=NP+1
      DO 439 II=2,NPP
      XUT(II-1)=XUT(II)
      EY(II-1)=EY(II)
439   CONTINUE
      CALL D01GAF(XUT,EY,NP,ANS,ER,IFAIL)
      WRITE(5,1002) ANS
1002  FORMAT(' INTEGRAL OVER THE DIFFUSED REGION IS ',F10.5)
      YLAST=EY(NP)
      WRITE(5,1005)YLAST
1005  FORMAT(' THE- EFIELD SQUARED IS' ,F10.5)
      STOP
      END
```

CHAPTER III

ANALYSIS OF BRAGG WAVEGUIDE FILTERS

The purpose of the present chapter is to present a theoretical analysis of the properties of the Bragg filters.

Thin film Bragg filters are produced by forming a thin phase grating on the surface of the guide, or by etching the pattern directly into the waveguide. The operation of Bragg filters can be pictured initially in terms of an optical ray approach (see Fig.3.1). A ray incident, at an angle θ_2 from medium with refractive index n_2 onto a grating, will be diffracted into many orders. The angle θ_q which these diffracted beams make with the normal in region with index n_1 is given by the well known grating equation

$$n_1 \sin\theta_q + n_2 \sin\theta_2 = \frac{q\lambda}{\Lambda}$$

where λ is the free space wavelength and q is the order of the diffracted beam. If the value of the period Λ is smaller than λ, there will be at most three diffracted beams corresponding to q = 0 and ±1. Consider now a guided mode which propagates with an effective guide index N. The ray will be incident on the grating at an angle given by equation (2.5), i.e.

$$N = n_1 \sin\theta_1$$

The q = 1 diffracted order will be collinear with the incident ray if $\theta_{q=1} = \theta_1$ and the forward travelling mode will be reflected off the grating in the reverse direction. Combining the grating formula with the equation for N we obtain the Bragg condition

$$\Lambda = \lambda/2N$$

The q=-1 order, in this case, is evanescent as $\theta_{q=-1} = \sin^{-1}(-N)$ and N>1.

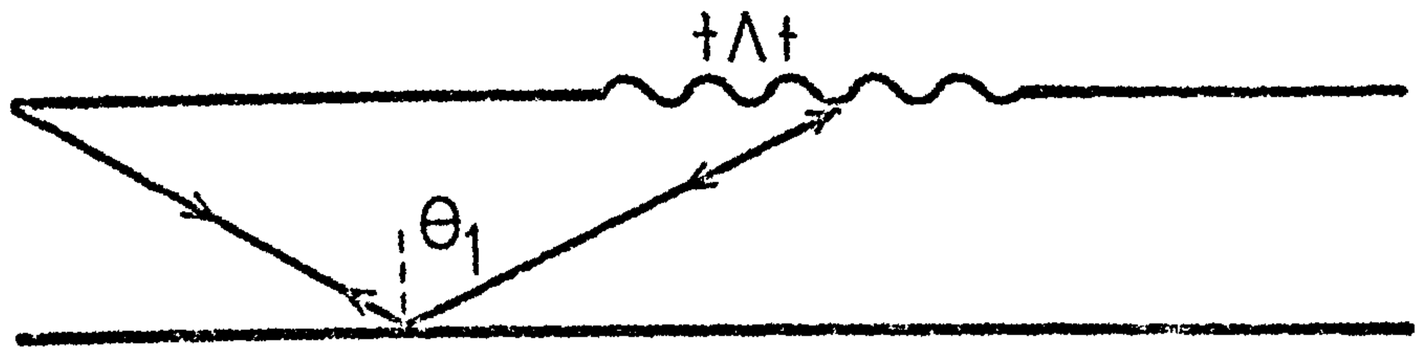

At $\lambda = \lambda_{Bragg}$

FIG 3.1 Ray Optics Representation of a Bragg Filter

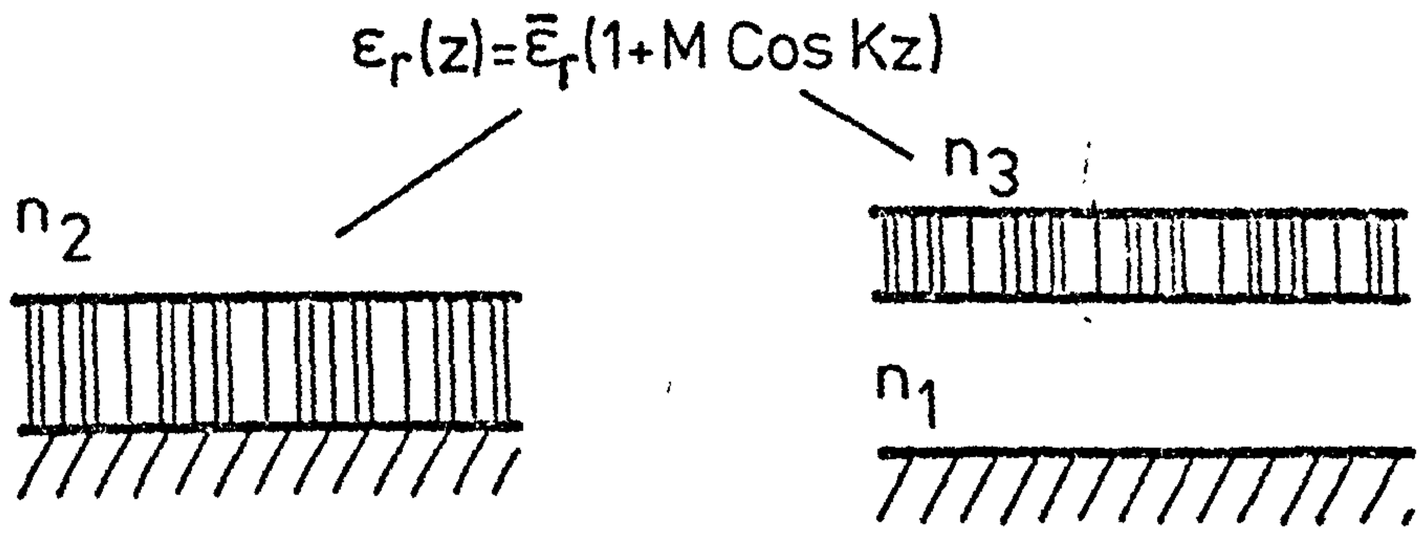

(a) Type I

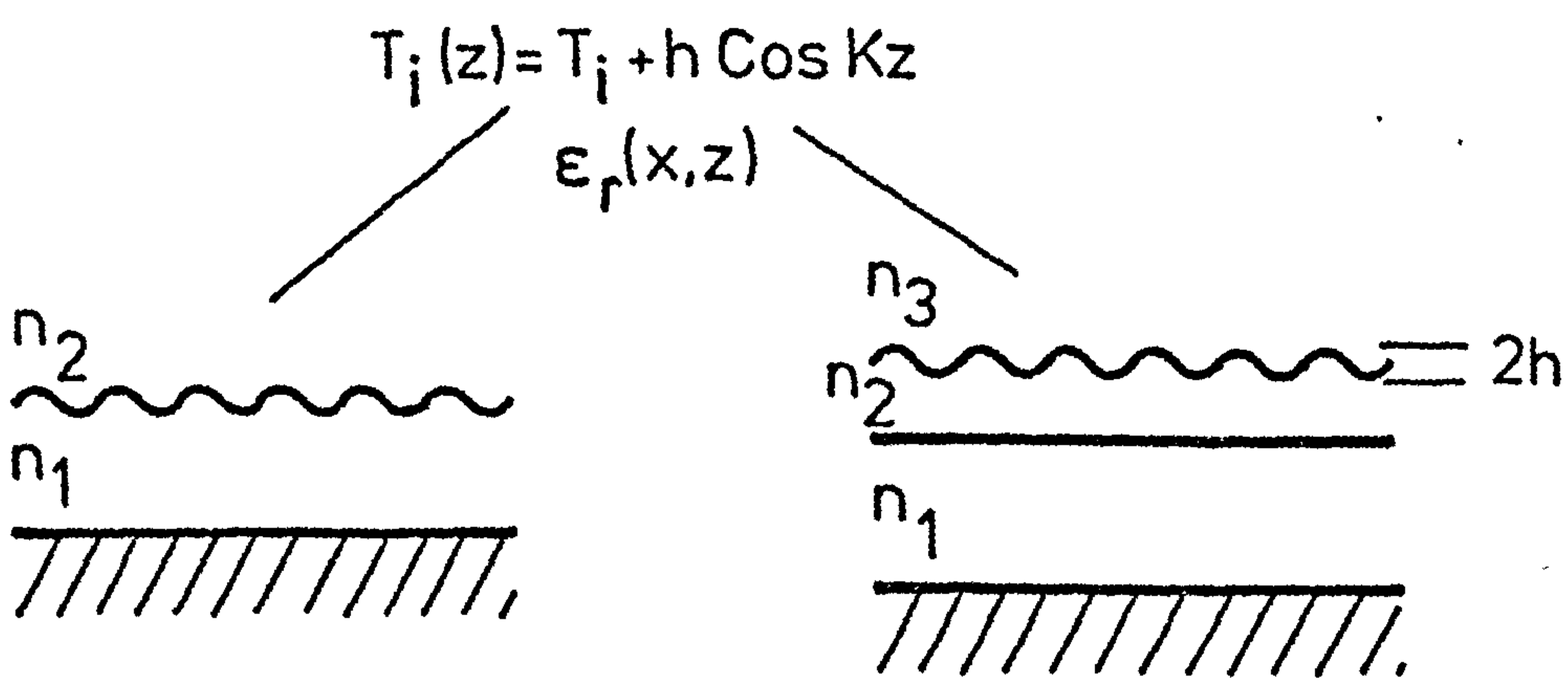

(b) Type II

FIG 3.2 Periodic Waveguides

The waveguide condition ensures that the q=0 order is also evanescent and there is no radiation into the superstrate. The specularly reflected ray will subsequently interact with the remaining portion of the grating and the power of the reflected mode will correspondingly increase. The simple ray optics approach is useful in giving a qualitative description of the filter. It does not, however, give a full account of the properties of the device and the electromagnetic theory approach must be used.

The rigorous solution of the problem poses computational difficulties due to the cumbersome functional form of the field expressions. Under certain conditions, simpler approximate solutions can be implemented with a good degree of accuracy. In this chapter, we present the analysis of Bragg filters, using the approximate coupled mode formalism. In order to justify the use of such formalism, we devote the first two sections of the chapter to showing its equivalence to the exact solution, in the case considered here. In the remaining sections of this chapter, we derive the expressions for the parameters which characterize the performance of Bragg filters and discuss their properties with numerical examples.

3.1 Wave Propagation in a Periodic Slab Waveguide

Periodic optical waveguides can be broadly classified into two main types depending on the way the periodic variation is introduced. We call type I those waveguides whose guiding layers have parallel planar boundaries; the periodicity being introduced by a longitudinal modulation of the refractive index of one layer (Fig.3.2(a)). Waveguides whose guiding layers are homogeneous, but the upper boundary has a spatial periodic variation are referred to as type II (Fig.3.2(b)).

The analysis of the fields in these structures is, in general, complicated. For type I waveguides, the wave equations for the TE and TM modes are given, respectively, by

$$\nabla^2 E_y + k^2(z) E_y = 0 \quad , \quad k^2(z) = k_0^2 \varepsilon_r(z) \tag{3.1(a)}$$

$$\nabla^2 H_y + k^2(z) H_y = 0 \quad , \quad k^2(z) = k_0^2 \varepsilon_r(z) - \frac{1}{\varepsilon_r(z)} \frac{\partial \varepsilon_r(z)}{\partial z} \frac{\partial H_y}{\partial z} \tag{3.1(b)}$$

and the corresponding expressions for the type II waveguides are given by

$$\nabla^2 E_y + k^2(z) E_y = 0 \quad , \quad k^2(z) = k_0^2 \varepsilon_r(x,z) \tag{3.2(a)}$$

$$\nabla^2 H_y + k^2(z) H_y = 0 \quad , \quad k^2(z) = k_0^2 \varepsilon_r(x,z) - \frac{(\nabla \varepsilon_r(x,z) . \nabla H_y)}{\varepsilon_r(x,z)} \tag{3.2(b)}$$

The general approach to solving the problem consists in, firstly, expressing the function $k^2(z)$ in a Fourier expansion; secondly, finding the fields inside the layer containing the periodic variation (grating) and, subsequently, applying the boundary conditions to determine the modal field amplitudes and propagation constants for the complete waveguide. Exact solution for equation (3.1(b)) exists and it has the form of a Floquet infinite series of space harmonics. Solution for the TM modes, equation (3.1(b)), depends on the functional form of the factor $k^2(z)$. Peng et al[87] have formulated rigorous solutions for both TE and TM modes in type I waveguides; in their work, the TM case is solved by expressing the $k^2(z)$ term into a series expansion. The case of type II waveguides presents a more complicated situation. The functional form of the wave equations (3.2) lead to eigenfunctions which can not be separated into the x and z coordinates and the associated boundary conditions pose a further problem, because the grating profiles are generally curved. However, rigorous solutions for the TE and TM modes in type II waveguides have been formulated by

Neviere et al[88,89]; the methods of solution are similar and each involves a numerical search for the eigensolutions in x and z and a subsequent numerical integration to find the amplitudes of the fields. The analysis of devices which use the properties of a type II waveguide requires closed form expressions for the fields. Since the solution to the wave equations (3.2) is the crux of the problem, approximations have been implemented, where possible, to transform the type II waveguide into a type I and thereby, using a solution of the latter. The building block in the transformation is a type II waveguide whose grating has a rectangular profile. The grating is then replaced by a layer of constant thickness, but modulated dielectric constant. A comparison study between the numerical results obtained for the original and transformed structures have been reported by Peng et al[137] who showed a discrepancy of 1% for cases where $\bar{\varepsilon}_r$ and M are taken as

$$\bar{\varepsilon}_r = \frac{\varepsilon_2 + \varepsilon_3}{2}$$

$$M = \frac{4}{\pi} \frac{\varepsilon_2 - \varepsilon_3}{\varepsilon_2 + \varepsilon_3}$$

In other words, $\bar{\varepsilon}_r$ is the averaged permittivity of the permittivities of the two media (ε_2 and ε_3) which are separated by the periodic boundary and M as the magnitude of the fundamental harmonic in a Fourier expression describing the periodic variation. The successful transformation, in this case, encouraged the application of the technique to gratings with a more general profile. Thin layers containing rectangular gratings with varying widths, but constant periodicity, were used to approximate the shape of the original grating profile. Subsequent results showed that good accuracy could be obtained only in cases when the original grating had a symmetrical profile with respect

to a vertical plane. The type II waveguide, with rectangular profile grating, has also been studied by Wang[138] and by De Wames et al[139], in terms of a periodic change of the waveguide thickness. The reported analyses showed that, if the value of the dielectric permittivity of the guide is kept the same, the approximate solution to the structure using equation (3.1(a)) is valid for cases where the grating height h is less than $T_1/(m + 1)$, where m is the mode number. However, such a large value of h is not required in most practical devices and hence, the reported results have very useful applications. In the specific case of Bragg waveguide filters, the aspect ratio of the sinusoidal grating height to grating periodicity is generally of the order of $h/\Lambda<0.2$ and it is not unreasonable to assume that the profile of the grating is close to rectangular. Furthermore, within the practical limitations in the fabrication of sinusoidal gratings, the higher-order Fourier components (in the expansion of $k^2(z)$) of a nearly-sinusoidal grating are much smaller than those corresponding to the rectangular case. The physical significance of this fact is that fewer terms in the Floquet infinite series are required, in order to calculate the relevant parameters with good accuracy. The results reported by Wang and DeWames et al consequently support the use of equation (3.1(a)) to analyse the periodic waveguides used in our investigation. The Floquet form of solution,obtained from the various techniques described above,requires, in most cases, lengthy numerical computations of the fields. In many applications, the magnitudes of the periodic variations are small and sufficient accuracy can be obtained from perturbational analysis. The latter approach has been successfully used to predict the performance of the grating coupler[90,91]. Devices operating in the Bragg regime have been mainly analysed by the coupled mode formalism[92]. The theoretical predictions of the

formalism have been borne out in the cases of the distributed feedback[93] (DFB) and distributed Bragg reflector[94] (DBR) lasers and in a more detailed manner in the case of Bragg filters[24,25].

In this section we shall not attempt to give detailed accounts of the rigorous analysis. Instead, we shall state the important Floquet theorem and the general expression for the fields. We shall next discuss the general form of the dispersion diagram. As discussed above, the corrugated waveguide is solved in terms of a type I structure and the peculiarities of the former will be pointed out as the theoretical expressions develop. Finally, we shall discuss the relationship between the truncated Floquet solution and the coupled mode formalism. The latter will be used to analyse the Bragg filter.

3.1.1 Wave Equation for Propagation in Periodic Media: Floquet Theorem and the Dispersion Diagram

The analysis of periodic transmission systems is based on the Floquet theorem[95,96]. For a given mode of propagation, the fields at one cross section in the direction of propagation differ from those, one period Λ away only by a complex constant, i.e.

$$F(x,y,z)e^{-j\beta z} = F(x,y,z+\Lambda)e^{-j\beta z}e^{-j\beta\Lambda}$$

The field $F(x,y,z)e^{-j\beta z}$, on the other hand, is given by the Fourier series

$$F(x,t,z)e^{-j\beta z} = \sum F_q(x,y)e^{-j\beta z}e^{-jqKz} \qquad (3.3)$$

$$q = 0,1,2, \ldots$$

where

$$K = 2\pi/\Lambda \qquad (3.4)$$

The q-th term in the summation is called the q-th space (Hartree) harmonic and has a propagation constant, given by the Floquet condition

$$\beta_q = \beta + qK \tag{3.5}$$

In analysing specific structures, the problem is usually to find β and the values of the fields as a function of ω, so as to satisfy the required boundary conditions.

In the present analysis, the periodic system takes the form of a thin layer which contains the grating. The field $G(x,z)$ inside this layer must, therefore, have a Floquet form and can be expressed as

$$G(x,z) = \frac{1}{2}\left[\sum_g G_g(x) \cdot \sum_q B_{gq}\exp(-j\beta_q z) + c.c.\right] \tag{3.6}$$

where c.c. = complex conjugate.

On applying the boundary conditions, the eigensolutions $G_g(x)$ of the grating field are modified to give the eigensolutions for the complete waveguide structure. This operation thus determines the propagation constants k_{xm} for the modes and their respective amplitudes A_m. The value of k_{xm} is real in the guiding layers and it is, in general, complex elsewhere. In the specific case of TE modes, the modal field can therefore be written in the form

$$E_y(x,z) = \frac{1}{2}\left[\sum_m (A_m^- \exp(+jk_{xm}x) + A_m^+ \exp(-jk_{xm}x)) \cdot \sum_q B_{mq}\exp(-j\beta_q z) + c.c.\right] \tag{3.7}$$

Every m-th modal solution of E_y thus contains an infinite set of space harmonics. In practice, the contributions to the field from high-order harmonics are small and can be neglected. By careful monitoring of the relative amplitudes of the coefficients B_{mq}, it is possible to truncate the series to a manageable size. We note here that equation (3.7) can also be used to represent the field of a uniform slab waveguide. In that particular case, each modal solution will only contain a single

harmonic.

Matching the fields at the boundaries results in a system of simultaneous equations which is infinite in extent. The nontriviality condition for the system is a determinant of the Hill[96] type which gives the dispersion relation. The dispersion diagram, on the other hand, can be assessed qualitatively from equation (3.7). The validity of the series expansion is based on the orthogonal properties of the modes and of the space harmonics. As equation (3.7) satisfies the wave equation for TE modes,

$$\nabla^2 E_y + k^2(z) E_y = 0 \qquad (3.1(a))$$

it follows that every space harmonic is also a solution of (3.1(a)). Consequently, each harmonic will possess a dispersion curve of its own and similar to that of the uniform waveguide (Fig.2.3). By virtue of equation (3.5), the curves will be displaced by qK from one another as shown in Fig.3.3. Since we are mainly interested in the bounded wave, the following conditions must be satisfied

$$\mu_0 \varepsilon_0 n_1^2 \omega^2 \geq \beta_q^2 \geq \mu_0 \varepsilon_0 n_0^2 \omega^2 . \qquad (3.8)$$

This is shown graphically in Fig.3.3 inside regions labelled (a) and (b). Region (c) corresponds to coupling between guided and substrate leaky modes and in region (d) we have coupling between guided and air leaky modes. The curves also show that only successive space harmonics intersect in the bounded regions. The points of intersection are known as the phase-matched points. For an infinitesimally small perturbation ($\Delta\varepsilon_r$ or 2h), the space harmonics do not interact. If the perturbation is increased, coupling occurs at the phase-matched points leading to stopband interactions between modes of successive space harmonics. As will be shown later, the value of β near those points becomes complex

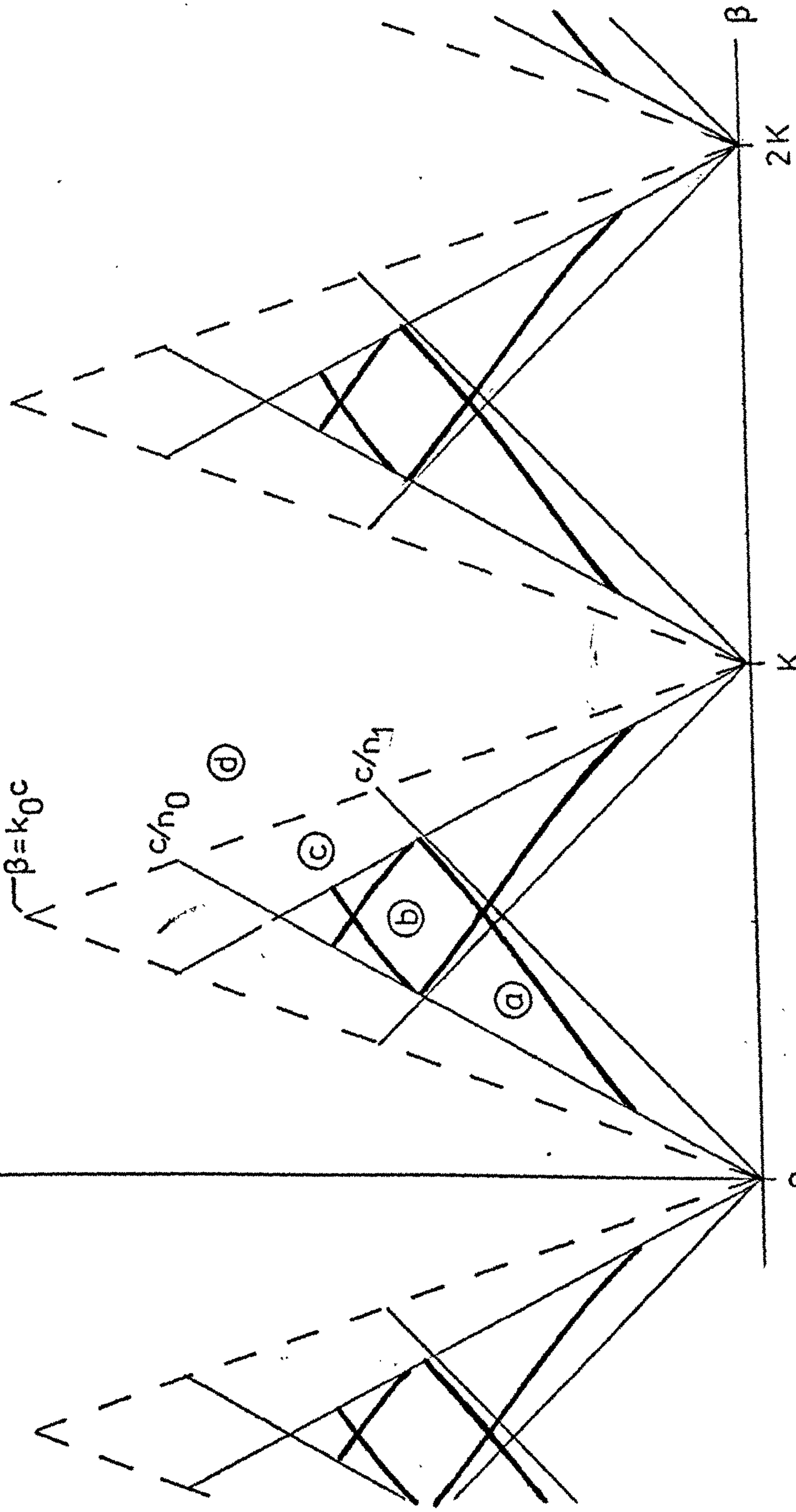

Dispersion Diagram for the Periodic Slab Waveguide

(Fig.3.4). As a result, the imaginary part of β introduces an exponentially decaying factor on the amplitude of the incident wave. Correspondingly, there is an exponentially growing factor on the amplitude of the wave travelling in the opposite direction (Fig.3.5). This penomenon is, in essence, equivalent to the well known Bragg diffraction of X-rays in crystal lattices. In our case, the analogous condition for constructive interference is given by

$$K = 2q\beta_o \tag{3.9}$$

for the q-th order interaction.

3.1.2 The Coupled Mode Formalism

Although the Floquet formulation is relatively simple, the numerical computation of the fields are involved. It has been shown[97] that, for strong sinusoidal perturbations and low q-order Bragg coupling, sufficient accuracy is obtained only if the Hill determinant is, at least, of the (2q+3)x (2q+3) order. As the perturbation becomes weaker, sufficient accuracy can be achieved by taking into account a fewer number of harmonics. Under this condition and restricting the analysis to regions in the vicinity of the first order Bragg coupling point, we will derive the coupled modes equations from the Floquet formula. Proof of the equivalence between the formalisms was given previously by Yariv et al[98] in a non-rigorous fashion.

Near the first stop band β can be written as

$$\beta = (K/2 + \Delta\beta) \quad \text{and} \quad \beta_o = K/2 \tag{3.10}$$

and let us assume that only first order harmonics, namely $q = \pm 1$, are non negligible.

For type I waveguides we write

$$\varepsilon_r(z) = \bar{\varepsilon}_1(1 + M \cos Kz) \tag{3.11}$$

where n_1 is the average index of refraction of the layer and M is called the modulation factor.

For type II waveguides, the boundary periodicity is given by the change in the film thickness

$$T_1(z) = T_1 + h \cos Kz \tag{3.12}$$

By virtue of equation (2.6), this implies that the propagation constant β is a function of z. Since β and k_{xm} are related by $\beta^2+k_{xm}^2=k_0^2n_1^2$ it is not unreasonable to assume the following*

$$k_{xm}^2(z) = k_0^2n_1^2 - \beta^2(z) \tag{3.13}$$

The wave equation (3.7) for TE modes can now be written as

$$\frac{d^2}{dz^2}\ U(z) + k^2(z)U(z) = 0 \tag{3.14}$$

if the wave number has the form

$$k^2(z) = k_0^2\varepsilon_r(z) - k_{xm}^2(z) = k_0^2\ \frac{1}{2}\left[\sum g_q e^{-jqKz} + c.c.\right] \tag{3.15}$$

where the Fourier coefficients g_q are known for a given grating and U(z) satisfies the differential equation

$$\left[\frac{d^2}{dz^2} + (k_0^2\varepsilon_r(z) - k_{xm}^2(z))\right]\ U(z) = 0 \tag{3.16}$$

---

* Even in the case of type I waveguides, we still face the problem created by the change of the field distributions in the transverse plane, because any change in $\beta(z)$ caused by $\Delta\varepsilon_r$ is necessarily accompanied by a corresponding change in k_{xm}.

The Floquet solution (3.6) can now be expressed in terms of the fundamental and first order harmonics. Making use of equation (3.10) yields

$$E_y(z) = A_m(x).((B_0 e^{-j\Delta\beta z} + B_{+1} e^{+j\Delta\beta z})\exp(-j\beta_o z) +$$

$$(B_0 e^{+j\Delta\beta z} + B_{-1} e^{-j\Delta\beta z})\exp(+j\beta_o z))$$

$$= A_m(x).(R(z)\exp(-j\beta_o z) + S(z)\exp(+j\beta_o z)) \qquad (3.17)$$

where the forward R(z) and reverse S(z) waves consist of, independently, the sum of the relevant harmonics with identical phase velocity.

Considering a sinusoidal periodic grating in equation (3.15) and assuming slow variation of the field amplitudes, i.e.

$$\left| \frac{d^2}{dz^2} R(z) \right| << \left| \beta_o \frac{dR}{dz}(z) \right| \text{ and } \left| \frac{d^2}{dz^2} S(z) \right| << \left| \beta_o \frac{dS}{dz}(z) \right| \qquad (3.16)$$

we substitute equation (3.17) into (3.14) and get

$$\left[-jKR' - \frac{K^2}{4} R + g_0 R + \frac{g_1}{2} S \right] \exp(-j\beta_o z) +$$

$$\left[+jKS' - \frac{K^2}{4} S + g_0 S = \frac{g_1}{2} R \right] \exp(+j\beta_o z) +$$

$$\frac{1}{2} \left[g_1 R \exp(-j\tfrac{3}{2}Kz) + g_1 S \exp(+j\tfrac{3}{2}Kz) \right] = 0 \qquad (3.18)$$

The last term of the above equation corresponds to the coupling to the second-order harmonic and can, in this case, be neglected. The remaining terms of equation (3.18) must be satisfied for all values of z. Equating each term to zero, we obtain

$$R' + j(g_0/K - K/4)R = -(jg_1/2K)S \qquad (3.19(a))$$

$$S' - j(g_0/K - K/4)S = +(jg_1/2K)R \qquad (3.19(b))$$

These are the well known coupled mode equations, which are normally written in the form

$$\frac{dR}{dz} + j\sigma R = -j\kappa S \qquad (3.20(a))$$

$$\frac{dS}{dz} - j\sigma S = j\kappa R \qquad (3.20(b))$$

where σ is called the wave vector mismatch and κ is the coupling coefficient. The solution of equations (3.20) is given by

$$S(z) = S_1\exp(+\nu z) + S_2\exp(-\nu z) \qquad (3.21(a))$$

$$R(z) = -\frac{(j\nu+\sigma)}{\kappa} S_1\exp(+\nu z) + \frac{(j\nu-\sigma)}{\kappa} S_2\exp(-\nu z) \qquad (3.21(b))$$

$$\nu^2 = \kappa^2 - \sigma^2 \qquad (3.21(c))$$

where the values of S_1 and S_2 are determined from the boundary conditions.

The above derivation gives a formal proof of the equivalence between the Floquet and coupled-mode formalisms. The latter presents a simpler form of solution and its accuracy has been checked by numerical comparisons of results with those obtained from the rigorous approach[99-101]. In the specific case of type I waveguides, Jaggard et al[97] found surprisingly good agreement for the value of κ, even in situations when M=1. Similar comparisons for the type II waveguides were given by Peng et al[87]. They found reasonable agreement for the case of a rectangular profile grating, whose height was $(2h/\lambda) \leq 0.2$. As the coupled-mode formalism does not take into account the effect of the exponential behaviour of the evanescent field, it tends to predict

larger values for κ as the grating height increases.

The position of the band gap, on the other hand, is not predicted accurately in either type of waveguide. This is not surprising, because the formalism assumes a known value of β which is normally taken to be that of the unperturbed guide, whereas, formally, it should be determined from the Hill determinant. Corrections to the unperturbed β can, however, be obtained by the following approximations: by evaluating the average change in β over one period[97]; by redefining the thickness of the waveguide[102] to a value of $T<T_1$; or by transforming the structure into a type I waveguide, assuming the grating layer to be parallel and to have a modulated index around an average value n_1[103]. The above evidence fully justifies the use of the formalism to analyse the Bragg filter. In our particular devices, we use a nearly sinusoidal corrugation, whose height 2h, is typically of the order of 50.0 nm. Working at a wavelength range of 6000A-6100A, the devices are well within the range of accuracy of the approach. Furthermore, the arguments of the higher order Fourier components, given in the introduction of this section lead us to expect adequate accuracy and extended range beyond the limit found by Peng et al.

3.2 Thin Film Bragg Filters

The analysis of Bragg filters using the coupled-mode equations requires the determination of the coupling coefficients. Subsequent application of the boundary conditions allows the evaluation of the amplitudes of the forward and reverse waves, as a function of the normalised frequency σ.

The structure under study in this work is a type II waveguide whose upper boundary has a sinusoidal periodicity. We present here

general expressions for the coupling coefficient and the parameters describing the filter response. These parameters are the fractional bandwidth ($\Delta\lambda/\lambda$) and the reflectivities of the main lobe (R_0) and first related sidelobes (R_1). Conditions under which the Bragg filter acts as a high frequency cut off device, are also given.

The analysis of filters, whose gratings are modulated by an amplitude and phase taper function, is presented next. It is shown that the theoretical response of these devices obeys a Riccati Differential equation, the solution of which requires a numerical computation[36]. Finally, we present the direct relation between the filter response and the Fourier transform of the taper function.

3.2.1 The Coupling Coefficient

The coupling coefficient can be evaluated from equations (3.13), (3.15) and (3.19). Substitution of equation (3.13) into (3.15) gives

$$k^2(z) = \beta^2(z) = \sum g_q e^{-jqKz} + c.c. \qquad (3.22)$$

The value of $\beta(z)$ can be expressed, to a first approximation, as[5]

$$\beta(z) = \beta_o \Big|_{T=T_1} + \frac{d\beta}{dT}\Big|_{T=T_1} \cdot h \cos(Kz) \qquad (3.23)$$

For TE modes, in a three layer structure, we use the dispersion equation (2.6) and obtain

$$\frac{d\beta}{dT}_{T=T_1} = {}^{b^2}/_{\beta_o T_e} \qquad (3.24)$$

Substitution of the above into equations (3.23) and (3.22) gives

$$g_0 = \beta_o^2 + (b_1^4 h^2)/(2\beta_o^2 T_e) = \beta^2 \qquad (3.25(a))$$

$$g_1 = (2 b_1^2 h)/T_e \qquad (3.25(b))$$

$$g_2 = (b_1^4 h^2)/(2\beta_o^2 T_e) \qquad (3.25(c))$$

From equation (3.19)

$$\kappa = \frac{g_1}{2K} = \frac{\pi h(n_1^2 - N^2)}{T_e N\lambda} \qquad (3.26)$$

$$\sigma = \frac{g_0}{K} - \frac{K}{4} = \frac{(\beta^2 - \beta_o^2)}{2\beta_o} \approx \beta - \beta_o \qquad (3.27)$$

The above expressions agree with those given by Flanders et al[24].

For the type I waveguides, a similar procedure gives

$$g_0 = k_0^2 n_1^2 - k_{xm}^2 = \beta^2 \qquad (3.28(a))$$

$$g_1 = k_0^2 n_1^2 \qquad (3.28(b))$$

correspondingly

$$\sigma = \beta - \beta_o$$

$$\kappa = \frac{\pi \cdot \varepsilon_1}{2\lambda\sqrt{\bar{\varepsilon}_1}} \quad , \quad \varepsilon_1 = M\,\bar{\varepsilon}_r \qquad (3.29)$$

and the above equations are the same as those given by Kogelnik[93,104] for the case of a no-gain, lossless medium.

The functional form of the dispersion equation (2.6) makes this derivation simple. However, for waveguides whose dispersion relation have more complicated forms, the method leads to cumbersome expressions. In general, the coupling coefficient can be determined from a consideration of the power, transferred from the forward wave to the reverse wave and vice versa. In our specific problem, the grating effectively introduces a polarization source which is proportional to

the field of one of the intervening waves. This polarization will, in turn, drive the second remaining wave. By consideration of power conservation we have, for a lossless medium,

$$\frac{d}{dz}\,(R^2(z) - S^2(z)) \;=\; 0 \qquad (3.30)$$

Using this principle, several workers[68,92,105] derived the expression for κ in terms of the fields of the unperturbed waveguide. For TE modes, the expression is given by

$$\kappa = \frac{\pi h}{2\lambda N} \cdot \frac{(n_1^2 - n_2^2)E_c^2}{\int_{-\infty}^{+\infty} E_y^2\, dx} \qquad (3.31)$$

where E_c (= A) is the value of the field at the film-superstrate interface.

Details of the derivation of equation (3.31) are given in Appendix 3A.

Equation (3.31) holds valid for any type of lossless slab planar waveguides. For the specific case of the three-layer structure, we can use equation (2.28) for the integral in the denominator of equation (3.31) and obtain equation (3.26) for the value of κ.

3.2.2 The Band-Gap Width

Equations (3.21) give the variation of the wave amplitudes as a function of the normalised frequency σ. The modal field expression of equation (3.17) can now be written as

$$E_y(z) = A_m(x).((R_1 e^{-j(\beta_o + j\nu)z} + R_2 e^{-j(\beta_o - j\nu)z}) +$$

$$(S_1 e^{+j(\beta_o - j\nu)z} + S_2 e^{+j(\beta_o + j\nu)z})) \qquad (3.32)$$

where

$$R_1 = -\frac{(j\nu+\sigma)}{\kappa} S_1 \quad , \quad R_2 = +\frac{(j\nu+\sigma)}{\kappa} S_2$$

and $\nu^2 = \kappa^2 - \sigma^2$

For $\kappa>\sigma$, ν is real and the z-dependence of the wave solution (3.32) are exponentials with propagation constants

$$\beta = \beta_o \pm j\,(\kappa^2 - (\beta(\omega) - \beta_o)^2)^{\frac{1}{2}} \qquad (3.33)$$

The imaginary part of the above equation is responsible for the exponential behaviour of the wave amplitudes. It is also related to the width of the stop-band and is given by

$$\kappa^2 - (\beta(\omega) - \beta_o)^2 \;\approx\; \kappa^2 - \left(\frac{d\beta}{d\omega}\right)^2 \cdot (\omega-\omega_o)^2$$

i.e.

$$\Delta\omega_{gap} = 2\kappa V_g \qquad (3.34)$$

where V_g is the group velocity defined in equation (2.36). The results of equation (3.33) is shown in Fig.3.4.

For $\kappa<\sigma$, ν is imaginary and the solutions which are periodic functions are in the pass-band.

3.2.3 Fractional Bandwidth and Reflectivities

As described in the introduction to this section, the amplitudes of the forward and reverse waves can be determined after the application of the boundary conditions. These are given in a normalized form by

$$R(z = 0) = 1 \qquad (3.35(a))$$

$$S(z = L) = 0 \qquad (3.35(b))$$

where L is the (interaction) length of the grating. Combining equations (3.35) and (3.21) we find

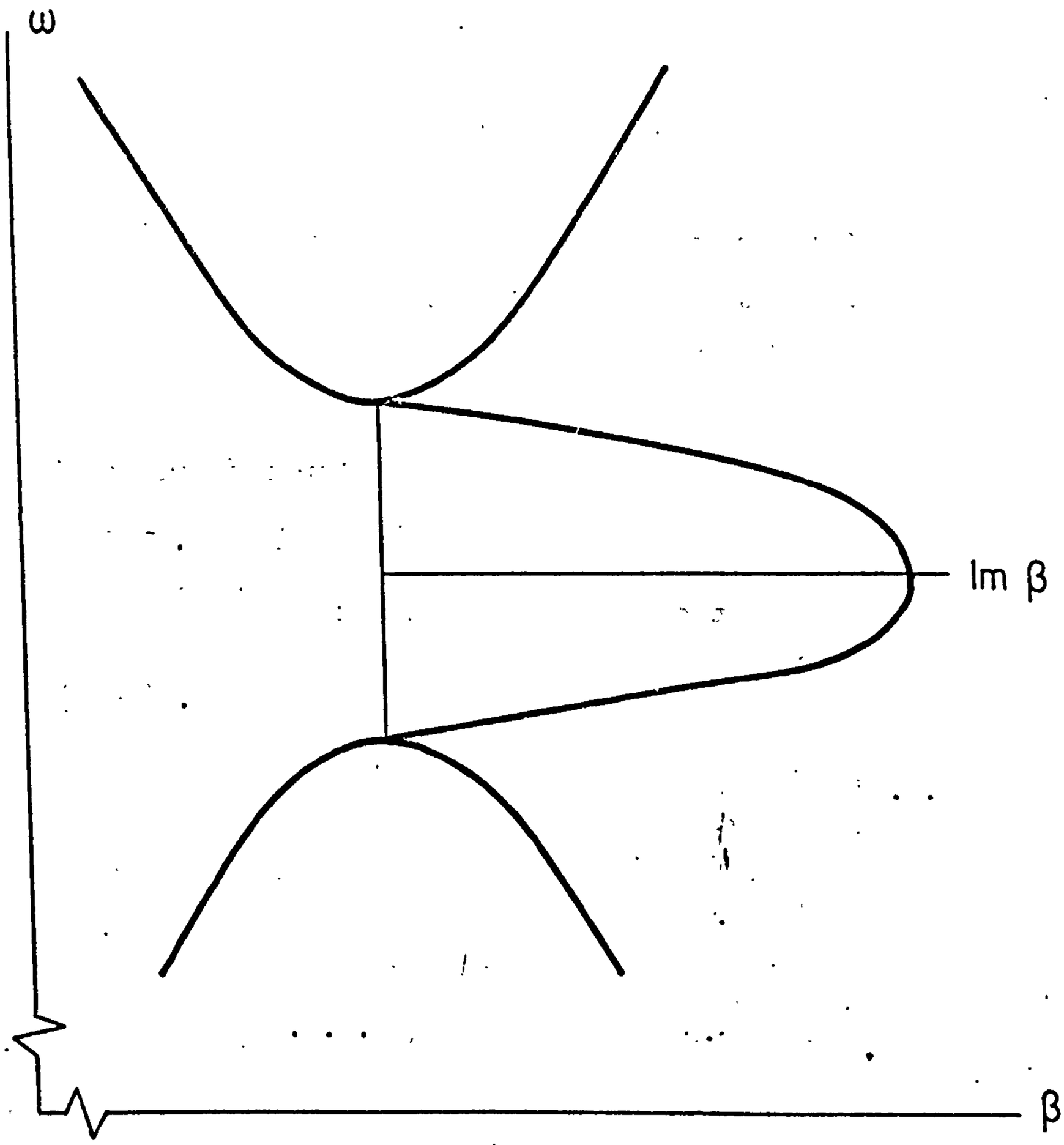

FIG 3.4 ω-β Diagram in the Region of the Stop-Band

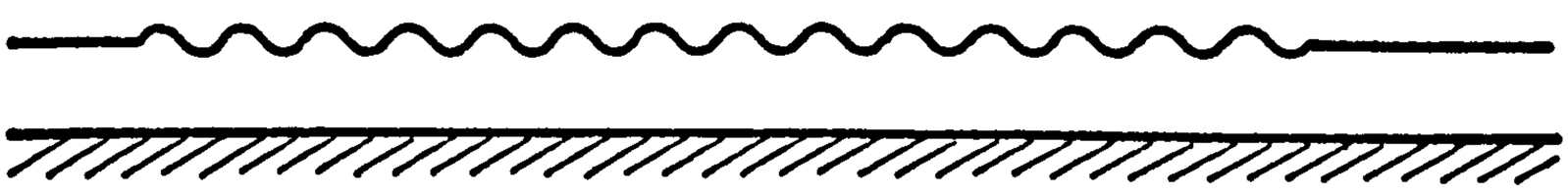

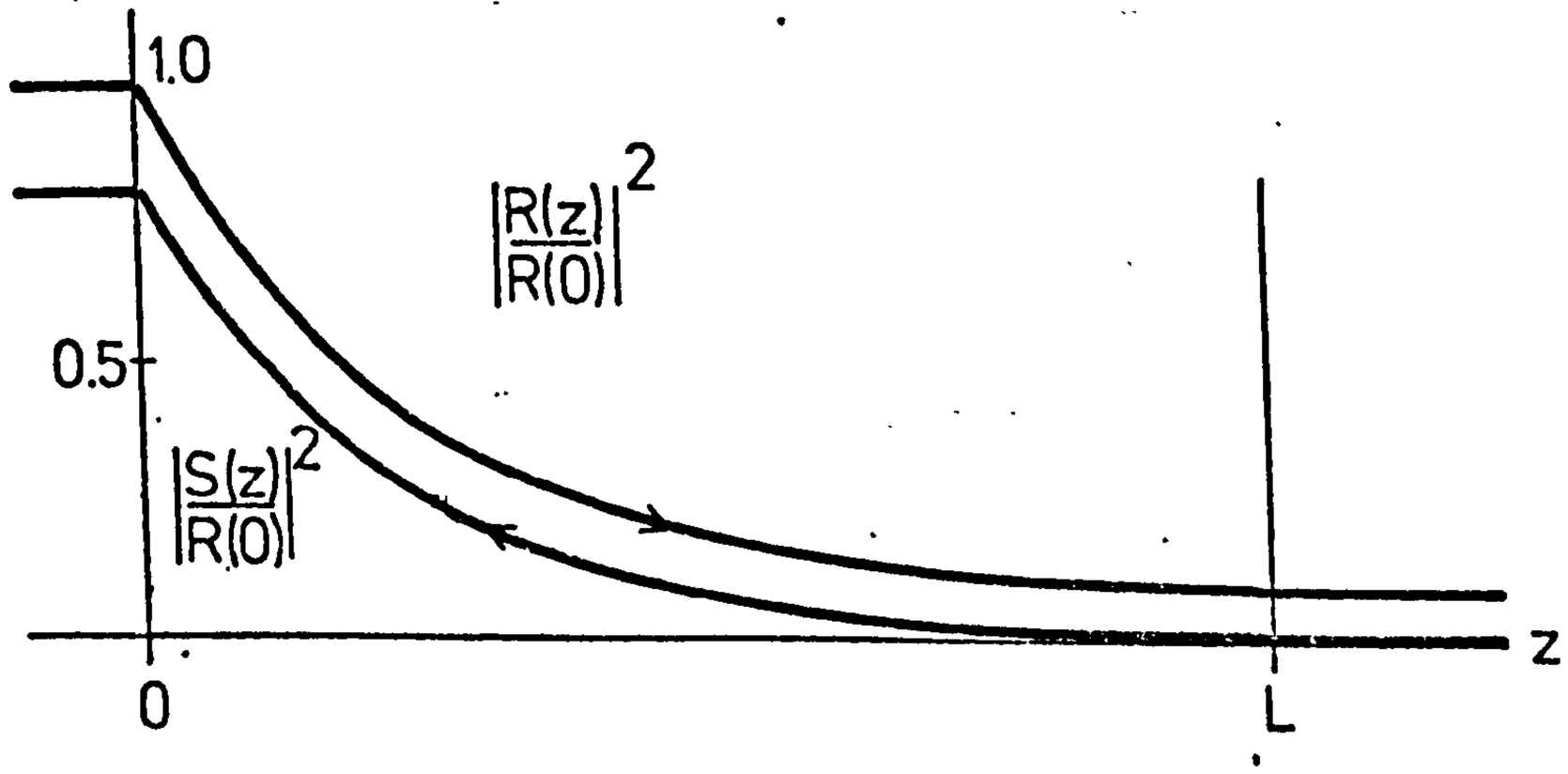

FIG 3.5 Normalized Power of the Forward and Reversed Waves.

$$R(z) = \frac{j\nu\cosh\nu(L-z) - \sigma\sinh\nu(L-z)}{j\nu\cosh(\nu L) - \sigma\sinh(\nu L)} \tag{3.36}$$

$$S(z) = \frac{\kappa\sinh\nu(L-z)}{j\nu\cosh(\nu L) - \sigma\sinh(\nu L)} \tag{3.37}$$

In Fig.3.5, we show the variations of $|R(z)|^2$ and $|S(z)|^2$, in normalized units, along the length of interaction.

Our quantity of interest is the coefficient of reflection $\rho(0)$ for the entire structure, i.e.

$$\rho(0) = \frac{S(0)}{R(0)} \tag{3.38}$$

The reflectivity is, therefore, given by

$$\rho\rho^* = \frac{\kappa^2\sinh^2(\nu L)}{\nu^2\cosh^2(\nu L) + \sigma^2\sinh^2(\nu L)} \tag{3.39}$$

Outside the stop band ν is complex and the reflectivity is given by

$$\rho\rho^* = \frac{\kappa^2\sin^2(\psi L)}{\psi^2\cos^2(\psi L) + \sigma^2\sin^2(\psi L)} \tag{3.40}$$

where

$$\psi^2 = \sigma^2 - \kappa^2 \tag{3.41}$$

The filter response curve can be assessed from equation (3.40) which can be written as

$$\rho\rho^* = \frac{\sin^2\left[\left[\frac{\sigma^2}{\kappa^2} - 1\right]^{\frac{1}{2}}(\sigma L)\right]}{\frac{\sigma^2}{\kappa^2} - \cos^2\left[\left[\frac{\sigma^2}{\kappa^2} - 1\right]^{\frac{1}{2}}(\sigma L)\right]} \tag{3.42}$$

For $\sigma/\kappa >> 1$ the above expression reduces to

$$\rho\rho^* = \left[\frac{\kappa\sin(\sigma L)}{\sigma}\right]^2 \tag{3.43}$$

This is the well known sinc function whose maximum peak (main lobe), in this case, lies inside the stop band at the Bragg condition $\sigma = 0$. From equation (3.39) we find the maximum to be given by

$$R_0 = \tanh^2(\kappa L) \tag{3.44}$$

The reflectivity then decreases slowly in the stop band and finally follows the curve given by equation (3.42) when ν becomes imaginary.

From equation (3.42), we can find the first null in the filter response, which corresponds to the point where

$$(\sigma^2 - \kappa^2)^{\frac{1}{2}} L = \pi \tag{3.45}$$

i.e.

$$\sigma = \left[1 + \frac{\kappa^2 L^2}{\pi^2} \right]^{\frac{1}{2}} \frac{\pi}{L} \tag{3.46}$$

From equation (3.27),

$$\sigma = \beta - \beta_o \simeq \frac{2\pi(\Delta f)}{V_g} = \frac{2\pi}{V_g} V_p \frac{\Delta\lambda_g}{\lambda^2_{go}} \tag{3.47}$$

where λ_{go} is the guide Bragg wavelength

$$\lambda_{go} = \frac{\lambda}{N} = 2\Lambda \tag{3.48}$$

With the above equation and equating (3.47) to (3.46) we obtain

$$\frac{\Delta\lambda}{\lambda_o} = \frac{N(2\Lambda)}{L\, n_g} \left[1 + \left[\frac{\kappa L}{\pi}\right]^2 \right]^{\frac{1}{2}} \tag{3.49}$$

where n_g is the group index defined in equation (2.35). Equation (3.49) gives the fractional bandwidth between the first zero points of the reflectivity curve.

The reflectivity of the first sidelobe can be similarly determined by equating the argument of the sine function to $3\pi/2$,

resulting in

$$R_1 = \frac{(\kappa L)^2}{(\kappa L)^2 + (3\pi/2)^2} \tag{3.50}$$

The above equation, in conjunction with equations (3.44) and (3.49) characterize the response of a given filter whose grating amplitude is constant along the interaction length. We note that they are all functions of the important parameter (κL). In section 3.3, we shall investigate the properties of these equations with numerical examples related to our experimental waveguide and grating parameters.

3.2.4 High Frequency Cut-Off Properties[23].

In our description of the dispersion diagram in Fig.3.3, we noted that the bounded modes couple to the radiation modes in regions (c) and (d). The physical significance of this is that the x-component of the propagation constants, for the fields outside the guiding layer become imaginary. This change in k_{xm} is brought about by the space harmonic terms in the value of β_q. For guided modes, the k_{xm} for the q-th space harmonic in the substrate region is given by

$$p_{0q} = (\beta_q^2 - k_0^2 n_0^2)^{\frac{1}{2}} \qquad - \qquad q = \pm 1 \tag{3.51}$$

Using equation (3.4), the high frequency (hf) cut-off λ can be derived from

$$\pm \left[\frac{N}{\lambda} + \frac{1}{\Lambda}\right] \leq \frac{n_0}{\lambda} \tag{3.52}$$

The above states that the $q = -1$ harmonic is related to the forward wave, whereas the $q = +1$ harmonic is to the reverse wave. In both cases, the solution is given by

$$\lambda_{c0} \leq \Lambda(N+n_0) \tag{3.53}$$

Similarly, for the leaky air modes we obtain

$$\lambda_{c2} \leq \Lambda(N+n_2) \tag{3.54}$$

We note here, that we only considered the q = ±1 harmonics in the above equations. This is justified because λ_c, for the higher harmonics, have values which are smaller than λ_{c2}.

Since $2N \leq (N+n_0)$, there is a range of wavelengths, $\lambda_0 > \lambda > \lambda_{c0}$, where the wave remains bounded. The separation between the Bragg and hf cut-off interactions is given by

$$\Delta\lambda_{oc0} = \Lambda(N - n_0) \tag{3.55}$$

Thus, for modes near cut-off the separation is at a minimum.

The hf cut-off phenomenon is analogous to the situation of the single-beam reverse coupler developed by Dalgoutte[22]. In that coupler the substrate mode is used to couple the guided mode by means of the superimposed grating on the waveguide.

3.2.5 Effects of Taper Functions

As discussed in Chapter I, side lobe supression in the filter response can be achieved by introducing a modulation envelope on the grating amplitude and/or a chirp in the periodicity. The effects of such modifications on the filter response have been analysed by several workers[34-37,43,106-110]. In what follows, we give the main points of the analysis given by Kogelnik.

For a grating filter with constant period, the phase change ϕ undergone by the wave between two adjacent grooves of the grating is constant and at the Bragg condition $\phi = \pi$. The chirp in periodicity for an aperiodic grating can, thus, be expressed by a phase factor $\exp(\pm\phi(z))$. By virtue of equation (3.31) the influence of chirp and

modulation function on the grating depth translates into $\kappa(z)$.

The coupled mode equations now have the form

$$\frac{dR}{dz} + j\sigma R = -j\kappa(z)S\exp(-j\phi(z)) \qquad (3.56(a))$$

$$\frac{dS}{dz} - j\sigma R = +j\kappa(z)R\exp(+j\phi(z)) \qquad (3.56(b))$$

where σ has the usual meaning.

For considerations of symmetry, the grating is assumed to extend from $z = -L/2$ to $z = +L/2$ and the boundary conditions are thus

$$R(-L/2) = 1 \qquad (3.57(a))$$

$$S(+L/2) = 0 \qquad (3.57(b))$$

The reflection coefficient is given by

$$\rho(z) = \frac{S(z)}{R(z)} \exp(-j\phi(z)) \qquad (3.58)$$

and its derivative has the form

$$\rho' = \frac{S'}{R} - SR'R^{-2} - j\phi' \frac{S}{R} \exp(-j\phi) \; . \qquad (3.59)$$

The filter response is obtained by solving a Riccati differential equation which results from the combination of equations (3.56) and (3.59). The Riccati equation is thus given by

$$\rho' = j(2\sigma - \phi')\rho + j\kappa(1 + \rho^2) \qquad (3.60)$$

The boundary condition for the above equation follows from (3.57), i.e.

$$\rho(+L/2) = 0 \qquad (3.61)$$

Equation (3.60) has been solved using the Runge-Kutta numerical technique. Theoretical filter response, due to linear and quadratic tapers and, linear and quadratic chirps, have been reported[35,36,110].

The main effect of tapers is to reduce the size of the sidelobes with a slight increase in the bandwidth. The downward parabolic taper being the most promising choice, with sidelobe levels as low as two per cent. The effect of a chirp is to broaden the bandwidth of the filter and raise the zero levels of the reflectivity. The quadratic chirp, unlike the other modifications, gives rise to an asymmetrical response. Recently, Marcatilli[109] reported the relationship between the filter response and the geometry of the grating. The reflectivity is related to the area under the modulating amplitude of the grating height; the bandwidth is related to the maximum height of the corrugation and the sidelobe levels to the first derivatives of the taper at the ends of the grating. The manufacture and the applications of chirped gratings[41] such as couplers[42] and demultiplexers[43], have also been reported recently. In our work, a computer program* has been written to solve the Riccati equation. The printout of the program is given in Appendix 3B.

3.2.6 Filter Response and Fourier Transform

For low reflectivities, the filter response can be simply related to the taper function. We define a new variable τ by

$$\rho = \tau \exp(2j\sigma z - j\phi) \tag{3.62}$$

which satisfies the differential equation

$$\tau' = j\kappa(\exp(-j2\sigma z+j\phi) + \tau^2\exp(j2\sigma z-j\phi)) \tag{3.63}$$

---

* By Dr. C.D.W. Wilkinson.

When the reflectivities are low, the term in σ^2 can be neglected and equation (3.62) can be written as

$$\rho(-L/2) = -je^{j(\sigma L-\phi)} \int_{-L/2}^{+L/2} \kappa(z)e^{-j(2\sigma z-\phi)}dz \qquad (3.64)$$

The above equation shows that the response function $\rho(\sigma)$ is the Fourier transform of the taper function $\kappa(z)\exp(j\phi(z))$. For the case of a uniform grating equation (3.64) gives

$$\rho(-L/2) = -j\kappa e^{j\sigma L} \int_{-L/2}^{+L/2} e^{-j2\sigma z}dz$$

and

$$\rho\rho^* = \left[\frac{\kappa\sin(\sigma L)}{\sigma}\right]^2$$

which is the same result as that derived previously in equation (3.43).

3.3 Waveguide Structures and Design Considerations

The properties of the equations describing the filter response will now be investigated.

We start the analysis by plotting the reflectivity curve as a function of σ/κ and with parameter κL. We shall then proceed to calculate the variation in the magnitude of the coupling coefficient, as a function of the effective guide index N, for each of the four different guiding structures described in Chapter II.

3.3.1 Normalized Reflectivity Curves

Filter reflectivity is given by equations (3.39) and (3.40). In order to obtain normalized curves, we re-write those equations in the following way

$$\rho\rho^* = \frac{\sinh^2\left[\left[1 - \frac{\sigma^2}{\kappa^2}\right]^{\frac{1}{2}} (\kappa L)\right]}{\frac{\sigma^2}{\kappa^2} - \cosh^2\left[\left[1 - \frac{\sigma^2}{\kappa^2}\right]^{\frac{1}{2}} (\kappa L)\right]} \qquad (3.65(a))$$

and

$$\rho\rho^* = \frac{\sin^2\left[\left[\frac{\sigma^2}{\kappa^2} - 1\right]^{\frac{1}{2}} (\kappa L)\right]}{\frac{\sigma^2}{\kappa^2} - \cos^2\left[\left[\frac{\sigma^2}{\kappa^2} - 1\right]^{\frac{1}{2}} (\kappa L)\right]} \qquad (3.65(b))$$

Using the above, we have plotted in Fig.3.6(a) the reflectivity as a function of σ/κ with parameter κL. The curves show increasing values for the reflectivity of the main lobe R_0 and its roll-off rate (slope), while the bandwidth decreases as the parameter κL is increased. For $\kappa L \geq 2$, R_0 approaches unity. The variation of the reflectivities of the main and first two side lobes, as functions of κL, is shown in Fig.3.6(b); we note that for large κL the side lobes become comparable to the main lobe. In Fig.3.6(a) it can be observed that as the roll-off rate increases, the separation between the first zero and the first side lobe becomes smaller. This separation can be calculated from equation (3.65(b)) and is given by

$$\lambda_2 - \lambda_1 = \left[{}^1/\lambda_o - ({}^{9\pi^2}/_4 + \kappa^2 L^2)^{\frac{1}{2}}/(2\pi NL)\right]^{-1} - \left[{}^1/\lambda_o - ({}^{\pi^2}/_4 + \kappa^2 L^2)^{\frac{1}{2}}/(2\pi NL)\right]^{-1} \qquad (3.66)$$

where λ_1 corresponds to the position of the null and λ_2 to the position of the peak of the first side lobe. Fig.3.6(c) shows the variation of $\lambda_2 - \lambda_1$ as function of κL with parameter L. It can be observed that, for a given κL, the separation decreases as the interaction length is increased.

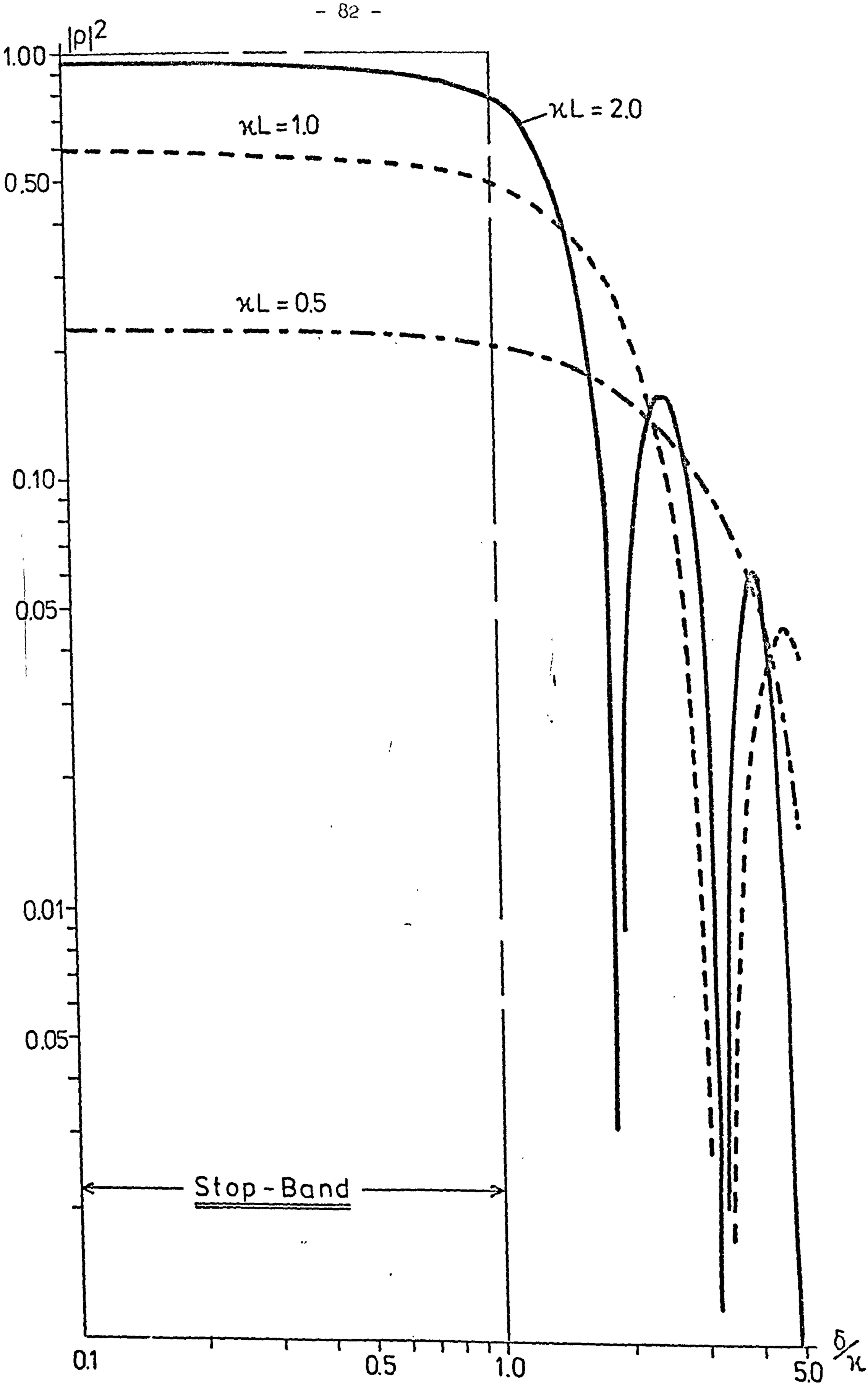

FIG 3.6 Filter Reflectivity

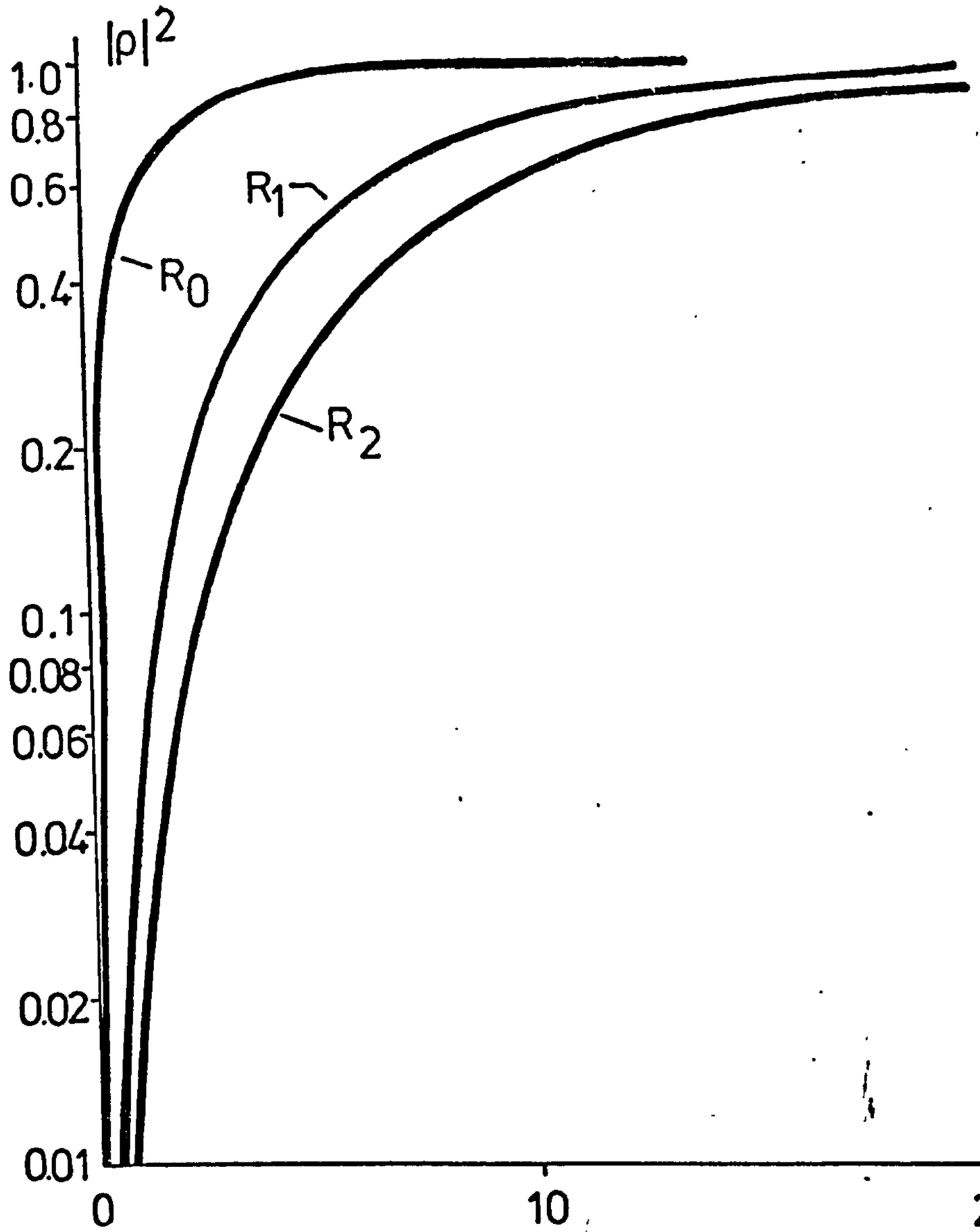

FIG 3.6b Reflectivities of Main- and first two Side-Lobes

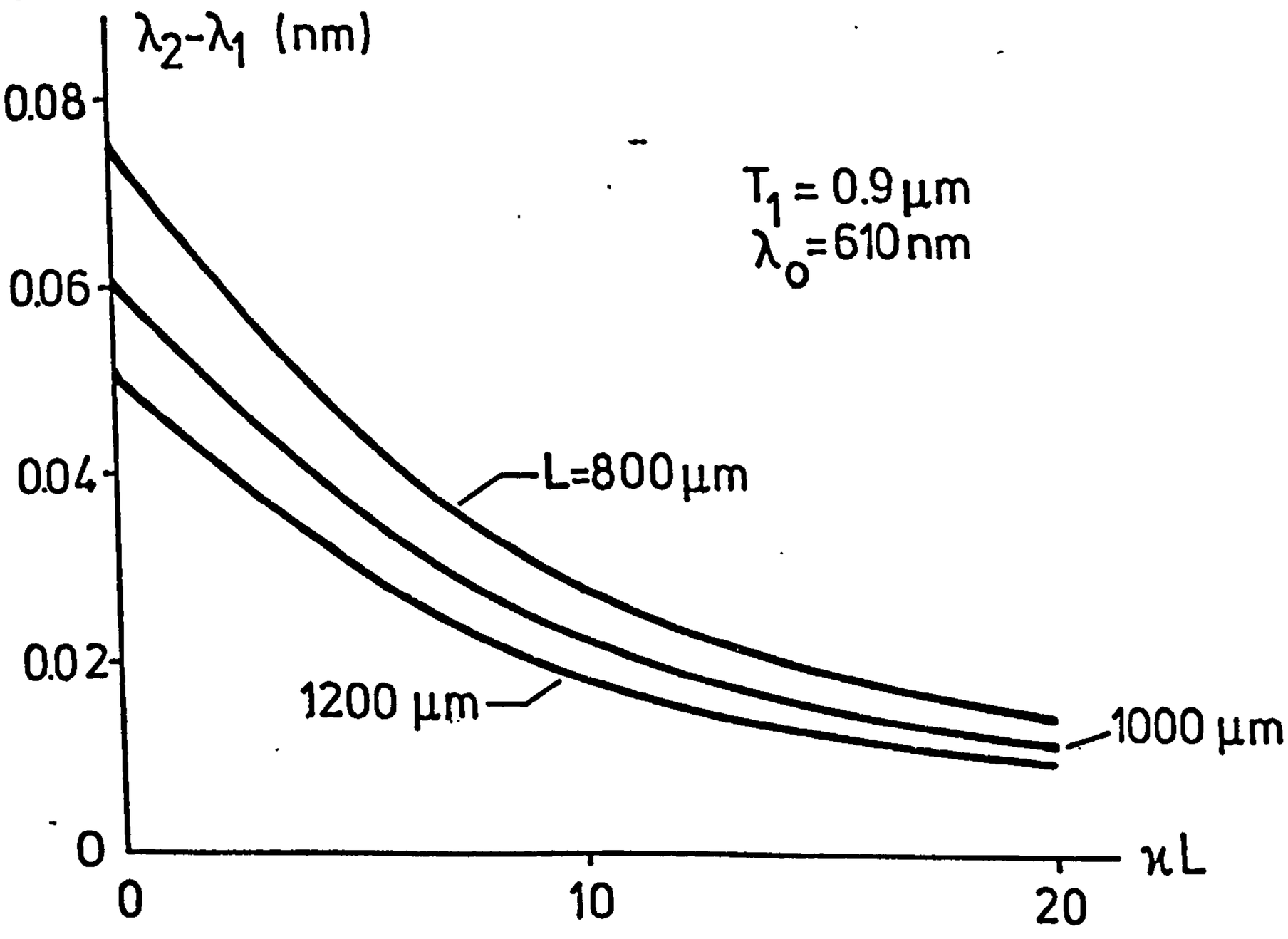

FIG 3.6c First Zero-First Sidelobe Bandwidth Separation

The variation in bandwidth, measured between the first zero points of the response, is calculated from equation (3.45). The results are shown graphically in Fig.3.6(d). It is observed that, for a given value of κL, the bandwidth decreases as the interaction length increases.

3.3.2 Normalized Coupling Coefficient Curves

Equation (3.31) gives the general expression for the coupling coefficient κ. In what follows, we normalize κ with respect to h, the grating height, and calculate its variation as a function of the guide parameters.

The results for the three-layer homogeneous waveguide filters are given in Fig.3.7. The curves show, that for a given mode, there is a sharp increase in the value of κ/h for thicknesses just above cut off and then, a steady decrease of κ/h is observed, as the guide thickness is increased. The physical significance of this behaviour is best explained in terms of the degree of field confinement in the guide. Near cut off, the perturbation is small because the peak of the field distribution lies close to the guide-substrate interface. As the thickness is increased the field tends to concentrate more in the guide and the degree of perturbation increases. Further increase in the guide thickness, however, results in an increased distance between the grating and the peak of the field leading to a smaller degree of perturbation. A measure of the field confinement in the guide is given by the effective guide thickness T_e. In fact, the curves in Fig.3.7 follow very closely the variation of $1/T_e$ (see Fig.2.4). The argument is corroborated by equation (3.26) which gives a closed form expression for κ in this case. For higher order modes, we thus expect smaller values of κ.

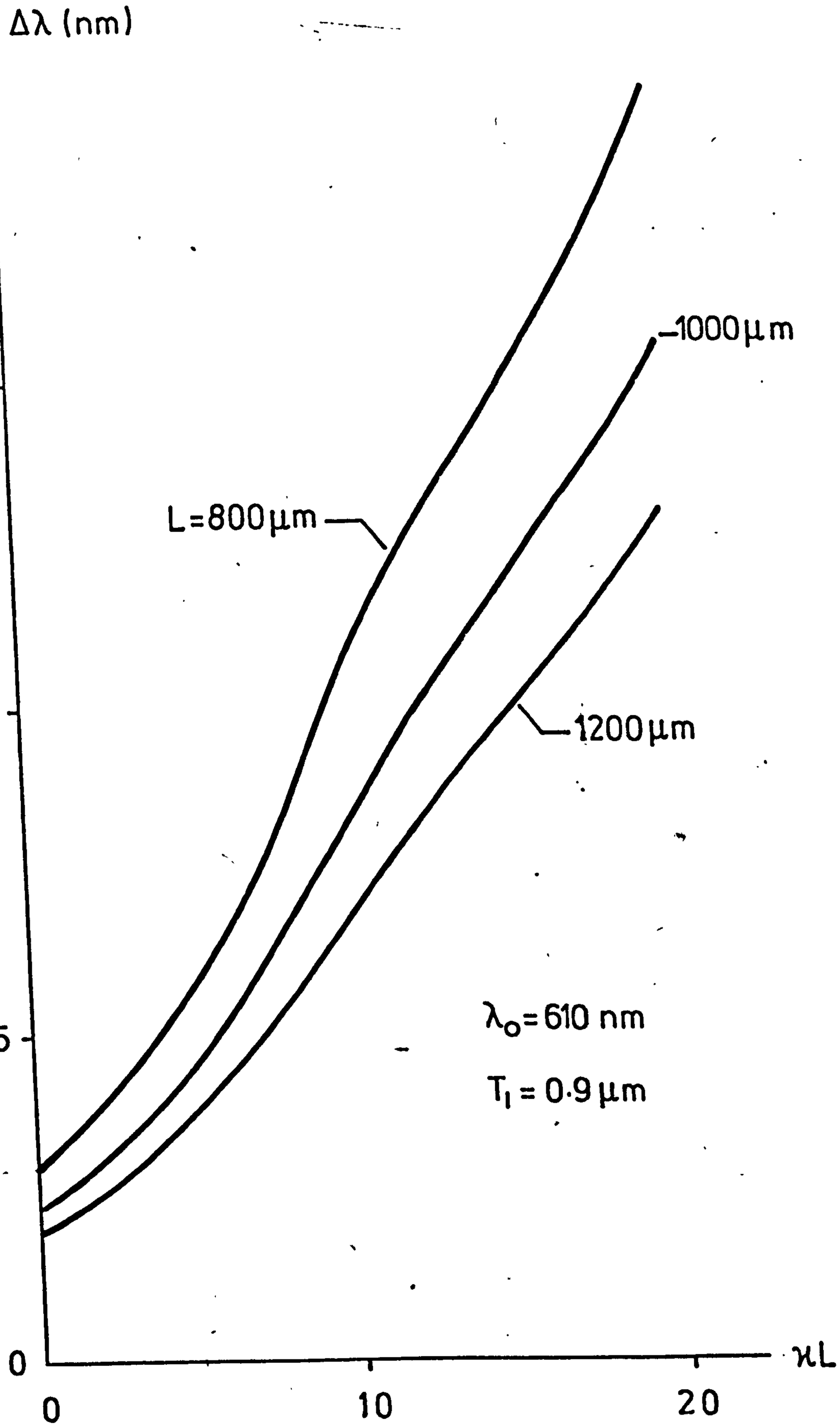

FIG 3.6d Variation of Bandwidth as Function of κL

($\Delta\lambda$ = Width Between First Zero Points of Response)

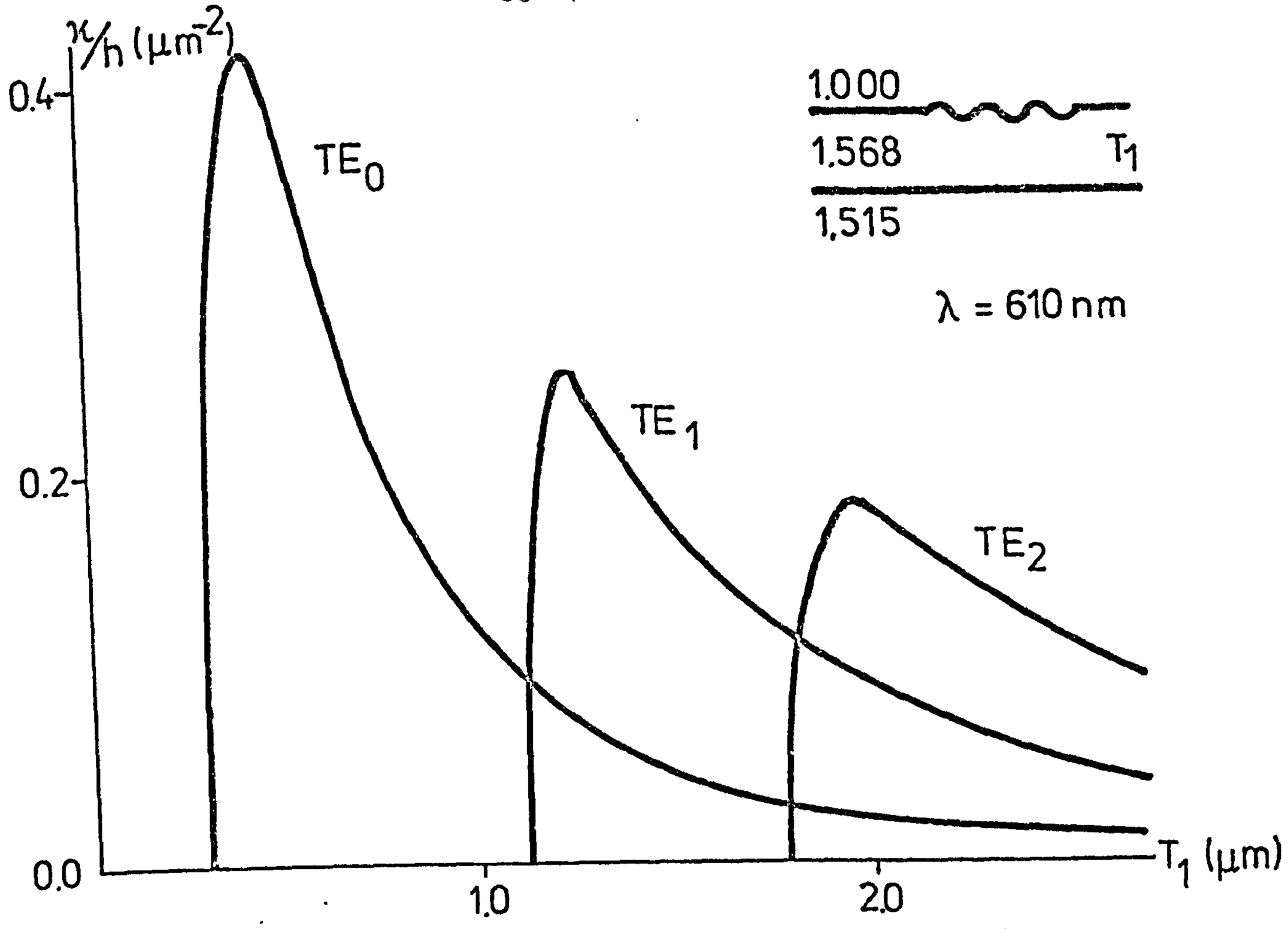

FIG 3.7 Normalized Coupling Coefficient vs Guide Thickness.

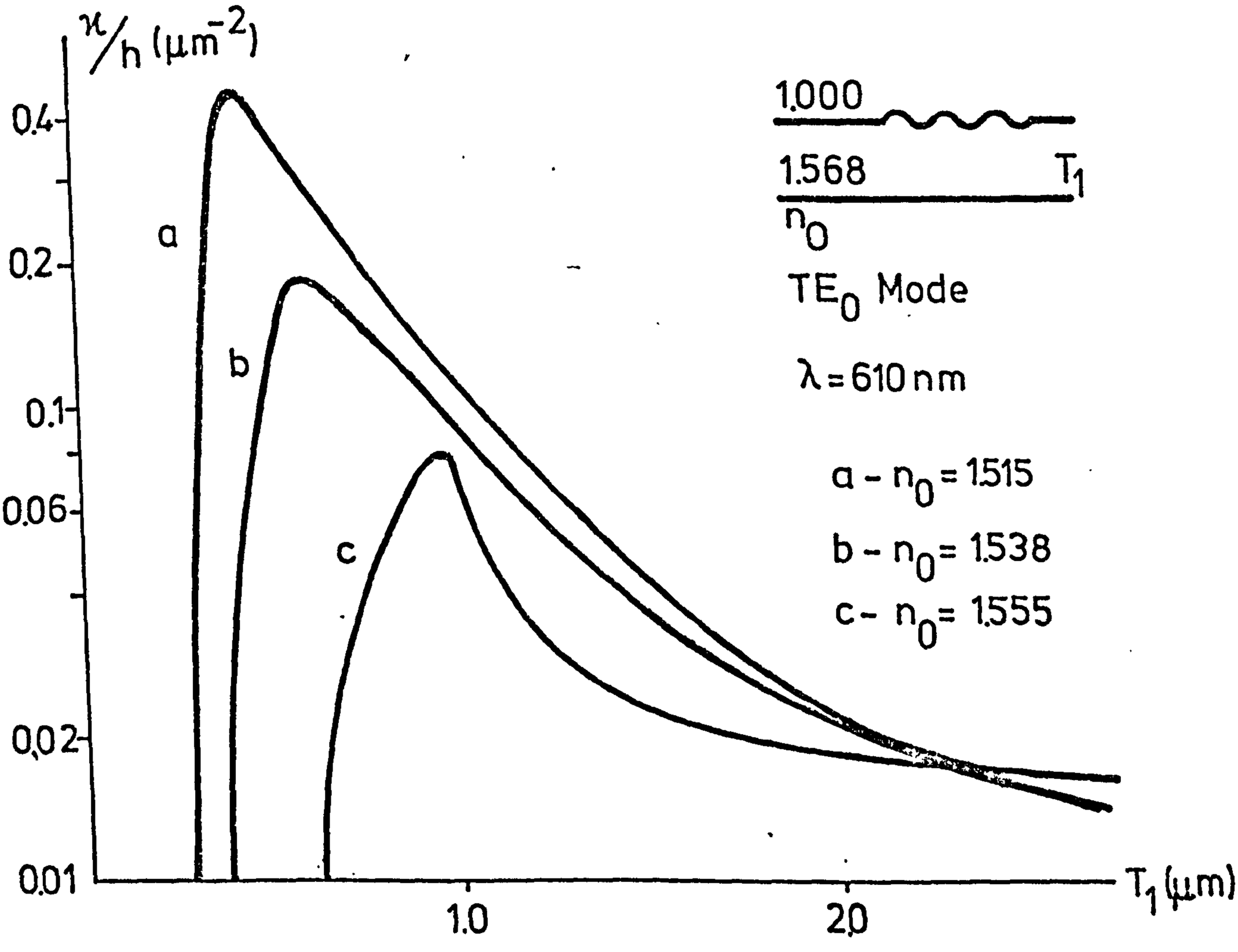

FIG 3.8 κ/h as Function of Substrate Index.

Although we calculated the values of κ/h for higher order TE modes, in practice, filters are realised in single mode films. The contribution from the space harmonics to the value of the propagation constant and the inherent material dispersion of the waveguide can lead to strong undesired intermode coupling. In what remains of this discussion, we shall concentrate the analysis on the case of the TE_0 mode only. Finally, we present in Fig.3.8 the change in κ/h as the value of the substrate index is increased. From the particular structures considered, we note a decrease in the peak value of κ/h by one order of magnitude for an increase in the substrate index by 0.04. A similar tendency is observed if the superstrate index value is increased.

Results for the four-layer waveguide filters are given in Fig.3.9 where κ/h is plotted as a function of T_2 with parameter T_1 for n_2=1.633 and n_2=1.803. We use equation (2.29) to evaluate the integral in the denominator of equation (3.31). The corresponding values for the coupling coefficients are consistently greater than those found in the previous three-layer case. This is as expected from an inspection of the field distributions shown in Fig.2.10. The field tends to concentrate more strongly inside the top high index layer T_2 and this gives rise to a greater degree of perturbation. The sharp drop at the right hand side of the graphs corresponds to the positions where the high index layer isolated as an independent waveguide on a substrate the index of which equals the index of the T_1 guiding layer. Beyond the cut off values for T_2 where κ/h=0 it is expected that the coupling coefficient variation follows the same behaviour as those given in Fig.3.7.

For the cases of inhomogeneous waveguides, the coupling

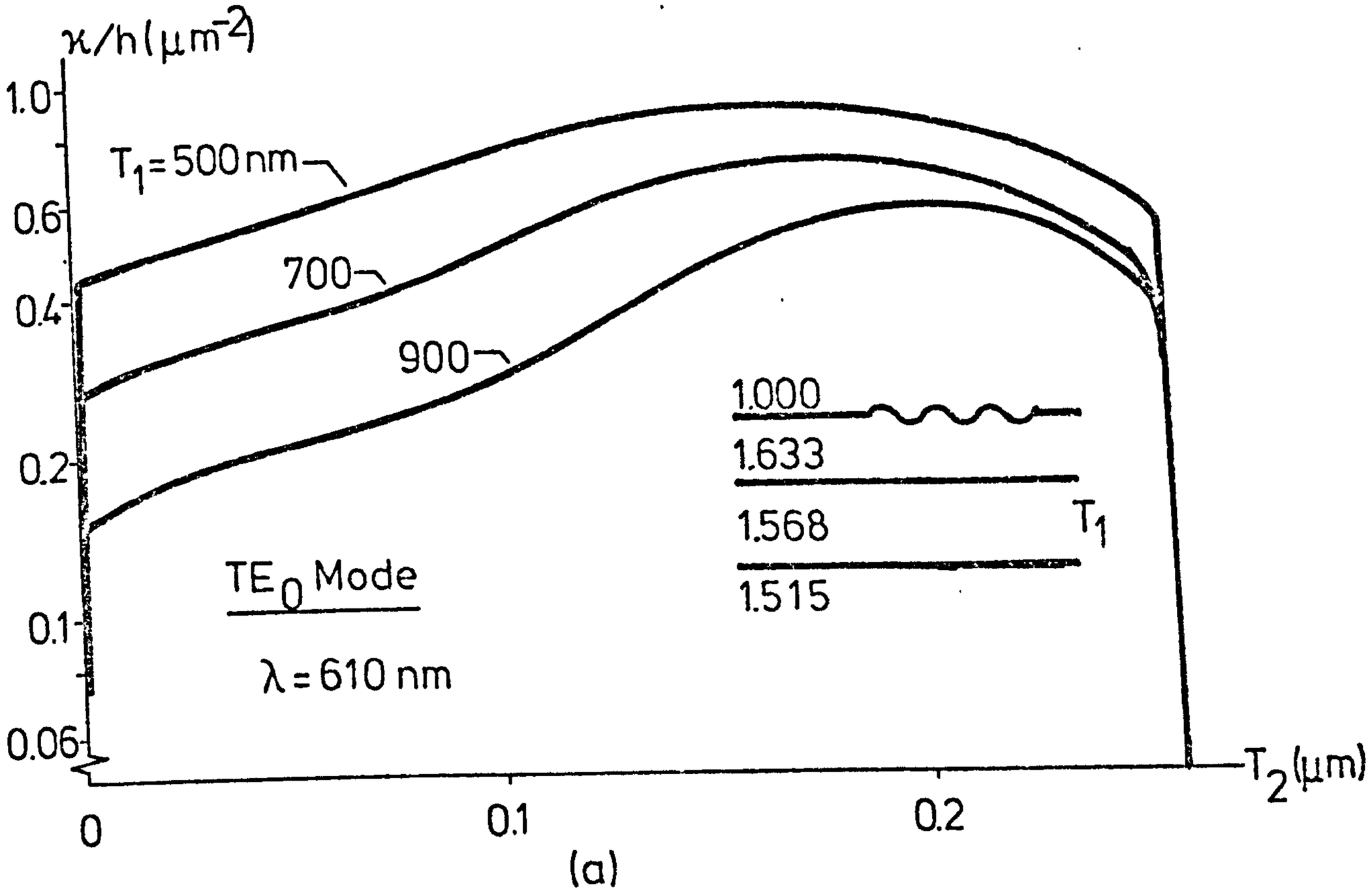

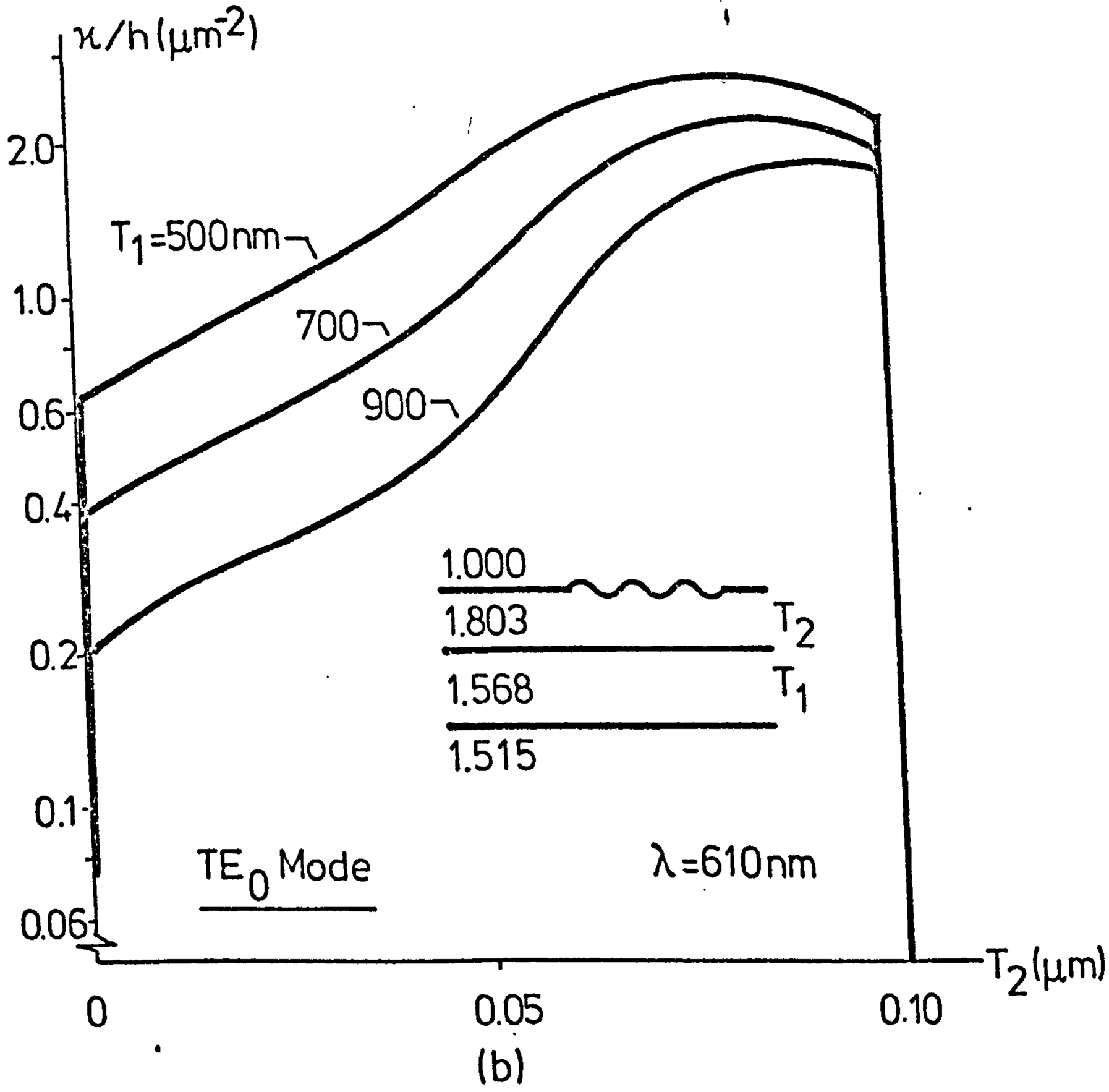

FIG 3.9 Normalized Coupling Coefficient for the Four-Layer Homogeneous Waveguide Filters

coefficients were calculated using a numerical technique to evaluate the corresponding integral in equation (3.31).

The results of these calculations for the three- and four-layer waveguide filters are shown, respectively, in Fig.3.10 and Fig.3.11.

The behaviour of the coupling coefficient as a function of diffusion depth is similar to that of the three-layer homogeneous case. Since the maximum value of the film index lies at the surface of the guide, the value of κ/h is larger (in this case by a factor of ~ 2) and the negative slope of the downward part of the curve for large d is smaller. For the four-layer cases, the higher surface index n_s of the diffused waveguides presents a better index match. Consequently, the rate of increase of κ/h at the lower end of T_2 values is less sharp and the peak values for the coupling coefficient are correspondingly smaller. In the case of n_2=1.633 the relation is almost linear. The sharp drop at the upper end of the T_2 values follows the same argument as in the case of the four-layer homogeneous waveguides.

Finally, we note that an approximate method to evaluate κ for guides with nonuniform index profiles has been reported by Haus et al[111]. The method consists in finding the value of the propagation constant β, assuming that the tangential electric field for TE modes is zero at the guide-superstrate interface. First order correction $\sigma\beta$ is then applied by applying a magnetic surface current large enough to cause a change in the electric field from zero to the desired value. The product $\beta\sigma\beta$ is then used in equation (3.31) to take account of the integral of the field squared. This technique is only valid for cases where the difference between the peak value of the index distribution and the substrate index is very small. In such cases, the assumption that the field is zero at the surface can be approximated by using extremely deep

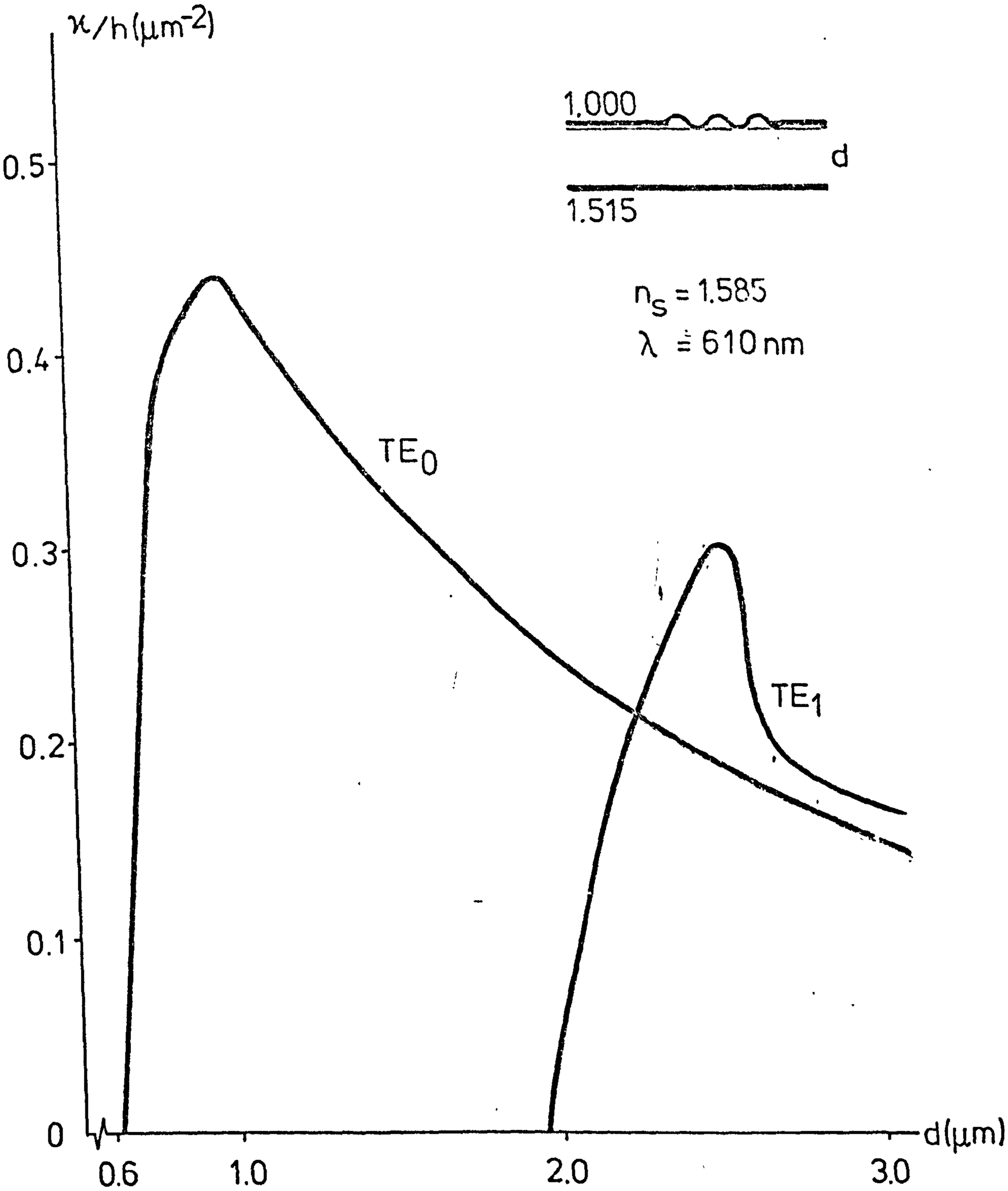

FIG 3.10 Normalized Coupling Coefficient for the Three-Layer Inhomogeneous Waveguide Filters

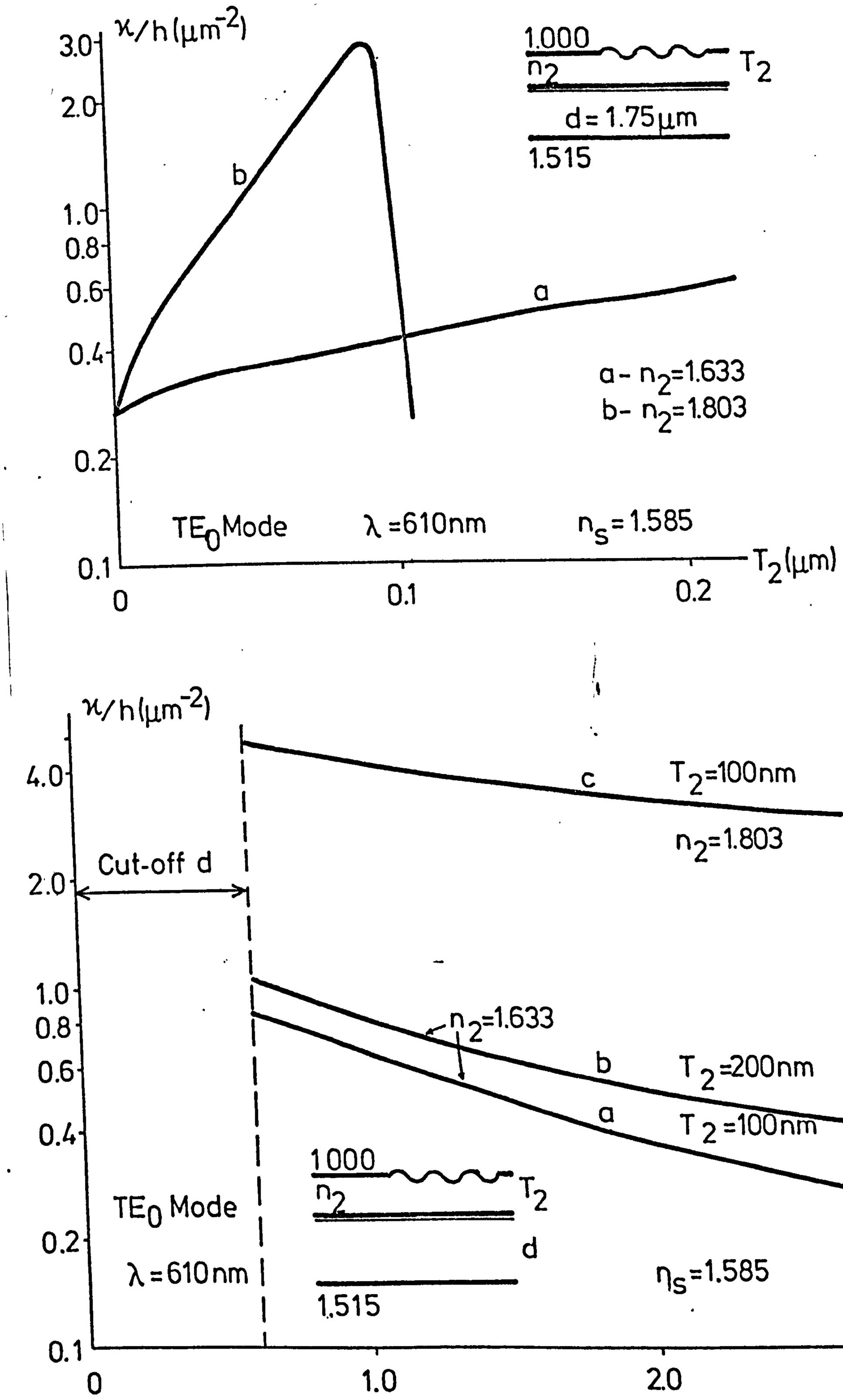

FIG 3.11 Normalized Coupling Coefficient for the Four-Layer Inhomogeneous Waveguide Filters

diffusion depth for the guide. Our diffused guides do not come into this category and implementation of the technique by Haus could lead to large errors.

3.3.3 Design Considerations

The properties of the filter parameters shown in the previous graphs indicate that the relative values of the coupling coefficient, κ, and, the interaction length, L, must be chosen carefully in the design of filters using a particular guiding structure. Ideally, filters should have high rejection (i.e. reflectivity) in the main lobe and low side lobe levels. As we have shown in Figs.3.6,the reflectivity is a function of κL and the bandwidth is inversely proportional to the interaction length,provided that $\kappa L << \pi$. If the product $\kappa L \geq \pi$, sidelobes become comparable to the main lobe; moreover, most of the light is reflected before it traverses the complete length of the grating. The physical significance of this fact is that the effective length of the grating is shorter and a correspondingly broader bandwidth results. Thus, for a given length L, the product κL should be sufficiently large to provide appreciable reflectivity; however, κL should be less than π in order that the bandwidth be completely determined by the complete length of the grating.

Ideally, it is desirable to design filters on waveguide structures which have low values of the normalised coupling coefficient. This factor provides larger latitudes of choice in the values of h and L. For a given three-layer structure, low values of κ/h can be had with waveguides,the thicknesses of which,lie in both limits of single mode operation, i.e. waveguides which are just above cut-off or just below the cut-off point of the next higher-order mode. The value of κ/h can also be reduced if the index difference between the film and the

substrate is lowered (see Fig.3.8). For the case of silver-sodium ion-exchange waveguide, the surface index can be lowered by diffusing a mixture of silver and sodium nitrate into the glass[140] In the particular four-layer-type waveguides considered in our work, the values for κ/h are inherently larger than those of the three-layer-type waveguides and as the thickness T_2 increases, the normalised coupling coefficient becomes larger until the point where the top layer isolates as an independent waveguide. The field distribution in these guides was shown in Chapter II; the effect of the higher-index film at the top of the guide has the effect of 'pulling' the field distribution towards the air-film interface. Thus, the presence of the grating on this surface results in a larger degree of perturbation. The value of κ/h in a four-layer type waveguide can be lowered if the index of the T_2 layer is smaller than n_1. In this case the field in the top layer will be exponentially decaying. Correspondingly, the field amplitude at the air-film interface will be smaller, the magnitude being dependent on the value of T_2.

The above discussion leads to the following conclusions in connection with the four different guiding structures considered in this work. The three-layer waveguides are best suited for the design of filters with narrow bandwidths. The larger values of the normalized coupling coefficient of the four-layer type waveguides do not allow easy control on the response of the filters; furthermore, they are not feasible in the design of narrow band filters with low sidelobe levels.

Appendix 3A

The coupling can be represented as a distributed perturbation polarization. For TE modes, the wave equation is given by

$$\nabla^2 E_y + \mu_0 \varepsilon_0 \omega^2 E_y = -\omega^2 \mu_0 P_y \qquad (3A.1)$$

where

$$P_y(x,z) = P(x,z) + P_p(x,z)$$

and

$$P(x,z) = (\varepsilon_r(x,z) - \varepsilon_0) E_y$$

$P(x,z)$ is the polarization induced by E_y in the unperturbed waveguide and P_p is the perturbation polarization. The field in the unperturbed guide can be expanded in an infinite series. Using equations (3.6) and (3.17) we write

$$E_y = \frac{1}{2} \cdot \sum_m A_m(x)\left(R(z)e^{-j\beta_m z} + S(z)e^{+j\beta_m z}\right) + c.c. \qquad (3A.2)$$

The above equation satisfies the wave equation given by

$$\nabla^2 E_y + \mu_0 \omega^2 \varepsilon_0 \varepsilon_r E_y = 0 \qquad (3A.3)$$

Substituting equation (3A.2) into (3A.1) yields

$$\sum_m \left[\left[Re^{-j\beta_m z} + Se^{+j\beta_m z} \right] \frac{1}{2} \left[-\beta_m{}^2 A_m(x) + \frac{\delta^2 A_m(x)}{\delta x^2} + \omega^2 \mu_o \varepsilon_o \varepsilon_r A_m(x) \right] + \frac{1}{2} \left[-2j\beta_m (R'e^{-j\beta_m z} + S'e^{+j\beta_m z}) + (R''e^{-j\beta_m z} + S''e^{+j\beta_m z}) \right] A_m(x) \right] + c.c.$$

$$= -\omega^2 \mu_o P_p \qquad (3A.4)$$

The first term of the summation in equation (3A.4) is zero by virtue of (3A.3). Making use of the slow variation condition as stated in equations (3.16) equation (3A.4) reduces to

$$\sum_m j\beta_m(S'e^{+j\beta_m z} - R'e^{-j\beta_m z})A_m(x) + c.c. = -\omega^2\mu P_p \qquad (3A.5)$$

We next multiply the above equation times $A_s(x)$ and integrate from - to + using the orthogonality property and equation (2.28) to obtain

$$S'e^{+j\beta_s z} - R'e^{-j\beta_s z} = \frac{-j\omega}{2P}\int_{-\infty}^{\infty} P_p(x,z)A_s(x)\,dx \qquad (3A.6)$$

The perturbation polarization can be written as

$$P_p = \Delta n^2(x,z)\varepsilon_0 E_y \qquad (3A.7)$$

The variation in index is a periodic function and it can be expressed in terms of a Fourier series as in equation (3.15)

$$\Delta_n{}^2(x,z) = \frac{\Delta n^2(x)}{2}\sum_g g_q \exp(jqKz) + c.c. \qquad (3A.8)$$

Substitution of equations (3A.2) and (3A.8) into (3A.7) results in an infinite sum of harmonics. For the first Bragg interaction q=1 and $K=2\beta_o$. The phase matching condition requires

$$\beta_s = -\beta_m + K \quad \text{for the reverse S wave} \qquad (3A.9(a))$$

$$-\beta_s = \beta_m + K \quad \text{for the forward R wave} \qquad (3A.9(b))$$

Equation (3A.5) will then give the following coupled mode equations

$$S'' = \frac{-j\omega\varepsilon_o}{8P}\int_{-\infty}^{\infty} \Delta n^2(x)A_s(x)\,(Re^{-2j\sigma z})g_1 dx \qquad (3A.10(a))$$

$$R' = \frac{j\omega\varepsilon_o}{8P} \int_{-\infty}^{\infty} \Delta n^2(x) A_s(x) \; (Se^{2j\sigma z}) \; g_1 dx \qquad (3A.10(b))$$

if the following substitutions are made in the above equation

$$R = R \exp(j\sigma z) \qquad (3A.11(a))$$

$$S = S \exp(-j\sigma z) \qquad (3A.11(b))$$

we obtain equations (3.20). By identification of terms, the coupling coefficient is given by

$$\kappa = \frac{\omega\varepsilon_o}{8P} \int_{\text{corrugation}} \Delta n^2(x) A_s(x) \; g_1 dx \qquad (3A.12)$$

For small corrugation height, it can be assumed that the field variation across the grating is negligible and has the value of the field at the surface of the guide. Also, the change in the square of the refractive index can be taken as

$$\Delta n^2 = (n_1^2 - n_2^2) \qquad \text{for } h \geq x \geq -h$$

$$= 0 \qquad \text{elsewhere}$$

equation (3A.11) can now be written as

$$\kappa = \frac{\omega\varepsilon_o}{4P} \left[n_1^2 - n_2^2 \right] E_c^2(2h)$$

Finally we use equation (2.28) for the power term P in the denominator. Allowing a factor of 2 to account for the peak value of $A_s(x) = E_c$ the coupling coefficient is given by

$$\kappa = \frac{\pi h (n_1^2 - n_2^2) E_c^2}{2\lambda N \int_{-\infty}^{\infty} E_y^2 dx} \qquad (3A.13)$$

Appendix 3B.

Program '11FA' computes the response of Bragg waveguide filters with quadratically tapered and chirped gratings. The program solves equation (3.60) using a Runge-Kutta numerical method.

The quadratic taper is characterized by a coupling coefficient $\kappa(z)$ which varies as

$$\kappa(z) = \kappa_0 \left[1 - \frac{T}{12} + \frac{Tz}{L^2}^2\right]$$

where T is the taper constant.

The quadratic chirp is characterized by the phase function $\phi(z)$ which varies as

$$\phi(z) = 4F \left[\frac{z}{L}\right]^3$$

where F is the chirp constant.

Input data:

ADL = Increment in normalised frequency $\Delta(\sigma L)$

GL = Product κL

F = Chirp constant

T = Taper constant

Output data:

DL = Normalised frequency

RHO = Reflectivity

```
C       FREQ.DEVIATION,COUPLING AND PHASE SHIFT ARE READ IN
        COMMON X,Y(2),DERY(2),AUX(8,2),DL,GL,F,PRMT(5),A(4),B(4),C(4),T
        COMMON NDIM,IHLF
         READ(5,103) NT
1       READ(5,101) ADL,GL,F,T
        DL=-10
2        WRITE(6,102)
        WRITE(6,101) DL,GL,F,T
        PRMT(1)=0.5
        PRMT(2)=-.5
         PRMT(3)=-0.1
        PRMT(4)= .0001
        Y(1)=0.
        Y(2)=0.
        DERY(1)=.5
        DERY(2)=.5
        NDIM=2
        CALL RKGS
         DL=DL+ADL
        IF(DL.LE.10) GOTO 2
        NT=NT-1
        IF(NT.NE.0) GOTO 1
103      FORMAT(I10)
101     FORMAT(4F10.5)
102     FORMAT(46H FREQ.DEV,COUPLING,PHASE SHIFT,QRADRATIC TERM )
         STOP
        END

       SUBROUTINE OUTP
       COMMON X,Y(2),DERY(2),AUX(8,2),DL,GL,F,PRMT(5),A(4),B(4),C(4),T
       COMMON NDIM,IHLF
       RHO=Y(1)*Y(1)+Y(2)*Y(2)
       WRITE(6,101)  X,Y(1),Y(2),RHO,IHLF
101    FORMAT( 10X,4F20.5,I10)
       RETURN
       END

       SUBROUTINE FCT
       COMMON X,Y(2),DERY(2),AUX(8,2),DL,GL,F,PRMT(5),A(4),B(4),C(4),T
       COMMON NDIM,IHLF
       GLX(0)=GL*(1.-T/12.*T*0*0)
       PDL(0)=12*F*0*0
       DERY(1)=-((2.*DL-PDL(X))*Y(2)+2.*GLX(X)*Y(1)*Y(2))
       DERY(2)=(2.*DL-PDL(X))*Y(1)+GLX(X)*(1.*Y(1)*Y(1)-Y(2)*Y(2))
       RETURN
       END

        SUBROUTINE RKGS
        COMMON X,Y(2),DERY(2),AUX(8,2),DL,GL,F,PRMT(5),A(4),B(4),C(4),T
        COMMON NDIM,IHLF
        DO 1 I=1,NDIM
1       AUX(8,I)=.06666667*DERY(I)
        X=PRMT(1)
        XEND=PRMT(2)
        H=PRMT(3)
         PRMT(5)=0.
        CALL FCT
        IF(H*(XEND-X)) 38,37,2
2       A(1)=.5
        A(2)=.2928932
        A(3)=1.7071067
        A(4)=.16666667
        B(1)=2.
        B(2)=1.
        B(3)=1.
        B(4)=2.
        C(1)=.5
        C(2)=.2928932
        C(3)=1.7071067
        C(4)=.5
        DO 3 I=1,NDIM
        AUX(1,I)=Y(I)
        AUX(2,I)=DERY(I)
        AUX(3,I)=0.
3       AUX(6,I)=0.
        IREC=0
        H=H+H
        IHLF=-1
        ISTEP=0
        IEND=0
4       IF((X+H-XEND)*H) 7,6,5
5       H=XEND-X
6       IEND=1
7       CALL OUTP
        IF(PRINT(5)) 40,8,40
8       ITEST=0
9       ISTEP=ISTEP+1
        J=1
10      AJ=A(J)
        BJ=B(J)
        CJ=C(J)
           DO 11 I=1,NDIM
        R1=H*DERY(I)
        R2=AJ*(R1-BJ*AUX(6,I))
        Y(I)=Y(I)+R2
        R2=R2+R2+R2
11      AUX(6,I)=AUX(6,I)+R2-CJ*R1
        IF(J-4) 12,15,15
12      J=J+1
        IF(J-3) 13,14,13
```

```
13    X=X+.5*H
14    CALL FCT
      GOTO 18
15    IF(ITEST) 16,16,20
16    DO 17 I=1,NDIM
17    AUX(4,I)=Y(I)
      ITEST=1
      ISTEP=ISTEP+ISTEP-2
18    IHLF=IHLF+1
      X=X-H
      H=.5*H
      DO 19 I=1,NDIM
      Y(I)=AUX(1,I)
      DERY(I)=AUX(2,I)
19    AUX(6,I)=AUX(3,I)
      GOTO 9
20    IMOD=ISTEP/2
      IF(ISTEP-IMOD-IMOD)21,23,21
21     CALL FCT
      DO 22 I=1,NDIM
      AUX(5,I)=Y(I)
22    AUX(7,I)=DERY(I)
      GOTO 9
23    DELT=0.
      DO 24 I=1,NDIM
24    DELT=DELT+AUX(8,I)*ABS(AUX(4,I)-Y(I))
      IF(DELT-PRMT(4))28,28,25
25    IF(IHLF-10) 26,36,36
26    DO 27 I=1,NDIM
27    AUX(4,I)=AUX(5,I)
      ISTEP=ISTEP+ISTEP-4
      X=X-H
      IEND=0
      GOTO 1R
28    CALL FCT
      DO 29 I=1,NDIM
      AUX(1,I)=Y(I)
      AUX(2,I)=DERY(I)
      AUX(3,I)=AUX(6,I)
      Y(I)=AUX(5,I)
29    DERY(I)=AUX(7,I)
       X=X-H
      CALL OUTP
        X=X+H
      IF(PRNT(5)) 40,30,40
30    DO 31 I=1,NDIM
      Y(I)=AUX(1,I)
31    DERY(I)=AUX(2,I)
      IREC=IHLF
      IF(IEND) 32,32,39
32    IHLF=IHLF-1
      ISTEP=ISTEP/2
      H=H+H
      IF(IHLF)4,33,33
33    IMOD=ISTEP/2
      IF(ISTEP-IMOD-IMOD)4,34,34
34    IF(DELT-.02*PRMT(4))35,35,4
35    IHLF=IHLF-1

      ISTEP=ISTEP/2
      H=H+H
      GOTO 4
36    IHLF=11
      CALL FCT
      GOTO 39
37    IHLF=12
      GO TO 39
38    IHLF=13
39    CALL OUTP
40    RETURN
      END
```

CHAPTER IV

PRODUCTION OF GRATING FILTERS AND OPTICAL PROPERTIES OF MATERIALS

The purpose of this chapter is to present the experimental procedures and techniques used to produce grating filters. The first five sections of the chapter give the experimental aspects of the individual steps in the construction of filters. These are arranged in the sequential order followed during the fabrication process. Results from some attempts to alter the geometry of the grating are presented in the next section. The chapter ends with a final section related to the description of the techniques employed in the measurement of optical constants and device parameters.

4.1 Production of Thin Film Waveguides by Sputtering

The use of high frequency potentials for the sputtering of dielectrics was first proposed by Wehner[112] in 1955. The technique has found useful applications in the fabrication of low loss optical waveguides for integrated optics. Sputtering is a low pressure gas discharge process whereby accelerated positive ions dislodge molecules from the surface of the material to be sputtered. The ejected material is collected by a receiver consisting of a substrate onto which the film is to be deposited. The bulk material is normally attached to an electrode and it is referred to as the target. The sputtering of metals is generally carried out using a dc potential because of the conducting properties of the material. For dielectrics, however, the phenomenon of charge build-up at the surface of the target has the effect of inhibiting the process, so high frequency potentials must be used. One half cycle of the field is then used for the sputtering, whereas the remaining half cycle has the effect of neutralising the

surface charge on the target.

Properties of sputtered film waveguides have been reported by several workers. Goell[59] first reported the formation of low loss waveguides by sputtering Corning 7059 glass, and later, the properties of sputtered films from various types of Barium Silicate glass targets[113]. A microscopic scale analysis on the sputtering of Corning 7059 glass was given by Pitt et al[114,115]. Coleman[116] and Deitch et al[117] separately reported the properties of sputtered films from a vast number of inorganic oxides.

In the present investigation, homogeneous slab waveguides were fabricated by sputtering Corning 7059 glass. Details of the experimental equipment used and properties of the resulting waveguides are presented in this section.

4.1.1 Sputtering Equipment

The construction of the sputtering unit was based on a design proposed by Holland and Jackson[118]. The unit consists of twin (Hydra) grounded diode sputtering heads. The heads are identical in construction and consist of an aluminium work table surmounted by a 30 cm diameter pyrex cylinder and an aluminium top plate (see Fig.4.1). Both the work table and the top plate are water cooled. Each head has a capacity of three standard microscope slides; these are loaded onto the work table after removal of the top plate from the head. The target material is attached to a concentric back plate electrode which forms an integral part of the top plate. This electrode is also water cooled to prevent thermally induced cracks in the material. With the top plate in position, the target is separated from the substrates by a distance of 3 to 4 cm. Finally, a toroidal electromagnet producing an axial field of 10 mT surrounding the pyrex cylinder is used to help plasma confinement.

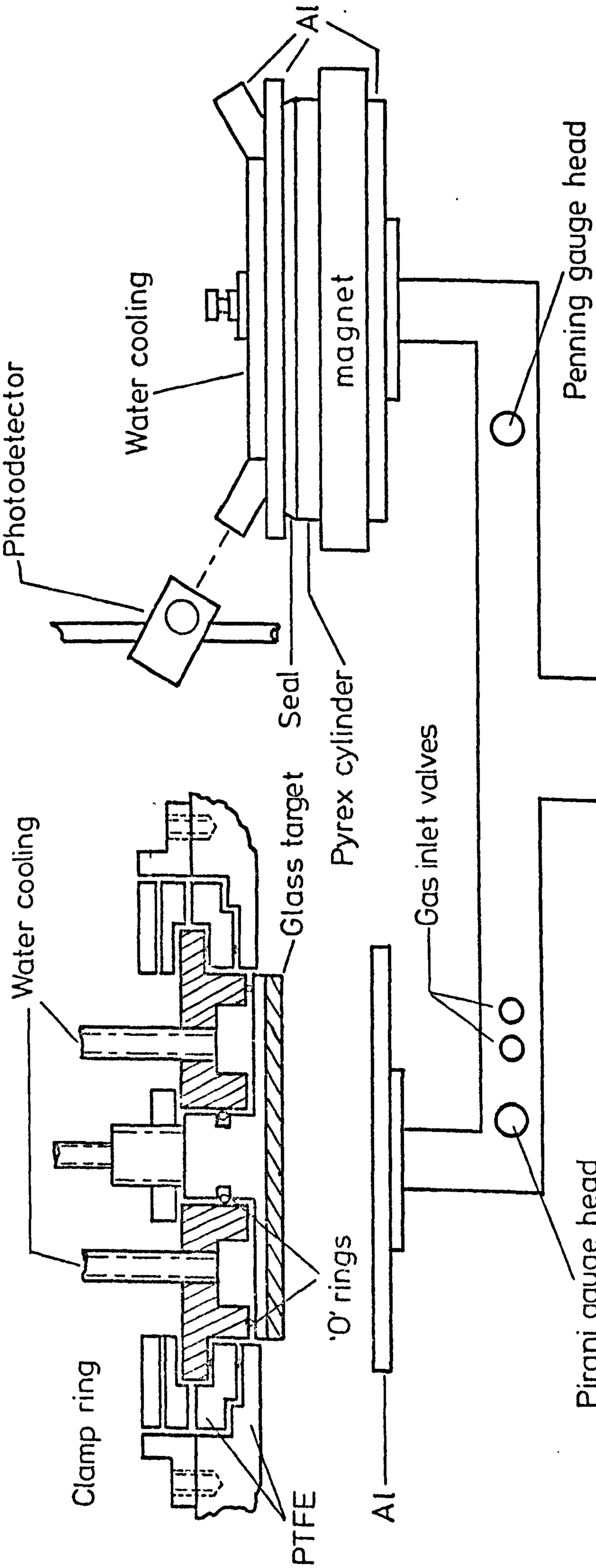

FIG 4.1 Schematic Diagram of Experimental (Hydra) Sputtering System.

R F power is generated by a crystal controlled oscillator. At the working frequency of 13.56 MHz the supply is capable of giving voltages up to 6kV peak-to-peak and power of over 1.5 kW. Power transfer to the heads is via a 50Ω transmission system and a π-type matching network. Tuning is carried out by monitoring the forward and reverse powers, measured by standing wave ratio detectors. R F currents into the heads are measured by thermocouple meters. The vacuum system consists of a standard Edwards High Vacuum 15 cm diffusion pump with a liquid nitrogen cold trap. The pump is backed by an ES 330 rotary pump. Ultimate pressure of 5×10^{-7} Torr can be attained with this system. A pumping speed of 430 lt/sec is obtained at the sputtering pressure of 1.5×10^{-3} Torr. Sputtering is carried out in an 80/20 argon-oxygen atmosphere.

The thickness of the films being deposited is monitored by optical techniques[119]. The accuracy of the system was checked by measuring the film thickness with a G V Planar surfometer. The discrepancy in the two sets of measured values was better than 10 per cent.

4.1.2 Experimental Waveguides

Optical waveguides were formed on Fisher soda lime glass substrates. These laboratory slides have good surface finish and consistency in the index of refraction for samples of a given batch. A maximum variation of ±0.005 in the index values (at 632.8 nm) was found for samples of different batches.

The composition of Corning 7059 glass is 50.2% SiO_2, 25.1% BaO, 13.0% B_2O_3, 10.7% Al_2O_3 and 0.4% As_2O_3 by weight[113]. The optical dispersion of the bulk material and that of Fisher slides were measured with an Abbe refractometer and a tunable laser (see Fig.4.2).

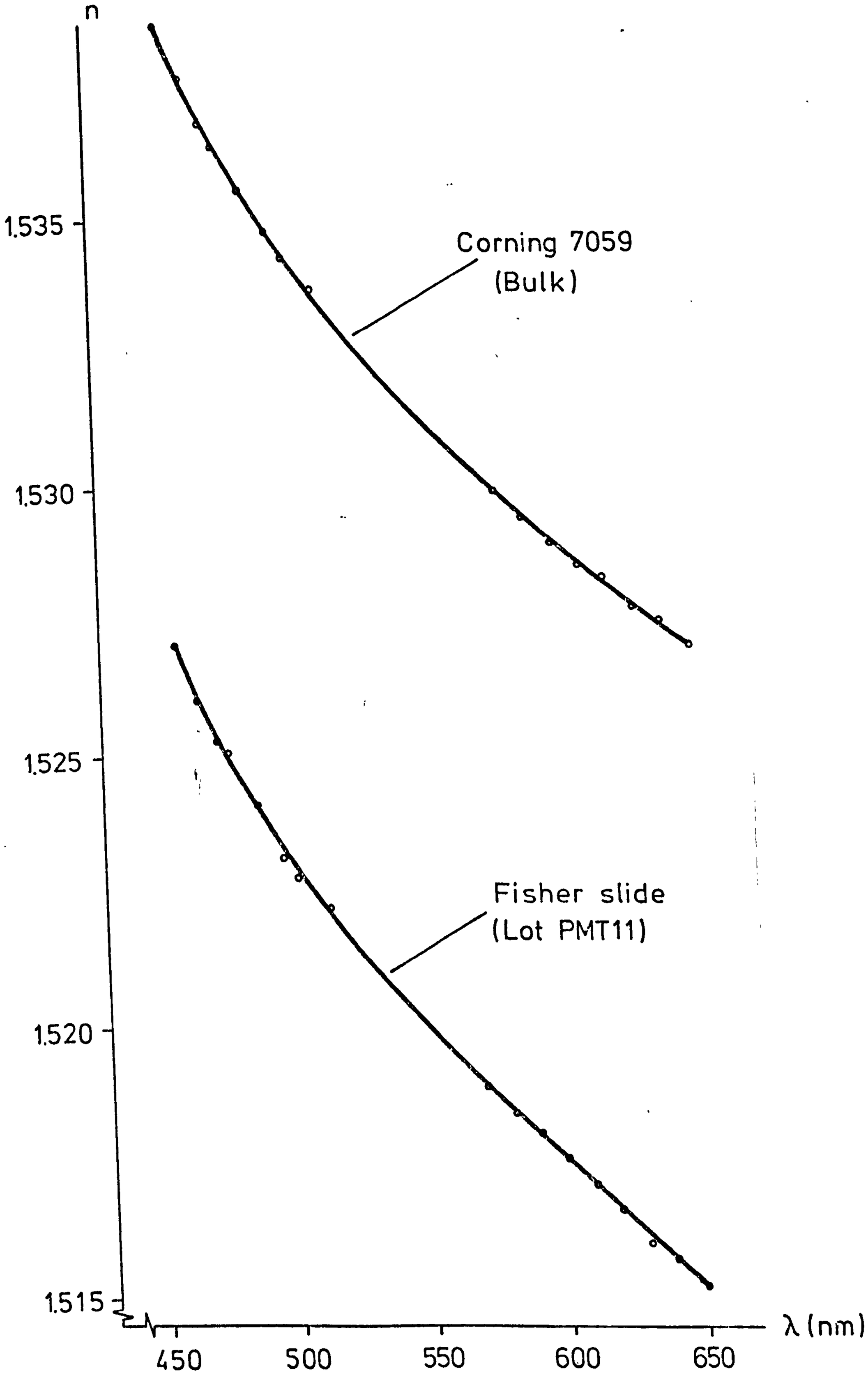

FIG 4.2 Refractive Indices of Experimental Glasses

Several experimental runs were made to determine the index of refraction of the sputtered films as a function of rf power. It is known that the deposition rate increases with power and the refractive index of the films follows some direct relation to the rate of deposition[120]. Since the measurement of rf power is generally difficult, the current readings of the heads were used to indicate the power levels in the experiments. The dispersion properties of the resulting films were calculated from mode angle measurements on multimode waveguides sputtered at different values of the head current. The results of the experiments are shown graphically in Fig.4.3. Optical losses of the sputtered films were measured on single mode waveguides and at the HeNe laser wavelength,the corresponding figures were less than 0.5 dB/cm for all different films. Spectrophotometric analysis of the samples indicated no observable absorption in the range of wavelength between 360 nm and 700 nm, however, for films sputtered at low head currents there was a marked tendency for a higher degree of absorption in the UV range. The qualitative results from the latter analysis indicate that the composition of the films changes according to the rf power. This is not unreasonable since, in general, the refractive index of the films is greater than that of the bulk material. The actual mechanism which accounts for the variation in composition is complex and not well understood. Goell[113] attributes the change in index values to the BaO content in the films and the variation in content to the rf power and substrate temperature. Index variations of a second type have also been observed in our experiments immediately after a change in power level. The film index appears to drift continuously towards a steady state value during the first runs provided the power level is left unchanged. This effect was first observed by Pitt et al[114] in similar

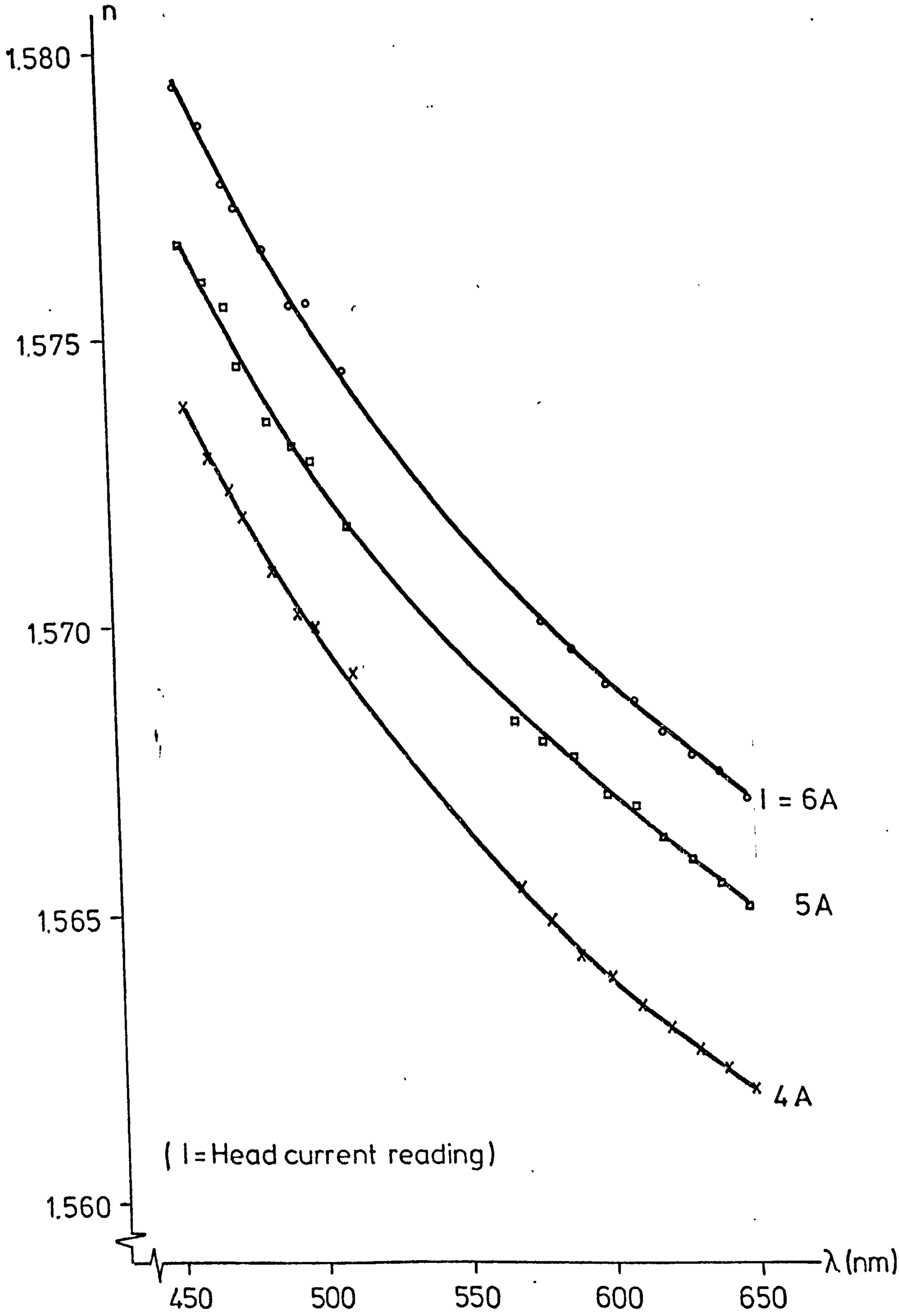

FIG 4.3 Refractive Indices of Sputtered Corning 7059 Glass Waveguides as Function of RF Power.

experiments, however, no satisfactory explanation has been given for the phenomenon.

In our work on filters, waveguides were fabricated at a power level corresponding to a head current reading of 6 Amps. The choice of this particular value was mainly determined by the use of the equipment by other workers. The deposition rate was measured to be 0.4/μm/hr and film uniformity was confined in the centre slide inside an area of 25 mn diameter. Losses were less than 0.5 dB/cm and the film index was consistent from run to run.

4.2 Production of Thin Film Waveguides by Diffusion

Thermal diffusion of ions can raise the refractive index of a surface layer in some substrate materials. The existence of such a layer complies with the fundamental requirements for light guiding. Low loss optical waveguides have been formed by this method; inexpensive and straightforward manufacturing, extremely uniform layer thickness and, most of all, accurate control over the propagation constant being the chief advantages.

Successful fabrication of waveguides has been achieved using different type of diffusion processes. Taylor et al[65] first reported the formation of guides by indiffusing Se into CdS. Kaminow et al[63] reported waveguides formed by outdiffusion of Li from $LiNbO_3$ and Giallorenzi et al[58] reported waveguides formed by ion exchanging sodium from a soda lime glass by silver from a $AgNO_3$ melt.

The second type of waveguides used in this investigation were formed by the silver-sodium ion exchange process. Description of these guides and properties of experimental waveguides are given in the following subsections.

4.2.1 Silver Ion Exchanged Waveguides

When a soda lime glass is immersed in a silver nitrate ($AgNO_3$) melt, an exchange process takes place in which the sodium ions in the glass are replaced by silver ions from the melt. Silver, having a higher specific refractivity than sodium, raises the index of refraction of a thin layer of the glass within a depth where the exchange process has taken place. Since the diffusion of ions is not linear with respect to the penetration depth and the increment of the index is related to the concentration of silver, the refractive index of the perturbed layer is not constant with depth. Waveguides formed by this process are, therefore, inhomogeneous. The actual profile of silver concentration is very difficult to determine experimentally; it is related in some way to the temperature of the melt, the diffusion time and the composition of the soda lime glass. However, using measured effective indices, a fit to an assumed refractive index profile can be made. Waveguides are fabricated by immersing soda lime glass substrates into a $AgNO_3$ melt at some fixed temperature between 213°C and 350°C. The $AgNO_3$ melt is heated in a temperature controlled furnace and the substrates immersed for periods which can result in highly multimode waveguides. The effective index N is then measured for each individual mode, using the prism coupler and their values inserted into the WKB integral (see Chapter II). The index distribution is given by the function n(x) which ideally brings equality to both sides of the equation. Results from this type of investigation have been reported by several workers and a variety of distributions have been obtained[58,77-79].

In our work on filters, we have used the results reported by Stewart et al.

4.2.2 Experimental Waveguides

Waveguides were formed by immersing Chance glass slide into a $AgNO_3$ melt at a temperature of 215°C and the exchange time was obtained from the graph shown in Fig.2.13 to give single mode guides with effective guide indices N between 1.514 and 1.545 nm at 610 nm. The temperature control on the particular furnace used in this work was ±0.5°C and the substrates were immersed without preheating. A typical drop of 1.0°C was observed immediately after the slides were introduced in the melt and steady state conditions were regained after a period of 3 to 4 minutes. The variation in N measured from a batch of similar waveguides was ±0.005 maximum and typically of the order of ±0.001. The latter figure is in close agreement with the theoretical variation in N calculated from the work of Millar et al[81] (see Chapter II). The experimental waveguides so obtained exhibited low loss with a moderate amount of scattering. The variation of N as a function of frequency was measured using a dye laser and the results are shown graphically in Fig.4.4.

4.3 Photoresist Materials

The properties of photoresists are, by now, well known through their extensive use in the formation of masks and in the holographic recording processes. Two types of resists, namely negative and positive, exist and their basic difference lies in the way the incident radiation of light affects the chemical properties of the material. On exposure to light,negative resists become insoluble when immersed in developer (normally Xylene based); the opposite effect takes place with positive resists. For submicron line patterns positive resists are preferred and they are generally composed of a photoactive compound which is also known as the inhibitor, a base resin, and suitable

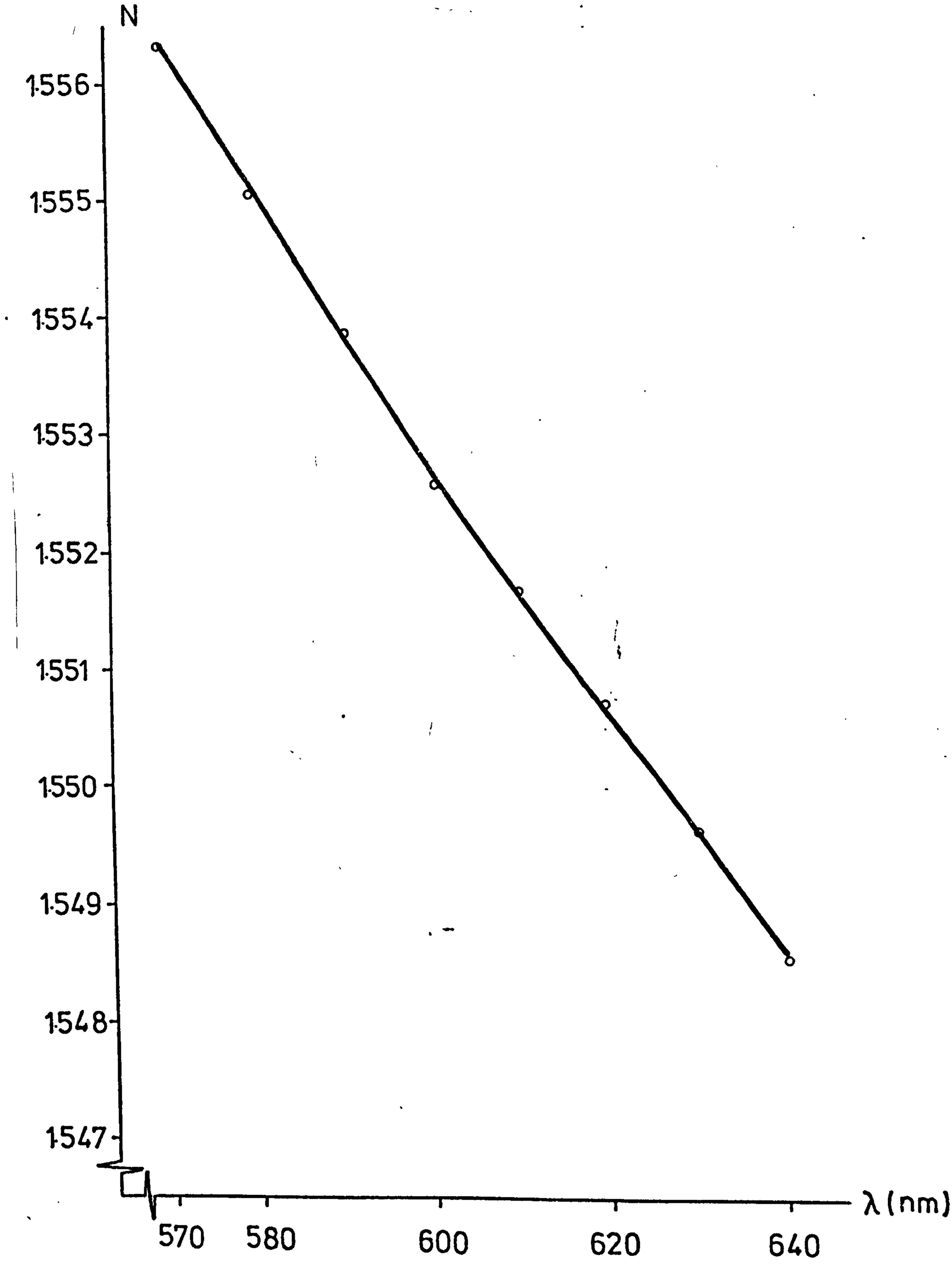

FIG 4.4 Effective Guide Index for Silver-Sodium Ion-Exchanged Waveguides.

organic solvents. On exposure to light, the inhibitor is destroyed, leaving the base resin in a soluble form when immersed in an alkaline solution known as the developer. Positive resists, therefore, allow for the possibility of 'add on' exposure technique for masking off and altering the topography of the patterns. Positive resists are commercially available from the Shipley Company Ltd. (AZ1300 and AZ2400 resist systems).

As with most photosensitive materials, the exposure or, equivalently, the depth of cut of resist films is in general not a linear function of the incident energy density. Moreover, the response varies with the wavelength of the incident radiation. There is an extensive literature on the behaviour of photoresist films. Beesley et al[44] determined the sensitivity of AZ1350 resist as a function of wavelength and incident power. Bartolini[45] found that the non linear response of AZ1350 can be relaxed by using a stronger developer. The characterization and theoretical modelling of AZ1350J resist were reported by Dill et al[46,47]. Their investigations was later extended to determine the effects of temperature on resist patterns[48,49]. Changes in the optical thickness of resist films during development was reported by Konnerth et al[50]. Standing wave effects during exposure could be reduced, in the final resist pattern, by thermal bake prior to development, as reported by Walker[51]. Line width variations caused by the use of different photographic masks were reported by McGillis et al[52]. The effects of profiled surfaces on the pattern line widths were also reported by Widmann et al[53]. The list of references cited here is by no means exhaustive. Unfortunately, as the behaviour of the resist films is a strong function of several parameters (temperature, humidity, etc.) while the above papers are useful in isolating problem areas, it is rarely possible to use their

precise processing methods and obtain the same results. In the following subsections we present the criteria governing the selection of resist material for our work on filters and the experiments performed to determine the properties of resist films.

4.3.1 Shipley AZ1300 Photoresists

In the manufacturing of holographic gratings the AZ1300 system of resists has been widely used because of its sensitivity to the radiation from argon and HeCd lasers. Resists from this system have different sensitivity and viscosity. Also, when subject to high temperature post bake,they have different degrees of plastic flow. The selection of the specific type of resist used in our experimental filters was based on two requirements. Firstly, high sensitivity and resolution to the argon 457.9 nm and HeCd 325.0 nm laser lines. Short exposure times are required to minimise the effects from acoustic and mechanical vibrations in the interference pattern. Secondly, repeatability and quality of films when the material is spun coated to a thickness of about 100 nm to 200 nm. The film thickness is dictated by the magnitude of the grating period required, typically of the order of 200 nm.

With these criteria in mind the properties of the following resists were investigated AZ1350J, AZ1370 and AZ1375. The remaining resists of the AZ1300 system, namely, AZ1350 and AZ1350H were not used because of their notorious problems in adhesion to the substrates. AZ1350B resist was not available at the time of this work.

Experiments to determine the thickness of spun coated films were carried out first. Photoresist was loaded at room temperature using a hypodermic syringe fitted with a 1μm Millipore filter onto cleaned half-microscope-slides which were then spun at a particular speed and

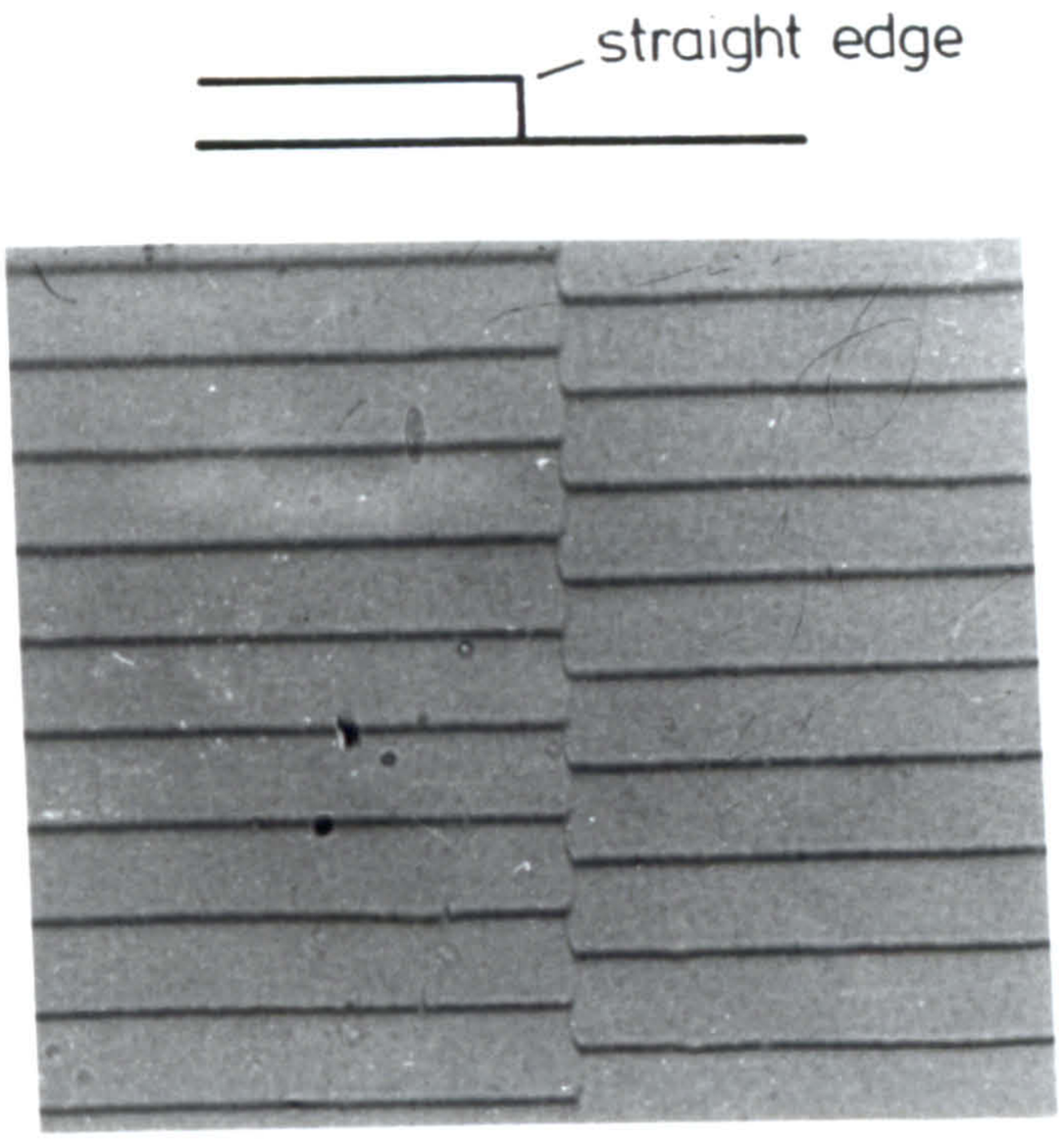

(a)

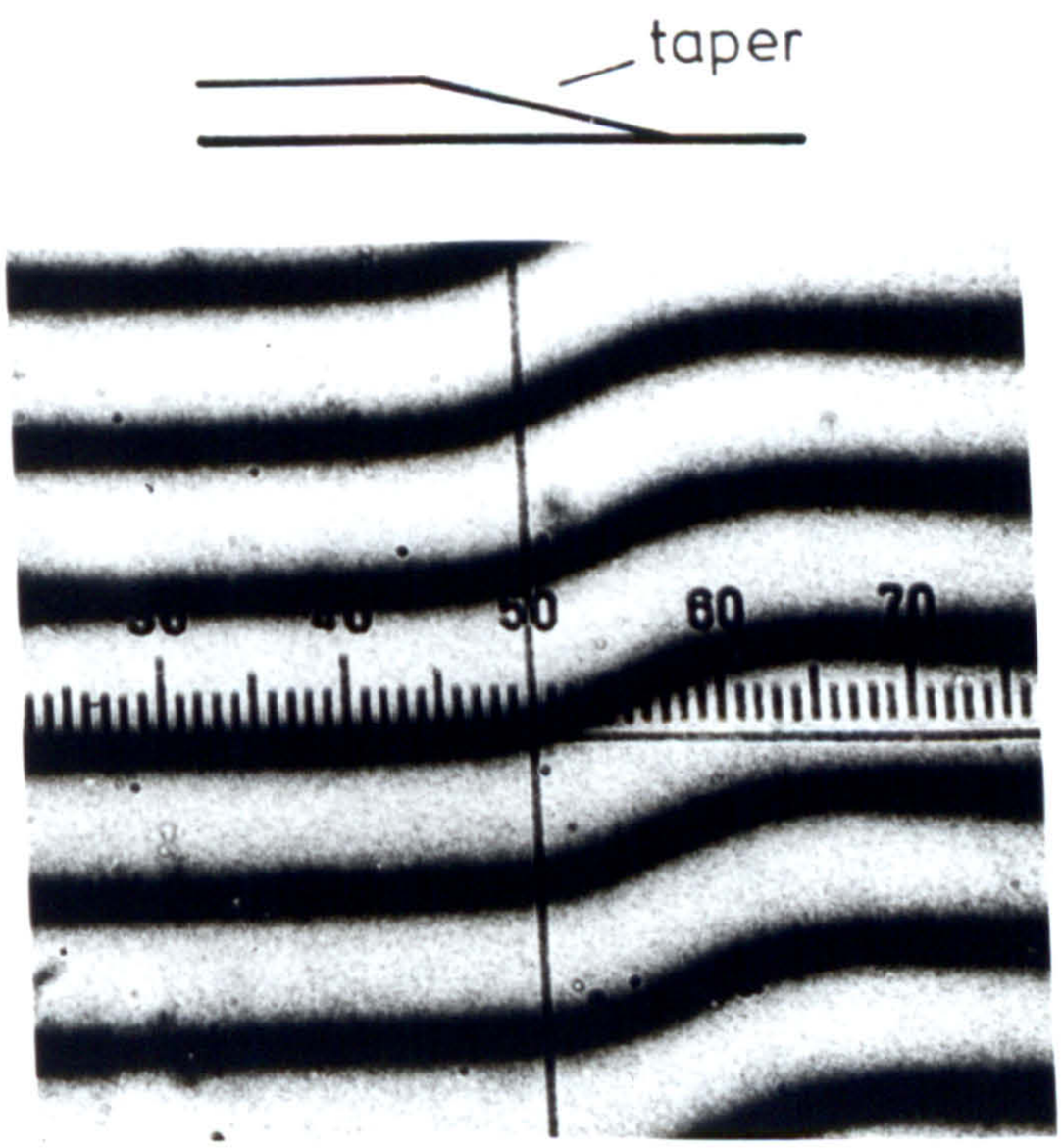

(b)

FIG 4.5 Measurement of Film Thickness and Taper Length Using Multiple Beam Interferometry. (Tolansky Fringes).

for a given time. Coated films were subsequently pre-baked at 80°C for 20 minutes in order to remove the liquid solvents. Spun coated films have an inherent thickness gradient[54] and in our experiments, thickness uniformity was confined to a circular area of around 20 mm diameter. To measure the absolute value of the film thickness, the portion of the film between the centre of the sample and the short edge of the slide was chemically removed using a concentrated solution of AZ303 developer. Immersion times of 5-10 seconds ensured total removal of the film, leaving a well defined step. This masking procedure is better than the conventional photolithographic technique because developers etch unexposed resist as is clearly demonstrated in the case of AZ303. The heights of the steps were measured by the optical technique of multiple beam interferometry. To this end samples were overcoated with a 50 nm thick film of aluminium by vacuum evaporation. Tolansky fringes showing the step height of a typical sample are shown in Fig.4.5(a). Results from initial runs using undiluted photoresist gave magnitudes of film thickness too large for our applications. In particular, AZ1375 resist, whose viscosity is the highest in the AZ1300 series, was found unsuitable for this work. Further runs were made by diluting AZ1350J and AZ1370 resists in AZ thinner. The effect of this operation is to lower the viscosity of the photoresist. A range of film thickness values was then obtained by changing the dilution ratio, spinning speeds and times. Fig.4.6 shows the variation in film thickness as function of the dilution ratio for the optimum spin coating conditions, namely 4000 RPM and 20 seconds. Results given in the graph are obtained from average and the deviation in thickness from batch to batch was typically of the order of 25%. The deviation was noted to increase at lower spin speeds whereas film quality deteriorated at the higher speeds.

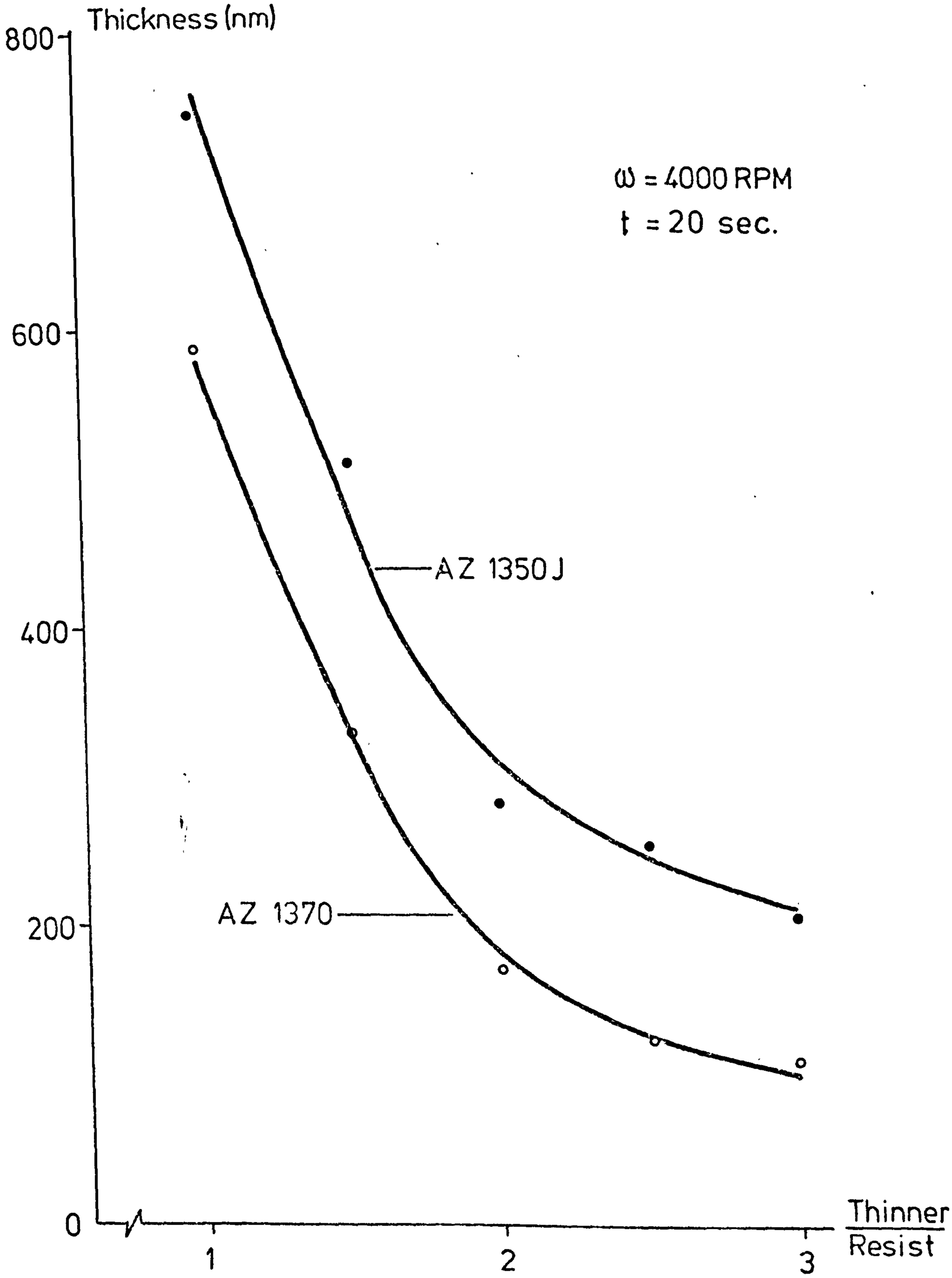

FIG 4.6 Thickness of Spin Coated (Thinned) Resist Films.

Following the selection of AZ1350J and AZ1370 resists a survey on the type of developer was found necessary. Three types of developers are available from Shipley Co.Ltd. and they are, in order of strength, AZ303, MF312 and AZ developer. These are normally used in diluted solution with water. The criterion for the selection of a suitable developer in this work was based on the consideration of the initial film thickness of resist and the etch rates of the unexposed material. Several tests were conducted using 200 nm thick resist films. The results indicated that for improved control of the development stage AZ developer was best suited because of its slower speed of reaction with exposed resist.

4.3.2 Properties of Shipley AZ1350J and AZ1370 Resists

The resolving capabilities of AZ1350J and AZ1370 resists were determined by recording gratings with very short periodicities. Typical 200 nm thick films of resist were exposed to the interference pattern from the HeCd and argon ion lasers and the resulting patterns in relief examined under a scanning electron microscope (SEM). On both resists, grating patterns with a period of at least 164 nm can be written with extremely good definition. The ultimate resolving capability of the resist was not approached in this work.

In the manufacture of short period holographic gratings it is desirable to use a monochromatic source with a very short wavelength radiation. The relative sensitivities of the resists were determined at the HeCd 325.0 nm and argon ion 457.9 nm radiation. The AZ1370/AZ1350J sensitivity ratio was nearly unity at the 457.9 wavelength, whereas at 325.0 nm the corresponding ratio was of the order of 2.6. These parameters were determined from measurements of the grating diffraction efficiencies for a given exposure time and fixed development period. The particular HeCd laser used in our experiments nullified

the advantage of using the higher sensitivity of AZ1370 resist in the fabrication of gratings because of its limited power output of 1 mW. The following tests to determine the exposure parameters are related to the argon 457.9 laser line.

The response of the resists was measured under the following conditions:

(i) Varying development times at fixed power density and exposure times.

(ii) Varying exposure times at fixed power density and development period.

In these experiments we used a photographic emulsion mask with a straight edge to obtain a step in the resist films. One of the collimated beam of the interferometer was incident upon the mask which had been previously contacted to the resist film. To reduce the air gap at the interface, the sample was pressed down by means of a weight. The total incident power of the beam was measured with the UDT Model 122 power meter calibrated at 457.9 nm. The exposure time was controlled by means of a timer-controlled shutter with an accuracy better than 0.05 seconds. Development time was monitored by a stop watch. Filtered water to 1μm was used in the rinsing stage and samples were subsequently blown dry with nitrogen gas.

Results from tests under conditions given in (i) are shown in Fig.4.7. Since developer etches unexposed resist, to obtain the absolute depths of cut of the exposed samples, the removal rate of unexposed resist were measured and the results were added to those found from the exposure tests according to the development period. The average results from tests under conditions given in (ii) are shown in Fig.4.8; it can be observed that the response of AZ1350J exhibits a

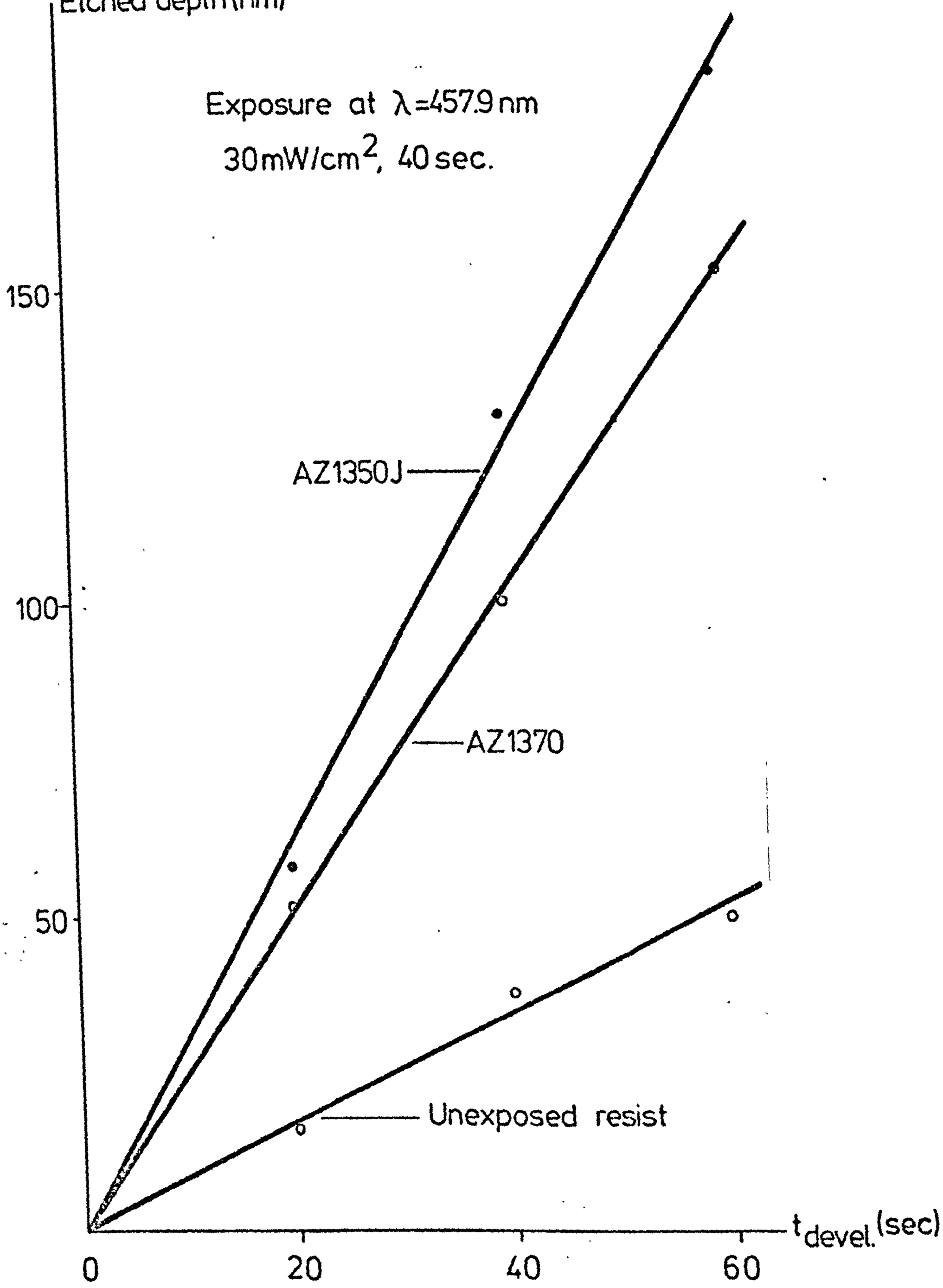

FIG 4.7 Etch Rates of Diluted AZ Developer (1:1 with water) for Typical Exposure Parameters of Resist.

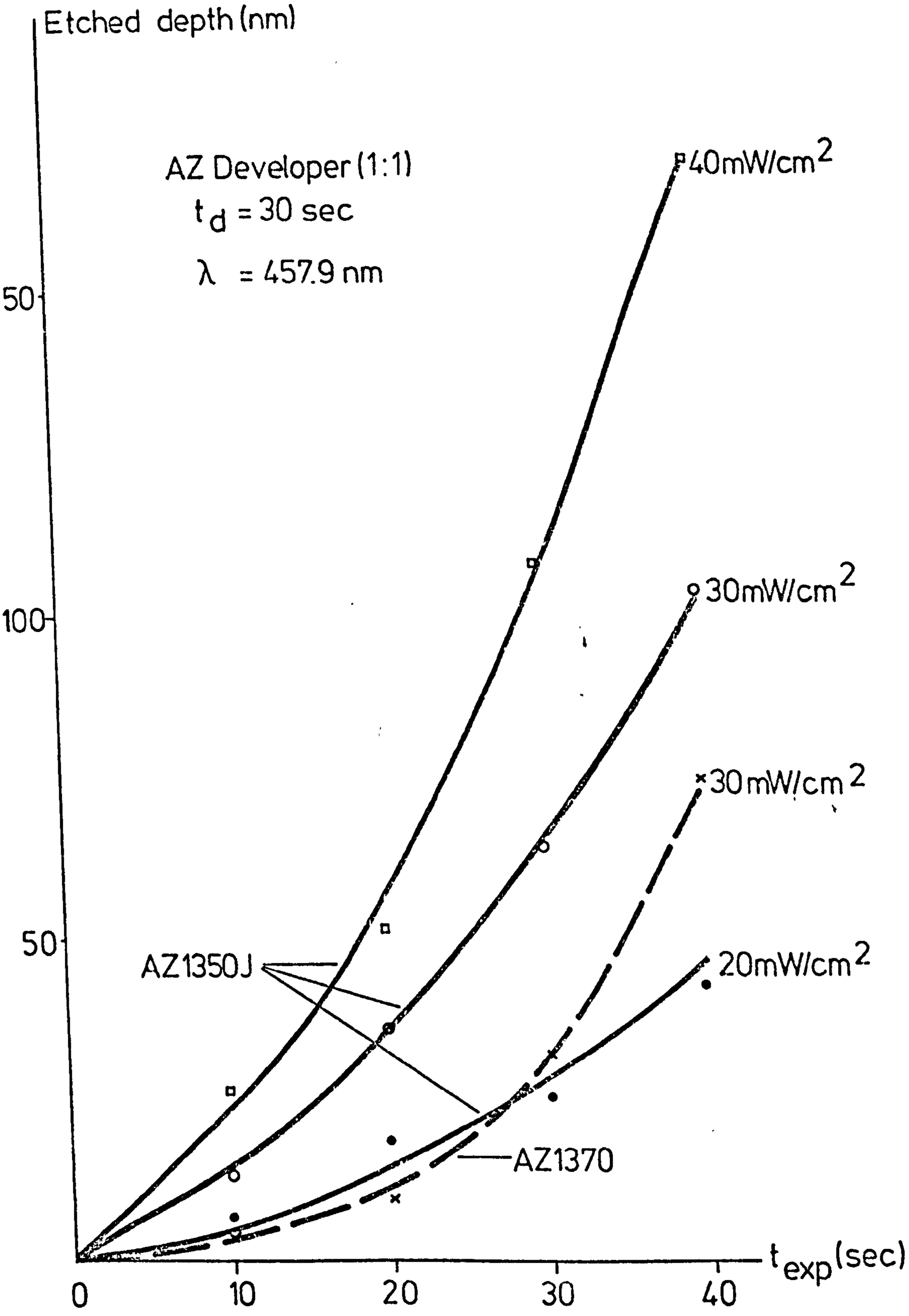

FIG 4.8 Response of Photoresist Films as Function of Exposure Parameters.

better linearity. In general, considerable variations were found in the depth of cut for samples of different batches. Humidity seemed to have some affects on the sensitivity of the films.

Final experiments were conducted to determine the refractive indices of the resists. The optical absorption of these materials were measured using a Unicam Model SP800 UV spectrophotometer. The response curves for films of similar thickness showed absorption starting at 650.0 nm and reaching complete opacity at 550.0 nm for AZ1350J and 500.0 nm for AZ1370. The value of the refractive index as function of wavelength was calculated from mode angle measurements using a symmetrical prism coupler (see subsection 4.7.1). Since resist films are extremely lossy when used as optical waveguides in the visible, the use of such a prism allows the light to be coupled out of the guide before it gets absorbed in the material. The particular prism used was made from Schott SF59 glass whose refractive index at 632.8 nm is 1.94325 according to manufacturers data. The index value of the glass was not checked in our experiments as the capability of the Abbe refractometer available for this work does not cover so high an indice. The dispersion properties of the glass was calculated from the relation given by the Glasswerk Schott Company. The index value of the resists at 325.0 nm was determined using Abeles method. Results from these measurements are shown in Fig.4.9 where it can be observed that AZ1370 has a higher index of refraction. The curves are fitted by a linear regression applied to the experimental data.

4.3.3 Effects of Temperature on AZ Resists

The properties of resist films and the quality of resist masks can be seriously affected by the baking processes used to remove the solvent from the material. In our experiments it was found that a minimum temperature of 60°C was required to remove the solvents from

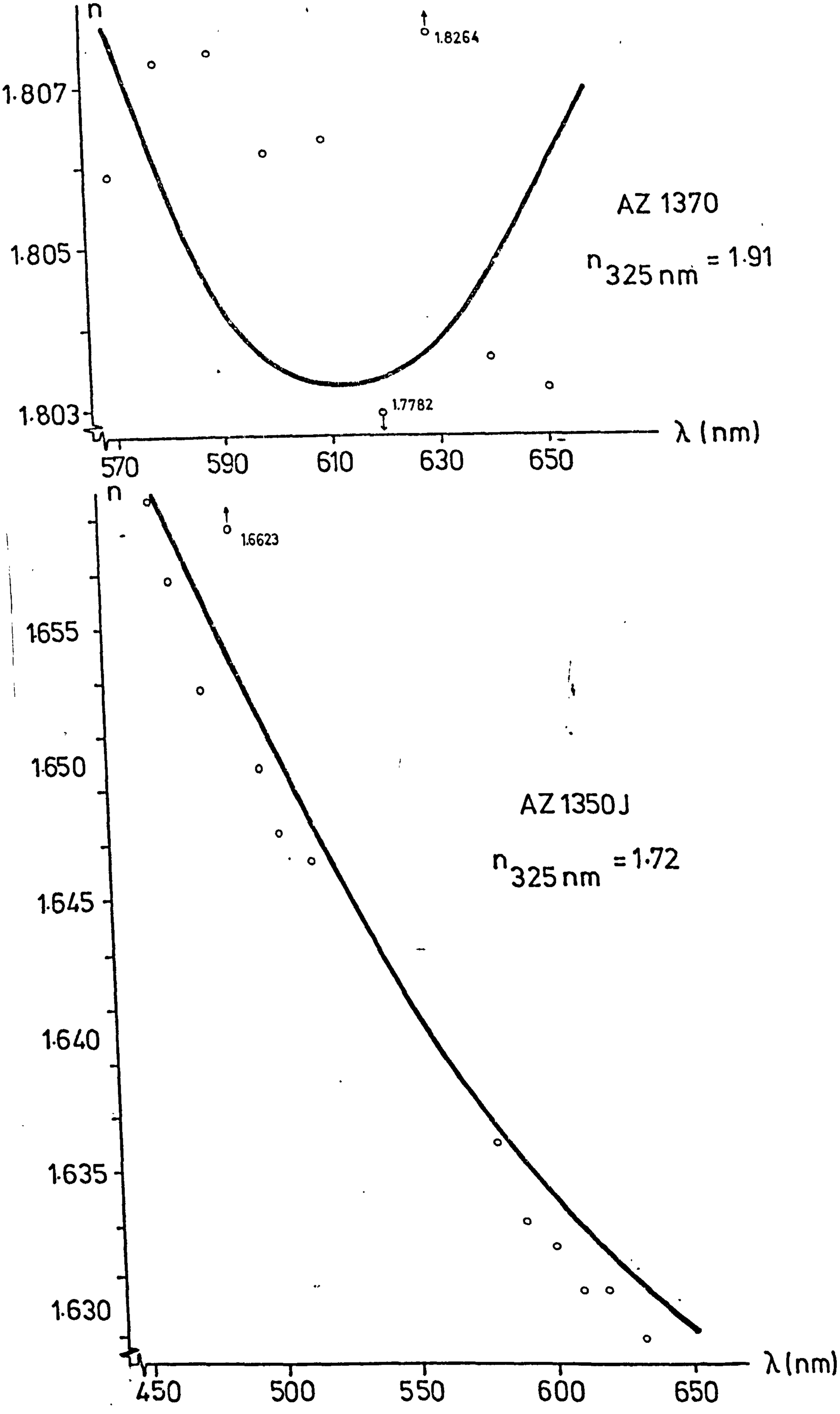

FIG 4.9 Refractive Indices for Photoresist Films.

the spin coated films. The evaporation of solvent was monitored by comparing the thickness of baked and unbaked samples. For a typical 200 nm thick film,the reduction in thickness was of the order of 15% to 20%. The use of a bake temperature of 80°C reduced the bake time from one hour to 15 minutes and, generally, an additional 5 minutes was given to account for any variation in the resist/thinner mixture and any other parameters affecting the coating process. Higher bake temperatures have deleterious effects on the response of the resist films[48-49]. In our experiments, complete destruction of the photoactive properties of the photoresist films was observed for samples baked at a temperature greater than 120°C. If gratings are to be subject to ion beam etching, hardening of the pattern can be achieved by postbaking the resist after exposure and development to improve durability of the masks. Early experiments on postbaking were carried out using resist gratings heated in air on a hot-plate and at a temperature of 120°C for 30 minutes. Subsequent examination of the gratings under the SEM showed a flattening effect of the resist lines for samples with grooves cut down to the substrate and almost complete disappearance of the patt rns in samples where an underlay film of resist existed between the grating and the substrate. At temperature levels of this order the amount of plastic flow in the material is comparatively high with respect to the dimensions of submicron lines. However, the results of these tests indicated that for lines cut down to substrate, the thermally induced deformation takes place along the vertical direction only. Patterns with an underlay film are subject to both vertical and lateral flows and, correspondingly, to a greater amount of deformation. Further tests were carried out at temperatures below 120°C, however, the resist patterns failed to harden as the solvents present in the material did not have a high enough vapour

pressure to escape into the atmosphere. In order to minimise thermally induced effects, post baking of resist gratings was next carried out under vacuum conditions. This allows for lower temperatures to be used since the partial pressure necessary for the solvents to escape from the material is lowered. Working at a pressure of 10^{-3}Torr, a temperature of 80^{o}C and bake periods of 1 hour, the degree of deformation of the patterns was drastically reduced. In the case of short period gratings, the amount of plastic flow was still significant and the processing of samples with an underlay film was, in general, not very successful. The degree of preservation of the pattern in these cases was directly related to the magnitude of the thickness of the underlay films.

4.4 Holographic Diffraction Gratings

The technique for producing holographic diffraction gratings was proposed by Rudolph et al[121] in 1967. Gratings are formed by recording onto photoresist the interference pattern of two amplitude divided beams from a single laser. In comparison to gratings made in a ruling machine, holographic gratings can be produced with a larger number of lines per millimeter and with negligible error in line spacing. The magnitude of the shortest grating period is determined by the wavelength λ of the laser light.

In the fabrication of optical devices, a precise control on the grating depth is required and, for certain applications, such as etching, it is also required that the grooves should be cut down to the substrate. Two methods have been reported in the fabrication of gratings, the expose and develop (ED) and the simultaneous exposure and development (SED)[55] techniques. The control over the grating depth during fabrication is in general difficult. Because the diffraction efficiencies of the grating orders are function of the

groove depth,it is possible to control the extent of development of the exposed films by monitoring the efficiency of one of the grating orders using a monochromatic source whose radiation does not affect the photoresist. This particular technique was reported by Beesley et al[122] and works well especially in cases where the development rate of the resist is slow. The sinusoidal variation in intensity of the interference pattern is not generally recorded faithfully in the resist because of the nonlinear properties of the material. However, the shape of the final pattern can be improved by pre- or post-exposure of the film using a uniform source before development. In the cases where the grating grooves are required to be cut down to the substrate,the ED technique of fabrication is not particularly useful. The optical mismatch generally encountered at the resist-substrate interface sets up in a standing wave pattern of the radiation across the thickness of the resist film and has the effect of distorting the shape of the groove walls. Moreover, since the pattern tends to modulate the intensity of the radiation in the film, the exposure parameters are difficult to control; the problem is increased if the varia'ility in thickness of the spun coated films is taken into account. For gratings of this particular type the use of the SED technique of fabrication is preferred. The method consists in exposing resist films inside a container filled with developer so that the exposure and development processes take place at the same time. The technique relaxes the effects of standing wave patterns and the non-linear response property of the resist material. Gratings with deep grooves and improved tooth shape and, also, with grooves cut down to the substrate have been successfully fabricated using this method. The implementation of the technique by Beesley et al to measure the groove depth renders the SED technique particularly attractive for the production of high quality holographic gratings. The fabrication of

high efficiency grating couplers, DFB lasers and band rejection filters for Integrated Optics requires gratings with magnitude of the periodicity below $\lambda/2$ in free space of the commonly used argon ion 457.9 nm laser line. This problem can be solved in two ways : firstly, by using an UV coherent source such as a HeCd laser (441.6 nm or 325.0 nm) or, secondly, by reducing the laser wavelength in a high index medium.

We continue this section with a description of the interferometer and experimental results for gratings formed using the ED and SED techniques. The feasibility of producing short period gratings and the experimental difficulties involved in the fabrication of gratings for waveguide Bragg filters are also discussed.

4.4.1 Interferometric Equipment

A three-mirror system interferometer was used in our experiments. The general lay out of the equipment is shown schematically in Fig.4.10. This particular interferometer operates with two non-laterally inverted beams so as to avoid the enhancement of any aberration in the wavefronts of the interfering beams. The coherent source used was a Spectra Physics Model 165 argon ion laser operating at the 457.9 nm line. The total power output from the laser at the transverse TEM_{01} mode was 180 mW. Single TEM_{00} mode operation was achieved by reducing the size of the intracavity aperture giving a total output power of 70 mW. Power measurements were made using an UDT Model 122 power meter which was calibrated against a Hilger Watts Model FT-4 thermopile with a flat response between the IR and the deep UV. The laser beam was vertically polarised and had a coherence length of 145 mm. The length was measured by monitoring the fringe visibility in a Michelson interferometric arrangement. The laser beam was spatially filtered by focussing it onto a 10μm circular pinhole by means of a Nikon x20 objective lens. The filtering stage has the effect of expanding the beam and, most

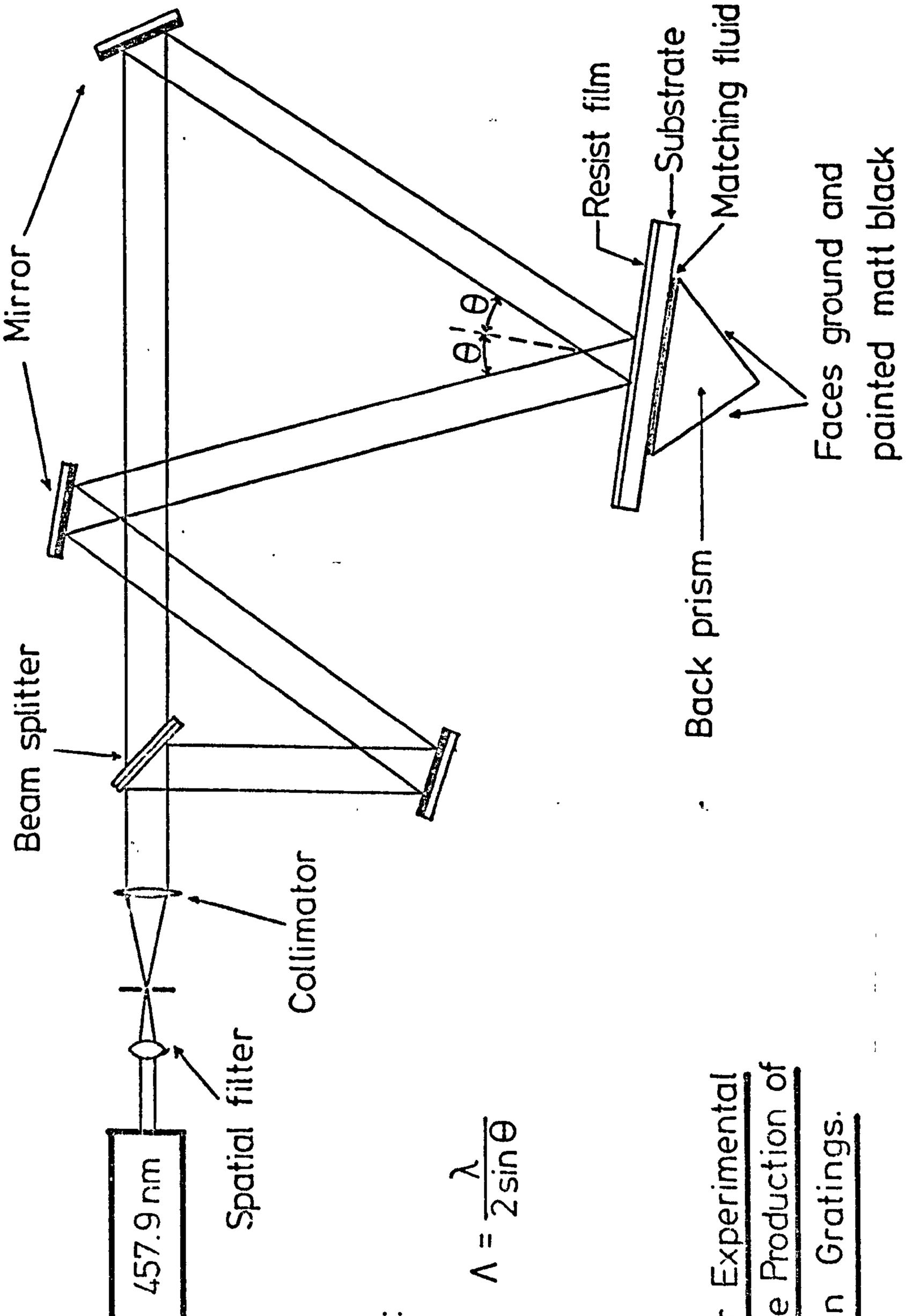

Grating period: $\Lambda = \frac{\lambda}{2\sin\theta}$

FIG 4.10 Three-Mirror Beam Interferometer for the Experimental Holographic Diffraction Production of Gratings.

importantly, of removing any off axis light in the original beam. The expanded beam was then collimated by a f/4.5 Taylor-Hobson lens which had a focal length of 106 mm. The overall diameter of the collimated beam was 25 mm and the intensity distribution along its diameter was measured by a scanning slit-apertured Mullard BPY14 photodetector. The result from this scan is shown in Fig.4.11 where the $1/e^2$ points in the distribution indicates an effective beam diameter of 11.2 mm. The collimated beam was next amplitude divided by means of a dielectric coated beam splitter. To maintain the wavefronts undistorted the splitter surfaces were optically flat to $\lambda/20$. The intensities of the transmitted and reflected beams from the splitter were monitored with two UDT PIN10 photodiodes. Equality of the beam intensities was obtained by changing the angle of incidence of the original beam onto the front face of the splitter. Accuracy of the division was better than 5%. The degree of beam collimation was checked with a shearing interferometer[123] consisting of a $\lambda/20$ quartz optical flat with faces parallel to 5' of arc. For a perfect plane wave no fringe should appear in the region of overlap of the sheared beam. Fig.4.12(a) shows a photograph of the pattern obtained from this test, the appearance of fringes is due to spherical aberrations in the collimator. Fringes were found to disappear if the lens was stopped down by one f/stop, however, the amplitude of the diffraction rings from the aperture became unacceptable. The quality of the interference pattern was assessed using a Michelson interferometer and the results are shown in Fig.4.12(b). The overall optical imperfections in the system limited the useful area of the beam to a diameter marginally smaller than the effective width. The amplitude divided beams were directed towards the mirrors forming the interferometer. The mirrors had a front surface flat to $\lambda/20$ and an overall diameter of 50 mm. For maximum fringe visibility of the interference pattern, mirrors were located at positions which allowed

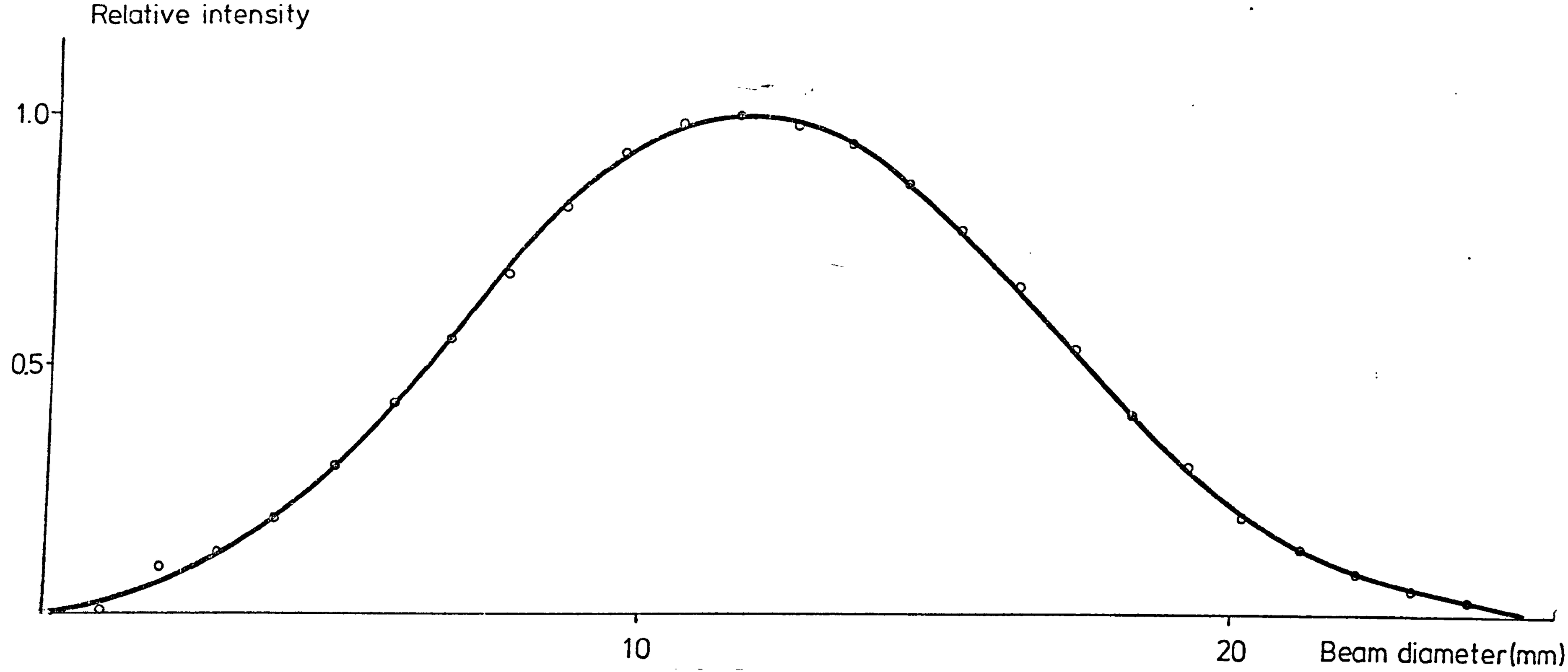

FIG 4.11 Intensity Distribution of Interferometric Beam.

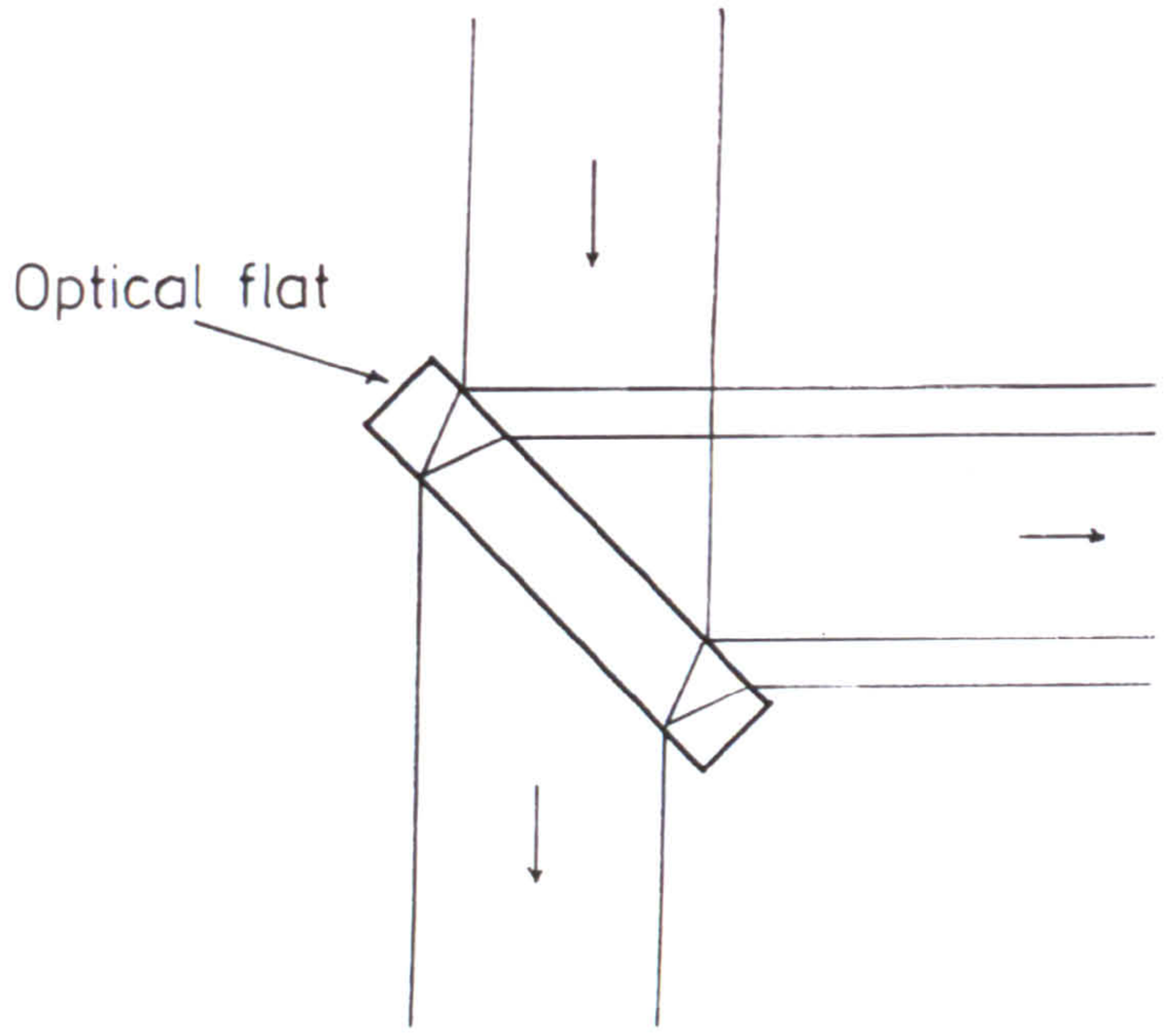

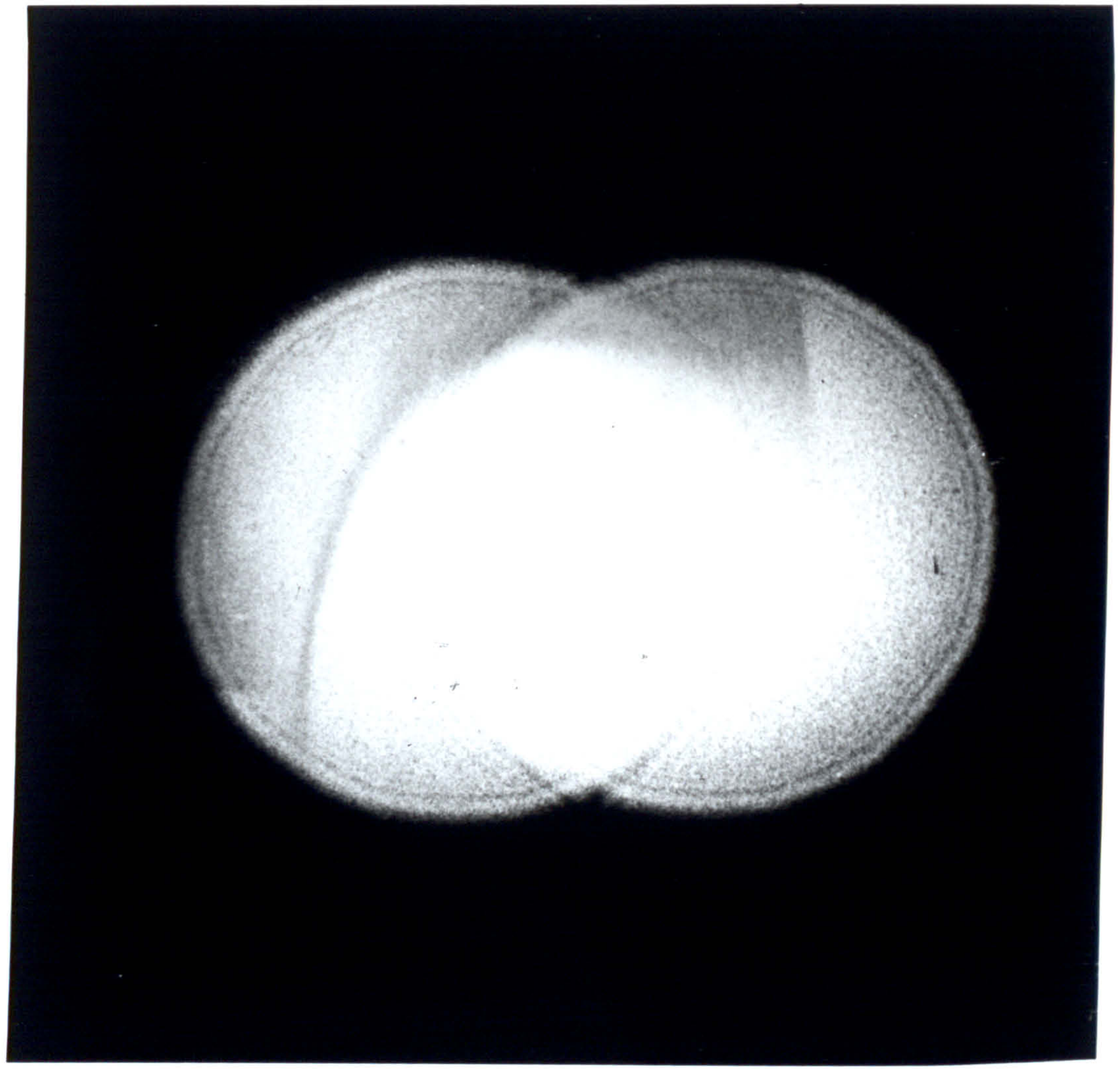

FIG 4.12a Shearing Interferometer - Test for Beam Collimation

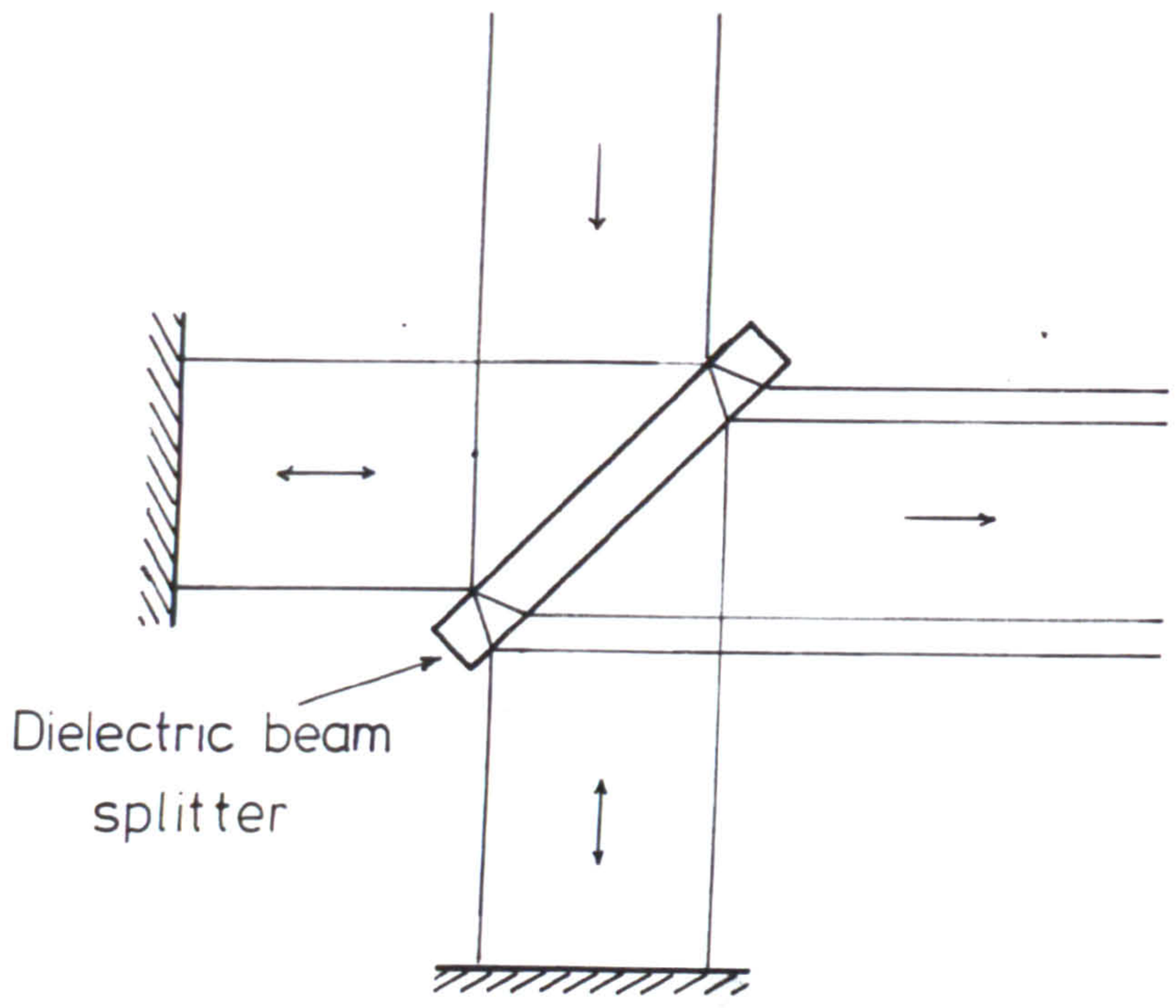

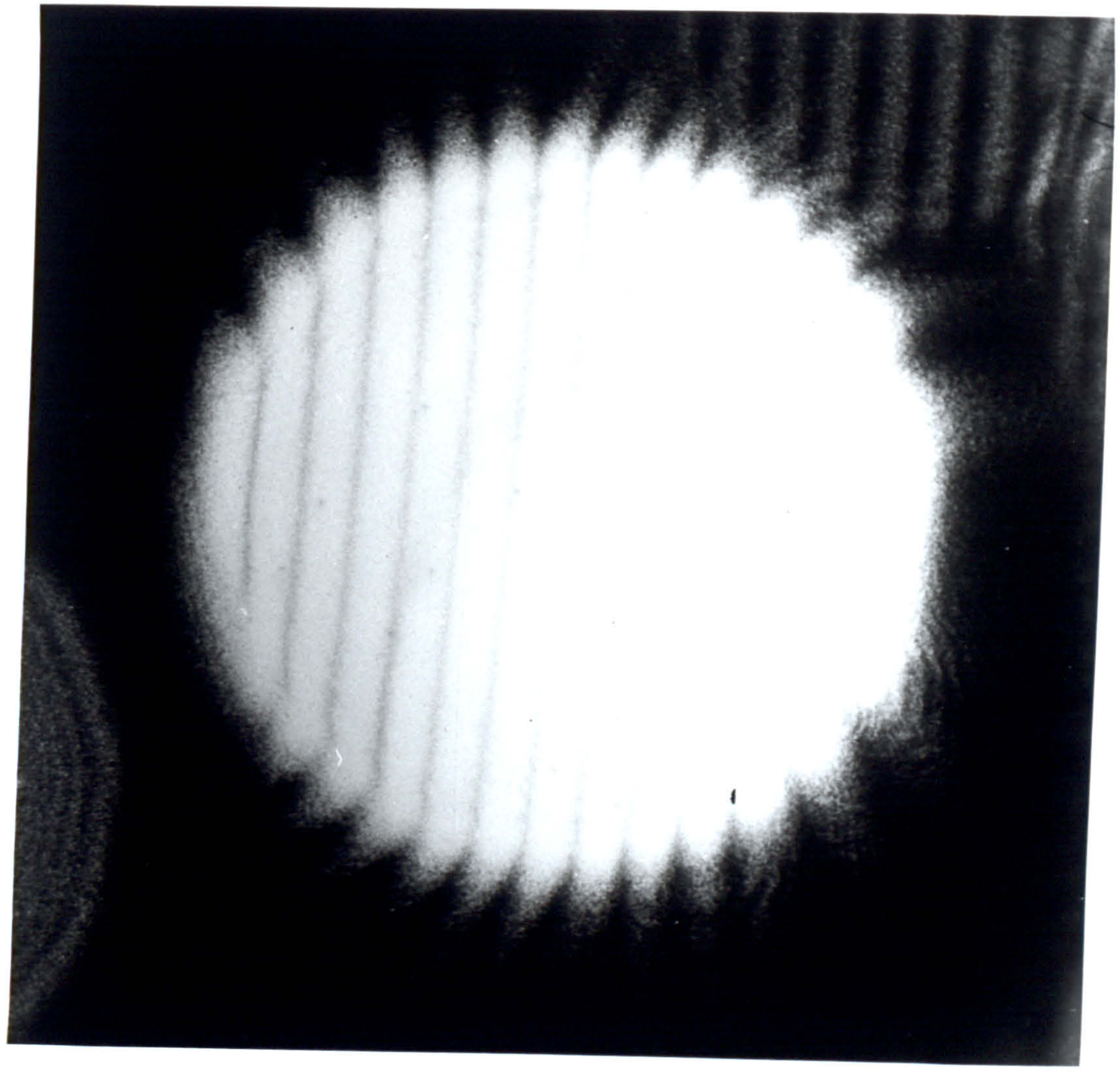

FIG 4.12b Michelson Interferometer - Test for Quality of Beam Wavefront

a maximum optical path difference of 10 mm during experimental settings. A goniometric stage was built to hold the resist coated samples and the stage is shown schematically in Fig.4.13. It provides rotational and lateral displacement in the plane of interference. A 45^{o}-90^{o}-45^{o} glass prism was located at the eucentric point of the stage; the shortest dimension of the prism had a square face of 25 mm x 25 mm. Coated samples were optically contacted to the front face of the prism with a matching fluid (CCl_4 with n = 1.47 at 457.9 nm) which does not chemically attack the resist layer. The remaining two faces of the prism were optically grounded and painted matt black to prevent reflections of the beams and associated interference patterns. In free space the periodicity of the grating is given by

$$\Lambda = \frac{\lambda}{2 \sin \theta} \qquad (4.1)$$

During the fabrication of gratings the x-axis of the stage was aligned to the bisector of the line joining the two main mirrors of the interferometer. The y-axis was located at a distance, along the bisector, given by the tangent of the angle of incidence θ of the beams. Mirrors were then rotated until the two beams overlapped on the front face of the prism. Small adjustment to ensure equal angle conditions were carried out by aligning the reflections from the prism to those on the main mirrors. The accuracy in obtaining a given value for the grating period was 2%. Experimental gratings covered an area marginally larger than the cross section of the beam. The position of the grating patch with respect to a standard microscope slide could be changed by means of the lateral displacement provided in the goniometric stage. The direction of the grating lines could also be changed by use of the vertical rotation; accuracy in angular positioning was estimated to be better than 0.5^{o}.

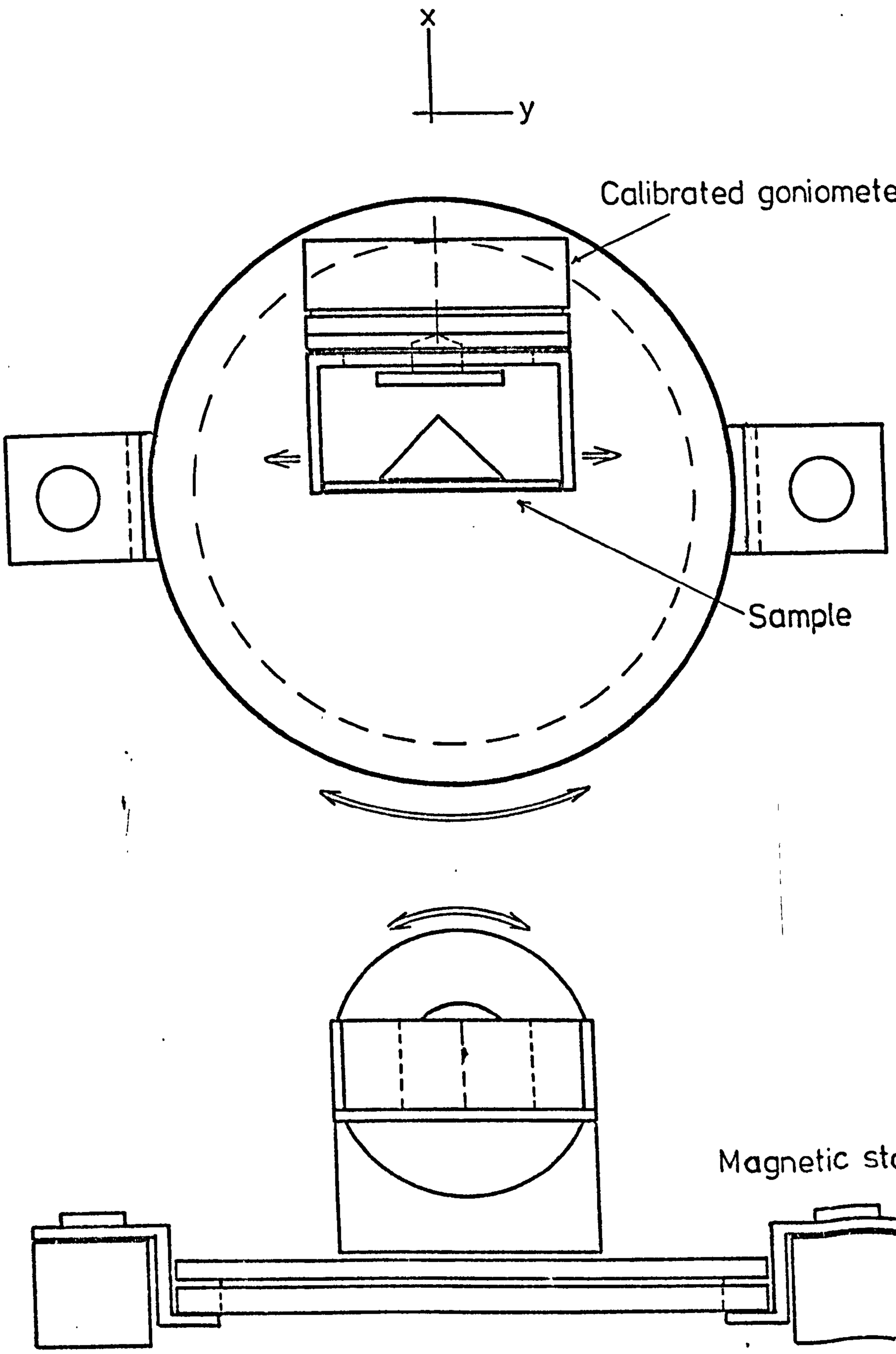

FIG 4.13 Goniometric Stage Used in Interferometer

With the present interferometer and using the ED technique, high quality gratings with $\Lambda \geq 270$ nm were manufactured. Diffraction efficiency measurements indicated uniformity in groove depth over an area of 6 mm diameter. Fig.4.14(a) shows an SEM picture of a typical grating produced with our equipment.

4.4.2 Experimental Limitations on the Grating Period

The theoretical limit to the grating periodicity is $\lambda/2$ for an incident angle $\theta = 90^{o}$. In practice, this limit is governed by two main factors which are directly related to the quality of the beam wavefronts and to the degree of optical mismatch at the layers comprising the samples. For large values of θ the beams expand laterally and any optical imperfections in the wavefronts become amplified. Also, since the reflectivity at the interfaces increases with angle of incidence, spurious modulations on the desired pattern start to appear. The periodicities of the spurious modulations do not necessarily coincide with the periodicity of the desired gratings. Non-parallel interfaces and the number of interference patterns from the multiple reflected beams are the major factors. In general, the reflections at the various interfaces of the samples are small compared to those arising from the resist-substrate interface. Decomposition of the wave vectors of the reflected beams along and across the resist layer shows the presence of modulation on the desired grating amplitude as well as a standing wave across the thickness of the resist layer. As discussed earlier, the standing wave pattern seriously affects the exposure parameters, especially when the air-resist interface is located in the vicinity of a node. Nodes are located at distances given by odd multiples of

$$y = \frac{\lambda}{4n\cos\theta} \qquad (4.2)$$

n = r.i. of resist

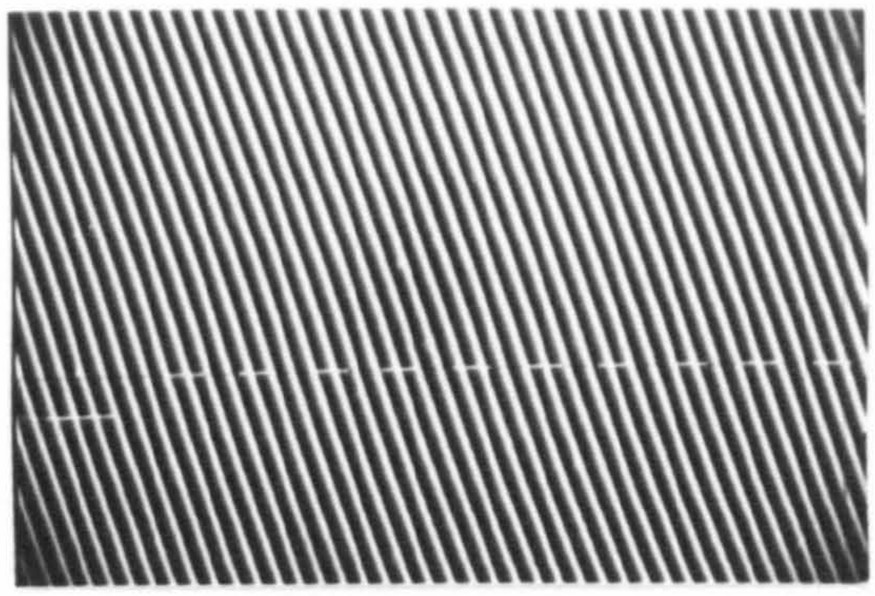

(a) Typical ED-ed grating.

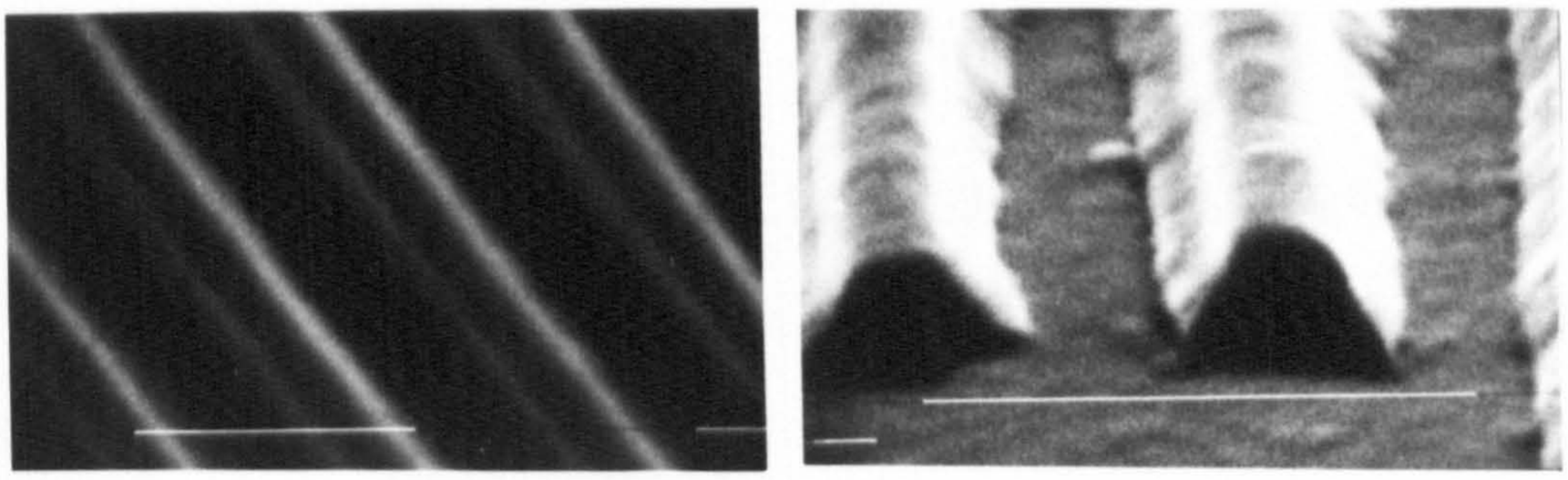

(b) Typical SED-ed grating with grooves cut down to substrate.

(Markers = 1 μm)

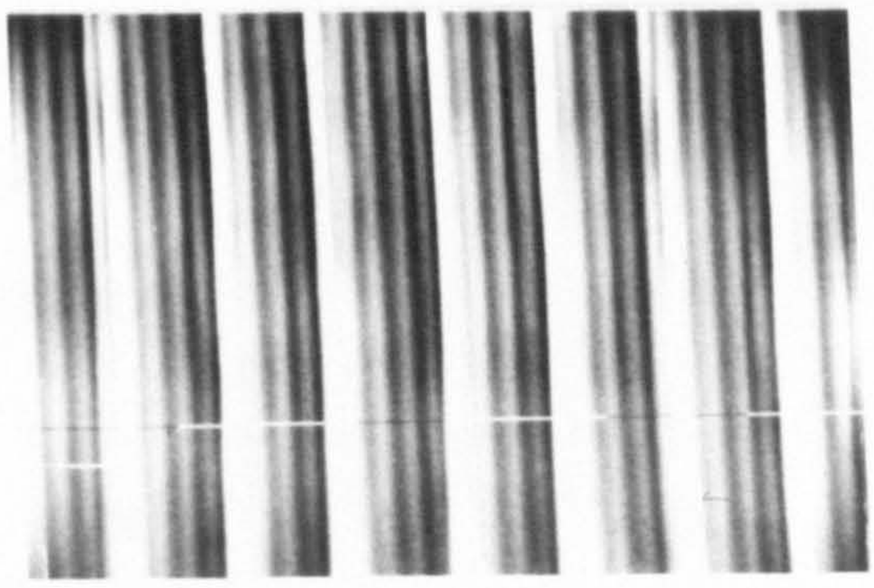

(c) FPT-ED-ed grating showing the effects of multiple beam reflections.

FIG 4.14 SEM Photographs of Experimental Gratings.

from the resist-substrate interface. At beam incident angles required to produce short period gratings, the effects of spurious modulations can be very strong. As an example we show in Fig.4.14(c) a SEM photograph of a grating produced under conditions of extremely high reflections using the front prism technique (see subsection 4.4.4). In this particular case the actual grating pattern has been swamped by the modulation. The sawtooth shape of the spurious modulation is genuine.

The practical limit in our experimental interferometer was Λ = 270 nm which corresponds to an angle of incidence $\theta = 58^{o}$.

4.4.3 Simultaneous Exposure and Development Technique

A cell was constructed with the purpose of applying the SED technique in the fabrication of gratings for etching. The cell was made from perspex material and had two quartz windows optically flat to $\lambda/20$ with faces parallel to 5' of arc (see Fig.4.15). Means were provided for rotating the specimen and moving it longitudinally inside the cell. For ease of translation along the axis of the interferometer the cell was fitted with small wheels and guided along a metallic rail. With a 45^{o} angle between the window and the main axis of the cell the grating periodicity is given by

$$\Lambda = \frac{\lambda}{2n_d \cos(45+\sin^{-1}(\sin\theta/n_d))} \qquad (4.3)$$

where n_d is the refractive index of the developer (n = 1.34 at 457.9 nm). AZ developer in a 1:1 solution with water was used in this case. Consistency in the development rate was checked by measuring the strength of the developer as a function of time. Resist developers are alkaline-based solutions and tend to absorb CO_2. The high pH value of developer (~13.9) restricted the use of normal pH meters. A titration analysis

Grating Period $\Lambda = \dfrac{\lambda}{2n_d \cos[\phi + \sin^{-1}(\sin\theta/n_d)]}$

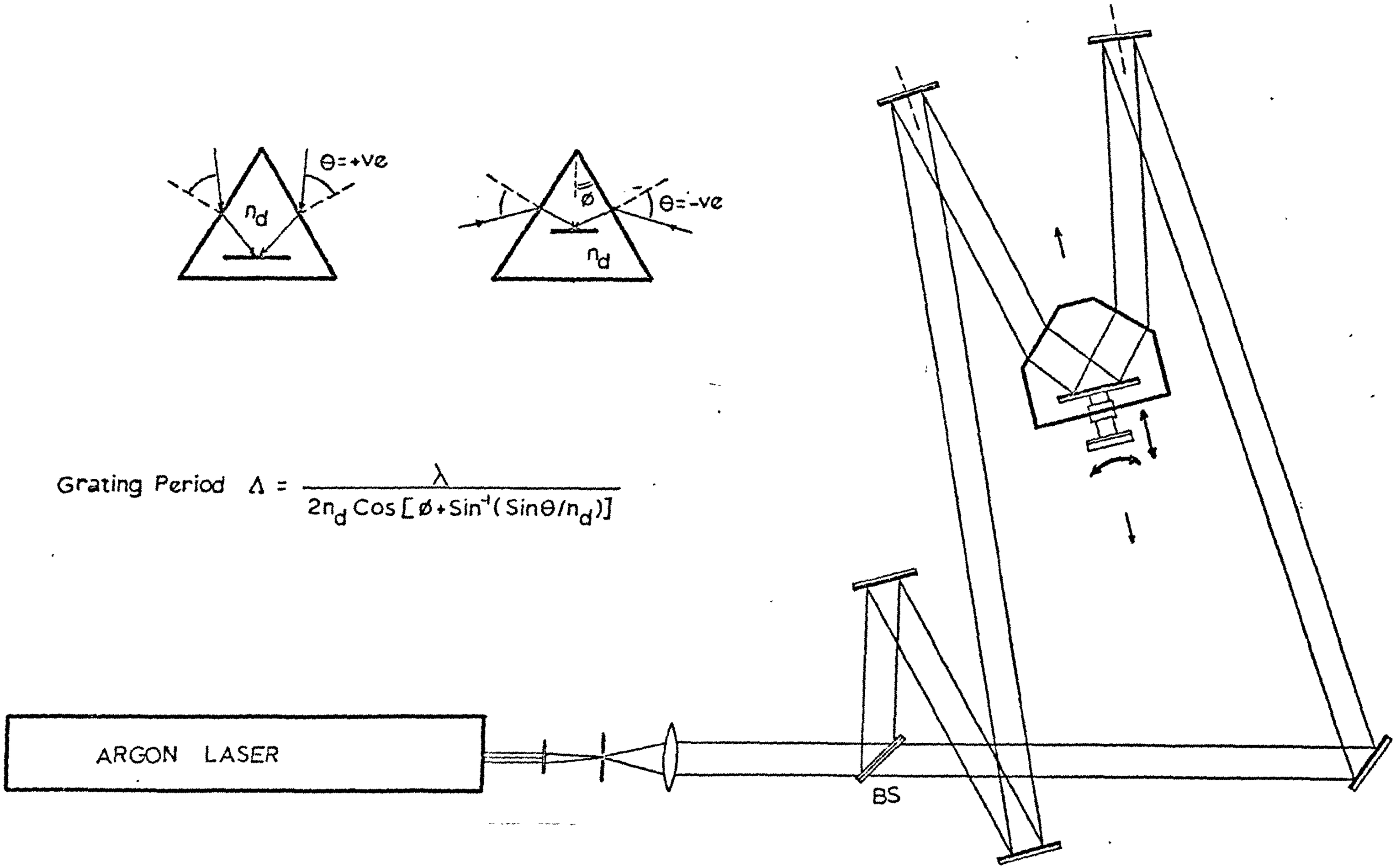

FIG 4.15 Simultaneous Exposure and Development (SED) Technique - Experimental Arrangement.

was used instead. Results from the tests showed a steady drop in normality of 0.02 per hour from an initial value of 0.52 for a concentrated solution exposed to ambient. No detectable change, however, was observed for a 1:1 diluted solution left in similar conditions.

Good quality gratings were successfully produced using the SED technique and in Fig.4.14(b) we show a SEM photograph of a typical grating whose grooves are cut down to the substrate. Fig.4.16(a) shows a two-dimensional grating fabricated on a chrome plate. The pattern was generated by a double exposure of the resist to the interference pattern of the beams. Both gratings have a period of 1000 nm and are orientated at 90^{o}. The result of subsequent chemical etch of the chrome and removal of the resist mask is shown in Fig.4.16(b).

The practical limit in periodicity using the present technique was Λ = 240 nm. The use of two auxiliary mirrors at opposite ends of the interferometer allowed for gratings with periods up to 4000 nm to be fabricated. Two sources of spurious periodicities are present when using the SED cell. One is caused by reflection from the quartz windows and the second one is caused by the stronger mismatch at the developer-substrate interface. In terms of the beam incident angle, the limit is given by $\theta \geq +2.0^{o}$.

The SED technique, within its limitations, proves to be a very useful method in the fabrication of gratings and especially in the case where grooves are required to be cut down to substrate. The elimination of standing wave effects results in a more faithful recording of the interference pattern. Repeatability of results is far superior to that of the ED technique and it is solely limited by the variations in thickness of the resist layers.

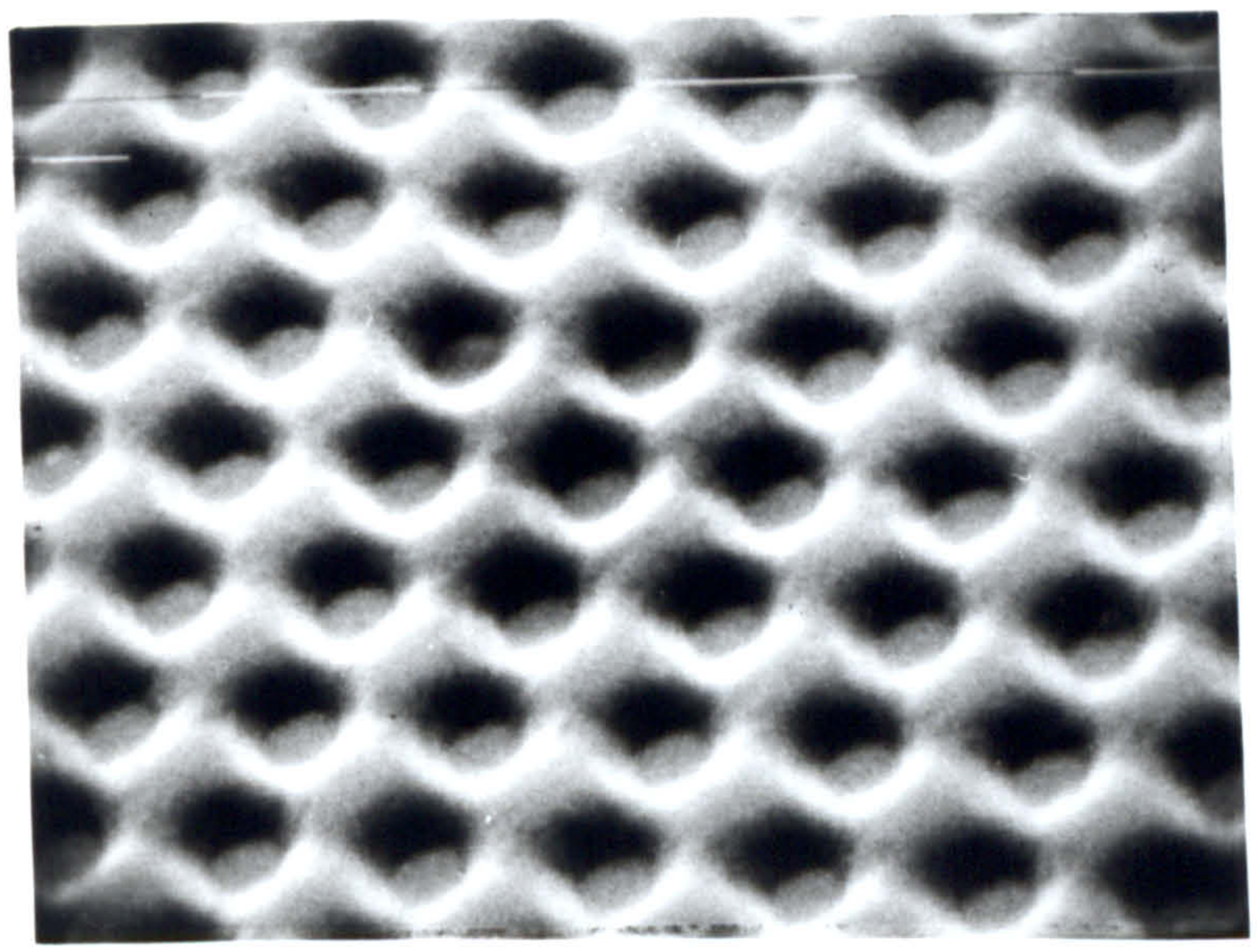

(a) Initial mask in photoresist (AZ 1350 J).

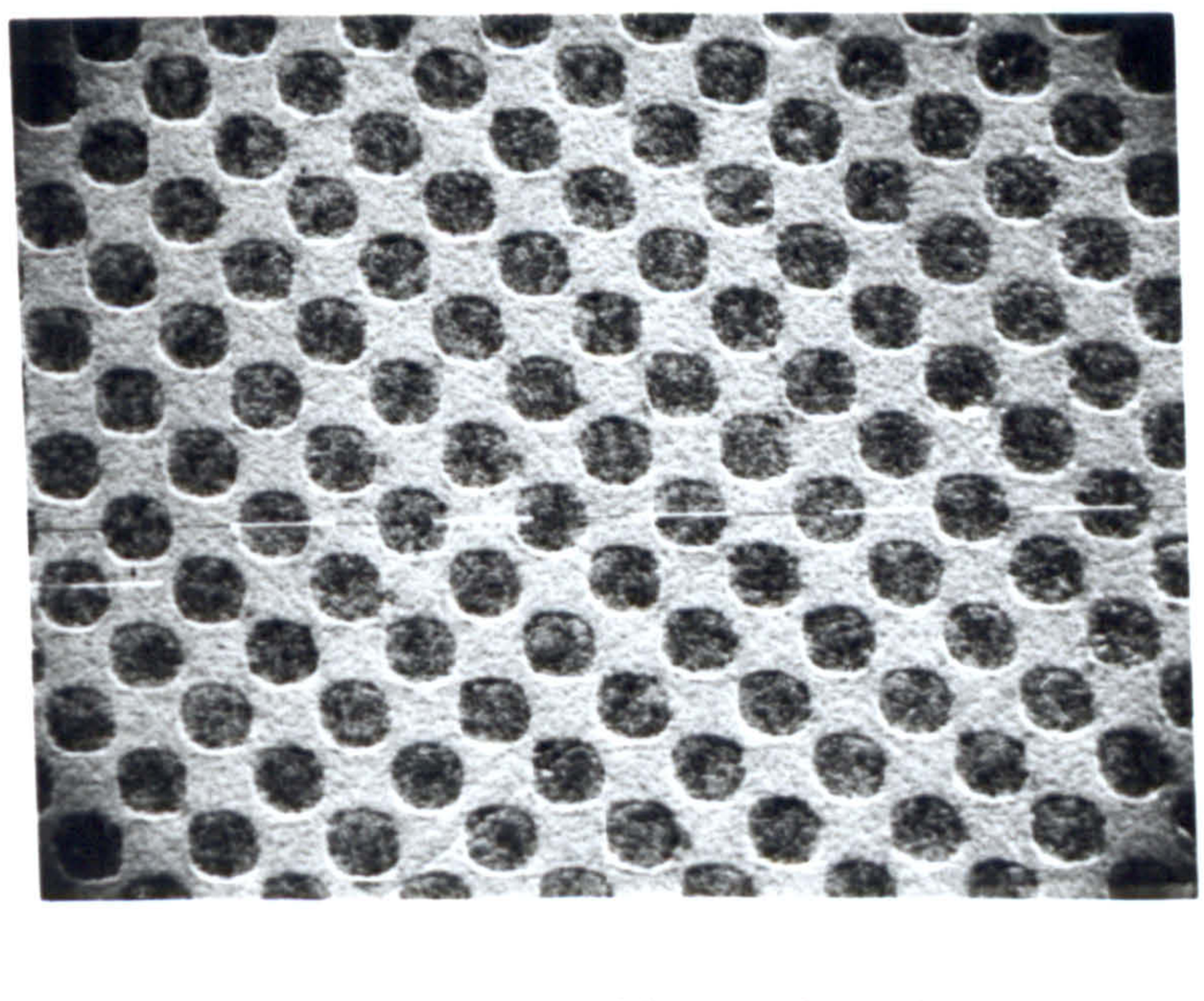

(b) Final etched pattern in chrome.

(Marker = 1 μm)

FIG 4.16 Results from Chemically Etching a Two-Dimensional SED-ed Photoresist Grating into a Thin Film of Chrome.

4.4.4 Holographic Short Period Gratings

Gratings with periodicities below the limit of $\lambda/2$ can be produced by reducing the laser wavelength. In an optically dense medium the free space wavelength is reduced by a factor equal to the refractive index of the medium. Dalgoutte[56] used this principle to develop a technique to fabricate short period gratings using the 476.5 nm line from an argon ion laser. The same technique was later reported by Shank et al[57]. The dense medium takes the form of a prism which is optically contacted to the resist film. This technique is referred to in this work as the front prism technique (FPT).

In general, the fabrication of short period gratings is difficult. The obvious alternative is to use shorter wavelengths, however, the choice of UV coherent sources is limited and the attenuation present in the optical components of the interferometer also introduces problems. We now give a brief description of three possible ways of producing gratings with periods $\Lambda \leq 200$ nm.

(i) HeCd UV Laser

A liconix Model 401 HeCd laser was used in this experiment. The laser was fitted with UV optics to operate at 325.0 nm. The beam was polarised in the vertical plane and the output mode was TEM_{00}. The total output power of 1 mW was measured with the Hilger Watts FT-4 thermopile and the coherence length was estimated to be 11 mm. Simple quartz lenses were used in the spatial filter and collimator stages. The collimated beam had an overall diameter of 7 mm and was amplitude divided by means of a special beam splitter. The effective width of the beam was measured to be 3 mm diameter. Due to low power density of the beam and the low response of the human eye to this wavelength a card with anthracene powder was used to aid detecting the position of

the beam. Using this laser in our basic interferometer, gratings were produced with a uniform area of 1 mm diameter. The practical limit was found at values of the periodicity of the order of ∿220 nm which corresponds to $\theta \tilde{=} 48^{o}$. The main problems in using this laser were the long exposure times required in the fabrication of gratings and the availability of suitable optical components. Working in the near UV presents difficulties with attenuation in normally available glass optical components. Only quartz and calcium fluorite have good transmission properties in the near UV. However, aplanatic lenses made entirely of these material are not available commercially. In these experiments we used uncorrected quartz lenses which introduced distortions in the wavefronts and allowed only a small useful area (cf. limit in θ for argon ion laser). The repeatability in the fabrication, on the other hand, was made more difficult by the moderately low power output and stability of the source. The laser is cooled by air convection and fluctuations of up to 15% were observed in the power output due to disturbance of the air in the surrounding medium. With a short coherence length, in this case comparable to the maximum optical path difference in the interferometer, serious variations of the fringe visibility were obtained after adjustment of the mirrors. Our results suggest that the method is plausible if higher power lasers are used in conjunction with specially made optics.

(ii) <u>High Index Liquid Media</u>

The principle of wavelength reduction was clearly demonstrated in the case of the SED process. The ratio of the periodicities of the ED and SED gratings formed at the same effective interfering angles equals the refractive index of the developer. In the following experiment the SED cell was used to contain the high index fluids. Organic clear liquids with an index of refraction of ∿1.5 were used.

The production of short period gratings was not particularly successful by this method. Several organic liquids were tested, among them di-n-butyl pthalate, Xylene, methyl salycilate and di-n-butanediol. The liquids were first checked for chemical reaction with resist. The results of these tests excluded the use of methyl salycilate. The remaining liquids were then individually loaded into the cell and attempts at grating fabrication were tried. Failure of the process was caused by chemical reaction of the liquids with the components of the cell (perspex and resin epoxy). The by-products of the chemical reaction deposited in the form of thin films on the windows with the results that severe deformation of the wavefronts prevented the formation of the desired interference pattern. The use of one particular liquid, however, proved successful. Carbon tetrachloride ($n = 1.47$ at 457.9 nm) allowed uniform gratings with $\Lambda \geq 200$ nm to be fabricated. The periodicity corresponds to $\theta = -9^{\circ}$. Improved matching at the substrate-liquid interface in this case allowed the use of a negative θ. Because of the hazardous effects of CCl_4 this method of producing short period gratings was abandoned.

The unfortunate use of perspex material for the cell rendered our experiments unsuccessful. The method, however, could be potentially useful if different materials are used for the construction of the cell.

(iii) Front Prism Techniques

Details of the experimental arrangement for the FPT technique are given in Fig.4.17. Three different prisms were used in this investigation and they were made from fused quartz ($n = 1.471$), Schott SF15 ($n = 1.721$) and Schott SF59 ($n = 2.001$) glasses. Their nominal internal angles were 45°-90°-45° with a height of 25 mm and short faces of 25 mm length. Optical flatness of the faces were compared against a standard type A optical flat. Fringes indicated uniformity

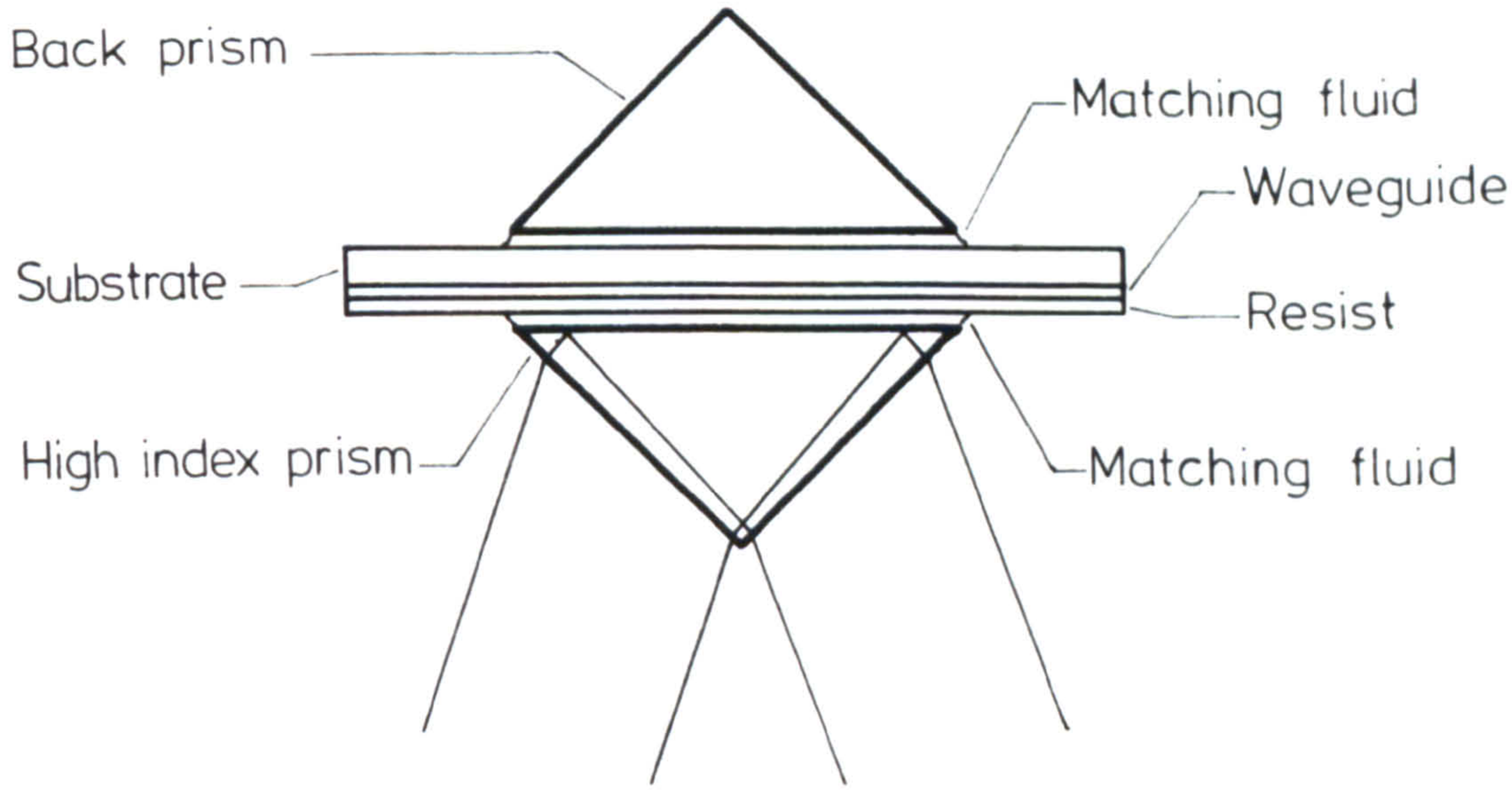

FIG 4.17 Details on Front Prism Technique (FPT) for the Production of Very Short Period Gratings.

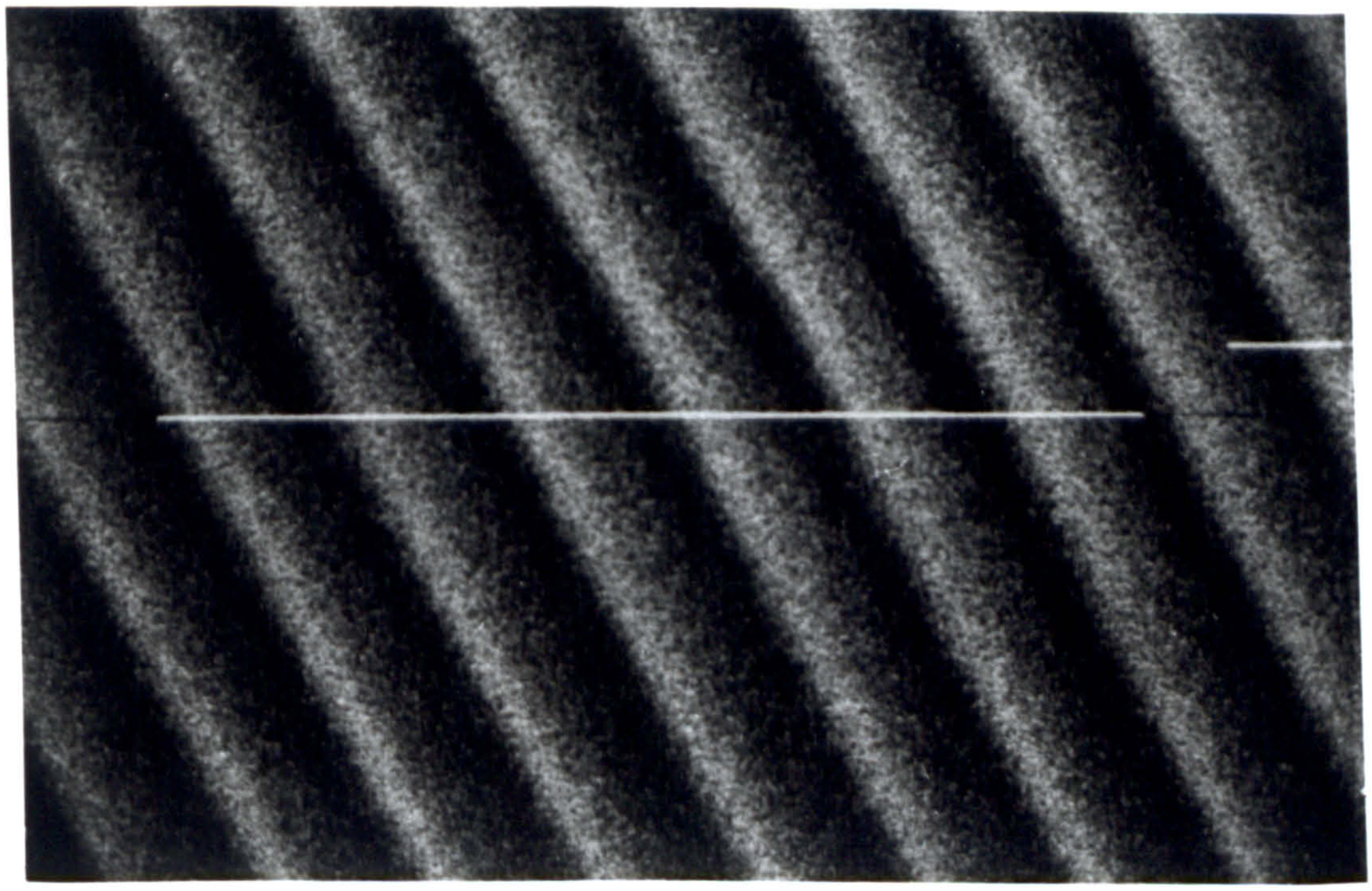

Marker = 1 μm

FIG 4.18 SEM Photograph of Shortest Period FPT Grating Produced in This Work. ($\lambda = 457.9$ nm)

of $\lambda/10$ over a centre area of 10 mm diameter. Exposures were made at the argon 457.9 nm laser line. Successful fabrication of short period gratings suitable for Bragg waveguide filters were obtained using SF15 glass prism. CCl_4 was used to optically contact the prism to the resist film and the practical limit in the periodicity for this arrangement was 189.0 nm. Moderate success was obtained using the quartz prism. Because of its lower value of refractive index the practical limit in Λ was 217.0 nm. For grating periods below this limit the effective angle of incidence in the CCl_4 was too large to maintain wavefront quality. With the Schott SF59 prism the optical mismatch at the prism-liquid interface introduced strong modulations at very short values of the periodicity. In this particular case Xylene was used as the matching fluid with an n = 1.520. The shortest periodicity obtained with this prism was 166.0 nm with a moderately weak modulation in the grating amplitude. Fig.4.18 shows a SEM photograph of such grating. The strong effects of spurious modulations using this prism was shown previously in Fig.4.14(c).

The implementation of the FPT technique requires careful selection of the prism glasses. For low index glass prisms the technique could be limited by total internal reflection at the prism-liquid interface. For high index glasses, on the other hand, the general problem is to find a suitable matching fluid. In our investigation we found that both CCl_4 and Xylene react with resist films at a very slow rate. The products of the chemical reaction normally formed films on the surface of the prisms.

Our investigation suggests that the use of SF15 glass prism is feasible for the fabrication of gratings with periods down to 189.0 nm. The use of a higher index matching fluid (n = 1.67) would be desirable in order to reduce the modulation effects on the grating amplitudes.

Careful alignment of the beams at the front face of the prism is required to make best use of the total useful area of the beam.

4.4.5 Experimental Gratings for Bragg Waveguide Filters

From all three different ways contemplated in the above investigations, the ED-FPT techniques proves best suited for our experiments. The use of AZ1370 resist calls for special considerations. The magnitude of the period of the standing wave pattern seriously affects the exposure parameters. For a typical waveguide filter the required period of the grating lies between 190.0 nm and 200.0 nm. Taking the average case of 195.0 nm, the corresponding effective angle of incidence of the beams in CCl_4 (n = 1.47) is 53^{o}. Using equation (4.2) the first node is located at 105.5 nm. The variation in film thickness was found to be 25% around the mean value of 100.0 nm. The surface of the resist film, therefore, lies on a very crucial position on the amplitude of the modulation pattern. In the fabrication of gratings, resist coated microscope slides were first tested to determine the process parameters. With AZ1370 resist variations of up to 40% in the exposure time was found for different samples. Smaller variations were found for the case of AZ1350J. Resist coated waveguides were then exposed for a fixed average period. During development, under-exposed films were normally immersed for longer periods of time. Since the sensitivity of resists to the HeCd 325.0 nm radiation is high, it was not possible to use the Beesley et al[44] technique to measure the grating depth during development. Consequently, it was not possible to make the grating depth the same for all samples. The development process was controlled by visual inspection of the grating area, the process being stopped when the appearance of the grating indicated the existence of a very thin layer of resist. Samples were subsequently rinsed with filtered water circulating in a 2 l beaker. The water flow

was kept low to avoid damaging the pattern. After rinsing, samples were left to dry in atmosphere. The effects of high water flow rates during the rinsing stage or the use of compressed gas to dry the samples are shown in Fig.4.19(a). Attempts to improve linearity by using pre- or post-exposure treatment with a mercury lamp were not successful. The method works well with relatively thick layer of resist; however, for the thin films it produced patchy gratings (see Fig.4.19(b)).

During the alignment procedures in the interferometer, the beam was masked with a vertical straight edge blocking half the beam and placed immediately after the collimator. To make best use of the effective beam area, the overlapping of the interfering beams was monitored at the front face of the prism. The uniformity and size of the useful area of the experimental gratings were affected to a certain extent by the chemical film produced by the CCl_4-resist reaction. This film on the front surface of the prism was removed using acetone and a lens tissue. Frequent cleaning was found necessary but this led to the deterioration of the optical finish of the prism faces. The optical mismatch at the prism-liquid interface introduced a modulation on the grating amplitude of the order of 20% on the main pattern for a typical grating with 195.0 nm period. Developed gratings were subsequently masked off using photographic emulsion mask and a mercury lamp. The exposure time for this process varied according to the temperature of the lamp. The variations in exposure were in general, compensated during the development stage. Rinsing and drying were carried out as in the previous case.

4.5 Ion Beam Etching

Micro engraving of submicron patterns can be successfully achieved by the technique of ion beam etching. The process consists in bombarding the surface of the samples by ions accelerated by a dc

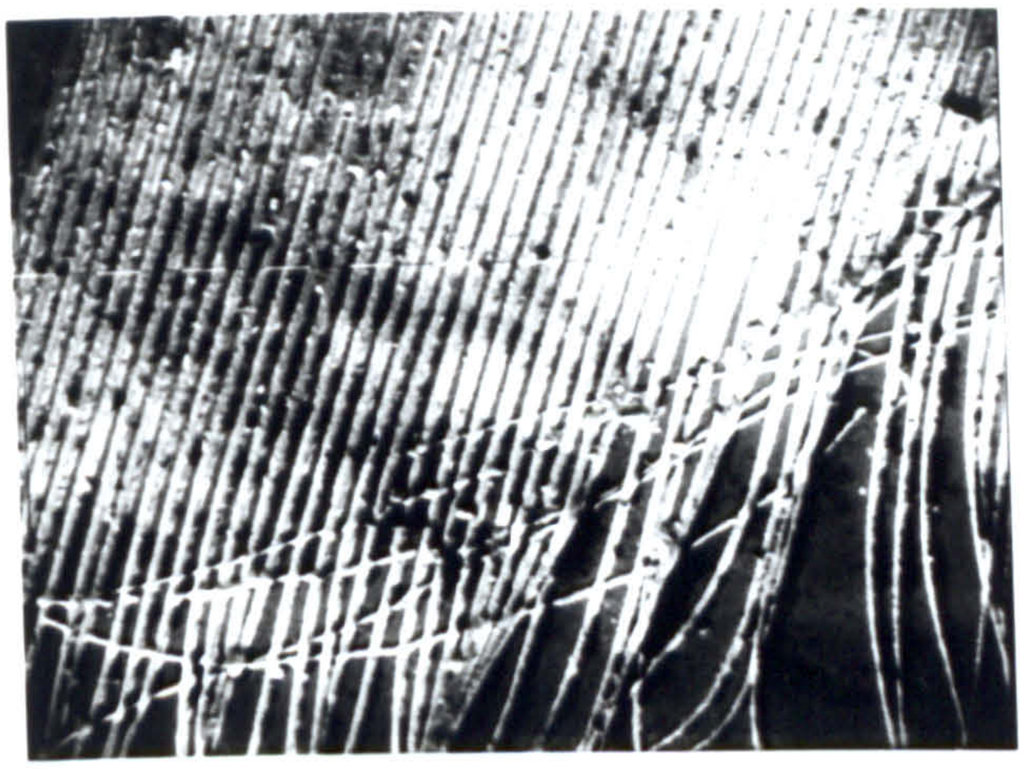

(a) Blow-drying after rinsing with water.

(b) Pre- or post-exposure on a 200nm-thick film of photoresist.

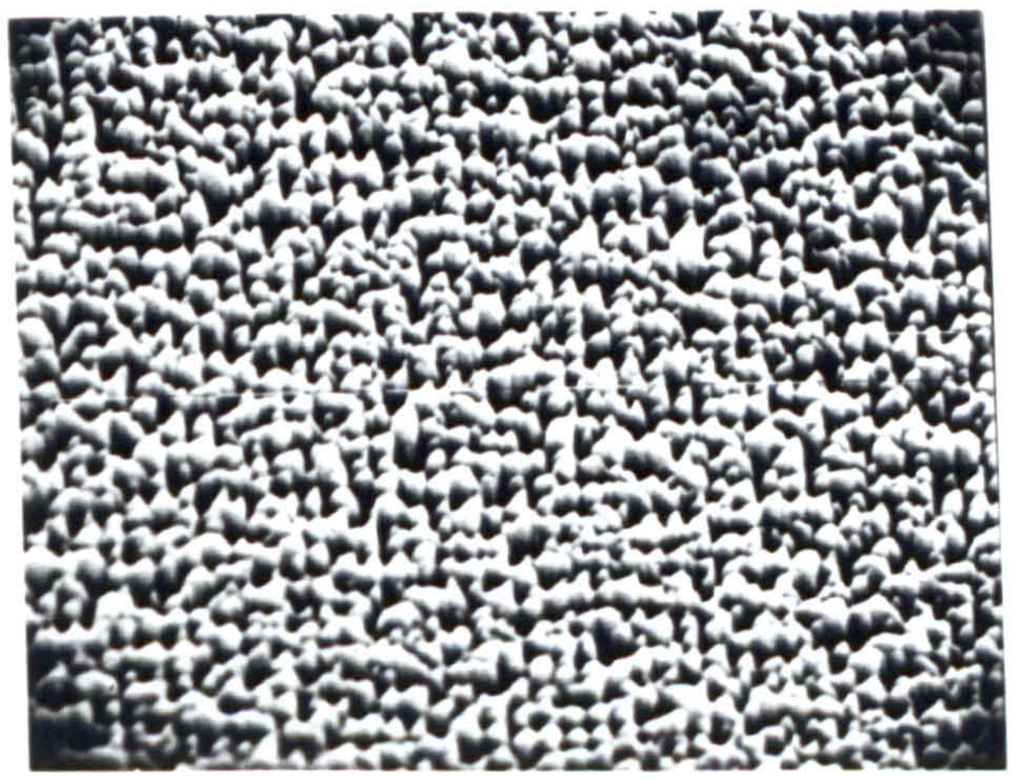

(c) Inadequate-resolution ion beam etching.

FIG 4.19 SEM Photographs Showing Some of the Problems Encountered During the Fabrication of Holographic Diffraction Gratings. (Markers = 1 μm).

potential. Ion beam etching offers the advantages of improved resolution and no undercutting of mask patterns when compared to chemical etching processes. In practice, patterns are delineated on the substrate or device; depending on the fabrication process the mask pattern can be made of metal or resist. The relative etch ratio of mask-substrate materials depends, primarily, on the beam current density, the accelerating potential and the angle of incidence of the beam on to the surface of the samples. Etch ratios can, in certain cases, be altered by changing the mask material and the gas used in the chamber. Successful pattern transfers by ion beam etching have been reported by many workers including, notably, Garvin et al[124]. The mechanisms affecting the linearity of the process have recently been reported by Cantagrel[125]. The effects of gas composition on the etch rates were also reported by Cantagrel et al[126,127]. Preferential etched gratings on GaAs substrates were reported by Somekh et al[128].

In this section we present the limitations encountered in the equipment available for this work, and also, the subsequent modifications introduced to improve its performance with an aim to etching short period gratings.

4.5.1 Experimental Equipment

We used a GV Planer Model IB7 ion beam etching equipment in this investigation. Details of the chamber are shown schematically in Fig.4.20. The filament and specimen holder are water cooled to prevent thermal damage to the parts. The filament consists of a tungsten wound wire coated with lanthanum hexaboride. The 10 cm diameter specimen holder plate (turret) is mechanically coupled to an electric motor rotating at 1 RPM. Samples are contacted to the plate by means of a high thermal conductivity paint which was made up from a mixture of 16% Indium and 84% Gallium by weight. The power supplies comprise

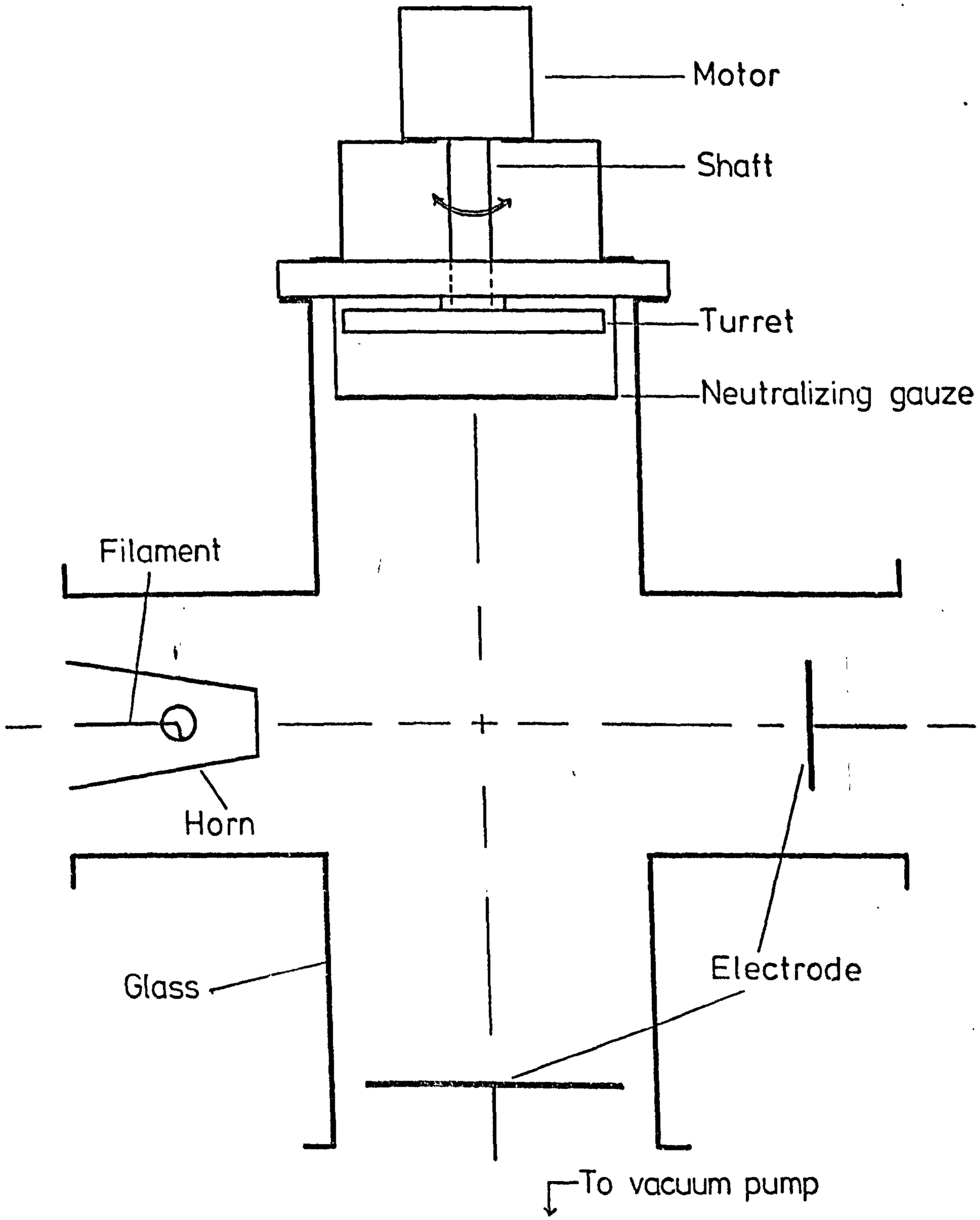

FIG 4.20 Schematic Diagram of Ion Beam Etch Chamber.

essentially three power modules. Low tension supply for the filament was rated at 16 V, 25 A, 50 Hz and fully insulated to 15 kV dc. High tension supply for the acceleration of the ion beam was variable from 0 to 7 kV and rated at 1.4 kW. Power supply for the generation of the ion plasma was variable from 0 to 50 V, 5 A dc. A700 V peak-peak plasma initiation supply was also incorporated in the unit.

During operation we used 4μm pressure of pure argon gas in the chamber. On starting, the accelerating dc potential was built up at a rate of 0.5 kV/min in order to avoid arcing effects inside the chamber. The uniformity of the ion beam was investigated by etching 5μm wide resist lines. The samples were aligned along the diameter of the turret and several runs were carried out at different settings of beam currents and dc potentials. The results from these tests showed bell-shaped curves for the etch ratio along the diameter of the turret. Reasonable uniformity was found in regions around the periphery of the turret when the beam current was set at the minimum value of 200μA/cm^2. For glass substrates a minimum potential of 5 kV was required. The effects of higher current densities were predominantly in overheating and distorting of the mask patterns. Experiments on the post-baking of resist patterns were run concurrently with these tests; pattern specimens used here were not post-baked. Resolution tests were next carried out at a 5 kV potential and minimum beam current density. Unbaked resist gratings with periodicities ranging from 700 nm to 300 nm were used in this investigation. Samples were positioned along the periphery of the turret and etched for periods of 30 minutes. Etched gratings were inspected under the SEM after removal of the residual resist from the glass surface by plasma ashing. The samples showed distortion of the grating lines and poor uniformity arising from spurious ring-like patterns. Tests to evaluate the evolution of the masks during

etching revealed a high degree of flow and considerable amount of pitting of the masks. Moderately good results were obtained only in cases where the grating grooves were cut down to the substrate. To improve the quality of the gratings we changed the angle of beam incidence on the samples[129]. For this, stainless steel wedges with tilt angles of 60°, 70° and 80° were positioned on the turret. The bases of the wedges were mechanically grounded to improve thermal contact with the surface of the turret. Samples were contacted onto the slanted faces of the wedges with the grating lines parallel with the ion beam. The angle between the surface of the samples and the beam was given by $90 - \theta$ where θ is the wedge tilt angle. This arrangement increased, in general, the resist-glass etch ratio and substantial improvement was obtained in the line quality. The overall uniformity remained poor but the condition of 'cut down to substrate' was greatly relaxed with a consequent increase of the success rate. Subsequent tests on gratings with $\Lambda \leq 400$ nm gave unsatisfactory results. Etched samples exhibited considerable deformation even in cases where grooves were clear of resist material (see Fig.4.19(c)). The most likely cause for failure in these cases was attributed to deviations of the ion beam whose magnitudes were comparable to the periodicity of the gratings.

4.5.2 Modifications on the Equipment

The ion beam etching equipment suffers from several design problems. The long separation between the ion source and samples far exceeds the mean free path of the ions at the recommended operating gas pressure of 4μm. Moreover, there is no provision for collimating grids to improve the uniformity of the beam. The construction of the chamber and design of the power supplies do not allow for major alterations to be introduced in the unit. Numerous tests using resist gratings were carried out to isolate each problem area and to introduce, where possible, the

relevant modifications in order to improve the performance of the etcher. Results from these tests revealed that the ring-like patterns appearing on the etched gratings were introduced by the thermal distortion of the neutralising gauze. Good uniformity and total absence of spurious patterns were obtained in the gratings when the gauze (woven wire type) was replaced by an extruded wire type grid. Resolution was steadily improved in two separate steps. First, the source-sample distance was reduced by replacing the existing wedges on the turret by steel blocks having an area of 75 mm x 25 mm and a height of 30 mm. Second, the mean free path of the ions was increased by lowering the gas pressure from 4μm to 2μm. Operating the etcher at 5 kV and 200μA/cm^2, plasma stability was acceptable and the resolution required to etch gratings with Λ = 190 nm was achieved. The success rate in obtaining etched gratings depended strongly on the magnitude of the resist layer thickness underneath the grating structure. For this reason the use of AZ1370 resist was preferred because of the smaller thickness attainable during the spin coating of samples. For a typical grating filter a process time of 12 to 14 minutes was required. Some degree of post-bake was observed in the u.hardened resist grating during the first 10 minutes of the process,where the accelerating voltage is built up at a rate of 0.5 kV/min. No apparent etch takes place during the build up time,as a minimum of 5 kV potential is required to etch glass. However, the temperature in the turret reaches high enough levels to provide small flows in the resist grating masks. Careful examination of the evolution of the mask during the build up time showed that the thermal flow had the beneficial effect of improving the shape of the grating corrugation to a more sinusoidal form (see Fig.4.21(a) and Fig.4.21(b)). This fortuitous effect removed the need to vacuum post-bake the resist gratings before loading them into the etcher. Experimental filters were,

(a) t = 0 min. Initial unbaked photo-resist grating mask (AZ 1370)

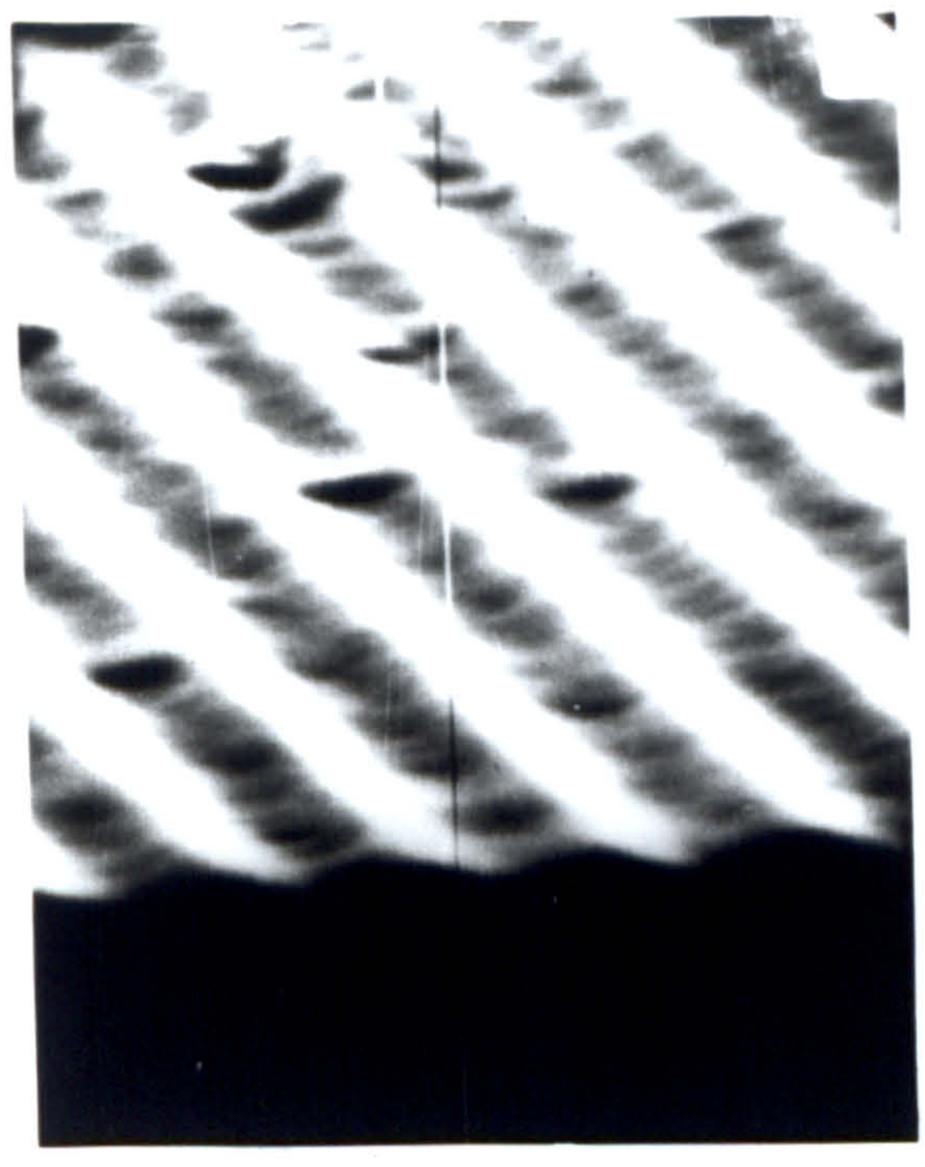

(b) t ≃ 10 min. Effects of high temperatures during build up time of accelerating potential. (No etching)

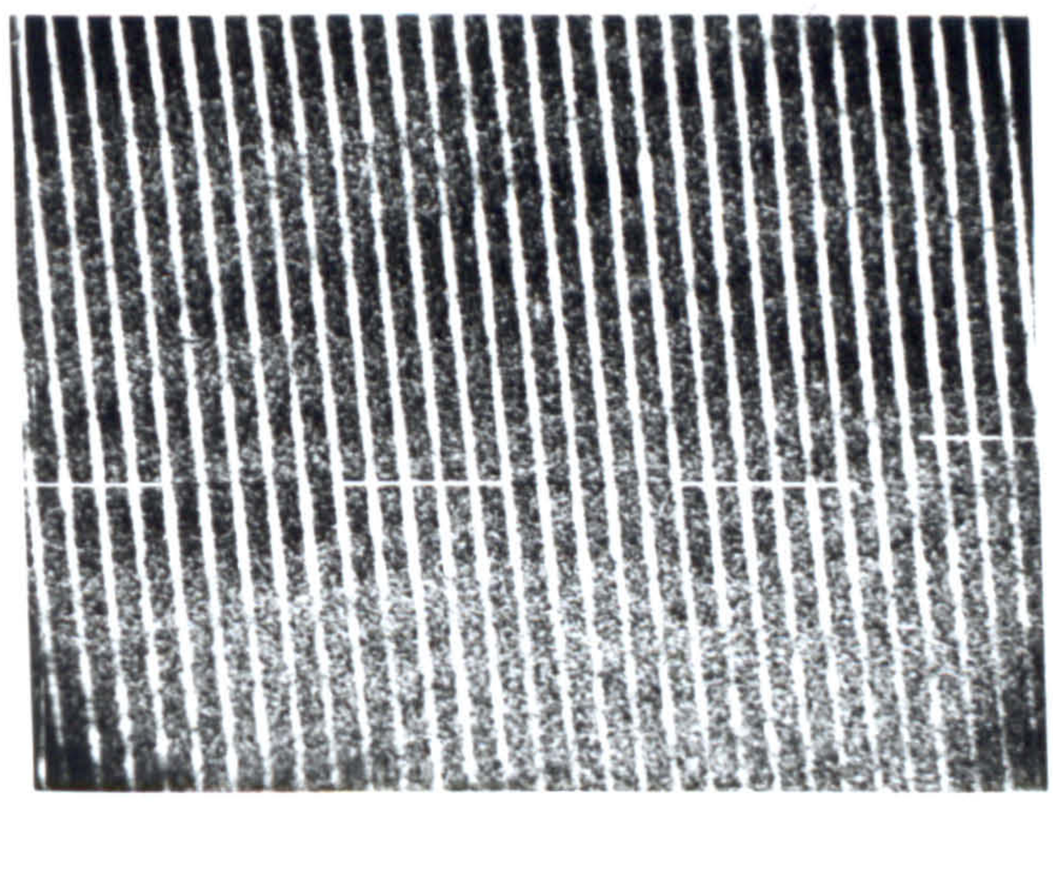

(c) Final etched grating in sputtered 7059 glass.

FIG 4.21 Pattern Evolution During Ion Beam Etching.

therefore, realised using unbaked resist grating masks and in Fig.4.21(c) we show a SEM photograph of a typical grating etched on sputtered Corning 7059 glass. The absolute etch rate of the waveguide glass was measured to be 12 nm/min and the resist-glass etch ratio was of the order of 4.0

The empirical modifications introduced in the system improved the resolution for our particular applications. Ideally the use of wedges should further improve the grating quality; however, the implementation of such wedges in this particular system calls for major alterations to the chamber and turret assembly.

4.5.3 Etched Gratings on Ion Exchanged Waveguides

High surface temperatures brought about by the ion beam etching process introduce drastic changes in the composition of the silver in these guides. Extremely high temperatures cause the silver ions to reduce and aggregate in coloidal form. In our experiments we found that the waveguides became either lossy or lost their guiding properties depending on the length of the etch period. Spectrophotometric analysis of the etched samples showed considerable variations on the position of the absorption gaps along the axis of optical frequencies in the UV for various magnitudes of the etch periods. We have not made further analysis to give a quantitative account of the degree of change undergone by the silver ions. However, it has been shown[130] that the position and size of the various absorption gaps can be directly correlated to the size of the colloidal silver. The latter, in turn, can be used to assess the surface temperature reached during the etch process. The existence of silver in the colloidal form was corroborated by a comparison with the spectrophotometric response obtained from similar guides which were not subject to the ion beam etch process. The absence of absorption gaps in the untreated guides and the physical coloration of

the etched samples are definite evidence for this assertion.

Because ion beam etching of ion exchange waveguides is not possible, gratings were formed on the surface of an untreated glass sample first and then subjected to ion exchange. This process was sometimes successful but the yield was low. The removal of residual material left behind by the resist mask was found to be extremely difficult. Most samples were thoroughly cleaned before immersion in the $AgNO_3$ melt; however, due to some chemical reaction between the melt and the residual material on the glass the exchange process was halted and the melt was invariably contaminated. The glass samples were covered by a film which had a brown appearance around the problem areas. The production of these devices calls for a detailed analysis of the chemical contents of the mask residual material and their reaction with molten silver nitrate.

4.6 Grating Modelling

Filter response can be tailored by properly shaping the geometry of the grating structure (see Chapter III).

In this section we present the limitations and results of attempts to change the geometry of gratings. The experiments are restricted to the photolithographic aspects only.

4.6.1 Singly Tapered Gratings

Amplitude tapered gratings with Λ = 1000 nm were produced on 400 nm thick resist films. A specially made density filter was used to obtain the desired intensity attenuation of the wavefront of one of the interfering beams. The density filter consisted of a 25 mm diameter quartz optical flat onto which a film of nichrome alloy had been deposited. The nichrone film covered one half of the area of the quartz substrate. A sharp razor blade was used as the shadowing element during the vacuum

deposition of the metal. The blade was positioned in the path between the substrate and the evaporation source. For improved uniformity of film thickness an electron beam gun was used to evaporate the alloy. The resulting nichrome film had a sharp edge and the density of the metal increased in a linear fashion towards the unmasked portion of the substrate. The optical profile for a typical taper obtained from multiple beam interferometry is shown in Fig.4.5(b). The length of the taper as a function of the substrate-blade separation is shown in Fig.4.22. The variation in groove depth of the resulting gratings was calculated from diffraction efficiency measurements. Fig.4.23 shows a comparison of the transmission characteristics of the filter and the variation in groove depth of the resulting grating. The actual geometry of the gratings produced with this process is shown schematically in Fig.4.24(a). The structure is not particularly useful because of the underlay film of resist in the structure which makes it difficult to ion beam etch. Ideally the structure should have the form shown in Fig.4.24(b). Using positive resist, a subsequent exposure is needed in order to convert the structure in Fig.4.24(a) into that given in Fig.4.24(b). This process is difficult as it is necessary to precisely align the density filter (used in the complementary transmission mode) with the grating area in consideration.

4.6.2 Doubly-Tapered Gratings

A second technique was designed to change the grating depth as a function of distance. This method relied on the cancellation of the nonlinear response of the resist by a nonlinear distribution of exposure radiation at the post-exposure treatment. Gratings were produced with grooves cut down to the substrate and were subsequently post-exposed using a mercury lamp and a density filter with a parabolic transmission distribution. The masks were made on photographic emulsion and tapers

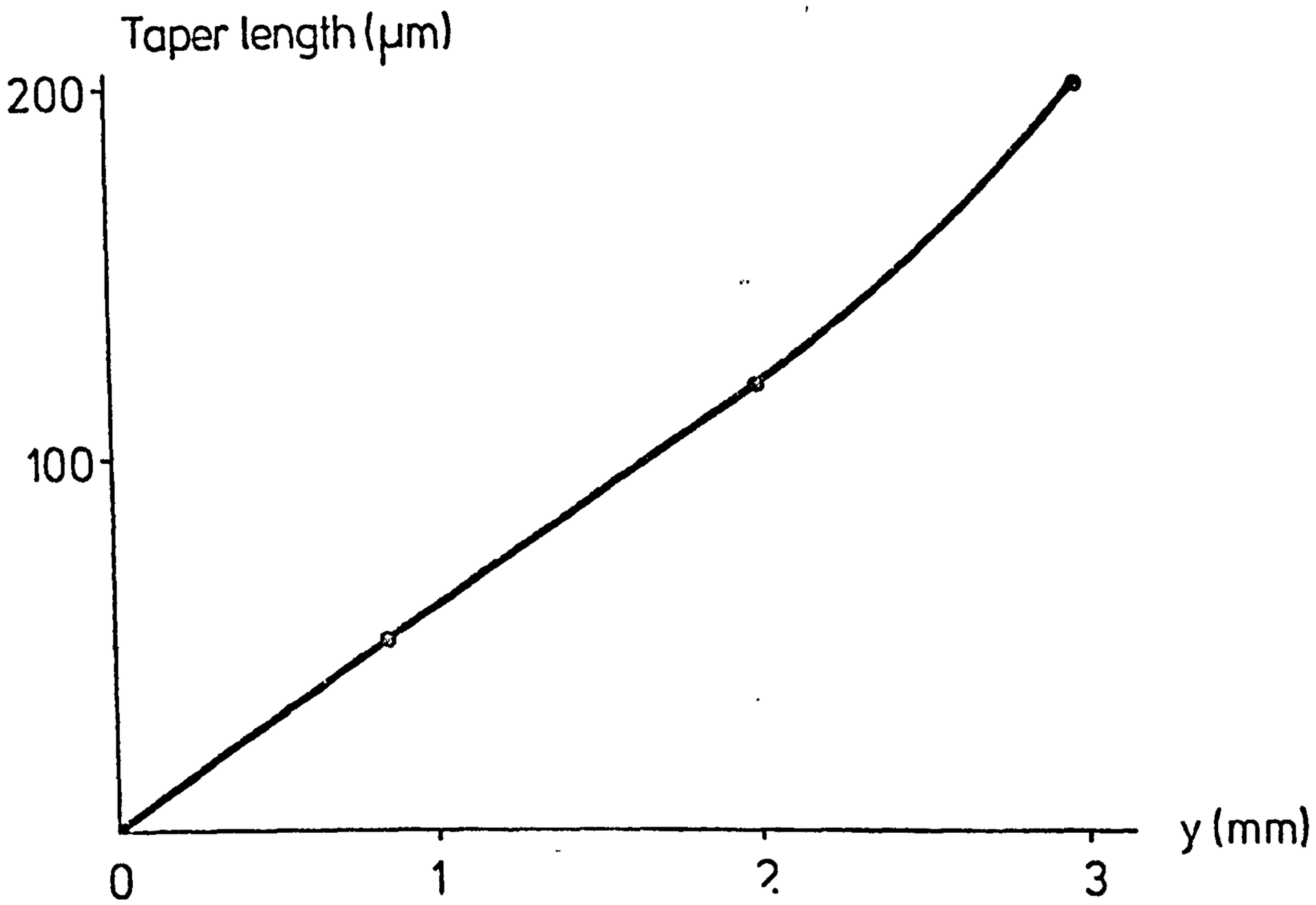

FIG 4.22 Taper Length of Evaporated Nichrome Film Density Filters as Function of Blade-Substrate Distance. (Source: Electron Beam Gun).

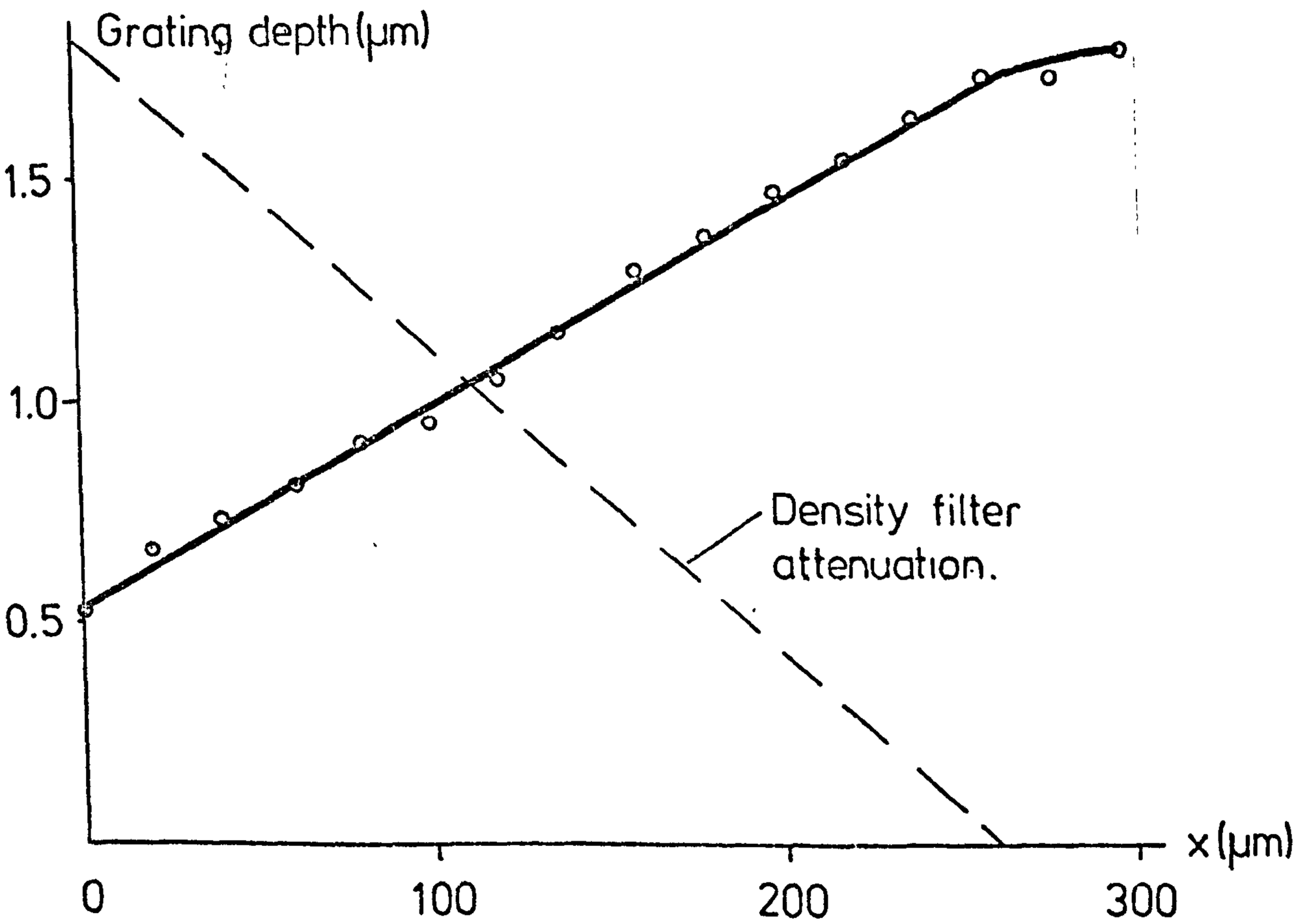

FIG 4.23 Results from Diffraction Efficiency Measurements on a 400nm Period Singly-Tapered Grating.

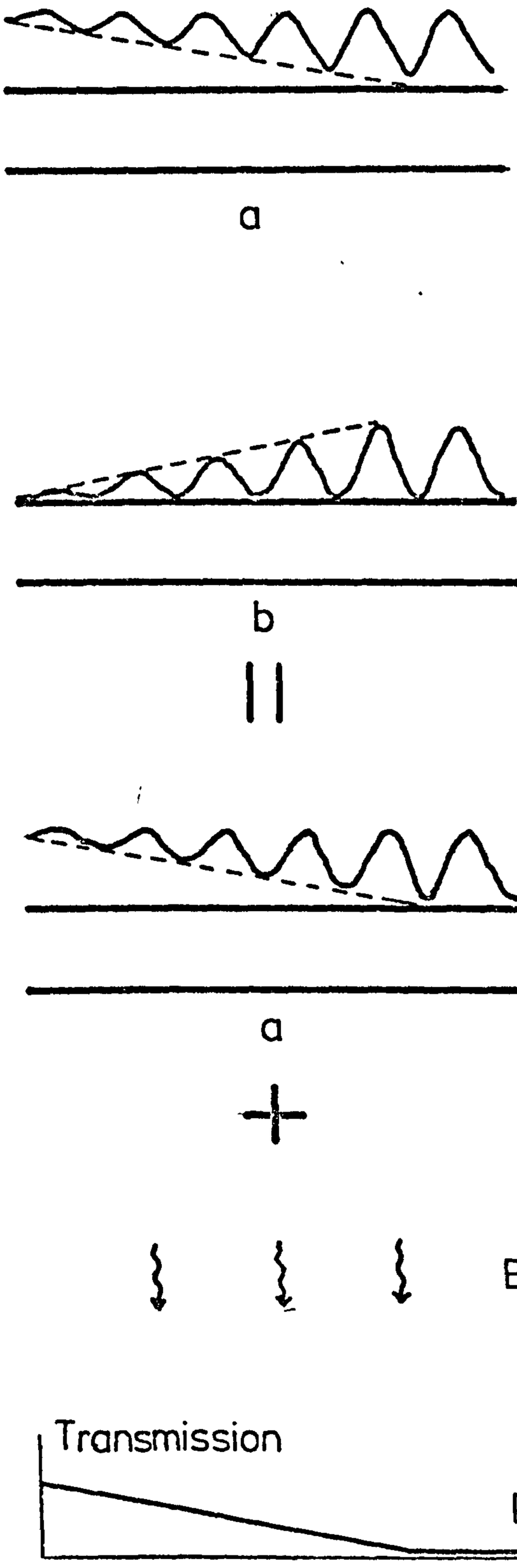

FIG 4.24 Tapered Gratings in Positive Resist Films

at both ends of the pattern were obtained by photographing the image of a rectangle using a slightly defocussed lens*. The transmission characteristics of the density filters can be tailored from a rectangular to a parabolic shape by varying the degree of defocussing of the lens. The problems associated with pre- or post-exposure was discussed earlier and gratings produced with this method had a patchy appearance which precluded the accurate measurement of the diffraction efficiencies. The method, however, can be used potentially with thicker layer of resist; that being the case, the SED technique could be implemented to obtain better groove quality and during the ion beam etching process wedges could be used to control the resist-glass etch ratio. For the work in filters, however, the limitations in the grating periodicity using the SED technique precludes the use of this method to produce symmetrically tapered gratings.

4.6.3 Abrupt Phase Change in Periodicity

An attempt was made to introduce a symmetrical π shift in the wavefront of one of the interfering beams during the fabrication of gratings. For this experiment we used a dielectric slit consisting of two dielectric half planes with an optical thickness of half a wavelength. The mask was made by spin coating an optical flat with photoresist; the slit window was obtained by a photomasking process. Gratings were formed with the mask positioned in the path of one of the interfering beams and close to the position of the samples. Subsequent analysis of the grating under the SEM showed strong modulation arising from the far field diffraction pattern but no clear evidence was observed of changes in the grating periodicity.

---

* Masks produced by G. Boyle

The analysis of the diffraction pattern of the dielectric half plane is difficult. Recently, Anderson[131] reported a rigorous analysis on the problem, the theory being valid for dielectric half planes with a maximum thickness of $\lambda/16$. In our work we have used the formalism of Anderson to calculate the diffraction pattern of the dielectric slit. Results from these calculations for our specific problem are shown in Fig.4.25. From the graphs it can be observed that the phase of the far field pattern has a periodic change which is proportional to the slit width in terms of the wavelength of the incident radiation. The phase change translates into a periodic chirp in the grating periodicity. The grating depth, on the other hand, is modulated by the number of lobes in the diffraction pattern; the number of lobes also being proportional to the slit width in terms of wavelength. The angular spread of the far field diffraction pattern and wavefront deformations due to the presence of too many optical elements in the path of the interfering beam made the realisation of filters with this type of gratings difficult. The basic relationships used to calculate the far field diffraction pattern of the dielectric slit is given in Appendix 4A.

4.7 Measurements of Device Parameters

A brief description of the several techniques used in the measurement of the optical constants and geometry of the devices is given in this section as well as the accuracy of each technique related to the equipment used in this work.

4.7.1 Refractive Index Measurements

A Bellingham & Stanley Type 60/ED Abbe refractometer was used in the measurement of refractive indices of bulk solid and liquid samples. The instrument is calibrated at the Sodium D line and the accuracy is ± 0.00005. At other wavelengths correction factors are applied to account

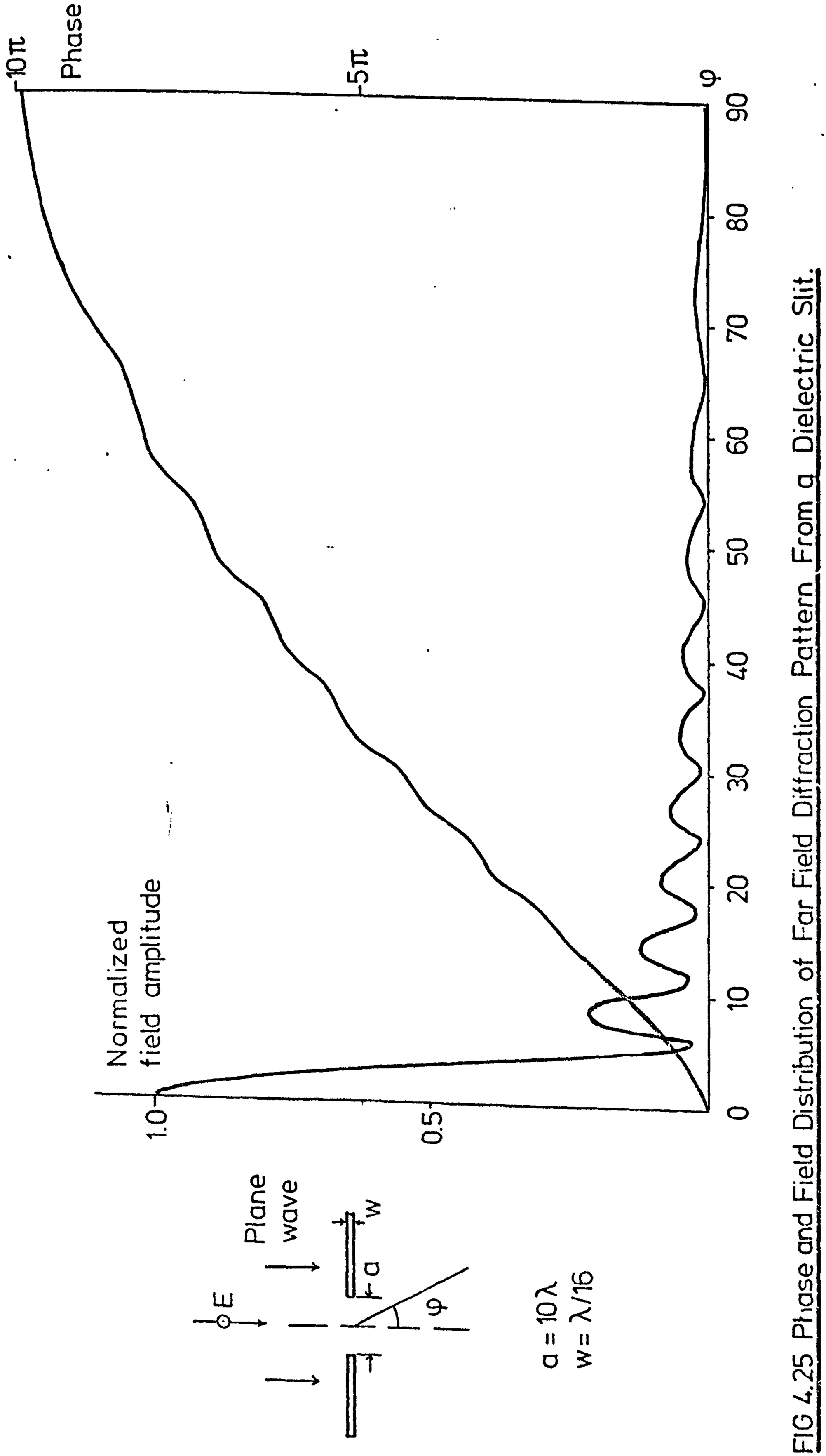

FIG 4.25 Phase and Field Distribution of Far Field Diffraction Pattern From a Dielectric Slit.

for the dispersion in the Amici prisms and the corresponding accuracy in the index values is ±0.0001.

The index of thin films were measured by two different techniques. For high index films on low index substrates the mode angle measurement technique was used. For low index films which can not act as waveguides and, also, for index measurements at the HeCd 325.0 nm laser line the Abeles method (132) was used instead. The mode angle measurement technique using the prism coupler offers a high degree of accuracy in the determination of the film indices especially in cases of highly multimode waveguides. Care must be taken to comply with the condition of weak coupling to avoid distorting the guide at the coupling point. For extremely lossy films,such as resists, the technique loses its accuracy because of the angular spread of the values for the synchronous angles. In our experiments, for instance, it was found necessary to focus the beam onto the coupling spot at the prism base. Furthermore, measurements were carried out at conditions of strong coupling. The inherent spread of the m-lines, together with wavefront curvature introduced by the lens, limited the accuracy of the measured values of the film index to ±0.01.

In the case of single mode waveguides the index can be calculated from mode angle measurements of the TE_0 and TM_0 modes. This results in a pair of simultaneous equations which can be solved for n_1 and T_1. The accuracy of the technique depends strongly on the mode separation between the TE and TM polarizations. The Abeles method is based on the properties of the Brewster angle θ_B. Light polarized in the plane of incidence has minimum reflectivity at the incident angle θ_B and the index is given by $n = \tan\theta_B$. For thin films deposited on a substrate, the corresponding θ_B for the film is given by the graphical intersection of the reflectivity curves for the substrate alone and for the film-substrate combination. The curves intersect at maximum angles when the film

thickness is an odd multiple of the wavelength of the incident radiation. For this type of measurement the back of the substrate was optically grounded and painted matt black to avoid the effects of reflection from it. Reflections at the film-substrate interface also introduce some degree of inaccuracy in the determination of the index. The effects of this reflection was analysed by Hacskaylo[133]. In our experiments, the dominant factor introducing errors in the value of the indices was noise level in the detection system and, additionally, the low power output from the HeCd laser. The accuracy in the index value using our equipment was limited to ±0.02.

4.7.2 Grating Constants

The periodicity of experimental gratings was measured by monitoring the autocollimation angle for the first diffracted order using the HeCd laser. The accuracy in the angular measurement was ±2' of arc and for a typical grating for filter application, this represented an error of ±0.1 nm in the value of the period.

Grating depths h can be calculated from diffraction efficiency measurements. For long period gratings, the Raleigh scalar criterion can be applied and the intensity of the i-th transmitted diffraction order is given by[134]

$$I_{i/I_{total}} = \left[J_i\left[\frac{2\pi}{\lambda} h\,(n-1) \right] \right]^2 \qquad (4.4)$$

where n is the refractive index of the grating.

The corresponding expression for gratings with a metal overcoat is

$$I_{i/I_{total}} = \left[J_i \left[\frac{4\pi}{\lambda} h \right] \right]^2 \qquad (4.5)$$

For short period gratings, the scalar approach can not be applied. To calculate the grating depth in this case the approximate

theory developed by Tomlinson et al[135] was used. Their equations relate the diffraction efficiency to the grating depth and are only valid for cases where the following conditions are satisfied

$$(2\pi h/\lambda) << 1$$

$$h < \Lambda/(2\pi\tan\theta) \qquad (4.6)$$

where θ is the incident angle of the beam. Most resist gratings used in our experiments had groove depths which were outwith the conditions given by (4.6) above. A computer program based on the exact solution by Marcuse[136] was available* to calculate the value of h and the numerical results are shown graphically in Fig.4.26. Comparison of the two theories with grating parameters satisfying the conditions given by Tomlinson et al showed complete agreement on the value of h. Within the experimental errors in determining the refractive indices of the film, the periodicity of the gratings and noise level in the detection system the grating depths were calculated with an accuracy better than ±2.5 nm.

4.7.3 Geometrical Measurements

The grating length of interaction, L, which is obtained after the photomasking process, was measured using a Union Microscope shearing eye piece. The graduated displacement drum in the eye piece was first calibrated against a standard graticule. Accuracy in the measurement of the value of L was better than 1%.

4.7.4 Waveguide Loss Measurements

Losses in waveguides were measured using an output prism coupler. Light in the guide was coupled out at equally spaced positions along the length of the guide. To avoid scattering introduced by the

---

* Program developed by Dr. J.A.H. Wilkinson

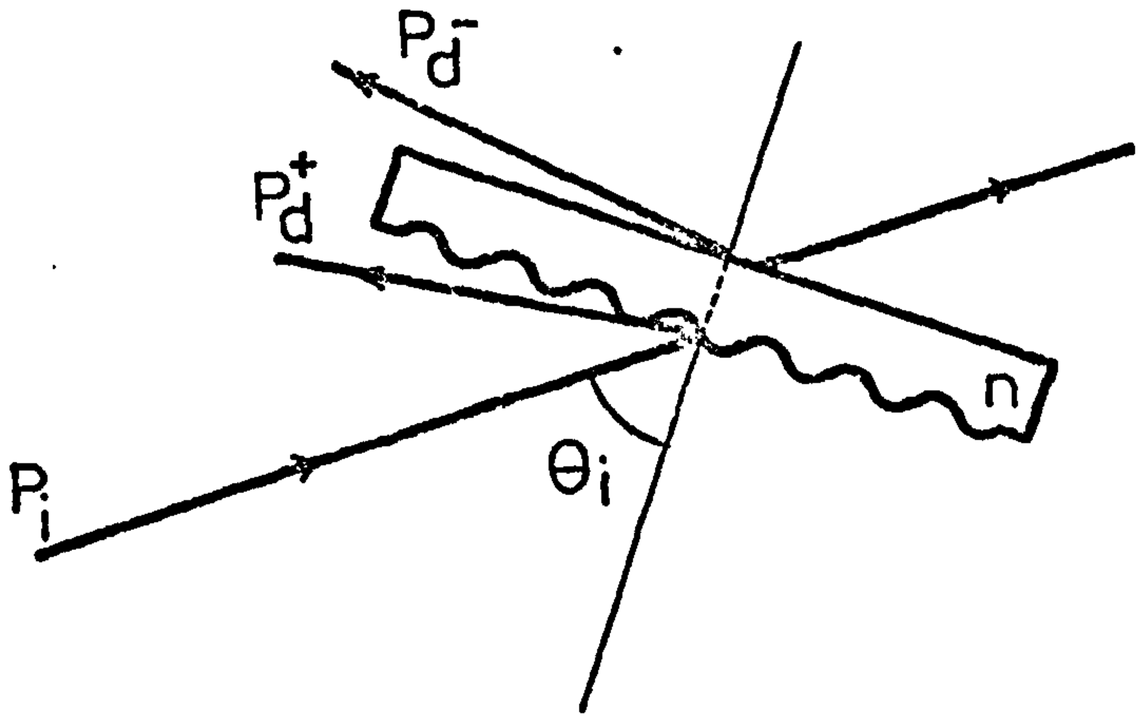

$$\eta = \frac{P_d^+ \text{ (Diffracted Power)}}{P_i \text{ (Incident Power)}}$$

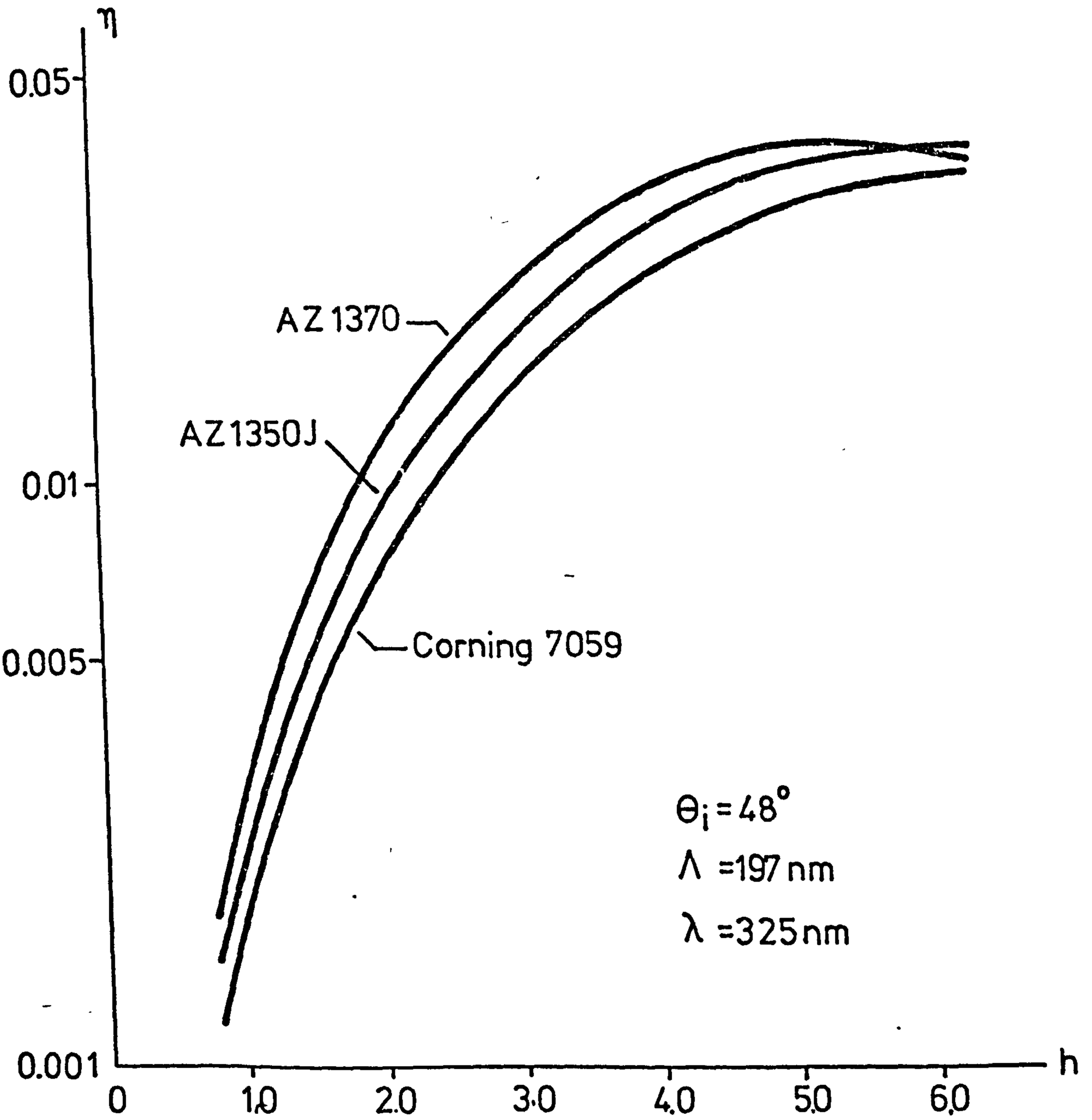

FIG 4.26 Determination of the Corrugation Height of Short Period Gratings from Measurements of diffraction Efficiencies.

effects of the mechanical contact of the prism on the guide, the output coupler was initially positioned at the far end of the guide. The coupler was then displaced towards the input prism coupler. Detection of light intensities of the beam from the coupler and that of a reference beam were made using two UDT PIN10 photodiodes. The input beam to the waveguide was mechanically chopped at a frequency of 5 kHz. The signal beam and reference beam were connected to a divider circuit. Relative power measurements were made with an accuracy of $\pm$0.2 dB.

Appendix 4A.

The diffracted field of an electromagnetic plane wave by a thin dielectric half plane is given by

$$E^d = \pm\sqrt{\frac{2}{\pi}}\,\frac{u\exp(j\pi/4)}{\sigma(\alpha)\,\sigma(\xi)}\,\frac{\cos\phi/2\cdot\cos\alpha/2}{\cos\phi+\cos\alpha}\,\frac{\exp(-jkr)}{kr} \qquad (4A.1)$$

where

α = incident angle

ϕ = observation angle

$$\xi = \begin{cases} \phi & 0 \leqslant \phi \leqslant \pi \\ 2\pi-\phi & \pi \leqslant \phi \leqslant 2\pi \end{cases}$$

$$\sigma(\alpha) = \sqrt{\cosh\gamma+\cos\alpha}\,\exp\left[\frac{j}{\pi}\left[\tan^{-1}\left[\frac{\sinh\gamma}{\sin\alpha}\right]+K(\alpha)\cos\alpha\right]\right]$$

$$\gamma = \sinh^{-1} u$$

$$u = \pi t(\varepsilon_r - 1)/\lambda$$

$$K(\alpha) = u-\sin\alpha\,\tan^{-1}(u/\sin\alpha)$$

t = thickness of the dielectric half plane.

The electric field of the incident wave has been assumed to be parallel to the edge of the plane. For normal incidence $\alpha = \pi/2$ and the diffracted field for two adjacent half planes forming the dielectric slit can be calculated using equation (4A.1) and it is given by

$$E_t^d = \frac{1}{\sqrt{2\pi}}\,\frac{ue^{j\pi/4}}{\sigma(\pi/2)}\,\frac{e^{-jkr}}{kr}\left[\frac{1}{\sin\phi}\left[\frac{\cos\phi/2-\sin\phi/2}{\sigma(\pi/2+\phi)}\,e^{-jka\sin\phi}-\right.\right. \qquad (4A.2)$$

$$\left.\left.\frac{\cos\phi/2+\sin\phi/2}{\sigma(\pi/2-\phi)}\,e^{-jka\sin\phi}\right]\right]$$

$$E_t^d\ (\phi = 0) = \sqrt{\frac{2}{\pi}}\ \frac{ue^{j3\pi/4}}{\sigma^2(\pi/2)}\ \ (ka)\ \frac{e^{-jkr}}{kr} \qquad (4A.3)$$

a = (slit width)/2

For a conducting half plane $u\to\infty$, $K(\alpha)=\pi(\pi-2\alpha)/(4\cos\alpha)$ and equation (4A.2) becomes

$$E^d = \frac{e^{-j(\pi/4+kr)}}{\sqrt{2\pi kr}}\left[\frac{\cos\phi/2-\sin\phi/2}{\sin\phi}\ e^{jka\sin\phi} - \frac{\cos\phi/2+\sin\phi/2}{\sin\phi}\ e^{-jka\sin\phi}\right] \qquad (4A.4)$$

The above equation agrees with the results given by Karp et al[140] for the case of a conducting slit.

CHAPTER V

EXPERIMENTAL RESULTS

Bragg waveguide filters have been fabricated using the various waveguide structures described in Chapter II and the results from their measured responses are presented in this chapter. The measurement procedures are described in detail and the experimental results are compared with the theoretical predictions given in Chapter III. Finally, the properties of a novel demultiplexer are discussed and its experimental results are presented.

5.1 Experimental Equipment for Filter Evaluation

The variation of reflectivity with wavelength for each filter was measured using a tunable dye laser. The general lay-out of the apparatus is shown schematically in Fig.5.1. The particular dye laser used in this investigation was a Coherent Radiation model 590 which incorporated an intracavity birefringent filter as the tuning element. The dye used was Rhodamine 6G whose lasing spectrum covered the range of wavelengths between 570nm and 650nm. The dye laser was optically pumped with a 4-watt Spectra Physics model 165 argon ion laser. Tuning of the dye laser was achieved by rotating the birefringent filter by means of a linearly calibrated micrometer. A synchronous motor was mechanically coupled to the micrometer to provide a constant scan speed. The output wavelength of the laser was calibrated against the micrometer reading and the results are shown in Fig.5.2. The linewidth of the output radiation from the dye laser was measured using a scanning Fabry-Perot interferometer and found to be better than 0.05nm.

The beam from the dye laser was first amplitude divided by a cube-type beam splitter (S_1). One of the deflected beams from the splitter was made incident onto a Rank-Hilger model D300 monochromator; the second deflected beam was incident onto a Bellingham & Stanley 60/ED Abbe refractometer. The accuracy of the monochromator was better than

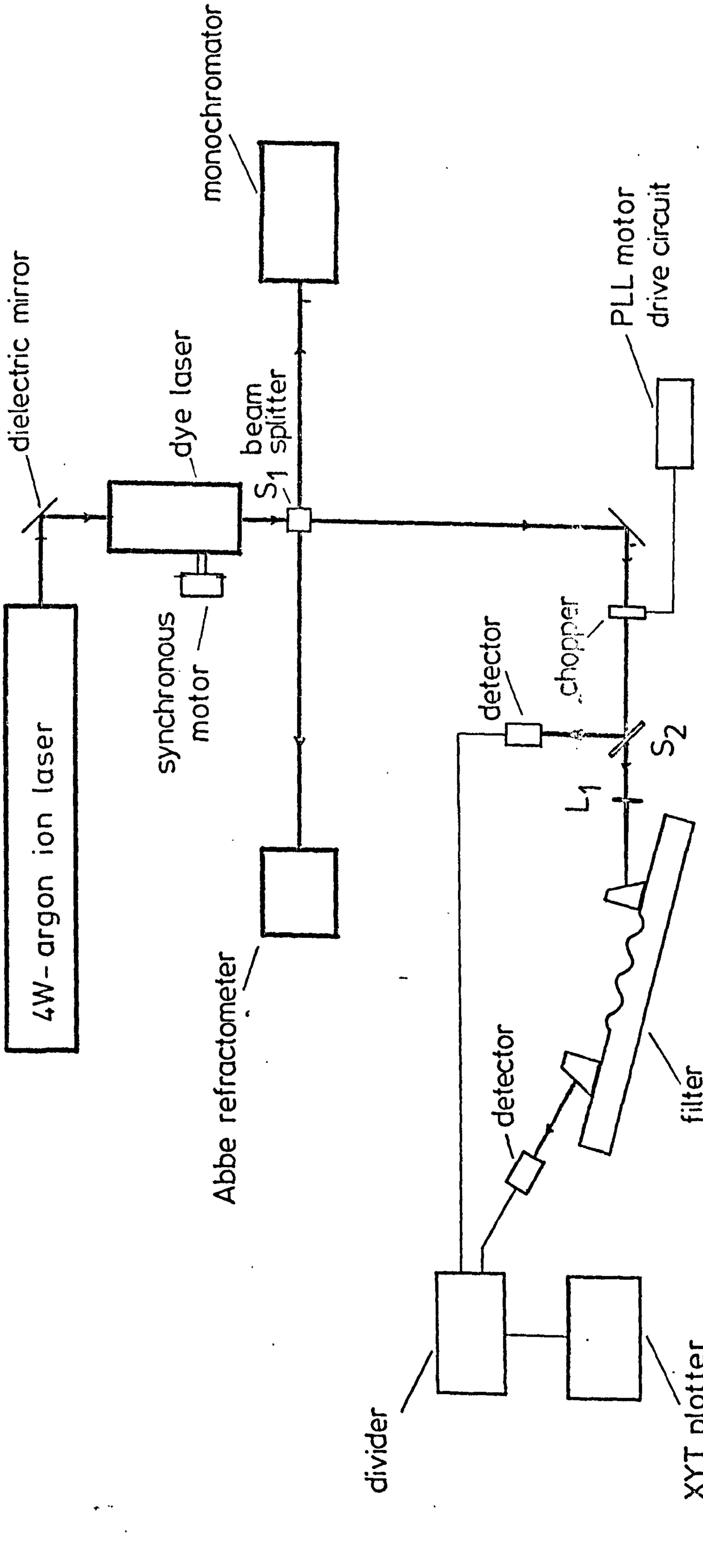

FIG 5.1 Schematic Diagram of Experimental Equipment for Filter Evaluation.

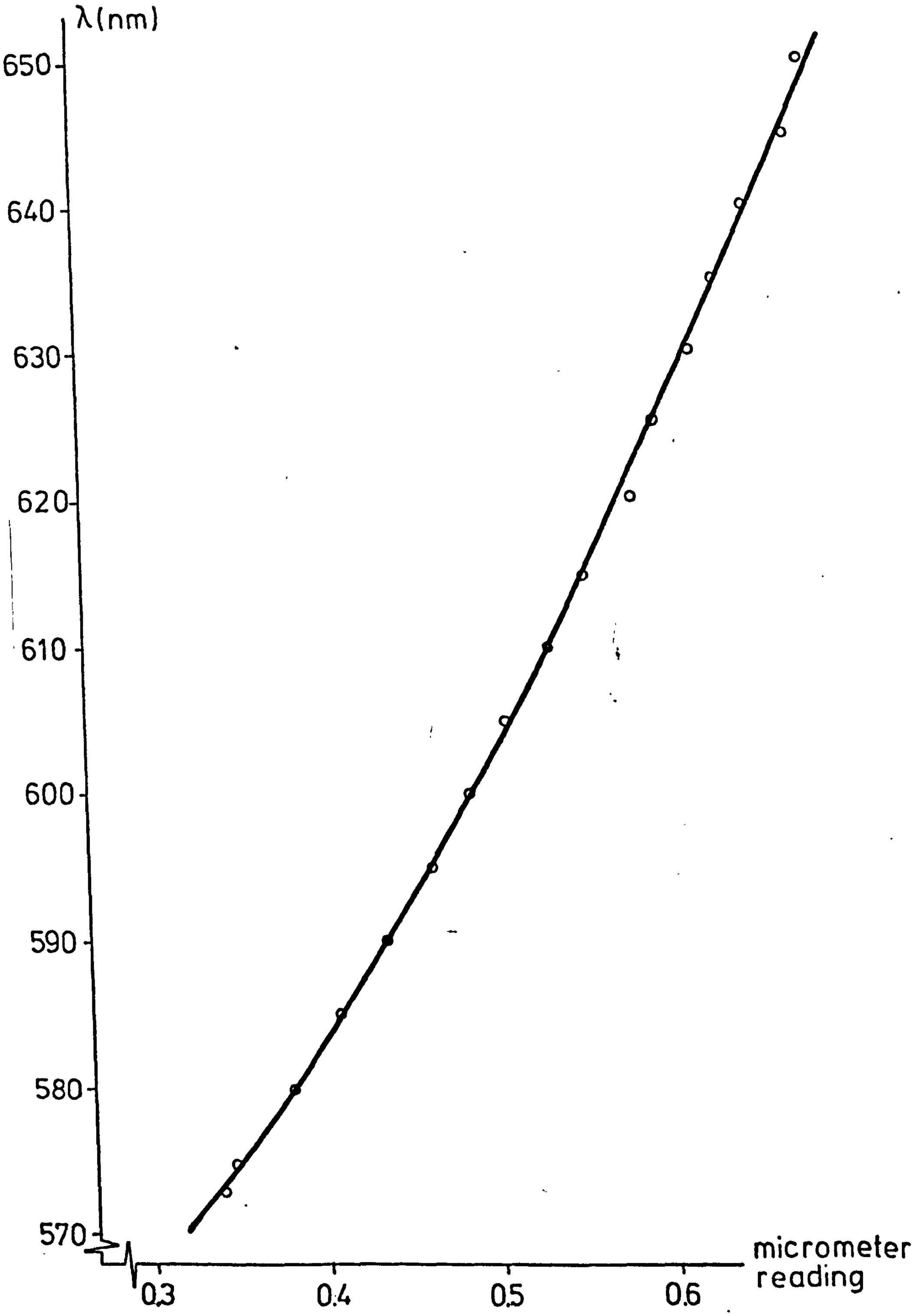

FIG 5.2 Calibration of Output Wavelength of Dye Laser against Micrometer Reading.

±0.03nm and that of the refractometer to ±0.0001 in the values of the measured refractive indices. The undeflected beam from the splitter was mechanically chopped at a frequency of 5KHz and directed towards the goniometer stage which contained the filter and two (input and output) prism couplers. The chopper motor was driven by a phase-locked loop circuit and it was located at the farthest position away from the laser to minimise the effects of vibration and associated noise in the cavity.

The gonimeter (see Fig.5.3) was rotated about a vertical axis through a worm and worm wheel drive with a 60:1 reduction. The worm drive carried a 8cm diameter scale drum reading to 1 minute of arc. The angular positioning accuracy of the goniometer was better than ±2' of arc at all settings. The goniometer carried a two dimensional translational stage whose positioning tolerance was better than ±20um on all axes. The stage carried an L-shaped bracket onto which a second smaller goniometer was attached to provide rotation in the vertical plane. An additional L-shaped bracket was mounted onto this goniometer and it carried a third translational stage which held a mount for the standard 75mm x 25mm microscope slide. The slide mount included an adjustable vertical movement with a total displacement of 5mm.

The prism couplers were held against the sample with U-shaped clamps. One arm of the clamp held the prism and the remaining arm housed a nylon screw the axis of which was directly opposite and perpendicular to the base of the prism. The prism was mechanically contacted onto the surface of the waveguide and clamped down by adjusting the screw against the back face of the substrate. Prisms were made from Schott SF15 glass which had a refractive index of 1.69545 at 610nm and a nominal internal angle γ of 60^{o}. The actual values of γ were determined by standard techniques and accurate to ±2' of arc.

FIG 5.3 Photograph of Goniometer.

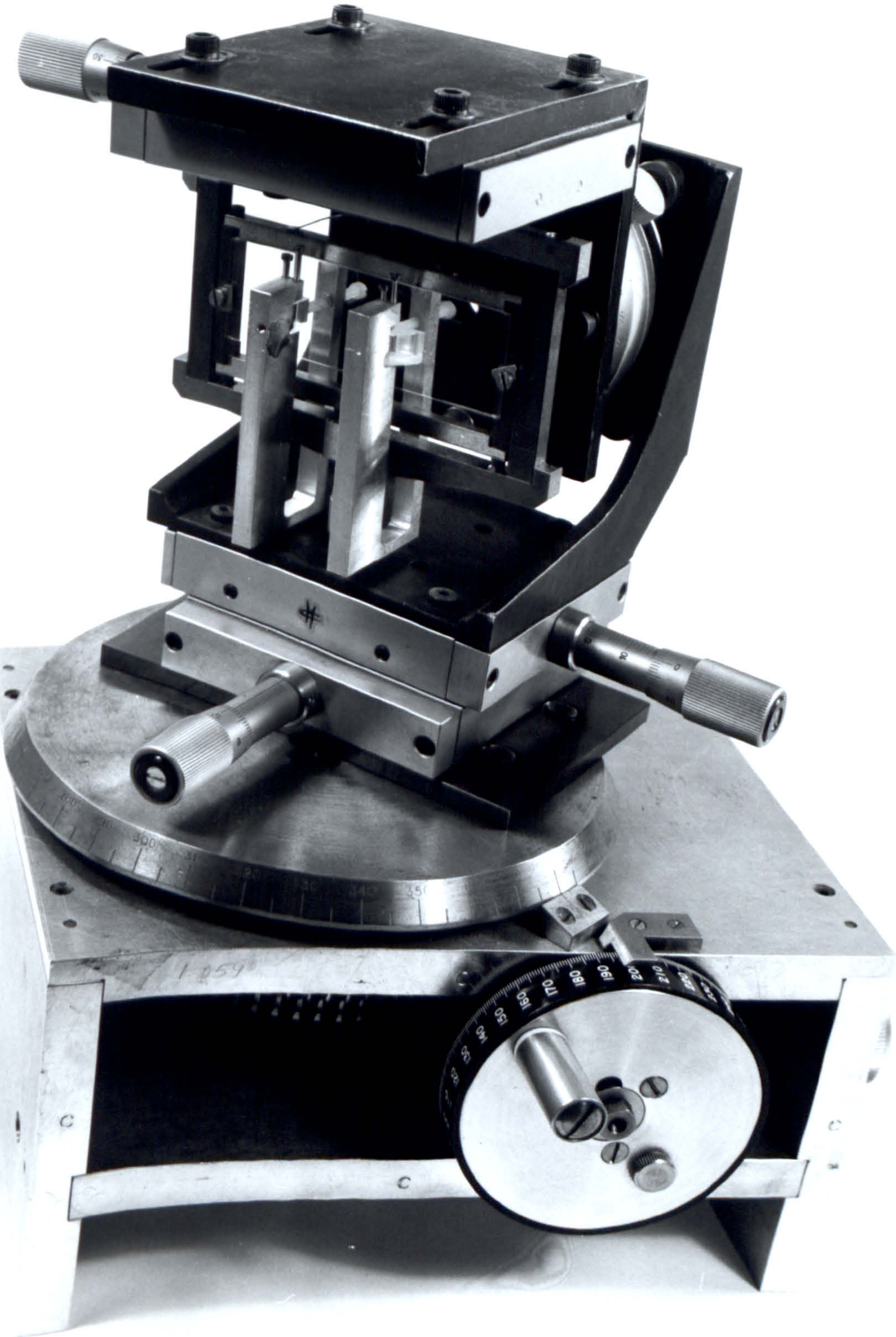

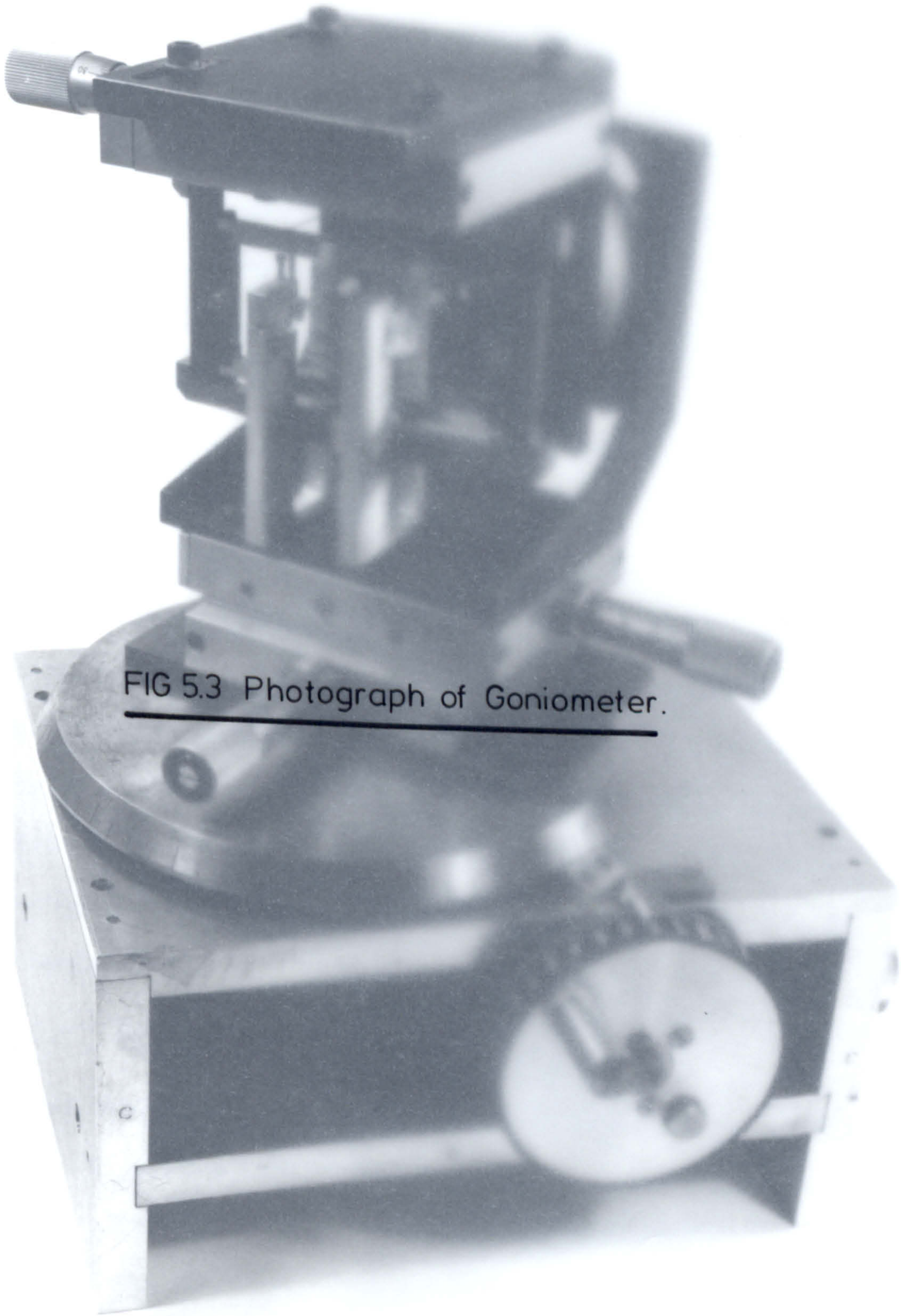

FIG 5.3 Photograph of Goniometer.

Since the power output from the dye laser is frequency dependent, it was found necessary to normalise the response of the filter with respect to a reference beam which was directly related to the power variation. To this end, a second beam splitter (S_2) was positioned in the path of the mechanically modulated beam. The optical power of the reflected beam from the splitter and the signal beam from the filter were detected by a matched pair of United Detector Technology PIN10 photodiodes. These photodiodes had a detection area of 10mm diameter and their responsivity had a maximum discrepancy of 5% throughout the output spectrum of the laser. The output from the photodiodes were connected to a Hewlett-Packard model 3575A gain-phase meter which had a dynamic range of 40dB and incorporated an analogue output and digital display of the ratio of the two input signals in dBV. The analogue output from the meter was finally connected to a Hewlett-Packard model 7045A X-Y-T plotter. The linearity of the overall detection system was checked by attenuating the signal beam, using Oriel fixed neutral density filters and recording the corresponding ratios on the plotter. The results of this test are shown graphically in Fig.5.4. The total noise level in the system was ±0.2dB maximum.

5.2 Measurement Procedure

Red laser light, with a wavelength in the vicinity of 630nm, was initially coupled into the waveguide filter using one of the prism couplers. The 2 mm diameter beam from the laser was focussed onto the coupling spot at the base of the prism by means of a lens (L_1), which had a focal length of 40 cm. The coupling spot had an area of 1 mm diameter and was located near the edge of the prism base. The coupler was located away from one of the sides of the grating (see Fig.5.5) and positioned in such a way that the guided mode (TE_0) was incident perpendicular to and in the middle of the grating area (typically

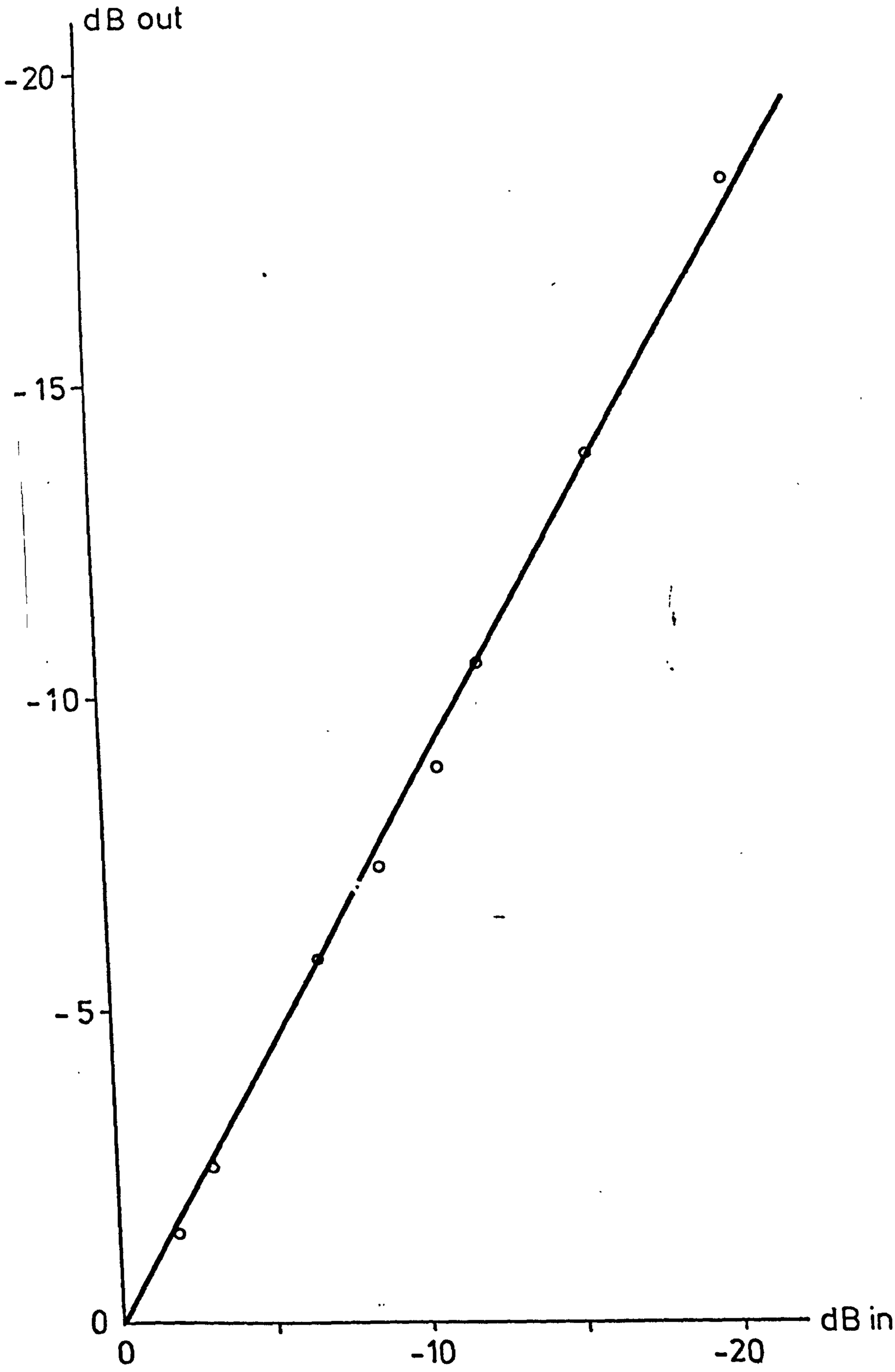

FIG 5.4 Results from Linearity Test on Detection System for the Evaluation of Filter Response.

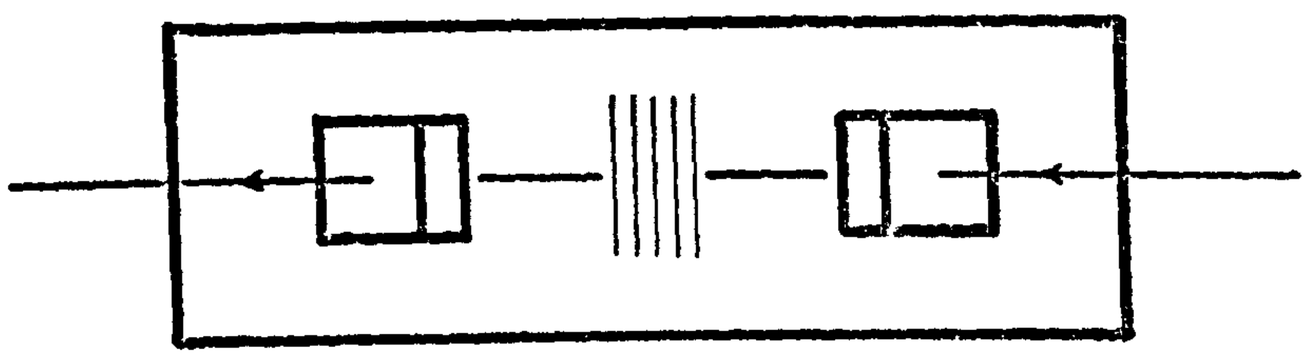

FIG 5.5 Position of Input and Output Couplers on Device.

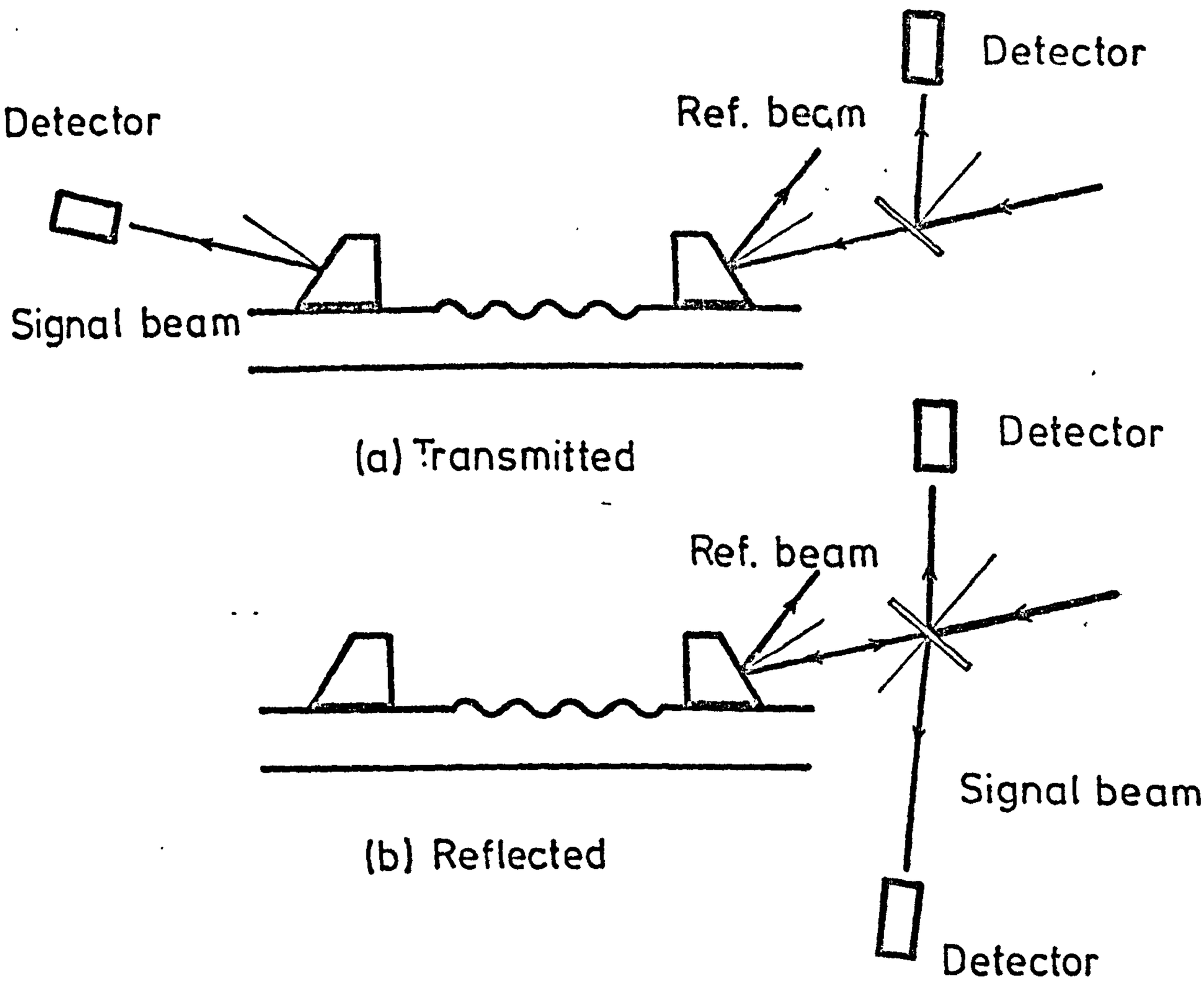

FIG 5.6 Experimental Arrangement for Power Measurement on Bragg Waveguide Filters.

5 mm x 1 mm). The dye laser was then scanned towards the green part of the spectrum and stopped at or near the Bragg wavelength. Small adjustments were made, at this point, to align accurately, the angle of incidence of the mode onto the grating lines. This operation was carried out by fixing the coupler in position, while rotating the vertical geniometer until the forward and reverse modes were collinear. The accuracy of the alignment was estimated to be better than $\pm 0.3^{\circ}$. The laser was next scanned towards the red and stopped at a wavelength well off the Bragg condition. The output coupler was then clamped onto the waveguide, on the opposite side of the grating and the intensity of the output m-line was monitored to adjust finely the main geniometer and ensure that the mode was well guided.

Filter response was obtained by measuring the variation, as a function of wavelength, of the mode power transmitted through and reflected from the grating. For the transmitted power, the intensity of the m-line from the output coupler was monitored as shown in Fig.5.6(a). For the reflected power, the reverse mode couples out of the guide through the input coupler and the corresponding m-line appears reflected off the near face of the beam splitter S_2(see Fig.5.6(b)). To avoid the effects of saturation in the photodetectors by high power levels, the pump power was set to give an output power of about 50 mW from the dye laser within the wavelength range of interest. From a consideration of the calibration graph given in Fig.5.2 and the small range of wavelength scanned in practice, it was reasonable to assume a linear relationship between the micrometer setting and output wavelength. Under this assumption, the laser was scanned at a rate of 0.025 nm/sec and the response of the filter recorded on graph paper. Wavelength measurements were made at the beginning and end of each scan; the Bragg wavelength was determined by graphical interpolation and the accuracy of its determination depended on

the shape of the filter response curve. Once the response had been obtained, the position on the grating where the mode was incident was marked for identification at the back of the substrate. The laser was next scanned to the Bragg wavelength and the value of the effective index N, associated with the unperturbed waveguide, was measured by determining the synchronous angle θ_s, after removing the 40 cm focal length lens. The filter was then removed from the goniometer and the refractive index of the substrate measured using the refractometer. The grating parameters, i.e. periodicity Λ, groove height h and interaction length L, were measured at the marked position using the techniques described in Chapter IV. The accurary in these measurements was ±0.1 nm in the values of Λ, ±2.5 nm in the values of h and a maximum error of 1% in the values of L.

The measurement procedures were repeated for each filter at different positions of the grating width and at normal incidence to the guided mode. In general, the responses obtained showed considerable amount of variation from position to position. These differences were attributed to variations in the thickness of the guide and in the depth of the corrugation. Consequently, the accurate determination of the shift in Bragg wavelength and associated filter response, as a function of the mode incident angle, was not possible.

For the three-layer type filters, the effective guide index N of the uncorrugated region of the waveguide filter was calculated from equation (2.63) with the measured value of θ_s. The required value of the index of refraction n_p of the SF15 glass prisms in this calculation was determined from the following dispersion relation

$$n_p = 1.691 + 5.182\times10^{2}a - 1.725\times10^{7}a^{2} + 1.654\times10^{11}a^{3} - 6.182\times10^{14}a^{4} + 8.520\times10^{17}a^{5} \qquad (5.1)$$

$$a = 1/\lambda \qquad (\lambda \text{ in Angstrom units})$$

$$454.4\text{nm} \leq \lambda \leq 650.0\text{nm}$$

The above equation was obtained by curve fitting to the experimentally measured indices of the original glass used to manufacture the prisms. In order to minimise errors, all prisms used in this investigation were made from the same batch of glass. Accuracy in the measurement of N was $\pm1.5\times10^{-4}$.

In the case of four-layer type filters, the effective guide index could not be measured directly since the pressure of the prism coupler on the resist layer tended to damage its grating pattern. However, from a knowledge of the Bragg wavelength and the periodicity of the grating, it was possible to calculate the effective index N_B of the waveguide with grating from the Bragg equation

$$2\Lambda N_B = \lambda_B \qquad (5.2)$$

Errors in the determination of λ_B from the response curve and the measured value of the grating period limited the accuracy in the calculated value of N_B to a maximum variation of

$$dN_B = \pm7 \times 10^{-4} N_B \qquad (5.3)$$

Curve fitting was also applied to the measured indices of sputtered Corning 7059 glass waveguides and photoresist films. Their corresponding dispersion relations are given, respectively, by

Sputtered Corning 7059 films;

$$n_1 = 1.608 - 8.957\times10^{2}a + 5.484\times10^{6}a^{2} - 9.145\times10^{9}a^{3} \qquad (5.4)$$

$$(457.9\text{nm} \leq \lambda \leq 650.0\text{nm})$$

AZ1350J resist films:

$$n_2 = -3.116 + 1.065\times10^{5}a - 8.959\times10^{8}a^{2} + 3.340\times10^{12}a^{3} - 4.635\times10^{15}a^{4} \qquad (5.5)$$

$$(457.9\text{nm} \leq \lambda \leq 650.0\text{nm})$$

AZ1370 resist films:

$$n_2 = 2.592 - 9.665\times10^{3}a + 2.961\times10^{7}a^{2} \qquad (5.6)$$

$$(570.0\text{nm} \leq \lambda \leq 650.0\text{nm})$$

where a in the above equations has the same meaning as in equation (5.1). To check the consistency of the index values of sputtered 7059 films, periodic runs to produce multimode waveguides were carried out. Results from subsequent mode angle measurements showed typical index variations of ±0.0001 and maximum differences of ±0.0002. The difficulties in the measurement of the index of refraction of resist films were pointed out in Chapter IV; accuracy in the value of n_2 was ±0.01.

Finally, the thickness T_1 of 7059 waveguides was calculated from equation (2.6) and in the cases of four-layer type waveguides, the value of T_2 was calculated from equation (2.39) using the value of N_B for the effective guide thickness. The diffusion depth d and resist film thickness T_2, for the inhomogeneous waveguides, were calculated from the Vassell multilayer computer program (see Chapter II).

5.3 Results for Three-Layer Experimental Filters

Several filters were constructed to verify experimentally the results predicted by the coupled mode theory. The waveguide and grating parameters of the devices are summarised in Table 5.1A. Due to the low yield in the fabrication of silver-sodium ion-exchanged waveguide filters (see Chapter IV), only one device of this type was successfully constructed. The experimental results are compared to the theoretical predictions in Table 5.1B, in all cases the figures are in excellent agreement.

Sample tracing of experimental responses are shown in Fig.5.7. The response curve of filter N23b (in solid line) is compared, in Fig.5.7(a), to the response predicted by theory (in dashed line); Fig.5.7(b) shows the response of filter D37a which was manufactured using the ion exchanged process. In general, the curves show a small degree of asymmetry and slight raising of the zero levels. These effects are caused by small variations in the thickness of the guide and, also, by irregularities in the grating patterns. Marked asymmetry was found in the case of filter N24c the response of which is shown in Fig.5.7(c). As discussed in Chapter III, asymmetric filter response results from a quadratically chirped grating on the surface of the guide. The same effect is also observed if the guide thickness has a quadratic variation along the length of interaction L.[24] On this basis, the theoretical response of an equivalent filter containing a quadratically chirped grating was calculated from the Riccati equation (3.60) and the results are shown, in dashed line, in Fig.5.7(c); apart from the raising of the zeroes, the agreement between the two curves is close. In order to correlate the discrepancies between the experimental and theoretical figures in Table 5.1B, the effects of measurement errors in the waveguide and grating parameters on the calculated value of the coupling

TABLES 5.1 - RESULTS FOR THREE-LAYER EXPERIMENTAL FILTERS.

TABLE 5.1A Waveguide and grating parameters.

FILTER	n_0	n_1	T_1(μm)	N	λ_o(nm)	L(μm)	h(nm)	Λ(nm)
N23b	1.51695	1.56844	0.9395	1.55045	605.91	432.24	25.20	195.52
N16b	1.51665	1.56815	0.9699	1.55070	612.26	815.89	21.80	197.52
N40b	1.51229	1.56809	0.9468	1.54963	613.86	1068.37	16.80	198.09
N24c	1.51617	1.56821	0.8716	1.54793	610.90	829.73	15.20	197.27
D37a	1.51615	1.585	d=2.1330	1.54916	610.97	1042.71	16.00	197.10

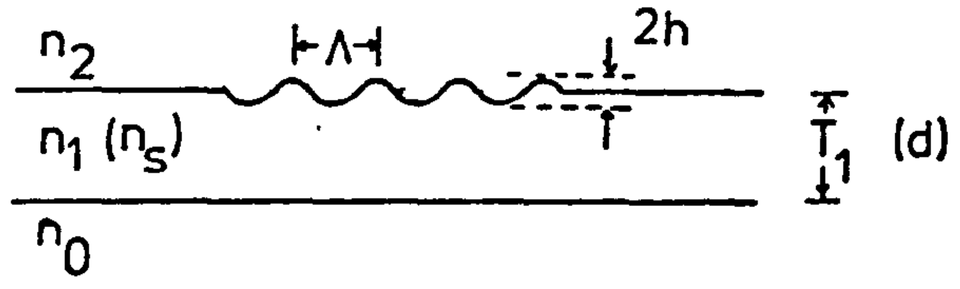

TABLE 5.1B Filter response-Experimental and Theoretical

FILTER	$\kappa/h(\mu m^{-2})$	κL	$BW_m(A)$	$BW_c(A)$	$R_{Om}(\%)$	$R_{Oc}(\%)$	$(R_1/R_O)m$	$(R_1/R_O)_c$	$\Delta BW/BW_c(\%)$	$\Delta R_O/R_{Oc}(\%)$	$d\lambda_o/dT_1$
N23b	0.14198	1.54647	6.46	6.10	89.54	83.39	0.1169	0.1166	-5.90	-7.37	0.01070
N16b	0.13304	2.36627	3.93	3.71	90.49	96.54	0.1633	0.2087	-5.93	+5.80	0.01024
N40b	0.14414	2.58714	2.82	2.95	94.89	97.76	0.2558	0.2369	+4.40	+2.94	0.01116
N24c*	0.16592	2.09251	4.27	3.49	88.66	93.82	0.3512	0.3008	-2.23	+5.50	0.01273
D37a	0.22210	3.70537	3.49	3.57	96.20	99.76	0.2734	0.3830	-2.24	+3.57	

(m = measured, c = calculated)

(* Theoretical response calculated for case of uniform period grating).

$$\frac{\kappa}{h} = \frac{\pi}{\lambda} \frac{(n_1^2 - N^2)}{N T_e}$$

$$R_1 = \frac{(\kappa L)^2}{(\kappa L)^2 + (3\pi/2)^2}$$

$$R_O = \tanh^2 (\kappa L)$$

$$\frac{d\lambda_o}{dT_1} = \frac{\lambda_o}{T_e} \left[\frac{n_1^2}{N^2} - 1\right]$$

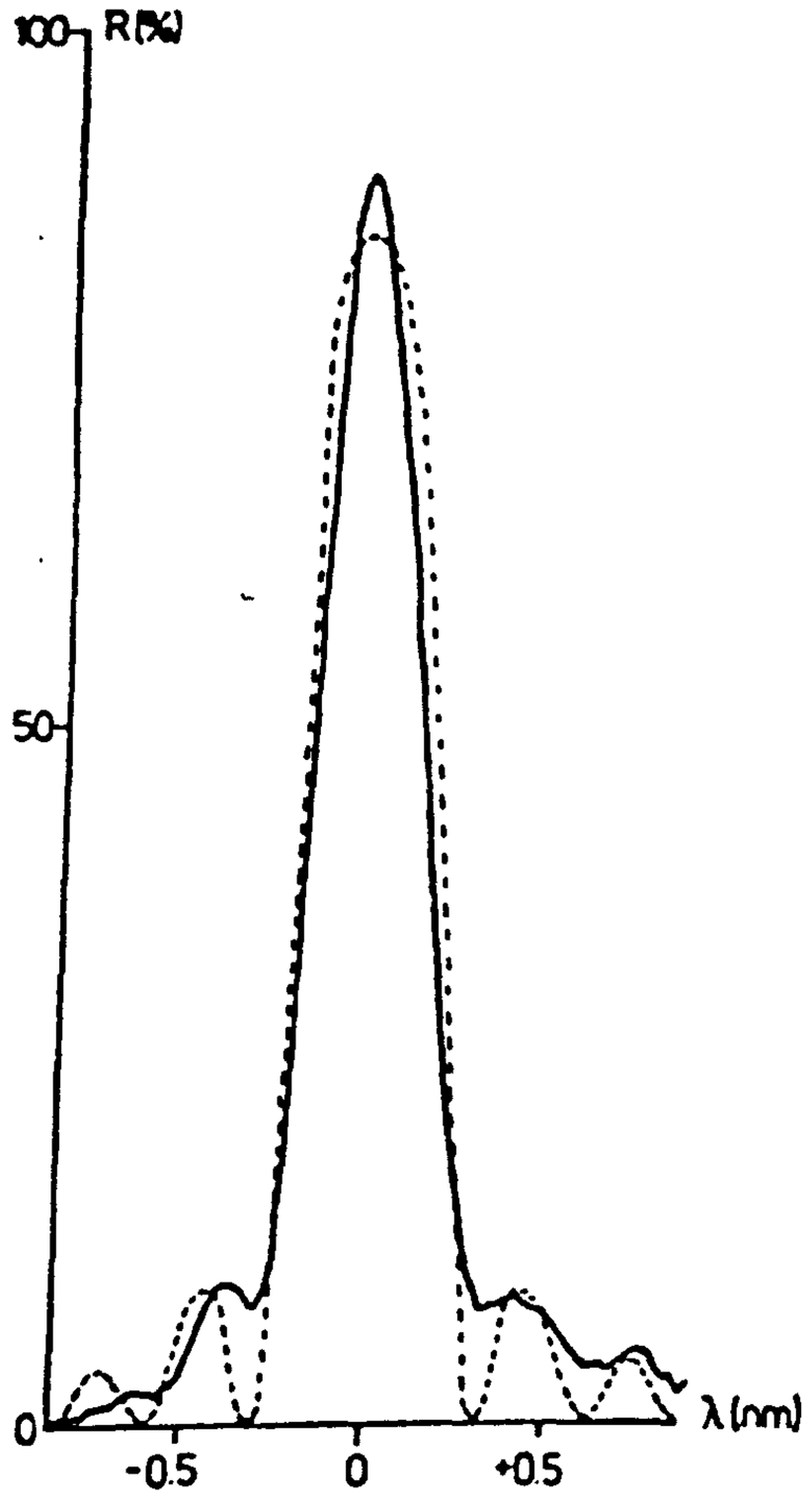

(a) Filter N23b

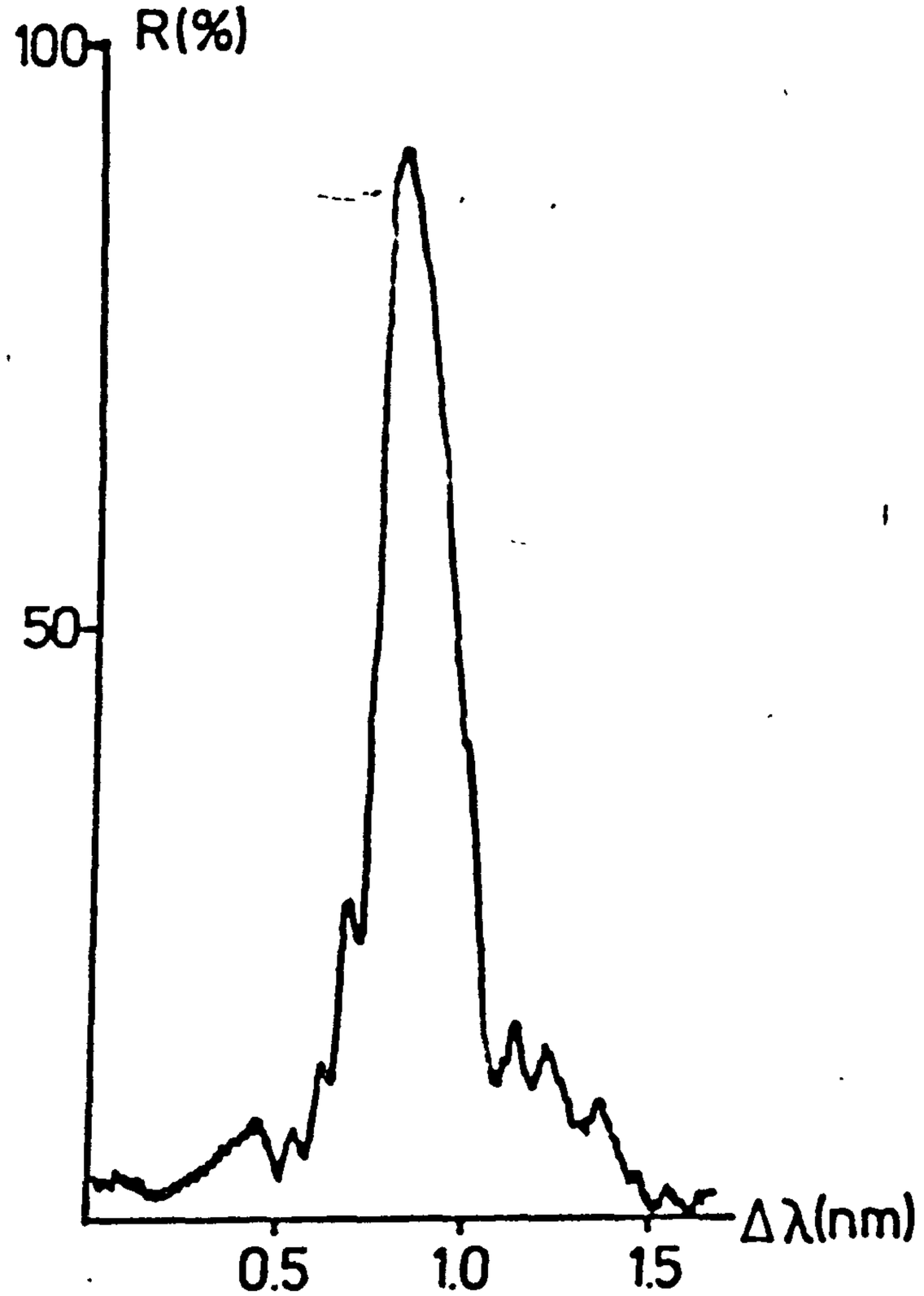

Filter D37a

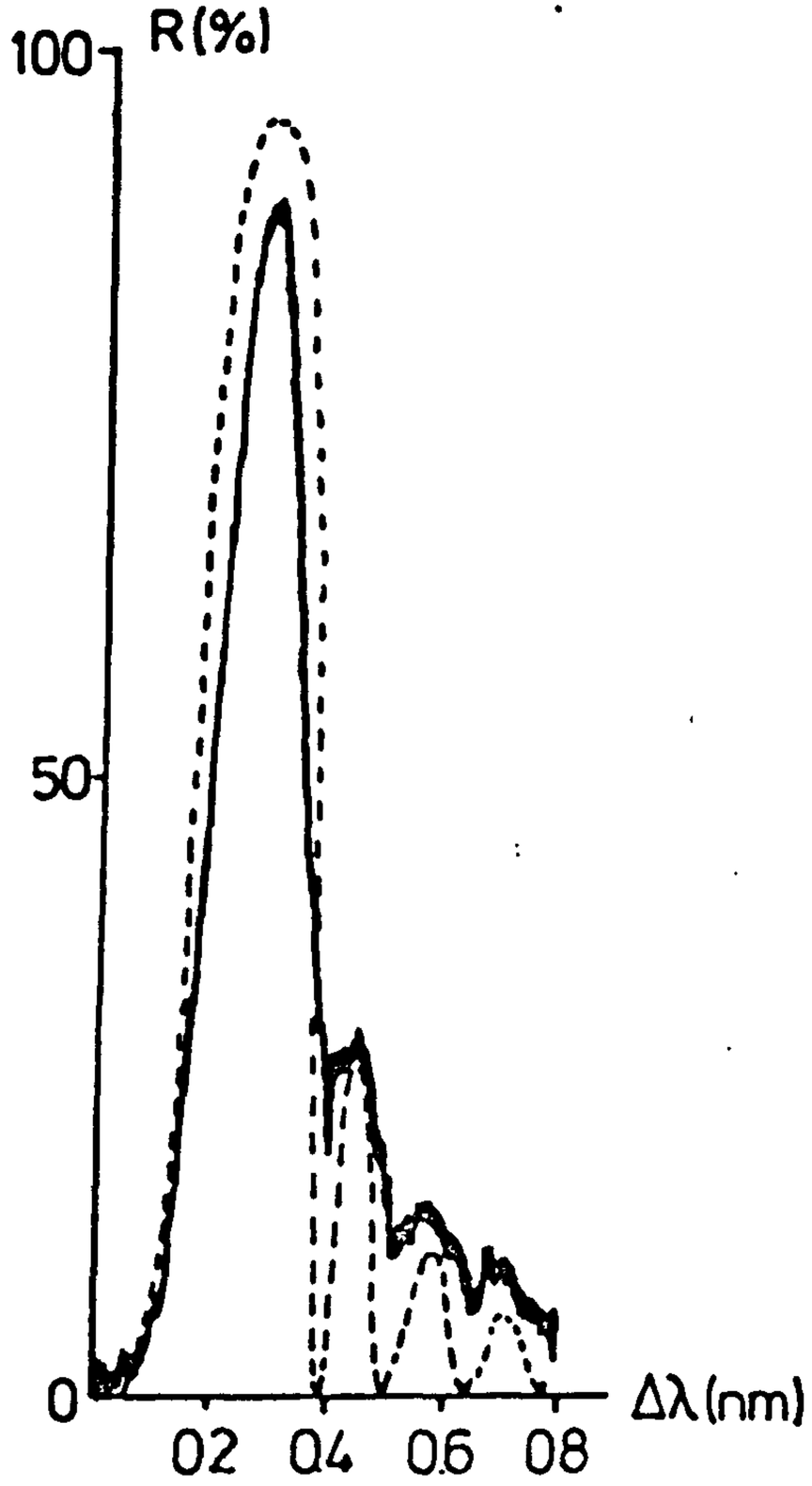

(c) Filter N24c.

FIG 5.7 Sample Tracing of Three-Layer Experimental Filters.

coefficient were evaluated from the following equations

$$d\kappa = h(d(\kappa/h)) + (\kappa/h)dh \qquad (5.7)$$

$$d\left(\frac{\kappa}{h}\right) = \frac{\partial(\kappa/h)}{\partial N}\,\frac{\partial N}{\partial n_0}\,dn_0 + \frac{\partial(\kappa/h)}{\partial N}\,\frac{\partial N}{\partial n_1}\,dn_1 + \frac{\partial(\kappa/h)}{\partial N}\,\frac{\partial N}{\partial T_1}\,dT_1 \qquad (5.8)$$

and the corresponding change in the fractional bandwidth (equation 3.45) from

$$\frac{d\sigma}{\sigma} = \frac{(\kappa L)^2}{\pi^2+(\kappa L)^2} \cdot \frac{d\kappa}{\kappa} \qquad (5.9)$$

The individual terms in equations (5.7) and (5.8) were obtained from equation (3.26) for the coupling coefficient and the mode equation (2.6) for the homogeneous waveguides. Table 5.1C shows the results from these calculations. The variations in the normalised coupling coefficient κ/h caused by the waveguide parameters are listed in the first three columns (i.e. $d(\kappa/h)/dn_0$, $d(\kappa/h)/dn_1$ and $d(\kappa/h)/dT_1$) and the theoretical bandwidths are expressed in terms of the normalised frequency, σ_c, using equation (3.46). The fractional change in the coupling coefficient, i.e. $d\kappa/\kappa$, was calculated in each case by introducing into equations (5.7) and (5.8) the magnitude of the errors of the relevant parameters. It was found during the calculations that the discrepancies between the predicted and measured parameters of the filter response can be accounted for by the experimental errors in the measurement of the indices and errors in the determination of the grating groove heights. Numerical results calculated from equations (5.7) and (5.8) using $dn_0=dn_1=\pm 0.0001$, $dh=\pm 2.5$ nm and $dT_1=0$ are listed in Table 5.1C in conjunction with the corresponding change in the fractional bandwidth $\left[\frac{d\sigma}{\sigma}\right]_c$ calculated from equation (5.9). The measured discrepancies were next expressed in terms of fractional change in bandwidth, i.e. $d\sigma_m/\sigma_c$, and subsequently compared to the theoretical

TABLE 5.1C Errors-Experimental and Theoretical (Homogeneous Waveguides)

FILTER	$d(\kappa/h)/dn_0$	$d(\kappa/h)/dn_1$	$d(\kappa/h)/dT_1$	$\sigma_c(\mu m^{-1})$	$d\kappa/\kappa$	A	$(d\sigma/\sigma)_c$	$d\sigma_m/\sigma_c$	$d\sigma_m/d\sigma_c$	dR_{0m}/dR_{0c}
N23b	-1.06242	-7.43980	-0.31114	8.10098×10^{-3}	0.33684	0.19505	0.06570	0.05742	0.87398	0.38926
N16b	-0.96904	-7.21821	-0.28543	4.82049×10^{-3}	0.39697	0.36197	0.14369	0.05917	0.41178	0.87739
N40b	-0.94918	-7.41901	-0.31829	3.80926×10^{-3}	0.49438	0.40411	0.19978	0.08110	0.40595	0.50707
N24c*	-1.35558	-7.57261	-0.37542	4.54929×10^{-3}	0.51849	0.30731	0.15934	0.22307	1.39996	1.25712

$$A = (\kappa L)^2/[\pi^2 + (\kappa^2 L^2)]$$

* Theoretical response calculated for case of uniform period grating).

values. In all cases, with the exception of filter N24c, $(d\sigma_m/d\sigma_c)<1$ which means that the experimental errors are smaller than the predicted figures. Finally, the change in the main lobe reflectivity is calculated from

$$dR_o = 2L\tanh(\kappa L)\operatorname{sech}^2(\kappa L)d\kappa \qquad (5.10)$$

with the same values of $d\kappa/\kappa$. The last column of Table 5.1C shows that the experimental errors also compare favourably. A careful consideration of the change in κ/h, due to variations in the values of the indices, shows that they are at least one order of magnitude larger than the corresponding change in κ/h, due to variations in the thickness of the guide T_1. Since index measurements can be accurate to ±0.0001, the relatively smaller magnitude of $d(\kappa/h)/dT_1$ can not be neglected; for the cases shown in Table 5.1C, thickness variations of the order of 2.0nm would cause a change in κ/h, comparable to those introduced by dn_0 or dn_1. Thickness variations of this order of magnitude can easily be introduced during the sputtering of the waveguide films. In terms of filter response, such changes in T_1 result in changes in the centre wavelength of the device and can also broaden the bandwidth of the filter. The change in centre wavelength can be calculated from equations (2.6) and (5.2) and is given by

$$\frac{d\lambda_o}{dT_1} = \frac{\lambda}{T_e}\left[\frac{n_1^2}{N^2} - 1\right] \qquad (5.10)$$

In the particular case of filter N24c, for instance, the discrepancy in bandwidth can be accounted for by a dT_1 of the order of 4.0nm.

The theoretical analysis on the effects of errors in the case of the ion-exchanged waveguide filter would require a great deal of computational time, since the analysis is basically carried out with a numerical technique. In any case, the value of the surface index n_s

is not known with good accuracy. However, it is not unreasonable to adopt the results from the homogeneous waveguide cases as guide lines to assess the results obtained in this particular filter. The agreement of experimental results with the predicted figures for bandwidth and reflectivities appear to indicate that the parameters used in the theoretical calculations are reasonable. The slight asymmetry and raising of the zero levels in the response curve can be attributed to irregularities in the grating geometry, brought about during the fabrication of the mask or in the ion beam etching process.

During the derivation of the coupled mode formalism in Chapter III, it was pointed out that the value of the effective index N is taken to be that of the unperturbed waveguide with the consequent result that the position of the band gap is not accurately determined. A corrected value, N_c, for the effective guide index associated with the perturbed guide, can be obtained by calculating the average change of the phase velocity over one period of the grating. For the homogeneous waveguides, equations (3.23) and (3.26) give

$$N(z) = N(1 + \eta \cos 2\beta z) \tag{5.11}$$

where

$$\eta = \frac{2\kappa}{k_0 N} << 1 \tag{5.12}$$

The average phase velocity is given by

$$V_{p(av)} = \frac{2}{\Lambda} \int_0^{N_2} \frac{c}{N} (1-\eta\cos 2\beta z+\eta^2\cos^2 2\beta z)dz \tag{5.13}$$

i.e.

$$V_{p(av)} = \frac{c}{N} \left[1 + \eta^2/_2 \right] \tag{5.14}$$

and

$$N_c = N/(1 + \eta^2/_2) \tag{5.15}$$

The correction in the value of N is generally small and, in the case of the experimental filters presented here $(N - N_c)$, is of the order of 10^{-8}, and the corresponding shift in the band gap, or equivalently, in the centre wavelength, is too small to be measured experimentally. Finally, the experimental results presented in Table 5.18 correspond to the response of the devices acting as band-stop filters. A comparison of these results with those obtained from measurements of the power variations in the reflected mode (band-pass) indicated good agreement for the value of the bandwidth; however, a maximum discrepancy of 15% was observed in the absolute value of the reflexivity R_0. The lower value of R_0 in these cases are a result of the small amount of scattering along the grating length of the filters.

5.4 Results for Four-Layer Experimental Filters

The waveguide and grating parameters of the devices are listed in Table 5.2A and, in Table 5.2B, the experimental results are compared with those calculated from theory. The agreement is found to be good for filters with low values of the parameter κL but the discrepancies are observed to increase as κL becomes large. The departure of the experimental figures from those predicted by theory are attributed to three main factors: firstly, accuracy in the determination of the effective guide index N_B; secondly, exact knowledge of the value for the refractive index n_2 of photoresist; and finally, the magnitude of the parameter κL. In comparison with the three-layer type of filters, the different method of evaluation of N_B leads to larger errors and the refractive index of photoresist cannot be measured with the same accuracy as the refractive index of Corning 7059 glass films. In what follows, a theoretical analysis on the effects of these factors in the filter response will be given for the cases of homogeneous waveguides.

TABLES 5.2 RESULTS FOR FOUR-LAYER EXPERIMENTAL FILTERS

TABLE 5.2(A) Waveguide and grating parameters.

FILTER	n_0	n_1	T_1(μm)	N	n_2	T_2(μm)	N_B	λ_o(nm)	L(μm)	h(nm)	Λ(nm)
N34b	1.51645	1.56828	0.8860	1.54855	1.63353	0.0618	1.55087	609.36	548.75	16.60	196.46
N18b	1.51653	1.56813	0.9044	1.54882	1.63318	0.0824	1.55188	612.92	475.23	19.30	197.48
N37b	1.51617	1.56830	0.7885	1.54516	1.63357	0.0798	1.54898	608.91	836.41	17.20	196.55
N13b	1.51300	1.56853	0.5615	1.53315	1.63407	0.0386	1.53628	603.92	555.41	18.80	196.55
N22b	1.51618	1.56827	0.7886	1.54510	1.63350	0.1144	1.55088	609.66	829.73	20.00	196.55
N30b	1.55495	1.56807	1.0895	1.55827	1.63306	0.2053	1.56246	612.41	836.49	35.70	197.35
D127	1.51732	1.585	d=0.7230	1.51873	1.63396	0.1540	1.53875	605.01	832.43	36.20	196.59
D37j	1.51753	1.585	d=1.7370	1.54406	1.63322	0.1837	1.55841	612.50	829.73	19.50	196.51
D37k	1.51304	1.585	1.6700	1.54132	1.63336	0.1660	1.55513	611.09	828.37	52.50	196.48
D37ℓ	1.51684	1.585	1.7670	1.54416	1.63294	0.2530	1.56607	615.39	1052.70	50.00	196.47
D37m	1.51536	1.585	1.5340	1.53945	1.63302	0.2404	1.56293	614.03	1041.67	48.00	196.63
D162	1.51072	1.585	0.7400	1.51458	1.80431	0.0602	1.53012	591.72	1255.41	24.00	193.36

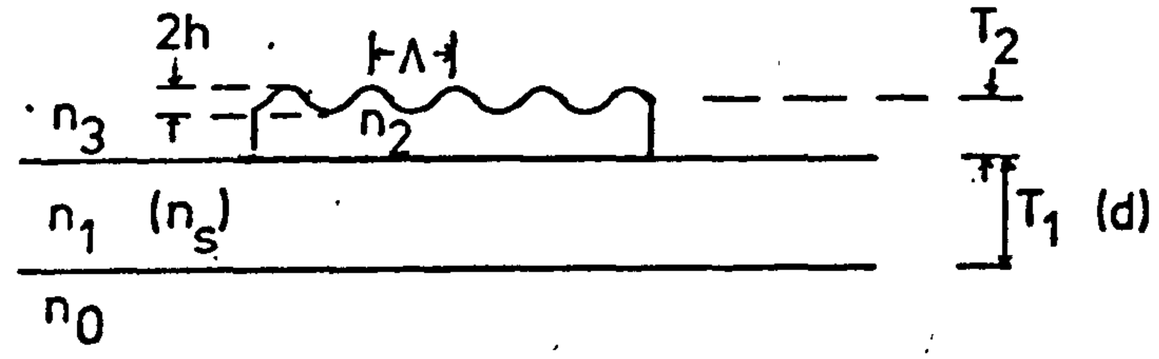

TABLE 5.2B* Filter Response-Experimental and Theoretical

FILTER	$\kappa/h(\mu m^{-2})$	κL	$BW_m(A)$	$BW_c(A)$	$R_{0m}(\%)$	$R_{0c}(\%)$	$(R_1/R_0)_m$	$(R_1/R_0)_c$	$\Delta BW/BW_c(\%)$	$\Delta R_0/R_{0c}(\%)$
N34b	0.20851	1.91079	5.06	5.25	87.18	91.61	0.0875	0.1541	+3.62	+4.84
N18b	0.21459	1.97841	6.28	6.02	94.52	92.63	0.1989	0.1617	-4.32	-2.04
N37b	0.27445	3.94872	4.89	4.60	93.78	99.85	0.4081	0.4131	-6.30	+6.08
N13b	0.43575	4.54998	6.64	7.53	89.16	99.96	0.2234	0.4827	+11.88	+10.80
N22b	0.31329	5.19893	6.31	7.50(2)	90.87	99.98	0.2443	0.3048(2)	+15.87	+9.11
N30b	0.22626	6.75684	7.35	8.43(2)	96.42	99.99	0.3619	0.4253(2)	+12.81	+3.57

FILTER	$\kappa/h(\mu m^{-2})$	κL	$BW_m(A)$	$BW_c(A)$	$R_{0m}(\%)$	$R_{0c}(\%)$	$BW_r(A)(r)$	$\Delta BW/BWc(r)$	$\Delta R_0/R_{0c}$
D127	0.94597	39.29328	33.17	26.28	95.10	100.0	37.15(9)	+10.71	+4.90
D37j	0.53732	8.69370	9.14	8.54	97.81	100.0	11.85(3)	+22.87	+2.19
D37k	0.55354	24.07343	24.21	22.44	99.73	100.0	30.16(7)	+19.73	+0.27
D371	0.60301	31.73943	32.63	23.37	98.77	100.0	41.68(17)	+21.71	+1.23
D37m	0.65316	32.65810	28.64	24.28	96.42	100.0	46.41(17)	+38.29	+3.58
D162	2.41915	72.88860	52.70	42.48	97.49	100.0	>205 (?)	?	+2.57

* Number (r) in parenthesis indicates r-th order zero in theoretical filter response.

The results will then be extended to discuss the case of inhomogeneous guides.

The accuracy in the determination of the effective guide index N_B is given by equation (5.3). Although the magnitude of the variation is relatively small, such changes in N_B can seriously affect the value of the calculated coupling coefficient κ. Numerical calculations were carried out, for each device, to determine the fractional change in κ, i.e. $d\kappa/\kappa$, as result of the change in N_B given by equation (5.3). The corresponding change in the fractional bandwidth was subsequently calculated from equation (5.9) and the results are shown in Table 5.2C. As in the case of three-layer filters, the measured discrepancies were expressed as a fractional bandwidth change, $d\sigma_m/\sigma_c$, and subsequently compared to $d\sigma_c/\sigma_c$. It can be observed from the results, that with the exception of filter N30b the ratio $d\sigma_m/d\sigma_c$ is greater than unity for all devices. This means that the total discrepancies of the results can not be attributed solely to errors in N_B. On the basis that the ratio $d\sigma_m/d\sigma_c$ is unity for $d\sigma_c$ contributed by dN_B alone, the additional change in κ, denoted by $(d\kappa/\kappa)_a$, which would account for the residual discrepancies, i.e. $(1-d\sigma_m/d\sigma_c)$. $(d\sigma/\sigma)_c$ can be calculated from equation (5.9). The results of these calculations are also given in Table 5.2C, where it can be observed that the additional changes in $d\kappa/\kappa$ range from 1% to 15%. Further calculations were next carried out to determine the change in $d\kappa/\kappa$ due to changes in the value of the refractive index n_2 of the resist layer. The results from these calculations showed that the magnitudes of $(d\kappa/\kappa)_a$ can be accounted for by changes in n_2. Fig.5.8 shows a graph of the variation of $d\kappa/\kappa$ as a function of n_2 for filters N13b and N37b; it can be observed that the required change in κ, i.e. $(d\kappa/\kappa)_a$, takes place within a variation in n_2 comparable to the accuracy with which the index

TABLE 5.2C Errors - Experimental and Theoretical (Homogeneous Waveguides)

FILTER	$N\pm$	$T_2(\mu m)\pm$	$(d\kappa/\kappa)\pm$	A	$(d\sigma/\sigma)_c\pm$	$(d\sigma_m/d\sigma_c)$	$(d\sigma/\sigma)_a$	$(d\kappa/\kappa)_a$
N34b	1.55192	0.0867	0.09524	0.27004	0.02572	1.42088	-0.01082	-0.04008
	1.54983	0.0351	0.07034		0.01899	1.92379	-0.01755	-0.06481
N18b	1.55293	0.1061	0.10781	0.28397	0.03061	1.39892	-0.01221	-0.04300
	1.55083	0.0562	0.08537		0.02424	1.76636	-0.01853	-0.06542
N37b	1.55002	0.0988	0.07491	0.61238	0.04587	1.38392	-0.01761	-0.02876
	1.54794	0.0596	0.06294		0.03854	1.64713	-0.02494	-0.04073
N13b	1.54984	0.0966	0.22276	0.67717	0.15085	1.69240	-0.10445	-0.15424
	1.53524	0.0260	0.33012		0.22355	1.14202	-0.03175	-0.04688
N22b	1.55193	0.1309	0.08080	0.73252	0.05919	2.68305	-0.09962	-0.13599
	1.54984	0.0966	0.06848		0.05016	3.16605	-0.10865	-0.14832
N30b	1.56351	0.2257	0.25173	0.53628	0.13499	0.95156	+0.00654	+0.01219
	1.56141	0.1768	0.25127		0.13475	0.95325	+0.00630	+0.01175

$N\pm = N \pm dN$

$A = (\kappa L)^2/[(r\pi)^2 + (\kappa L)^2]$

$(d\delta/\delta)a = (d\delta/\delta)_c\ (1-d\delta m/d\delta c)$

$(d\kappa/\kappa)a = (d\delta/\delta)_a/A$

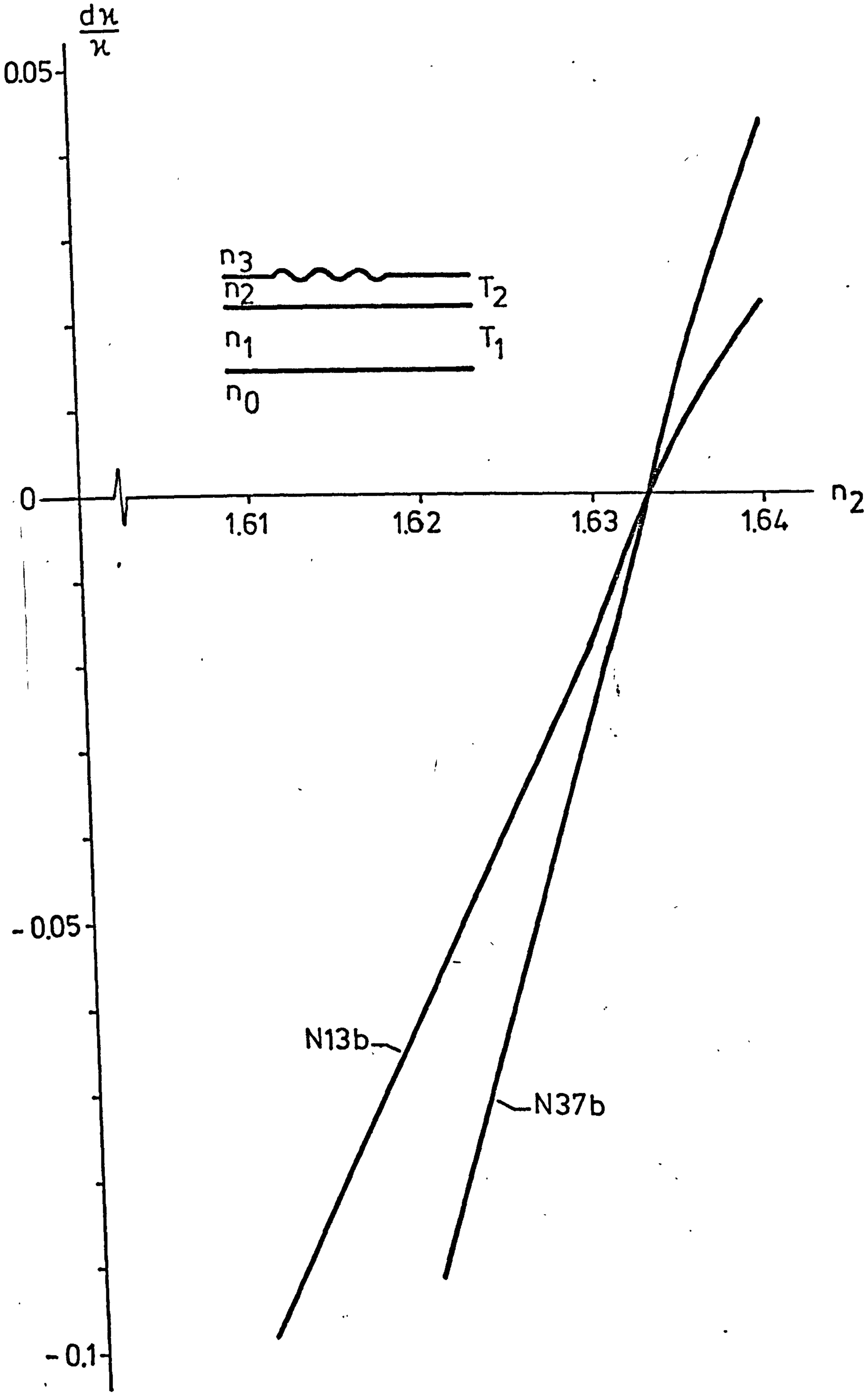

FIG 5.8 Variation of the Coupling Coefficient as Function of the Refractive Index of Photoresist for two Experimental Filters.

value is measured (see Chapter IV).

The exact determination of the individual contributions of errors in κ/L by dN_B and dn_2 is difficult; however, the above analysis gives a good idea of the maximum bounds of possible errors which could be introduced by these two specific parameters. The theoretical analysis of the effects introduced by variations of the remaining waveguide parameters, i.e. n_0, n_1 and T_1, is complicated, however, a consideration of the field distribution in the guide and the rate of change in the value of the effective guide index as a function of the thickness T_2 (or refractive index n_2) of the top layer leads to the conclusion that such variations would have relatively minor effects in the performance of the filters (see Fig.2.8 and column $T_2\pm$ in Table 5.2C). Fig.5.9(a) shows the experimental response of filter N34b.

The results for the inhomogeneous waveguide filters show larger difference between the experimental and predicted results. The much higher values of the product κL, in these cases, did not allow a detailed plotting of the response of the filters since the zero to first sidelobe separation was smaller than the resolvable linewidth of the laser. The bandwidth figures, in these filters, were compared to the theoretical figures by successively monitoring the zero to sidelobe separation up to the point where this distance in wavelength was comparable to the linewidth of the laser. The value of the bandwidth of the envelope is given in Table 5.2B under the heading BW_r. Uncertainty in the exact linewidth of the laser and errors in the calculated coupling coefficient made the exact correlation of the filter response to the bandwidth of the calculated envelope difficult. In addition to this source of errors, the additional differences of results can be accounted for by similar arguments applied to the case of homogeneous waveguide filters. The effects of errors in $d\kappa/\kappa$ in these

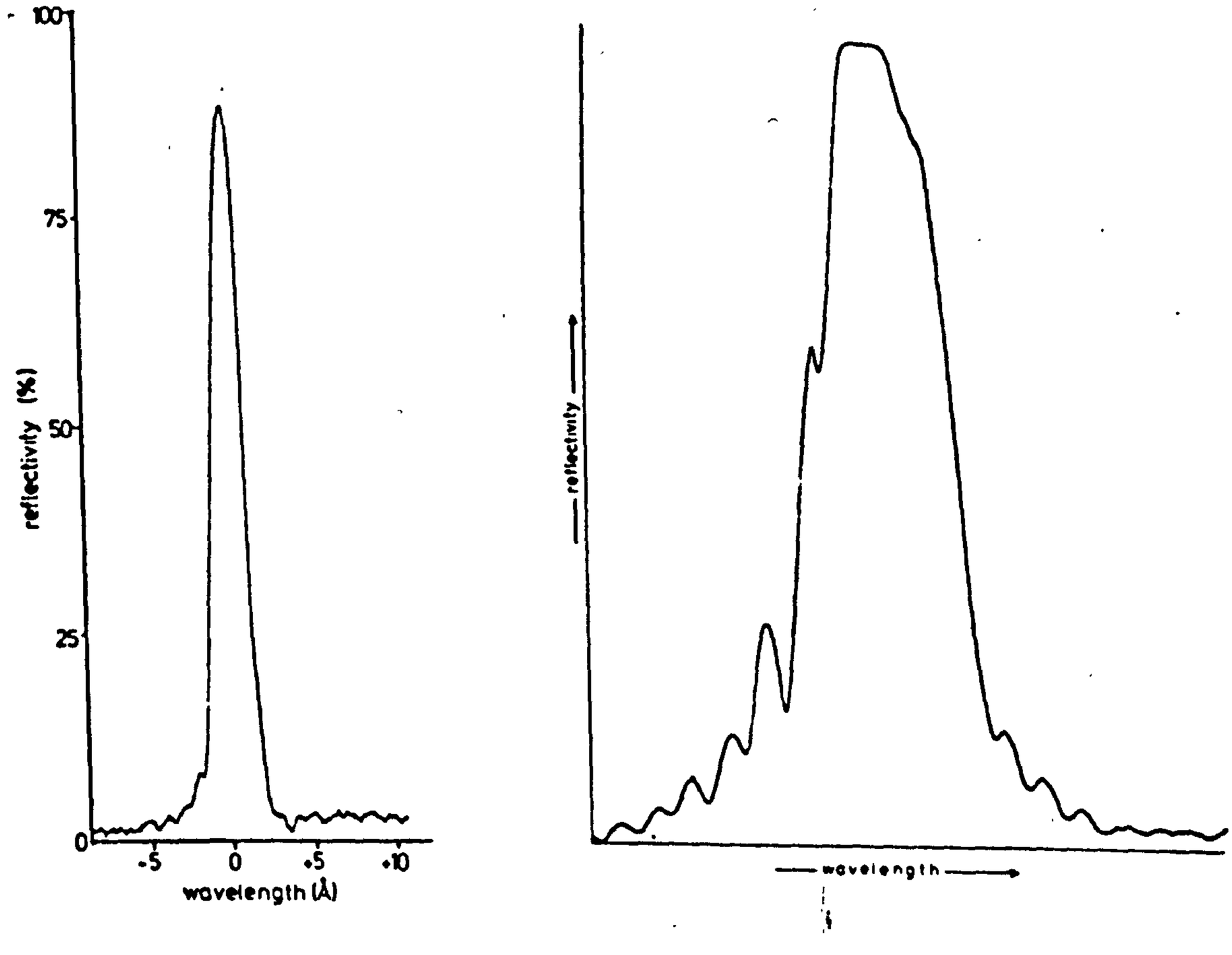

FIG 5.9 Sample Tracing of Four-Layer Experimental Filters.

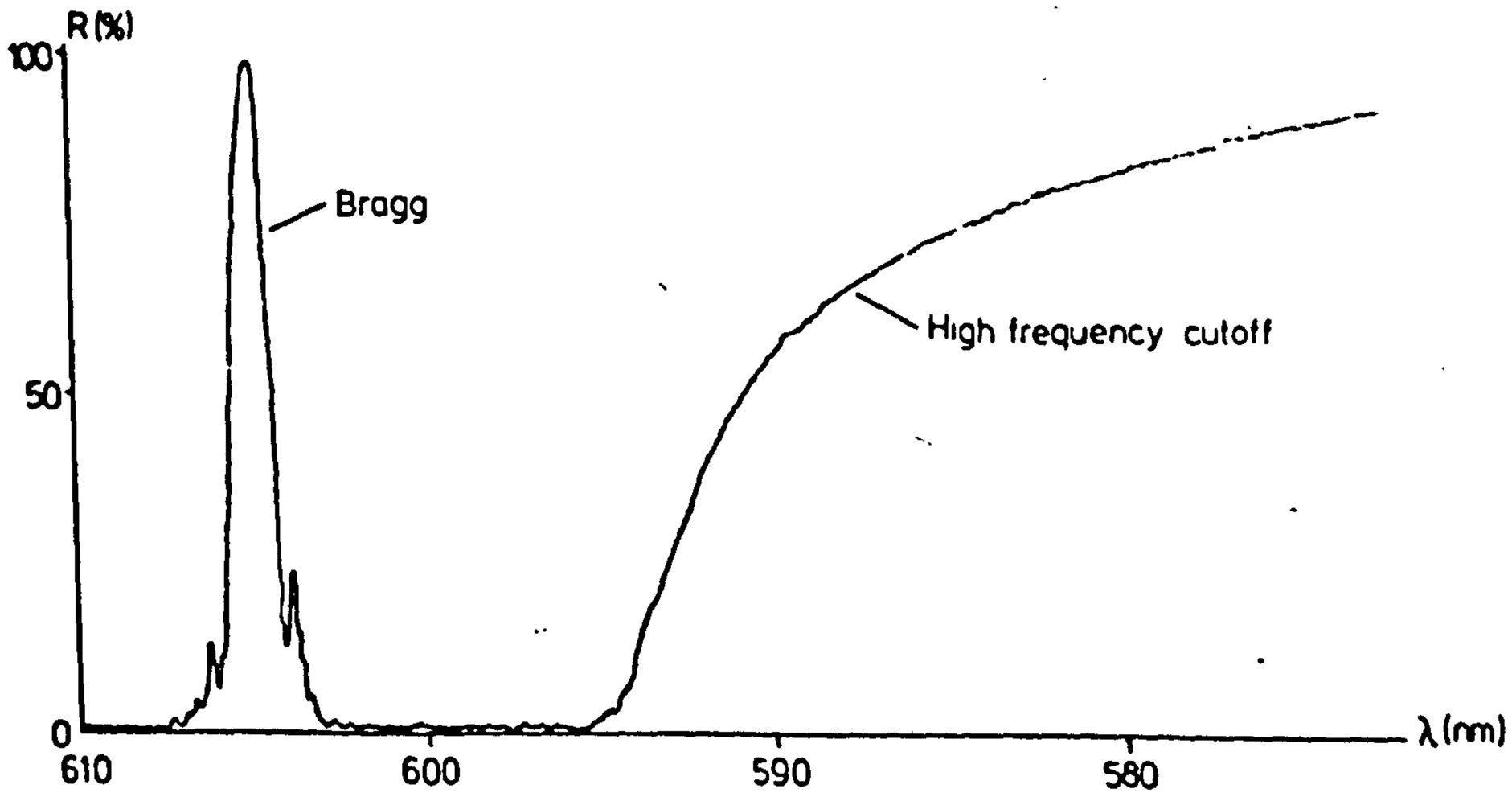

FIG 5.10 Experimental Curve Showing Bragg Interaction and High Frequency Cut off Properties of a Filter.

cases are related to the fractional change in bandwidth in a near unity relationship as dictated by equation (5.9) and the high values of the product κL. Finally, all four-layer filters show good agreement in the figures for the reflectivity of the main lobe. With a large value of κL, the variation in R_0 is generally negligible (equation 5.10) and the small discrepancies in the results can be attributed solely to measurement errors. A qualitative sample tracing of a typical four-layer inhomogeneous waveguide filter is shown in Fig.5.9 where large out of band ripples arising from high sidelobe levels as predicted by theory can be observed. Fig.5.10 shows the Bragg interaction and the high frequency cut-off properties of filter D127.

5.5 An Experimental Unit Cell Demultiplexer

Demultiplexers have been realized using chirped gratings on the surface of the waveguides. Such devices work on the basis of a distributed Bragg condition, in space, along the length of the grating structure. In order to provide a spatial separation among the demultiplexed channels, the mode is required to be incident at an angle to the grating. Demultiplexers of this type, however, suffer from limitations on design which can not easily be overcome. For a given value of the coupling coefficient κ, the bandwidth and reflectivity are related to the interaction length. With a chirped grating, the Bragg condition is satisfied inside a small portion of the grating only; this implies that the reflectivity is generally low and the bandwidth of the individual channels relatively large. If the chirp function, on the one hand, is slow, i.e. the Bragg condition is allowed to exist over a longer portion of the grating, the deflected beams tend to widen laterally; if, on the other hand, the function is fast, the deflected beams will have minimum spatial separation. In either case, the situation reduces to a problem of channel cross talk and a problem of

FIG 5.11 Schematic Diagram of a Two-dimensional Crossed Grating Demultiplexer.

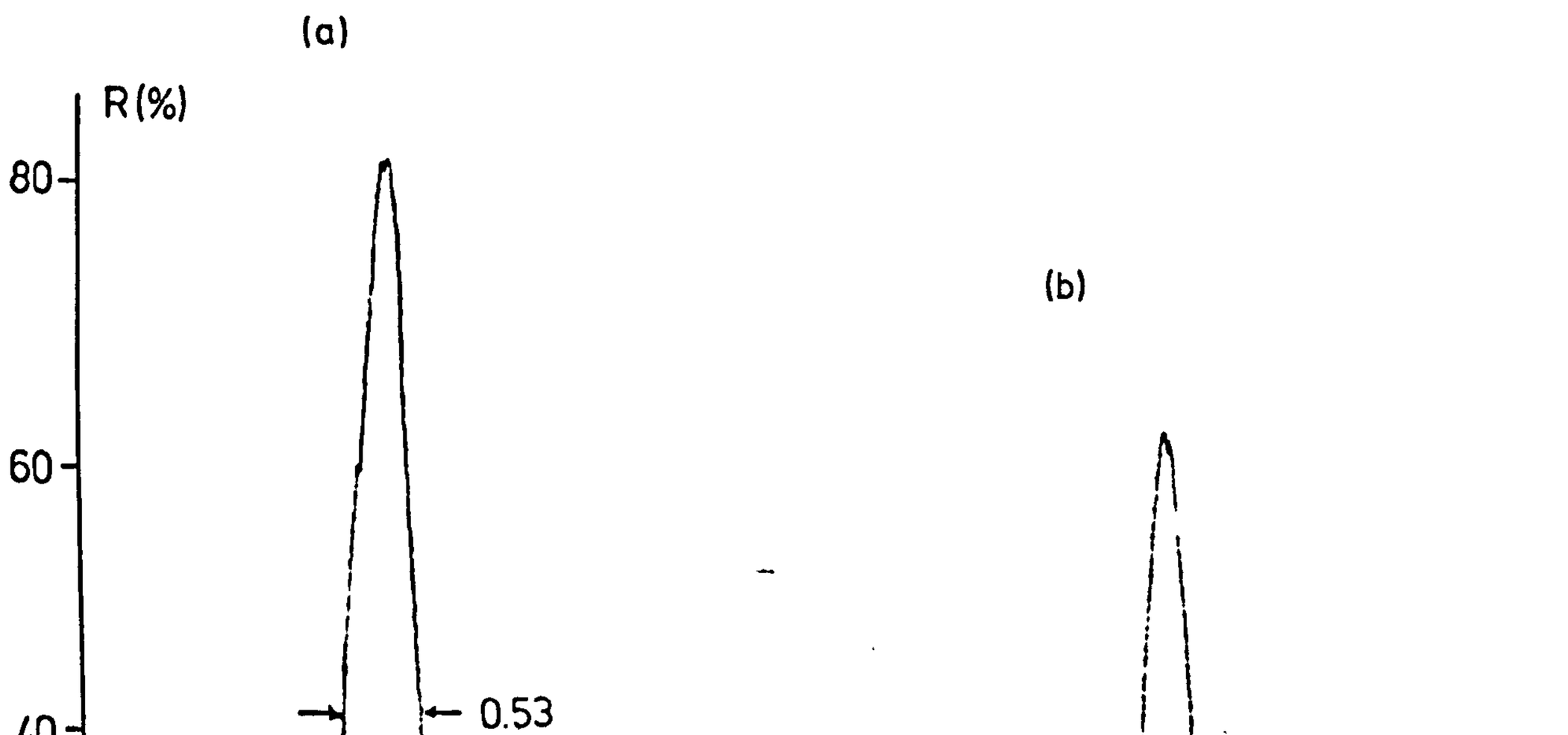

FIG 5.12 Response of Demultiplexer Depicted in Fig 5.11

interfacing the demultiplexer with other devices on the same substrate.

In this work, a novel design for a unit cell demultiplexer is proposed. The device is constructed on a homogeneous waveguide and using a two-dimensional (photoresist) crossed grating. The individual one-dimensional gratings have the same (constant) periodicity, but are orientated at 10.0° and 10.5° on either side of an axis which is parallel to the short side of the standard microscope slide (see Fig.5.11). Light was launched into the guide and reflection of the mode from the combined grating structure was observed at wavelengths which satisfied the Bragg condition. The separation of the Bragg wavelengths could be varied by changing the incident angle of the guided mode onto the grating structure. Simultaneous interaction was also observed at an incident angle which was collinear to the bisector of the two set of grating lines. A typical response curve of the device is shown in Fig.5.12 and Fig.5.13 shows a photograph of the performance of the demultiplexer. It can be observed that the spatial separation of the deflected beam prevents the existence of cross talking, furthermore, using small angles of orientation for the grating lines, the emerging beams from the structure do not expand laterally to a great extent.

The advantage of the device are threefold. Firstly, the bandwidth and reflectivity can be controlled by choosing a proper length of interaction. Second, the spatial positions of the deflected beams provide easy access, for instance in the coupling to a fiber or other related devices, and dispense with the problem of channel cross talk. Third, since the Bragg condition can be varied by changing the orientation of the grating line, a bank of demultiplexers can be integrated into a small area of the substrate by a simple mechanical movement during the fabrication process (see Chapter IV).

FIG 5.13 Photograph of Demultiplexer.

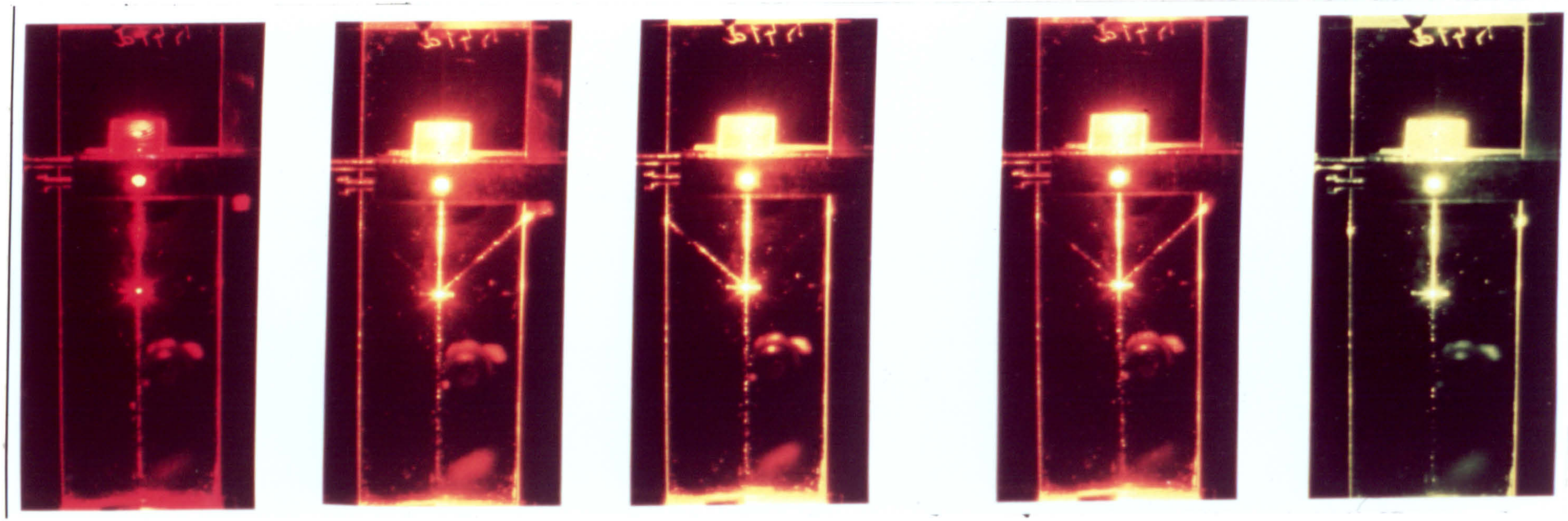

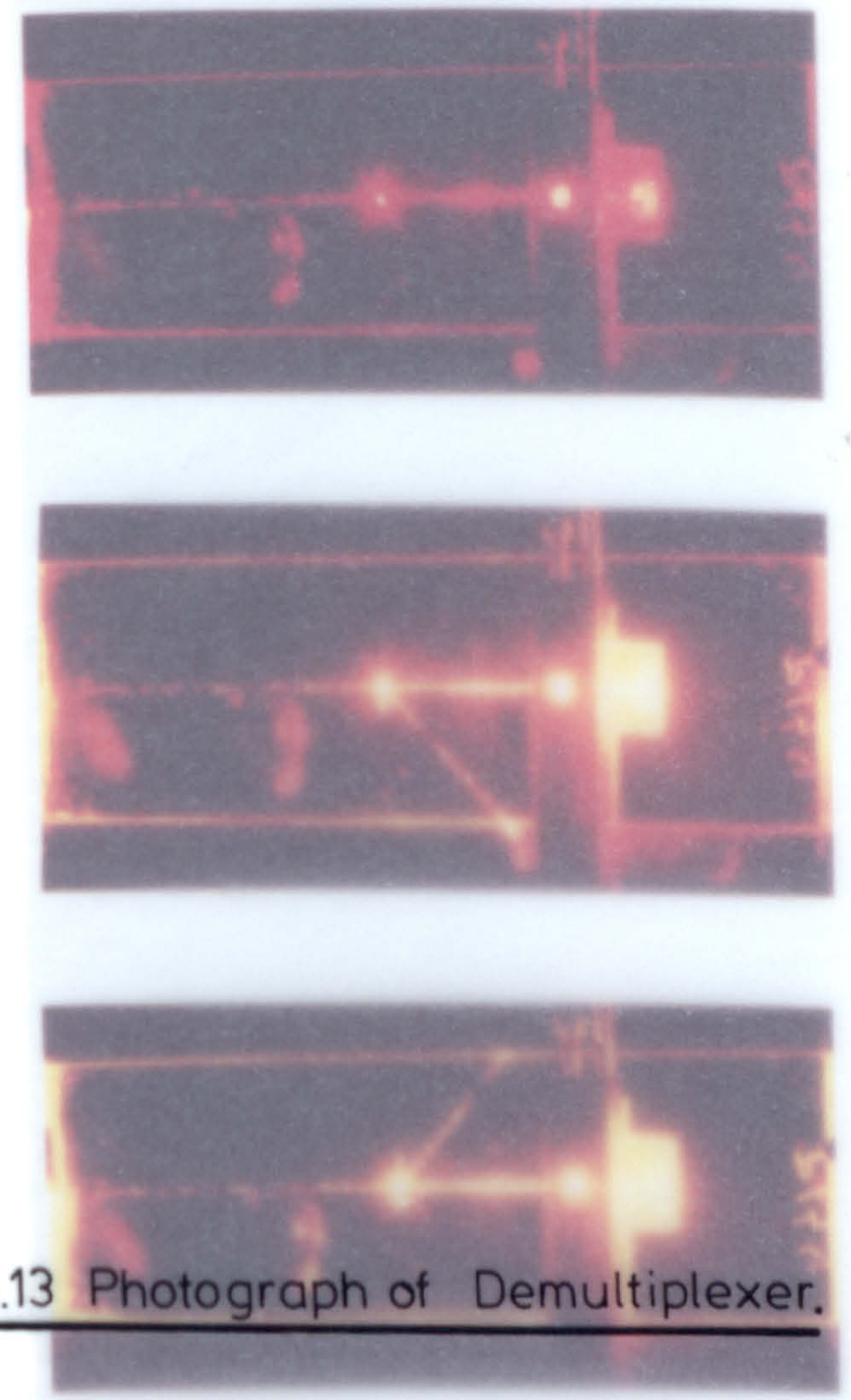

FIG 5.13 Photograph of Demultiplexer.

CHAPTER VI

CONCLUSIONS

6.1 Summary and General Conclusions

This thesis is concerned with the theoretical and experimental analysis of Bragg waveguide filters formed in single-mode homogeneous and inhomogeneous planar waveguides.

Homogeneous waveguides were formed by sputtering Corning 7059 glass onto standard microscope glass slides; inhomogeneous waveguides were formed by the silver-sodium ion exchange process. Filters were fabricated by forming a thin phase photoresist grating on the surface of the guide or by etching the pattern directly onto the surface of the waveguide; accordingly, filters were further classified into three- and four-layer types.

The theoretical analysis in Chapter II describes the properties of wave propagation in the basic guiding structures, that is, in waveguides without the periodic corrugation on the surface. It is shown that the ray optics approach can be successfully used in the determination of the dispersion relation for guided modes in the various waveguides considered. Homogeneous waveguides are studied using an analytical solution to the wave equation. Inhomogeneous waveguides are assumed to have a refractive index distribution which follows a second order polynomial and has a surface peak index of 1.585. The analysis of inhomogeneous guides were carried out using approximate WKB and multilayer division techniques. It was shown that both techniques predict well the value of the propagation constant; however, discrepancies were found in the evaluation of the corresponding field distributions. These discrepancies arise from the inherent failure

of the WKB equations in regions near the turning point of the guided mode. The multilayer technique proved to give a better approximation and has been used throughout this work. In all four-layer waveguides, the index of refraction of the resist films was higher than the index of the original guiding layers; consequently, the field tended to concentrate more strongly within the thickness of the overlay film. In the homogeneous cases, it is shown that the dispersion relation can be calculated from a transmission line analogue model. In the inhomogeneous cases, the large index mismatch at the resist-diffused layer interface and associated reflection of the wave preclude, in principle, the use of the WKB technique in their analysis; however, it is shown that this apparent limitation does not have serious drawbacks in the calculated propagation constant for the mode.

The properties of sinusoidally corrugated (type II) Bragg waveguide filters are analysed using the coupled mode formalism. The use of this perturbational method is justified primarily by the small magnitude of the corrugation height h of the grating. For small values of h, the analysis of the fields in a type II waveguide can be carried out using the rigorous Floquet infinite series solution which is associated with periodic waveguides with index modulation (type I). It is shown that for shallow sinusoidal corrugation, the coupled mode formalism can be derived from a direct analysis on a truncated Floquet series, where only the fundamental and related first harmonics are taken into account. A coupled wave analysis which relates the power exchange of the incident and reflected waves in terms of a coupling coefficient κ and the wavelength dependence of the interaction by a normalised frequency σ is given. It is shown that κ is a function of the waveguide parameters and of the grating height h; the normalised frequency σ is shown to be related to the length of interaction L.

The relation between filter response and the Fourier transform of the function which modulates the corrugation height and grating periodicity is presented. For a uniform grating the corresponding filter response follows a $(\text{sinc})^2$ function and the reflectivities of the main lobe and related sidelobes are function of the product κL.

It is pointed out that, in the design of filters, it is desirable to use waveguides structures with low κ/h; narrower bandwidth could then be obtained and the response could be tailored by the most accessible parameters, namely the grating height h and the length of interaction L. From the various waveguide structures considered in this work, the three-layer type waveguides have the lowest values for κ/h. In the four-layer type waveguides, the value of the field at the surface of the guide is increased by the presence of a high index film of resist; accordingly, a greater degree of perturbation resulted and the values of κ/h are correspondingly larger. It was shown in the case of three-layer waveguides that the value of κ/h can be reduced by minimising the difference between the film and substrate (superstrate) indices. For Corning 7059 glass waveguides, lower film indices can be obtained if the rf power is reduced; alternatively, higher index substrates can be used to achieve the same effect.

Interferometric techniques in the manufacture of gratings were investigated in some detail. It was shown that the quality of holographic gratings is limited by the wavefront quality of the beam and, also, by the effects of multiple reflections at the several layer interfaces comprising the samples. The expose and develop technique (ED) was successfully used in the production of gratings in very thin film of resist. For gratings with grooves cut down to the substrate, the simultaneous exposure and development (SED) technique was superior; the

nature of the process allowed for thicker layer of resist to be used with no apparent deterioration of the groove shape. Gratings for Bragg waveguide filters were fabricated using the argon laser 457.9 nm line, in conjunction with the front prism technique (FPT). As a very thin film is required in this ED process, an investigation on the properties of AZ1300 positive resists was necessary. It was shown that the AZ1350J and AZ1370 resists were best suited for this application, because of their resolving capabilities and, most of all, their low viscosities. Used in dilution with thinner in the proportion of 1 to 3, the optimum spin coating conditions were found to be 4000 RPM and 20 seconds. The refractive indices of these resists were determined from mode angle measurements using a high index symmetrical prism. It was shown that AZ1370 resist has a higher index value than AZ1350J.

Tapering of the corrugation height of short period resist gratings by a weighted post-exposure proved unsuccessful. It is felt that this failure can be attributed in part to the need to employ very thin resist films. It was shown that, even in cases of unweighted pre- or post-exposure of gratings in thin film of resist a patchy appearance of the patterns resulted. The technique was, however, successful in samples where the grating period was long and the resist layer was thick. Attempts to introduce chirping effects were also carried out experimentally. It was shown that, theoretically, the use of a dielectric slit positioned in the path of one of the beams in the interferometer could result in gratings whose periodicity had a nearly periodic chirp, while the amplitude was modulated by the far field diffraction pattern of the slit. The implementation of the slit with the FPT technique to produce short period grating was not successful because of the wavefront

filters were produced by ion beam etching the resist grating onto the surface of the guide. It was shown that, the reduction of the sample to neutralizing grid distance, is of paramount importance in this process. During etching, samples are subject to high temperatures which cause the resist pattern to flow. Success in the transfer of the pattern depends primparily on having the resist film cut down to the substrate. For the cases of ion-exchanged waveguides, it was shown that the high temperatures arising from the process destroy the waveguiding properties of the samples. An alternative solution was demonstrated whereby the grating pattern was first etched onto the substrate glass and then ion-exchanged. It appeared that the success rate, in these cases, is dependent on the cleanliness of the substrates before the ion-exchange process.

Experimental filters were successfully fabricated and their responses were compared with theory. It was shown that for the three-layer filters the results are in excellent agreement. Some discrepancies were found in the cases of four-layer type homogeneous filters, however, the differences were fully accounted for by evaluating the effects of errors in the determination of the effective guide index of the four-layer region and in the determination of the index of resist films. The experimental results from the four-layer inhomogeneous waveguide filters showed poor agreement with the theoretical figures. In these cases, the magnitudes of the product κL were extremely high; consequently, any small variation in the value of κ was directly reflected in the value of the bandwidth. With high values of κL, the variation in the reflectivities are negligible, however, sidelobe levels become comparable to the main lobe and the zero to sidelobe separations become smaller. Since the linewidth of the laser was much broader than these separations for the first few sidelobes, it was found difficult, in

general, to correlate exactly the experimental responses with those calculated from theory.

In conclusion, Bragg waveguide filters have been successfully analysed theoretically and experimentally. Results have shown that the three-layer cases are the most viable structures in the realisation of these devices, because they allow greater control on the design. The introduction of tapers and chirps in the grating structure at the photolithographic stage was, in general, unsuccessful. Such modifications might be introduced successfully if a shorter wavelength UV source is used in the production of gratings; this would relax the effects of multiple reflections and dispense of the use of the front prism.

6.2 Future Work

It is apparent that, with the presently available integrated light sources, notably the DFB laser, filters will be required to be narrow-band and have low sidelobe levels for improved discrimination of the multiplexed signals. Narrow-band filters can be realised using waveguide structures with low value of κ/h, sidelobe levels can be reduced by introducing a parabolic taper in the grating corrugation. The difficulties in introducing tapers in the photolithographic stage were highlighted in Chapter IV, however, it may be possible that such alterations can be introduced during the ion beam etching process by aperturing the ion beam with a slit. The width of the slit could then be varied with time according to the shape of the taper function. An investigation would be required to establish the possibility of controlling accurately the movement of the slit and to incorporate such unit into a viable ion beam etching equipment.

The advantages of the two-dimensional grating demultiplexer demonstrated in this work were pointed out in Chapter V. A theoretical analysis is required to determine the properties of this device, in order

to realise its full potential. The basic problem is to investigate the effects of non-normal incidence of the mode onto the grating and the associated mixed polarisation of the resulting source driving the reflected wave.

It is now well established that devices in future integrated optical circuits will be interconnected by means of rectangular or stripe waveguides. These guiding structures, with their lateral confinement of the guided light, provide lower cross-talk interference and enable closer packing of devices on a substrate. A logical development from the study of slab Bragg waveguide filters is the applications of their results in the realisation of Bragg filters in rectangular guides. Bragg reflection can also be used to advantage at the junction points of the interconnecting stripe waveguides. In the specific case of Y-junctions, power division and mode conservation are seriously affected by the change in width at the junction point. These effects have restricted the angular separation of the output arms to angles below 2^{o}. The conceptual model of ray optics suggests it may be possible to use a grating to deflect the guided wave from the input guide into the branching arm; power division could, then, be controlled by altering the geometry of the grating structure. A viable Y-junction for this application is given in Fig.6.1 where it can be observed that the direction of propagation of the guided wave is opposite to the direction normally used in the conventional Y-junctions.

The theoretical and experimental analysis of Bragg devices in stripe waveguides are considerably more difficult. Several approximate techniques exist to predict the modal propagation constant for stripe waveguides, however, a careful analysis will be needed to find out the required degree of accuracy with which the field distribution must be calculated in these analyses. Experimentally, it will be required to

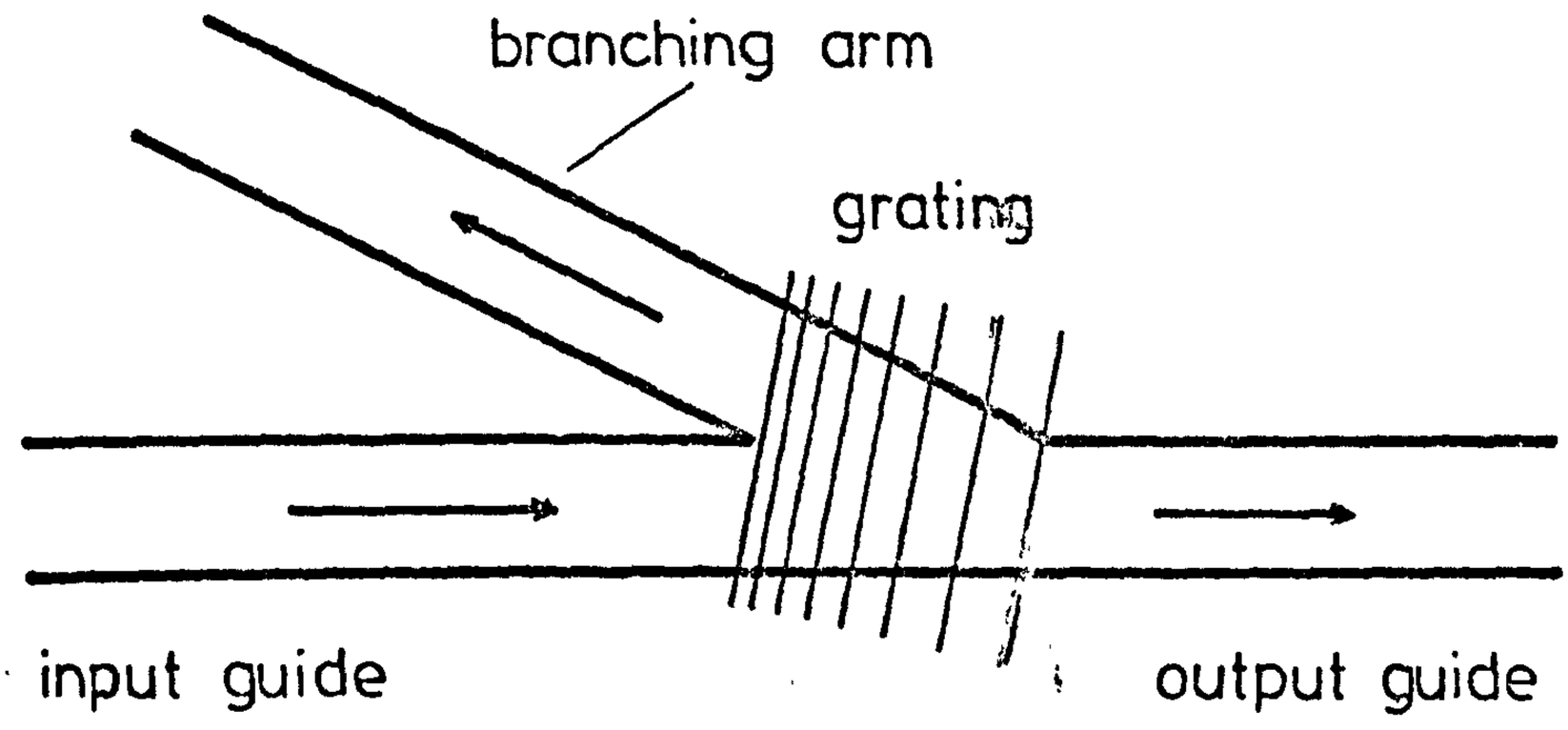

FIG 6.1 Proposal for a Y-Junction which Uses a Grating to Deflect the Incident Mode into the Branching Arm.

develop accurate techniques to align the angular position of the grating with respect to the waveguide. The spin coating of resist, when using ridge waveguides, may pose a problem, however, this can be circumvented if the grating pattern is first etched down to the substrate, as in the case of ion-exchanged planar Bragg filters.

REFERENCES

1. MILLER, S.E.
   Integrated Optics : An Introduction.
   BELL SYST. TECH. J., 48, 7, p.2059 (1969).

2. MILLER, S.E., E.A.J. MARCATILI, and T. LI.
   Research Toward Optical-Fiber Transmission Systems. (Part I and Part II).
   PROC. IEEE, 61, 12, p.1703 (1973).

3. TAYLOR, H.F., and A. YARIV.
   Guided Wave Optics.
   PROC. IEEE, 62, 8, p.1044 (1974).

4. INTEGRATED OPTICS.
   Topics in Applied Physics, Volume 7,
   T. TAMIR Ed., SPRINGER-VERLAG, HEIDELBERG (1975).

5. TIEN, P.K.
   Integrated Optics and New Wave Phenomena in Optical Waveguides.
   REV. MODERN PHYS., 49, 2, p.361 (1977).

6. HONDROS, D. and P. DEBYE.
   Elektromagnetische Wellen an Dielektrischen Drahten.
   ANN. PHYS., 32, p.465 (1910).

7. COLLIN, R.E.
   Field Theory of Guided Waves.
   McGRAW HILL, NEW YORK, p.470 (1960).

8. KAPLAN, R.A.
   Optical Waveguide of Macroscopic Dimensions in Single Mode Operation.
   PROC. IEEE, 51, 8, p.1144 (1963).

9. BOND, W.L., B.G. COHN, R.C.C. LEITE, and A. YARIV.
   Observation of Dielectric-Waveguide Mode of Light Propagation in p-n Junctions.
   APPL. PHYS. LETT., 2, 3, p.57 (1963).

10. TIEN, P.K., R. ULRICH, and R.J. MARTIN.
    Modes of Propagating Light Waves in Thin Deposited Semiconductor Films.
    APPL. PHYS. LETT., 14, 9, p.291 (1969).

11. SOMEKH, S., E. GARMIRE, and A. YARIV.
    Channel Optical Waveguides and Directional Couplers in GaAs - Imbedded and Ridged.
    APPL. OPT., 13, 2, p.327 (1974).

12. HARPER, J., and E. SPILLER.
    High Resolution Lens for Optical Waveguides.
    PAPER WB11, SECOND TOPICAL MEETING ON INTEGRATED OPTICS, NEW ORLEANS (1974).

13. PENNINGTON, K.S., and KUHN, L.
    Bragg Diffraction Beam Splitter for Thin Film Optical Waves.
    OPT. COMM., 3, 5, p.357 (1971).

14. TIEN, P.K., S. RIVA SANSEVERINO, R.J. MARTIN, and G. SMOLINSKY.
    Two-Layer Construction of Integrated Optical Circuits and Formation of Thin Film Prisms, Lenses and Reflectors.
    APPL. PHYS. LETT., 24, 11, p.547 (1974).

15. PANISH, M.B.
    Heterostructure Injection Lasers.
    IEEE Trans. MTT., 23, 1, p.20 (1975).

16. TIEN, P.K.
Optical Second Harmonic Generation in Form of Coherent Cerenkov Radiation from a Thin-Film Waveguide.
APPL. PHYS. LETT., 17, 10, p.447 (1970).

17. SCHMIDT, R.V., and I.P. KAMINOW.
Acoustooptic Bragg Deflection in $LiNbO_3$ Ti-diffused Waveguides.
IEEE. J. QUANT. ELECT., 11, 1, p.57 (1975).

18. HALL, D., A. YARIV, and E. GARMIRE.
Observation of Propagation Cut-Off and its Control in Thin Optical Waveguides.
APPL. PHYS. LETT., 17, 3, p.127 (1970).

19. KAMINOW, I.P.
Optical Waveguide Modulators.
IEEE TRANS. MTT, 23, 1, p.57 (1975).

20. DAKSS, M.L., L. KUHN, P.F. HEIDRICH, and B.A. SCOTT.
Grating Couplers for Efficient Excitation of Optical Guided Waves in Thin Films.
APPL. PHYS. LETT., 16, 12, p.523 (1970).

21. KOGELNIK, H., T. SOSNOWSKI.
Holographic Thin Film Couplers.
BELL SYST. TECH. J., 49, 7, p.1602 (1970).

22. DALGOUTTE, D.G.
A High Efficiency Thin Grating Coupler for Integrated Optics.
OPT. COMM., 8, 2, p.124 (1973).

23. DABBY, F.W., M.A. SAIFI, and A. KESTENBAUN.
High-Frequency Cut-Off Periodic Dielectric Waveguides.
APPL. PHYS. LETT., 22, 4, p.190 (1973).

24. FLANDERS, D.C., H. KOGELNIK, R.V. SCHMIDT, and C.V. SHANK.
Grating Filters for Thin-Film Optical Waveguides.
APPL. PHYS. LETT., 24, 4, p.194 (1974).

25. SCHMIDT, R.V., D.C. FLANDERS, C.V. SHANK, and R.D. STANDLEY.
Narrow Band Grating Filters for Thin Film Optical Waveguides.
APPL. PHYS. LETT., 25, 11, p.651 (1974).

26. KOGELNIK, H., and C.V. SHANK.
Stimulated Emission in a Periodic Structure.
APPL. PHYS. LETT., 18, 4, p.152 (1971)

27. KAMINOW, I.P., H.P. WEBER, and E.A. CHANDROSS.
Poly (Methyl Methacrylate) Dye Lasers with Internal Diffraction Grating Resonator.
APPL. PHYS. LETT., 18, 11, p.497 (1971).

28. GIA RUSSO, D.P., and J.H. HARRIS.
Electrooptic Modulation in a Thin Film Waveguide.
APPL. OPT., 10, 12, p.2786 (1971).

29. OGAWA, K., W.S.C. CHANG, B. SOPORI, and F.J. ROSENBAUN.
Grating Mode Convertor/Directional Coupler for Integrated Optics.
J. OPT. SOC. AM., 63, 4, p.478 (1973).

30. KINSEL, T.S.,
Wide-Band Optical Communication Systems: Part 1 - Time Division Multiplexing.
PROC. IEEE, 58, 10, p.1666 (1970).

31. DE LANGE, O.E.
Wide-Band Optical Communication Systems : Part II - Frequency Division Multiplexing.
PROC. IEEE, 58, 1, 10, p.1683 (1970).

32. BLUM, F.A.,
Monolithic GaAs Circuit Elements for Integrated Optics.
J. OPT. SOC. AM., 66, 3, p.288 (1976).

33. HILL, K.O.
Aperiodic Distributed Parameter Waveguides for Integrated Optics.
APPL. OPT., 13, 8, p.1853 (1974).

34. MATSUHARA, M., and K.O. HILL.
Optical-Waveguide Band-Rejection Filters: Design.
APPL. OPT., 13, 12, p.2886 (1974).

35. MATSUHARA, M., K.O. HILL, and A. WATANABE.
Optical-Waveguide Filters : Synthesis.
J. OPT. SOC. AM., 65, 7, p.804 (1975).

36. KOGELNIK, H.
Filter Response of Nonuniform Almost-periodic Structures.
BELL. SYST. TECH. J., 55, 1, p.109 (1976).

37. STREIFER, W., D.R. SCIFRES, and R.D. BURNHAM.
Perturbation Analysis of Nonuniform Almost-periodic Bragg Reflectors.
J. OPT. SOC. AM., 66, 12, p.1359 (1976).

38. AIKI, K., M. NAKAMURA, and J. UMEDA.
Frequency Multiplexing Light Source with Monolithically Integrated Distributed - feedback Diode Lasers.
APPL. PHYS. LETT., 29, 8, p.506 (1976).

39. SITTIG, E.K., and G.A. COQUIN.
Filters and Dispersive Delay Lines Using Repetitively Mismatched Ultrasonic Transmission Lines.
IEEE TRANS. SON. ULTRAS., 15, 2, p.111 (1968).

40. Computer-Aided Design of SAW Devices.
WAVE ELECTRONICS - Special Issue.
(various papers) 2, 1-3 (1976).

41. LIVANOS, A.C., A. KATSIR, A. YARIV.
Fabrication of Grating Structures with Variable Period.
OPT. COMM., 20, 1, p.179 (1977).

42. KATSIR, A., A.C. LIVANOS, A. YARIV.
Chirped-Grating Output Couplers in Dielectric Waveguides.
APPL. PHYS. LETT., 30, 5, p.225 (1977).

43. LIVANOS, A.C., A. KATSIR, A. YARIV, and C.S. HONG.
Chirped-Grating Demultiplexers in Dielectric Waveguides.
APPL. PHYS. LETT., 30, 10, p.519 (1977).

44. BEESLEY, M.J., J.G. CASTLEDINE, and D.P. COOPER
Sensitivity of Resist-Coated Silicon Slices to Argon-Laser Wavelengths.
ELECT. LETT., 5, 12, p.257 (1969).

45. BARTOLINI, R.A.
Improved Development for Holograms Recorded in Photoresist.
APPL. OPT., 11, 5, p.1275 (1972).

46. DILL, F.H., W.P. HOENBERGER, P.S. HANGE, and J.M. SHAW.
Characterisation of Positive Photoresit.
IEEE TRANS. ELECT. DEVICES, 22, 7, p.445 (1975).

47. DILL, F.H., W.P. HOENBERGER, P.S. HANGE, and J.M. SHAW.
Modelling Projection Printing of Positive Photoresists.
IEEE TRANS. ELECT. DEVICES, 22, 7, p.456 (1975).

48. DILL, F.H., and J.M. SHAW.
Thermal Effects on the Photoresist.
AZ 1350J.
IBM J. RES. DEVELOP., 21, 3, p.210 (1977).

49. SHAW, J.M., M.A. FRISCH and F.H. DILL
Thermal Analysis of Positive Photoresist Films by Mass Spectrometry.
IBM J. RES. DEVELOP., 21, 3, p.219 (1977).

50. KONNERTH, K.L.
In-Situ Measurement of Dielectric Thickness During Etching or Developing Processes.
IEEE TRANS. ELECT. DEVICES, 22, 7, p.452 (1975).

51. WALKER, E.J.
Reduction of Photoresist Standing-Wave Effects by Post-Exposure Bake.
IEEE Trans. ELECT. DEVICES, 22, 7, p.464 (1975).

52. McGILLIS, D.A., D.L. FEHRS.
Photolithographic Linewidth Control.
IEEE TRANS. ELECT. DEVICES, 22, 1, p.471 (1975).

53. WIDMANN, D.W.
Linewidth Variations in Photoresist Patterns on Profiled Surfaces.
IEEE TRANS. ELECT. DEVICES, 22, 7, p.467 (1975).

54. WASHO, B.D.
Rheology and Modeling of the Spin Coating Process.
IBM J. RES. DEVELOP., 21, p.190 (1977).

55. TSANG, W.T., and S. WANG.
Simultaneous Exposure and Development Technique for Making Gratings on Positive Photoresist.
APPL. PHYS. LETT., 25, 7, p.415 (1974).

56. DALGOUTTE, D.G.
Periodic Couplers for the Excitation of Optical Guided Waves in Thin Films.
Ph.D THESIS, DEPT. of ELECTRICAL ENGINEERING.
UNIVERSITY OF GLASGOW (1973).

57. SHANK, C.V., and R.V. SCHMIDT.
Optical Technique for Producing 0.1μm Periodic Surface Structures.
APPL. PHYS. LETT., 23, 3, p.154 (1973).

58. GIALLORENZI, T.G., E.J. WEST, R. KIRK, R. GINTER, and R.A. ANDREWS.
Optical Waveguides Formed by Thermal Migration of Ions in Glass.
APPL. OPT., 12, 6, p.1240 (1973).

59. GOELL, J.E., and R.D. STANDLEY.
Sputtered Glass Waveguides for Integrated Optical Circuits.
BELL SYST. TECH. J., 48, 12, p.3445 (1969).

60. TIEN, P.K.
Light Waves in Thin Films and Integrated Optics.
APPL. OPT., 10, 11, p.2395 (1971).

61. BORN, M., E. WOLF.
Principles of Optics.
4th EDITION, PERGAMON PRESS, LONDON, (1970).

62. RAMO, S., J.R. WHINNERY, and T. VAN DUZER.
Fields and Waves in Communication Electronics.
2nd EDITION, JOHN WILEY INC., NEW YORK, (1965).

63. KAMINOW, I.P., and J.R. CARRUTHERS.
Optical Waveguiding Layers in $LiNbO_3$ and $LiTaO_3$.
APPL. PHYS. LETT., 22, 7, p.326 (1973).

64. SCHMIDT, R.V., and I.P. KAMZNOW.
Metal-Diffused Optical Waveguides in $LiNbO_3$.
APPL. PHYS. LETT., 25, 8, p.458 (1974).

65. TAYLOR, H.F., W.E. MARTIN, D.B. HALL, and V.N. SMILEY.
Fabrication of Single-Crystal Semiconductor Optical Waveguides by Solid State Diffusion.
APPL. PHYS. LETT., 21, 3, p.95 (1972).

66. NODA, J., T. SAKU, and N. UCHIDA.
Fabrication of Optical Waveguide Layer in $LiTaO_3$ by Cu Diffusion.
APPL. PHYS. LETT., 25, 5, p.308 (1974).

67. WEI, D.T.Y., W.W. LEE, and L.R. BLOOM.
Quartz Optical Waveguide by Ion Implantation.
APPL. PHYS. LETT., 22, 1, p.5 (1973).

68. KOGELNIK, H.
Theory of Dielectric Waveguides.
TOPICS IN APPL. PHYS. VOLUME 7, CHAPTER 2,
SPRINGER-VERLAG, HEIDELBERG (1975).

69. HARRIS, J.H., R. SHUBERT, and J.N. POLKY.
Beam Coupling to Films.
J. OPT. SOC. AM., 60, 8, p.1007 (1970)

70. VASSELL, M.O.
Structure of Optical Guided Modes in Planar Multilayers of Optically Anisotropic Materials.
J. OPT. SOC. AM., 64, 2, p.166 (1974)

71. GORDON, J.P.
Optics of General Guiding Media.
BSTJ, 45, 2, p.321 (1966).

72. See for Example LANDAU L.D., and E.M. LIFSHITZ.
QUANTUM MECHANICS, PERGAMON PRESS, OXFORD (1958)

73. BREKHOVSKIKH, L.M.
Waves in Layered Media.
ACADEMIC PRESS, NEW YORK (1960).

74. TIEN, P.K., S. RIVA-SANSEVERINO, and R.J. MARTIN.
Optical Waveguide Modes in Single-Crystalline $LiNbO_3$ Solid-Solution Films.
APPL. PHYS. LETT., 24, 10, p.503 (1973).

75. MARCUSE, D.
TE Modes of Grated Index Slab Waveguides.
IEEE J. QUANT. ELECT., 9, 10, p.1000 (1973).

76. GEDEON, A.
Formation and Characteristics of Grated-Index Optical Waveguides Buried in Glass.
APPL. PHYS., 6, 2, p.223 (1975).

77. SAVATINO, I.
Lightguiding in Ion-Exchanged Glasses.
APPL. PHYS., 11, 3, p.273 (1976).

78. STEWART, G., C.A. MILLAR, P.J.R. LAYBOURN, C.D.W. WILKINSON, and R.M. DE LA RUE.
Planar Optical Waveguides Formed by Silver-Ion Migration in Glass.
IEEE J. QUANT. ELECT., 13, 4, p.192 (1977).

79. GALLAGHER, J., and R.M. DE LA RUE.
TE and TM Mode Analysis of Planar Ion-Exchanged Waveguides.
MICROW. OPT. AND ACOUST., 1, 6, p.215 (1977).

80. GEDEON, A.
Comparison Between Rigourous Theory and WKB Analysis of Modes in Grated-Index Waveguides.
OPT. COMM., 12, 3, p.329 (1974).

81. MILLAR, C., and R.H. HUTCHINS.
Manufacturing Tolerances for Silver-Sodium Ion Exchanged Planar Optical Waveguides.
J. OF PHYS D. (Accepted for publication) (1977).

82. CONWELL, E.
WKB Approximation for Optical Guided Modes in a Medium with Exponentially Varying Index.
J. APPL. PHYS., 46, 3, p.1407 (1975).

83. SHUBERT, R., and J.H. HARRIS.
Optical Surface Waves on Thin Films and their Application to Integrated Data Processors.
IEEE TRANS. MTT, 16, 12, p.1048 (1968).

84. TIEN, P.K., and R.J. MARTIN.
Experiments on Light Waves in a Thin Tapered Film and a New Light-Wave Coupler.
APPL. PHYS. LETT., 18, 9, p.398 (1971).

85. ULRICH, R.
Optimum Excitation of Optical Surface Waves.
J. OPT. SOC. AM., 61, 11, p.1467 (1971).

86. ULRICH, R., and R. TORGE.
Measurements of Thin Film Parameters with a Prism Coupler.
APPL. OPT., 12, 12, p.2901 (1973).

87. PENG, S.T., T. TAMIR, and H.L. BERTONI.
Theory of Periodic Dielectric Waveguides.
IEEE TRANS. MTT, 23, 1, p.123, (1975).

88. NEVIERE, M., R. PETIT, and M. CADILHAC
About the Theory of Optical Grating Coupler-Waveguide Systems.
OPT. COMM., 8, 2, p.113 (1973).

89. NEVIERE, M., P. VINCENT, R. PETIT, and M. CADILHAC.
Systematic Study of Resonances of Holographic Thin Film Couplers.
OPT. COMM., 9, 1, p.48 (1973).

90. DALGOUTTE, D., and C.D.W. WILKINSON.
Thin Grating Couplers for Integrated Optics : An Experimental and Theoretical Study.
APPL. OPT. 14, 12, p.2983 (1975).

91. OGAWA, K., W.S.C. CHANG, B.L. SOPORI, and F.J. ROSENBAUM.
A Theoretical Analysis of Etched Grating Couplers for Integrated Optics.
IEEE J. QUANT. ELECT., 9, 1, p.29 (1973).

92. YARIV, A.
Coupled Mode Theory for Guided Wave Optics.
IEEE J. QUANT. ELECT., 9, 9, p.919 (1973).

93. KOGELNIK, H., and C.V. SHANK.
Coupled-Wave Theory of Distributed Feedback Lasers.
J. APPL. PHYS., 43, 5, p.2327 (1972).

94. WANG, S.
Principles of Distributed Feedback Lasers and Distributed Bragg-Reflector Lasers.
IEEE J. QUANT. ELECT., 10, 4, p.413 (1974).

95. See for Example COLLIN, R.E.
Foundations for Microwave Engineering.
McGRAW HILL, NEW YORK (1966).

96. BRILLOUIN, L.
Wave Propagation in Periodic Structures.
DOVER, NEW YORK (1953).

97. JAGGARD, D.L., and C. ELACHI.
Floquet and Coupled-Waves Analysis of Higher-Order Bragg Coupling in a Periodic Medium.
J. OPT. SOC. AM., 66, 7, p.674 (1976).

98. YARIV, A.,and A. GOVER.
Equivalence of the Coupled Mode and Floquet-Bloch Formalisms in Periodic Optical Waveguides.
APPL. PHYS. LETT., 26, 9, p.537 (1975).

99. SAKUDA, K., and A. YARIV.
Analysis of Optical Propagation in a Corrugated Dielectric Waveguide.
OPT. COMM., 8, 1, p.1 (1973).

100. DABBY, F.W., A. KESTENBAUM, and U.C. PAEK.
Periodic Dielectric Waveguides.
OPT. COMM., 6, 2, p.125 (1972).

101. STOLL, H., and A. YARIV.
Coupled-Mode Analysis of Periodic Dielectric Waveguides.
OPT. COMM., 8, 1, p.5 (1973)

102. STREIFER, W., D.R. SCIFRES, and R.D. BURNHAM.
Coupling Coefficients for Distributed Feedback Single-and Double-Heterostructure Diode Lasers.
IEEE J. QUANT. ELECT., 11, 11, p.867 (1975).

103. HANDA, K., S.T. PENG, and T. TAMIR.
Improved Perturbation Analysis of Dielectric Gratings.
APPL. PHYS., 5, 4, p.325 (1975).

104. KOGELNIK, H.
Coupled Wave Theory for Thick Hologram Gratings.
BELL. SYST. TECH. J., 48, 9, p.2909 (1969).

105. MARCUSE, D.
Theory of Dielectric Optical Waveguides.
ACADEMIC PRESS, NEW YORK (1974).

106. KATZIR, A., A.C. LIVANOS, J.B. SHELLAN and A. YARIV.
Chirped Gratings in Integrated Optics.
IEEE J. QUANT. ELECT., 14, 4, p.296 (1977).

107. CROSS, P.S., and H. KOGELNIK.
Sidelobe Suppression in Corrugated Waveguide Filters.
OPT. LETT., 1, 1, p.43 (1977).

108. CROSS, P.S., and H. KOGELNIK.
Sidelobe Suppression and Band-Broadening in Corrugated-Waveguide Filters.
PAPER A2-1 INTERNATIONAL CONFERENCE ON INTEGRATED OPTICS AND OPTICAL FIBER COMMUNICATION, TOKYO, JAPAN (1977).

109. MARCATILI, E.A.J.
Reflection from Tapered and Chirped Gratings.
PAPER A2-2, INTERNATIONAL CONFERENCE ON INTEGRATED OPTICS AND OPTICAL FIBER COMMUNICATION, TOKYO, JAPAN (1977).

110. SHELLAN, J.B., C.S. HONG, and A. YARIV.
Theory of Chirped Gratings in Broad Band Filters.
OPT. COMM., 23, 3, p.398 (1977).

111. HAUS, H.A., and R.V. SCHMIDT.
Approximate Analysis of Optical Waveguide Grating Coupling Coefficients.
APPL. OPT., 15, 3, p.774 (1976).

112. WEHNER, G.K.
Sputtering by Ion Bombardment.
ADVANCES IN ELECTRONICS AND ELECTRON PHYSICS, VOL. VII, p.239, ACADEMIC PRESS, NEW YORK (1955).

113. GOELL, J.E.
Barium Silicate Films for Integrated Optical Circuits.
APPL. OPT., 12, 4, p.737 (1973).

114. PITT, C.W.
Sputtered Glass Optical Waveguides.
ELECT. LETT., 9, 17, p.401 (1973).

115. PITT, C.W., F.R. GFELLER, and J. STEVENS.
R F Sputtered Thin Films for Integrated Optical Components.
THIN SOLID FILMS, 26, 1, p.25 (1975).

116. COLEMAN, W.J.
Evolution of Optical Thin Films by Sputtering.
APPL. OPT., 13, 4, p.946 (1974).

117. DEITCH, R.H., E.J. WEST, T.G. GIALLORENZI, and J.F. WELLER.
Sputtered Thin Films for Integrated Optics.
APPL. OPT., 13, 4, p.712 (1974).

118. HUTCHINS, R.H., and C.R. STANLEY.
Sputtering.
in TECHNICAL MEMORANDUM OF THE DEPARTMENT of ELECTRICAL ENGINEERING, UNIVERSITY of GLASGOW (1973).

119. HUTCHINS, R.H., and C.R. STANLEY.
Thin Film Thickness Monitor.
in TECHNICAL MEMORANDUM OF THE DEPARTMENT OF ELECTRICAL ENGINEERING, UNIVERSITY OF GLASGOW (1973)

120. ZERNIKE, F.
Fabrication and Measurement of Passive Components.
in TOPICS IN APPLIED PHYSICS, VOL 7,
CHAPTER 5, SPRINGER-VERLAG, HEIDELBERG (1975).

121. RUDOLPH, D., and G. SCHMAHL.
in High Precision Spectroscopic Diffraction Gratings Produced with Laser Light and Photoresist Layers.
OPTIK, 30, 5, p.475 (1970).

122. BEESLEY, M.J., and J.G. CASTLEDINE.
The Use of Photoresist as a Holographic Recording Medium.
APPL. OPT., 9, 12, p.2720 (1970).

123. MURTY, M.V.R.K.
The Use of a Single Plane Parallel Plate as a Lateral Shearing Interferometer with a Visible Gas Laser Source.
APPL. OPT., 3, 4, p.531 (1964).

124. GARVIN, H.L.
Ion Beam Micromachining of Integrated Optics Components.
APPL. OPT., 12, 3, p.455 (1973).

125. CATAGREL, M.
Considerations on High Resolution Patterns Engraved by Ion Etching.
IEEE TRANS. ELECT. DEVICES, 22, 7, p.483 (1975).

126. CANTAGREL, M. and M. MARCHAL
Argon Ion Etching in a Reactive Gas.
J. MAT. SCIENCE, 8, p.1711 (1973).

127. CANTAGREL, M.
Comparison of the Properties of Different Materials Used as Masks for Ion Beam Etching.
J. VAC. SCI. TECHNOL., 12, 6, p.1340 (1975).

128. SOMEKH, S., H.C. CASEY, and M. ILEGEMS
Preparation of High Aspect Ratio Periodic Corrugation by Plasma and Ion Etching.
APPL. OPT., 15, 8, p.1905 (1976).

129. SCHINKE, D.P., R.G. SMITH, E.G. SPENCER, and M.F. GALVIN.
Thin Film Distributed Feedback laser Fabricated by Ion Milling.
APPL. PHYS. LETT., 21, 10, p.494 (1972).

130. ARNOLD, G., and J.A. BORDERS.
Aggregation and Migration of Ion-Implanted Silver in Lithia-Alumina-Silica Glass.
J. APPL. PHYS., 48, 4, p.1488 (1977).

131. ANDERSON, I.
Diffraction of an Electromagnetic Plane Wave by a Thin Dielectric Half-Plane.
TO BE PUBLISHED.

132. See for Example HEAVENS, O.S.
Optical Properties of Thin Solid Films.
BUTTERWORTHS SCIENTIFIC PUBLICATIONS LTD., LONDON (1955).

133. HACSKAYLO, M.
Determination of the Refractive Index of Thin Dielectric Films.
J. OPT. SOC. AM., 54, 2, p.198 (1964).

134. KOGELNIK, H.
Reconstructing Response and Efficiency of Hologram Gratings.
PROC. SYMP. MODERN OPTICS,
POLYTECHNIC PRESS, BROOKLYN, NEW YORK (1967).

135. TOMLINSON, W.J., and H.P. WEBER.
Scattering Efficiency of High-Periodicity Dielectric Etchings: Experiment.
J. OPT. SOC. AM., 63, 6, p.685 (1973).

136. MARCUSE, D.
Higher-Order Scattering Losses in Dielectric Waveguides.
BELL SYST. TECH. J., 51, 8, p.1801 (1972).

137. PENG, S.T., and T. TAMIR.
Effects of Groove Profile on the Perfomance of Dielectric Grating Couplers.
PROC. SYMP. OPTICAL AND ACOUSTICAL MICRO-ELECTRONICS, POLYTECHNIC PRESS, BROOKLYN, NEW YORK (1974).

138. WANG, S.
Proposal of Periodic Layered Waveguide Structures for Distributed Lasers.
J. APPL. PHYS., 44, 2, p.787 (1973).

139. DE WAMES R.E., and W.F. HALL
Conditions for Laser Oscillations in Distributed-Feedback Waveguides.
APPL. PHYS. LETT., 23, 1, p.28 (1973).